Microstructure-Sensitive Creep-Fatigue Interaction Crystal-Viscoplasticity Model for Single-Crystal Nickel-Base Superalloys

A Dissertation
Presented to
The Academic Faculty

by

Ernesto Alejandro Estrada Rodas

In Partial Fulfillment
of the Requirements for the Degree
Doctor of Philosophy in Mechanical Engineering in the
George W. Woodruff School of Mechanical Engineering

Georgia Institute of Technology
May 2017

Microstructure-Sensitive Creep-Fatigue Interaction Crystal-Viscoplasticity Model for Single-Crystal Nickel-Base Superalloys

Approved by:

Dr. Richard W. Neu, Advisor
Woodruff School of Mechanical Engineering
School of Materials Science and Engineering
Georgia Institute of Technology

Dr. Rosario Gerhardt
School of Materials Science and Engineering
Georgia Institute of Technology

Dr. Surya Kalidindi
Woodruff School of Mechanical Engineering
School of Materials Science and Engineering
Georgia Institute of Technology

Dr. David L. McDowell
Woodruff School of Mechanical Engineering
School of Materials Science and Engineering
Georgia Institute of Technology

Dr. Oliver Pierron
Woodruff School of Mechanical Engineering
Georgia Institute of Technology

Date Approved: April 7th, 2017

I dedicate this thesis to my wife, and to my family

ACKNOWLEDGEMENTS

I want to express my deepest gratitude to my advisor Prof. Rick Neu for his invaluable guidance and support. It has been a privilege and a fantastic journey to have worked and learned from such a distinguished scholar. I am also very grateful to my committee members, Prof. Rosario Gerhardt, Prof. Surya Kalidindi, Prof. David McDowell, and Prof. Oliver Pierron for their insights and discussions and for reviewing this dissertation. I also want to extend special thanks to James D. Huggins for all his support, none of my experimental work would be possible without his expertise and guidance. I also want to thank my wife Gena, my parents José and Susana, and my brother José Jr. for their unconditional backing and love. Lastly, I want to acknowledge my sponsors: The U.S. Department of Energy and Siemens Energy Inc., this research and its results could not be possible without their input and without their generous financial support.

TABLE OF CONTENTS

LIST OF TABLES

LIST OF FIGURES

LIST OF SYMBOLS

b	Burgers vector magnitude
C_{44}	*44* Component of the crystallographic elastic tensor in Voigt notation
$\chi_{\gamma}^{(\alpha)}$	Backstress in the γ phase in the α^{th} slip system
δ	Lattice misfit parameter
E	Error function of the Newton-Raphson algorithm
F_{attack}	Debye frequency
$f^{(\alpha)}$	Level function of the α^{th} slip system in the Newton-Raphson algorithm
f_{γ}	Volume fraction of the γ phase
$f_{\gamma'}$	Volume fraction of the γ' phase
$\dot{\mathbf{F}}^{in}$	Inelastic deformation gradient rate
G	Bulk shear modulus as a function of temperature
γ_{APB}	Antiphase boundary energy
$\dot{\gamma}_{\gamma}^{in(\alpha)}$	Inelastic strain rate in the γ phase on the α^{th} slip system
$\dot{\gamma}_{L1_2}^{in(\alpha)}$	Inelastic strain rate in the γ' phase on the α^{th} slip system
$\mathbf{J}$	Jacobian of the Newton-Raphson algorithm
k	Boltzmann constant
$\kappa_{\gamma}^{(\alpha)}$	Threshold stress in the γ phase on the α^{th} slip system
$\kappa_{L1_2}^{(\alpha)}$	Threshold stress in the γ' phase on the α^{th} slip system

$\lambda_{\gamma}^{(\alpha)}$	Average dislocation spacing in the γ phase on the α^{th} slip system
$\lambda_{L1_2}^{(\alpha)}$	Average dislocation spacing in the γ' phase on the α^{th} slip system
L_{γ}	γ phase channel width
$L_{\gamma'}$	γ' precipitate size
$\mathbf{L}^{in}$	Inelastic velocity gradient
$L_{\rho}^{(\alpha)}$	Average spacing of forest dislocations on the α^{th} slip system
n	Strain sensitivity exponent
N_{slip}	Number of slip systems
Q_{slip}^{110}	Activation energy for slip in the γ phase
Q_{slip}^{112}	Activation energy for slip in the γ' phase
$\dot{R}_{\gamma}^{(\alpha)}$	Void radius in the γ phase on the α^{th} slip system
$\dot{R}_{\gamma'}^{(\alpha)}$	Void radius in the γ' phase on the α^{th} slip system
$\dot{R}_{pb}^{(\alpha)}$	Void radius in the γ/γ' interphase (phase boundary) on the α^{th} slip system
$\rho_{F}^{(\alpha)}$	Forest dislocation density in the γ phase on the α^{th} slip system
$\rho_{\gamma}^{(\alpha)}$	Dislocation density in the γ phase on the α^{th} slip system
$\rho_{L1_2}^{(\alpha)}$	Dislocation density in the γ' phase on the α^{th} slip system
$\rho_{P}^{(\alpha)}$	Parallel dislocation density in the γ phase on the α^{th} slip system

$\rho_{P_{pb}}^{(\alpha)}$	Parallel dislocation density in the γ/γ' interphase (phase boundary) on the α^{th} slip system
$\rho_{pb}^{(\alpha)}$	Dislocation density in the γ/γ' interface (phase boundary) on the α^{th} slip system
T_{melt}	Melting temperature of the γ phase
τ_{APB}	Antiphase boundary resistance
$\tau_{applied}^{(\alpha)}$	Applied resolved shear stress without damage parameter
$\tau_{eff_{\gamma}}^{(\alpha)}$	Effective resolved shear stress in the γ phase on the α^{th} slip system
$\tau_{eff_{\gamma'}}^{(\alpha)}$	Effective resolved shear stress in the γ' phase on the α^{th} slip system
$\tau_{\gamma}^{(\alpha)}$	Resolved shear stress in the γ phase on the α^{th} slip system including damage parameter
$\tau_{\gamma'}^{(\alpha)}$	Resolved shear stress in the γ' phase on the α^{th} slip system including damage parameter
$\tau_{\gamma\,pass}^{(\alpha)}$	Dislocation passing stress in the γ phase on the α^{th} slip system
$\tau_{L1_2\,pass}^{(\alpha)}$	Passing stress in the γ' phase on the α^{th} slip system
$\tau_{mis}^{(\alpha)}$	Misfit stress on the α^{th} slip system
Θ	Diffusivity parameter
$V_{c1}^{(\alpha)}$	Activation volume in the γ phase on the α^{th} slip system
$V_{c2}^{(\alpha)}$	Activation volume the γ' phase on the α^{th} slip system

SUMMARY

In this research an enhanced generation temperature-dependent crystal viscoplasticity model targeting the creep-fatigue interactions in Ni-base superalloys single-crystals is developed. The model is fitted to experimental data obtained on CMSX-8. CMSX-8 was first presented in the Superalloys International Symposium in 2012. CMSX-8 is a reduced rhenium (Re) variant of second generation superalloy CMSX-4. Re is a rare element helpful in improving the creep performance of superalloys, however Re is expensive and rare and therefore efforts have been made to reduce Re content in newer superalloys.

At the microstructure level of interest, these alloys are comprised of two phases, an ordered and a disordered face-centered cubic phases, which experience distinct deformations mechanisms at different regimes of temperature and stress. Few models are available which explicitly account for the deformation mechanisms that are active during the deformation of Superalloys. Moreover, those models do not permit direct application of the constitutive response to the component length scale. In this research this issue is addressed by developing a crystal viscoplasticity model with a novel homogenization technique that can be used to bridge several length scales at each integration point on a displacement-based element. Moreover, a physically-based approach is used to model the microstructure of the alloy by considering its morphology, the distinct deformation mechanisms that become active on each material phase, and the evolution of dislocation densities, which are responsible for inelastic deformation in crystalline metals. These microstructure considerations make the model very accurate and relatively easy to calibrate in comparison with available models.

The model presented in this work is implemented in two forms. The first form is a one-dimensional stress-based routine that can be used to quickly predict the creep deformation of superalloys. This quick implementation makes the routine well suited to perform rapid design trade-offs studies which can be useful for alloy and component design. The second form of the model implementation is a three-dimensional displacement-based routine that can be used on commercially available Finite Element software. The three-dimensional implementation makes it possible to simulate realistic creep-fatigue and thermomechanical fatigue loading.

The increased fidelity of the physical model used in this research leads to challenges in implementation. To address these challenges a novel numerical technique is also developed. This technique is a quasi Newton-Raphson algorithm that enables numerical integration of the constitutive equations in commercially available Finite Element Analysis software. This feature is crucial to allow realistic geometries and boundary conditions. The model can help designers to predict component response using thermomechanical boundary conditions, to understand the influence of thermal transients associated with efficient and effective cooling strategies, to perform component analysis investigating the interaction between geometric discontinuities and crystal orientation of the material. Finally, this model can also be used in enhancing our understanding of superalloys and in alloy design through sensitivity studies.

CHAPTER 1

INTRODUCTION

Industrial Gas Turbines (IGTs) and aero-engines are used in many industries to generate power. Their usage is wide and can range from powering aircraft and large naval vessels, to electricity generating power plants. With the continuous push for increased thermodynamic efficiency, higher temperatures are constantly being required at the hot gas path [1, 2]. This requirement produces an increasingly hostile environment for components inside IGTs and aero-engines. The turbine blades, which are responsible for extracting the work from the working fluid, are in direct contact with this hostile environment where stress and strain fields are complex, and temperatures can be above the melting temperature of the blade material [2, 3]. To achieve these extreme temperatures, turbine blade designers recur to the usage of advanced alloys, special thermal coatings, and specially designed turbine blades with internal cooling passages. All of the above promote several types of damage mechanisms that rise from oxidation and corrosion, diffusion, thermomechanical loading, and the kinetics of microstructure evolution whose interactions are intricate and to this date not well understood [4]

Traditionally turbine blades have been made of nickel-base superalloys due to their excellent high temperature properties. During this past decade, next generation industrial gas turbines (IGT) have been moving toward the employment of single-crystal blades, which are now ubiquitous in aerospace gas turbine propulsion systems. Completely eliminating grain boundaries improves creep behavior. At the microstructure scale of relevance, the superalloys are a composite material comprised of a disordered γ phase and a γ' strengthening phase with unique deformation mechanisms. The superior high temperature behavior of these single-crystal superalloys is attributed to this two-phase microstructure [5]. Second generation single-crystal (SX) superalloys commonly used in current generation aerospace propulsion systems (CMSX-4, PWA1484, René N5) contain 3 wt% rhenium (Re), which reduces creep deformation in the γ channels and maintains the stability of the microstructure.

Consequently, these second generation superalloys have become the benchmark in the development of superalloys more suitable for IGT applications that are characterized by considerably larger blade sizes and cross-sections and longer operation times compared to aircraft gas turbines. The cost of the rare elements, specifically Re, is one of the limiting constraints in selecting these superalloys for IGT applications. In addition, there are challenges in developing casting protocols for these larger sectioned components that have propensity for developing casting anomalies and microstructure variations through the blade and its platform. Therefore, there is a large push to develop SX superalloys with no or reduced Re content that have properties suitable for IGT applications. Accordingly in this work, CMSX-8 is used as this modified second generation SX superalloy is becoming of great relevance to the industry due to its reduced Re content which significantly reduces the cost of parts [6].

In the development of SX alloys, the focus has primarily been placed on creep performance and conventionally this has been used as the design metric for new alloys [7-10]. A common measure of performance for superalloys is the time to creep-rupture, which is typically characterized with the Larson-Miller parameter. The derivation of this parameter is based on assuming that the creep strain rate is constant and that it follows the form [8],

$$\dot{\varepsilon}_{ss} = A\sigma^{n} \exp\left\{-\frac{Q}{RT}\right\} \tag{1}$$

Additionally, it is assumed that the time to rupture follows the Monkman-Grant relationship [11],

$$t_r \dot{\varepsilon}_{ss} = C \tag{2}$$

By substituting the creep strain into the Monkman-Gran relationship, one can arrive at the Larson-Miller parameter,

$$P = T\left(K + \log_{10} t_r\right) \tag{3}$$

where K is a constant typically close to 20 [12].

However, during operation, components are not only subject to creep but also to thermomechanical loads during the engine start-up and shut-down as schematically illustrated in Figure 1.

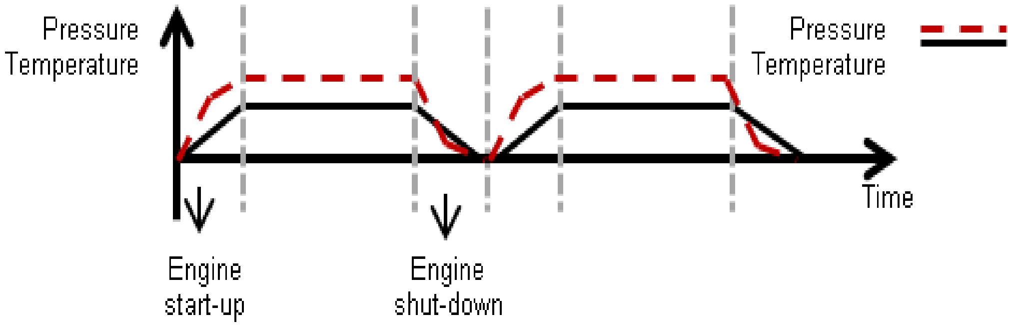

Figure 1: Schematic representation of the loading profile for a turbine blade component

During the engine start-up, the loading conditions resemble a thermomechanical fatigue (TMF) cycle because both the loading and the temperature are changing concurrently. Once the engine reaches its operating condition the loading conditions are similar to those seen during creep. Finally, once the engine is shut-down and then later re-started, another TMF cycle takes place. Due to the complex geometry of most turbine blades, some regions of the blade develop in-phase (IP) TMF cycles while others develop (OP) out-phase TMF cycles and hence studying of both loading conditions becomes necessary. Therefore, the conditions inside IGTs and aero-engines require the understanding of creep, fatigue and their coupling or interactions. Insufficient understanding of the material behavior under these conditions often forces designers to the imposition of large safety factors and strict inspection and replacement intervals which can be costly and inefficient.

Constitutive models available in commercial finite element codes used to address creep-fatigue interactions in SX Ni-base superalloys are limited to non-interaction creep and plasticity models which do not explicitly describe the physical processes of the movement of dislocations in the two distinct material phases that form the alloy. The deformation behavior of superalloys is complex and the properties of these alloys are the result of intricate relationships between the processing and the microstructure of the alloy as illustrated in Figure 2,

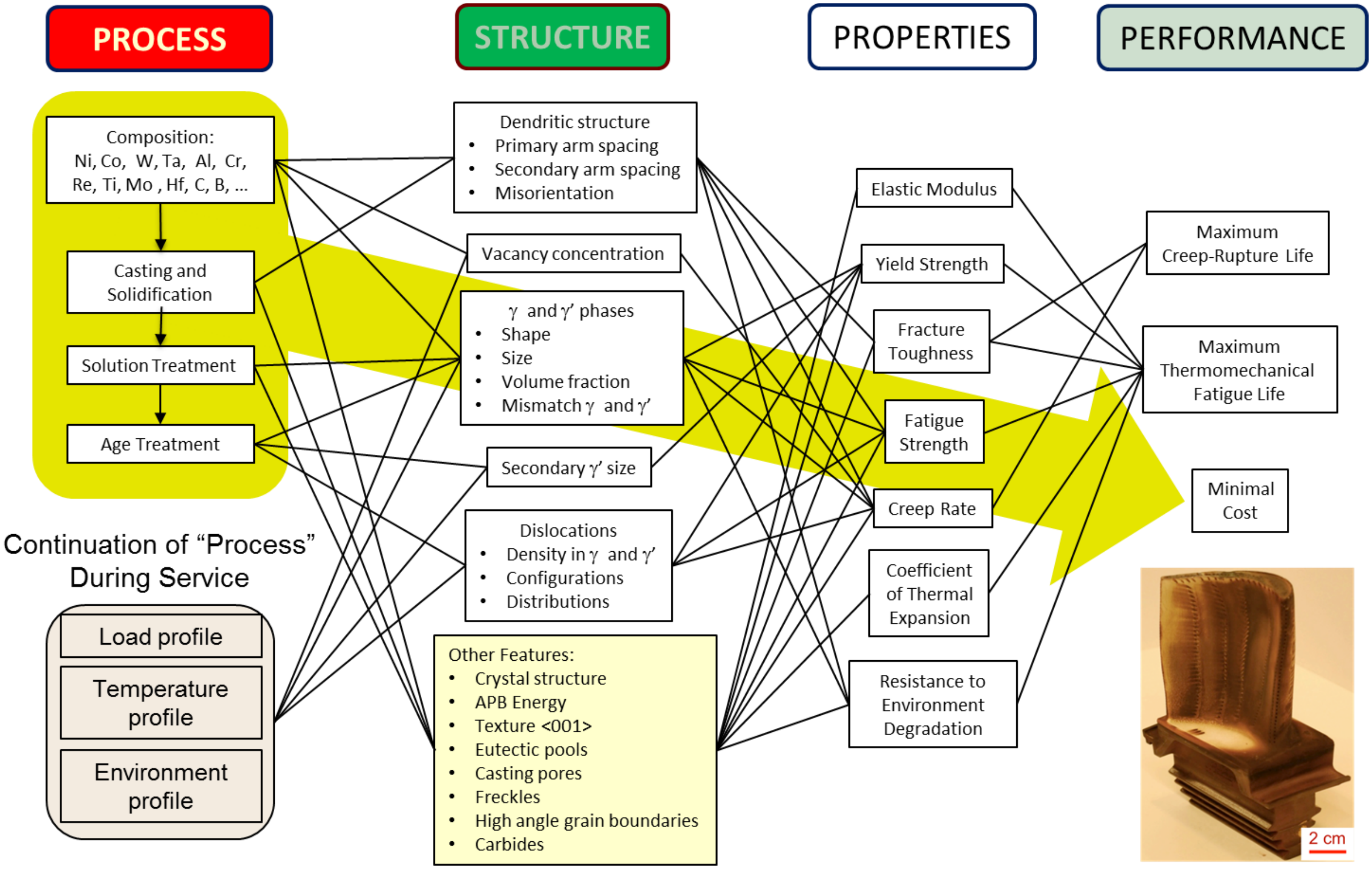

Figure 2: Processing-Structure-Properties-Performance (PSPP) map for Ni-base superalloy airfoils

Figure 2 is a Processing-Structure-Properties-Performance (PSPP) map of SX Ni-base superalloys. The use of maps such as this one in material design was pioneered by Olson [13] and recently has become a very important tool in Integrated Computational Materials Engineering (ICME) [14-16]. This map helps bringing clarity in the modeling of the intricate relationships or links that exists between the processing, the structure, the properties and the performance of the alloy. The processing of superalloys involves the selection of the weight fractions of the elements that will compose it and the techniques that are involved in the solidification and in the heat treatments that result in their traditional two-phase microstructure. Some design parameters typically considered during the processing stage are the weight fractions in the elemental composition, the rate of withdrawal used during solidification, and the temperature and time used during subsequent solution treatment and age treatment.

The structure of the material is a result of the process. For instance, during the solidification of superalloys, a dendritic structure forms along the energetically preferred material orientation, achieved in great part due to the temperature gradient that results from the controlled withdrawal rate of the molten material from the vacuum furnace. Subsequent solution treatment allows the ordered $L1_2$ phase to precipitate in the γ matrix phase, while age treatment enables a cuboidal and coherent microstructure. The superalloys owe their impressive high temperature capabilities to this microstructure, therefore the modeling needs to explicitly include aspects of the morphology of their microstructure such as the size and volume fraction of the precipitates, their anti-phase boundary energy (APBE) and initial dislocation density.

Finally, in Figure 2 the properties and performance of the alloy are a direct consequence of the type of microstructure that the alloy possesses. Therefore, modeling the attributes of the superalloys' microstructure is necessary to enable predictions on of their properties and of their performance. Constitutive models available in commercial finite element codes utilized to address creep-fatigue interactions in SX Ni-base superalloys are limited to non-interaction creep and plasticity models which do not explicitly describe the physical processes of the movement of dislocations in the two distinct material phases that form the alloy or any of the attributes of the microstructure. The deformation behavior of superalloys is intricate and the properties of these alloys are the result of complex relationships between the processing and the microstructure. Consequently, motivated by improving the prediction of mechanical behavior of superalloys, multiple authors have proposed several microstructure-sensitive models [17-20]. However, these models often do not account for the unique deformation mechanisms of the γ and γ' material phases and their interphase, or require explicit meshing of the microstructure and very complex homogenization methods. This work aims at connecting the structure and property linkages through an enhanced generation of microstructure-sensitive crystal viscoplasticity (CVP) models that can predict the deformation of these alloys directly at the component level and that can help in better understanding the superalloys' behavior. In the CVP model, we place special emphasis on acknowledging the physics of the distinctly different deformation mechanisms that take place in the γ phase, γ' phase, and the γ/γ' interfaces.

CHAPTER 2

DEFORMATION MECHANISMS OF NICKEL-BASE SUPERALLOYS

2.1 Crystallography and length-scales in Ni-base superalloys

Ni-base superalloys are mainly comprised of two face-centered cubic (FCC) material phases: a γ phase that serves as a matrix and an ordered $L1_2$ primary γ' precipitate phase that hardens the material. For this reason, these alloys are often considered a composite material. In addition, superalloys can also exhibit a secondary γ' phase of much smaller size than the primary one and other phases such as δ, carbides and borides which can form during casting and whose presence is highly dependent on alloying chemistry, solidification conditions, and heat treatments. The γ' precipitate size typically ranges from 0.3 to 0.5 μm measured in the <001> crystallographic orientation. Moreover, in modern superalloys the volume fraction of the precipitates is approximately 70%; however early generation alloys such as Nimonic 80A had volume fractions as low as 17% [7]. A very typical γ/γ' microstructure morphology for single-crystal superalloys is shown in Figure 3, which is a scanning electron micrograph of superalloy CMSX-4; the gray features are the γ' precipitates while the darker thin features are the γ channels.

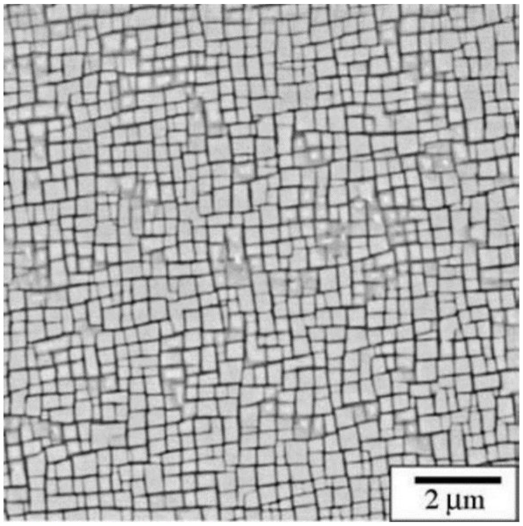

Figure 3: Scanning Electron Microscope (SEM) image of the γ/γ' microstructure for a Nickel-base superalloy single-crystal [7]

Although both material phases are FCC, they have a slightly different crystal structure due to a mismatch in lattice parameter which manifests in a lattice misfit that is characterized by the misfit parameter, δ, where,

$$\delta = \frac{2\left(a_{\gamma'} - a_{\gamma}\right)}{a_{\gamma'} + a_{\gamma}} \tag{4}$$

The lattice parameters of the γ and γ' phases are functions of the mole fraction of the added solutes and since during casting different alloying elements segregate to each phase, then a slight mismatch is generated between the lattices. In modern alloys used in the turbine section, the misfit parameter is negative and they are commonly referred to as negative misfit alloys [21].

Several length scales can be invoked when studying superalloys, the most relevant microstructure features in single-crystal Ni-base superalloys and their length-scales are illustrated in Figure 4.

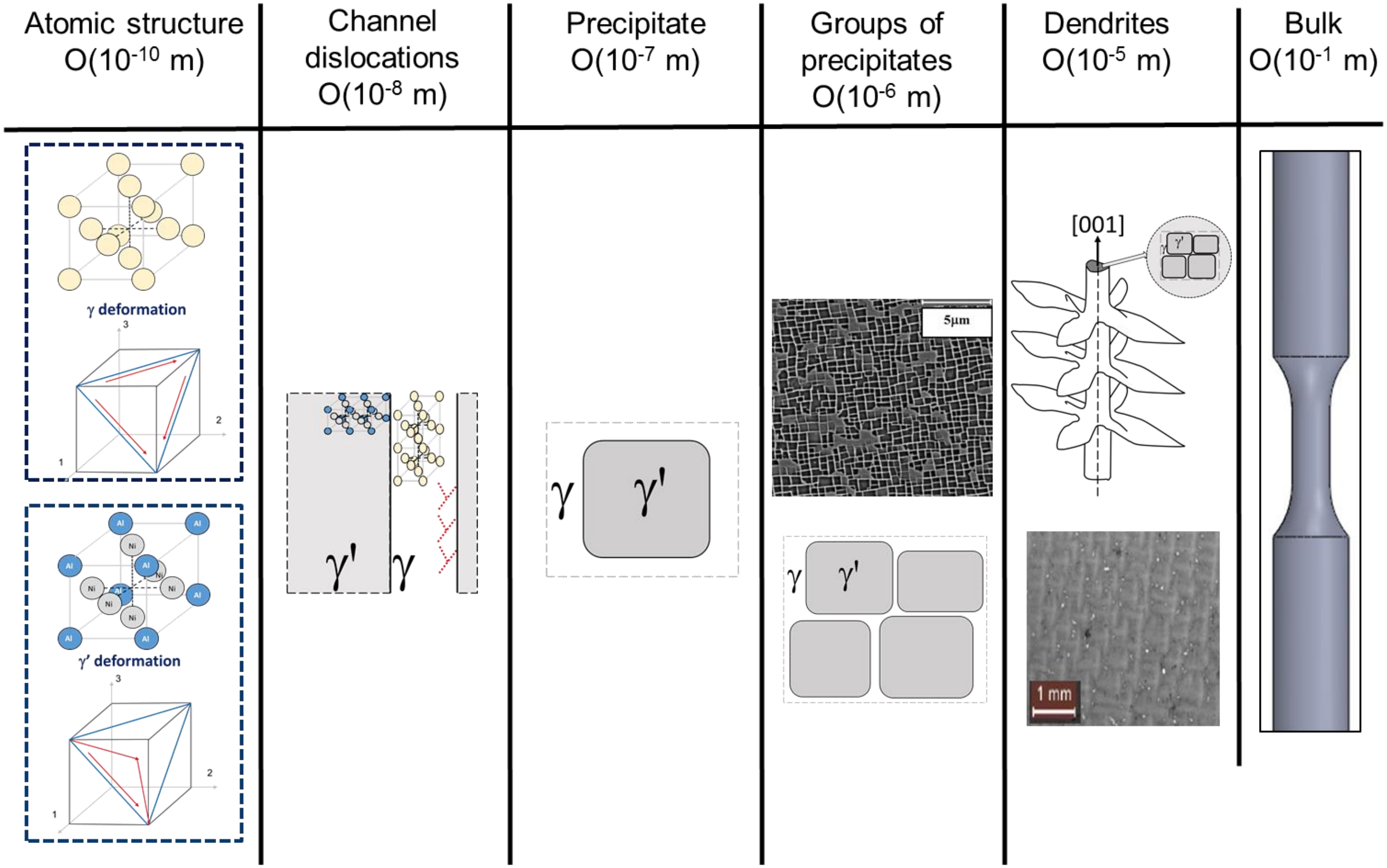

Figure 4: Length-scales in Ni-base superalloy single-crystals

At the atomic level, single-crystal superalloys have FCC lattices that are either ordered $L1_2$ or disordered. These two material phases have different lattice parameters and distinct slip systems; in Figure 4 the slip systems are illustrated below the lattices. Also shown in Figure 4 are the dislocations in the γ channels, which reside in a length-scale two orders of magnitude larger than the atomic scale. Dislocations typically climb and glide or shear through the precipitates on the active slip systems. At one order of magnitude larger than the channel dislocations, an individual precipitate residing in a γ channel can be observed. After adequate material sample preparation, at the micrometer order of magnitude, groups of precipitates residing in a matrix of γ channels can be found using Scanning Electron Microscopy (SEM). During solidification, superalloy single-crystals form a dendritic structure, which is in the order of magnitude of 10^{-5} *m*. This feature can be easily revealed using traditional optical microscopes after adequate polishing and etching has been performed on a sample. At larger length-scales the bulk material is observed.

2.2 Composition and heat treatment of single-crystal Ni-base superalloys

The blades used in the turbine section are cast and machined to very tight tolerances with respect to the engine casing to minimize the gap between them, therefore SX superalloys are preferred in blade applications because of their resistance to creep. During the last two decades several SX superalloys have been developed and their chemistry has been optimized to render superior mechanical properties. In Table 1, a list of some Directionally Solidified (DS) and SX superalloys currently used in turbine blade applications is presented. Note that in modern single-crystal superalloys, at least 10 alloying elements are present and that there has been significant additions of Re and a reduction of the concentrations of Ti and Mo [22, 23] when compared to their directionally-solidified (DS) predecessors. Moreover, typically SX alloys do not contain additions carbon and boron; these are known grain-boundary-strengthening elements because they tend to segregate to the grain boundaries forming obstacles that prevent dislocation motion and crack growth. However, sometimes these elements can still be added to single-crystals to improve vacuum induction refining, alloy cleanness and machinability [23].

Table 1: Chemical composition (%w) of superalloys commonly used the hot gas path [6, 7, 23, 24]

Alloy	Cr	Co	Mo	W	Al	Ti	Ta	Re	Hf	C	B	Zr	Ni
Mar-M247LC-DS	8.4	10.0	0.7	10.0	5.5	1.0	3.0	-	1.5	0.07	0.015	0.05	Bal
CM247LC-DS	8.1	9.2	0.5	9.5	5.6	0.7	3.2	-	1.4	0.07	0.015	0.01	Bal
CMSX-4	6.5	9.0	0.6	6.0	5.6	1.0	6.5	3.0	0.1	-	-	-	Bal
SC16	16	0.17	3.0	0.16	3.5	3.5	3.5	-	-	-	-	-	Bal
PWA1484	5.0	10.0	2.0	6.0	5.6	-	8.7	3.0	0.1	-	-	-	Bal
CMSX-8	5.4	10.0	0.6	8.0	5.7	0.7	8.0	1.5	0.2	-	-	-	Bal

Re was added to second generation SX superalloys in order to optimize their creep-rupture response [23]. Adding Re has many strengthening effects on single-crystal superalloys. Re had been shown to retard the rate of coarsening of the γ' phase because, for the precipitates to coarsen, the Re which segregates almost exclusively to the γ channels, needs to diffuse away from the γ/γ' interface. Since Re is a larger atom compared to Ni, its diffusion is slow [25, 26]. Moreover, Re has the lowest diffusion rate among all refractory elements used in superalloys; therefore, it reduces the climb rate of dislocations [27]. However, in alloys containing W, like in CMSX-4, some Re (about 20%) segregates to the γ' phase [28]. Re also provides a solid solution strengthening effect, increasing the yield strength [27, 29, 30]. Furthermore, the addition of 3 wt. % Re reduces the minimum creep rate by an order of magnitude and increases the rupture lifetime, in addition to increasing the yield strength [29, 30].

In the creep-fatigue study conducted on CMSX-4 at 1,100°C by Yandt et al. [31], increasing Re content also increased the cyclic stress amplitude and also led to the best fatigue resistance. Yandt et al. [31] showed that the degree of γ' coarsening was notably greater in the low-Re and Re-free alloys, consistent with the increased diffusion kinetics in the γ channels with the reduction in Re. However, Re is a rare element with limited production and its addition to superalloy parts adds significant cost, particularly for larger IGT blades. As a result, there has been efforts in developing second-generation single crystal superalloys, such as CMSX-7 and CMSX-8, with lower Re content [6]. The lower Re is observed to affect the creep rupture of the alloys for temperatures greater than 1,000 °C.

A representative heat treatment for a single-crystal component involves first a 4 hour solution treatment at temperatures close to 1,300°C, followed by precipitation treatment with gas fan cooling at temperatures close to 1,140 °C for another 4 hours, followed by an aging treatment at 870 °C for 20 hours with gas fan cooling [23, 24, 31]. For example, a typical heat treatment for superalloys is illustrated in Figure 5,

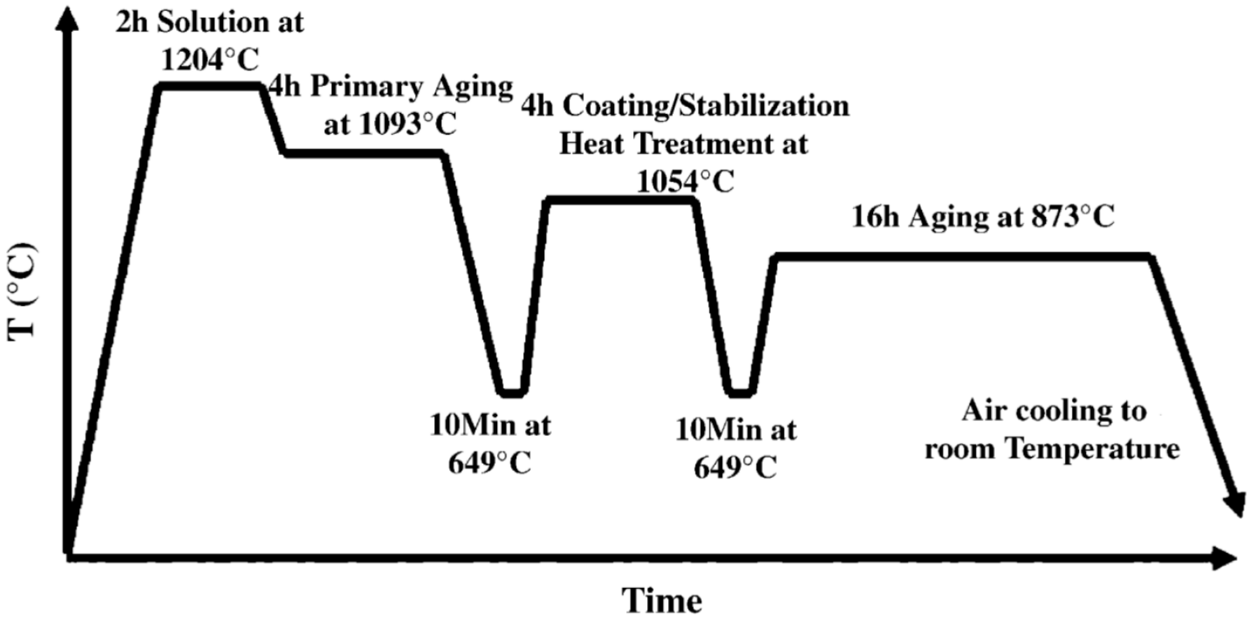

Figure 5: Representative heat treatment for Ni-base superalloys [32]

All treatments are conducted in a vacuum furnace. This results in a microstructure containing both primary γ' and secondary γ' precipitates as shown in Figure 6,

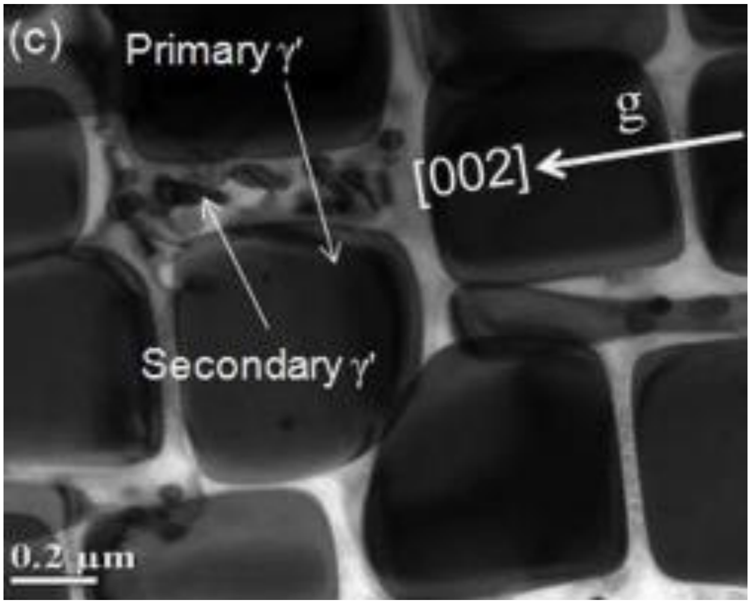

Figure 6: Primary and Secondary precipitates on Ni-base superalloy[33]

Secondary γ' precipitates are much smaller (in the order of 100nm) than the primary precipitates (in the order of 800nm). The secondary precipitates form at high temperatures during cooling from the solution heat treatment due to the interplay between the kinetics of γ particle nucleation, growth and coarsening during solutioning and ageing heat treatments [7].

2.3 Anisotropy and deformation mechanisms of Ni-base superalloys

2.3.1 Anisotropy of Ni-base superalloys

Mechanical properties of the superalloys are highly anisotropic; examples of these are the elastic properties, creep, and yield strength. The anisotropy arises from microstructural features of the material such as the cuboidal symmetry of their FCC lattices and also from the resulting internal stresses generated from their lattice misfits. As an example, the elastic modulus at room temperature of a single crystal is shown in Figure 7. It can be seen that the modulus is the lowest in the [001] direction at 126 GPa while the highest value of 303 GPa, two and a half times greater, is in the [111] direction. Performing experiments on all orientations results impractical and the elastic moduli tensor for and FCC material is typically derived from the alloy's response in the <001> direction assuming cubic symmetry using linear elasticity formulations [34],

$$C_{11} = \frac{E_{<001>}\left(1-\nu_{<001>}\right)}{1-\nu_{<001>}-2\nu_{<001>}^{2}} \tag{5}$$

$$C_{12} = \frac{E_{<001>}\nu_{<001>}}{1-\nu_{<001>}-2\nu_{<001>}^{2}} \tag{6}$$

$$C_{44} = G_{<001>} \tag{7}$$

with the elastic moduli tensor at hand, the observed moduli on a given orientation can then be obtained simply by applying a rotation matrix in the direction of the Euler angle of interest.

As illustrated in Figure 8, another example of anisotropy in superalloys is in the creep response, in this example measured in rupture life at 750°C and 750 MPa.

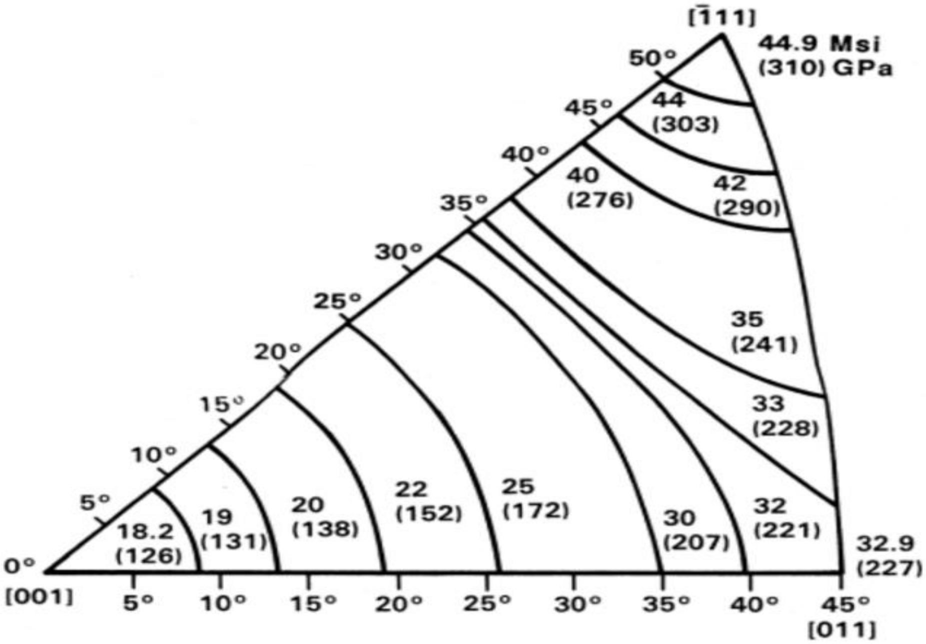

Figure 7: Elastic modulus as a function of orientation of PWA 1480 at room temperature [35]

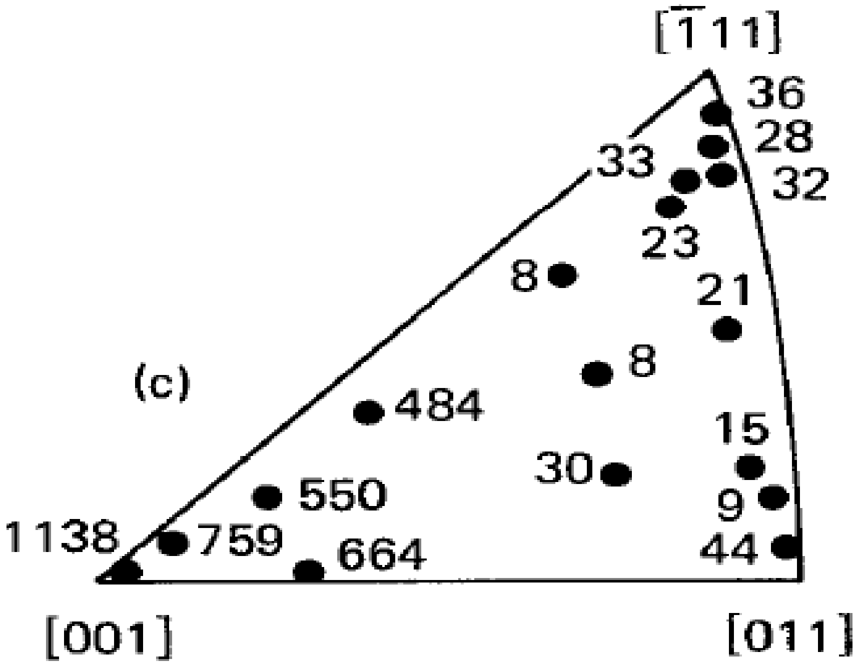

Figure 8: Orientation dependence of stress rupture life (in hours) at 760 °C and 750 MPa of CMSX-2 [36]

2.4 Deformation mechanisms of superalloys

When dislocations meet a γ' precipitate they can either shear it or loop around it. Whether one or the other takes place is dependent on the size and volume fraction of the γ' precipitates. Shearing of the γ' particles by dislocations is favored by small precipitates, high volume fraction, low anti-phase boundary (APB) energy of the precipitates, and low mismatch at γ/ γ' interface. Looping of dislocations around precipitates is favored by large γ' particles, low volume fraction, high APB energy, and high mismatch at γ/ γ' interface. These conditions are summarized in Table 2.

Table 2: Conditions for shearing of γ' and dislocation looping

	γ' size	**Volume fraction**	**APB energy**	**γ/γ' mismatch**
Shearing of γ'	Small	High	Low	Low
Dislocation looping	Large	Low	High	High

Due to the stoichiometric order of the *L1₂* phase, dislocations are unable to move through γ' precipitates unless they travel in pairs. The first dislocation entering a γ' forms an APB and the second $a/2\,\langle 1\overline{1}\overline{1}\rangle\{111\}$ trailing dislocation removes it, hence providing a resistance for the material to deform [7, 37-39]. The number of energetically unfavorable Ni-Ni and Al-Al bonds is dependent on the plane on which the APB resides, hence the APBE is an anisotropic property of the material, first principle estimations of values of ABPE are listed in Table 3. The APBE in the $\{001\}\langle 110\rangle$ is zero because in this slip system no unenergetically favored Al-Al or Ni-Ni bonds are formed, however in practice this value is not zero but rather close to zero [7].

Table 3: ABPE in different slip systems. Ω_{NiAl}, Ω_{AlAl} and Ω_{NiNi} are the Ni-Al, Al-Al, and Ni-Ni bond energies respectively; *a* is the lattice parameter [7]

Slip System	**APBE**
$\{111\}\langle 110\rangle$	$2\left[\Omega_{NiAl} - \frac{1}{2}(\Omega_{NiNi} + \Omega_{AlAl})\right]/(a^2\sqrt{3})$
$\{110\}\langle 110\rangle$	$2\left[\Omega_{NiAl} - \frac{1}{2}(\Omega_{NiNi} + \Omega_{AlAl})\right]/(a^2\sqrt{2})$
$\{001\}\langle 110\rangle$	0

As shown in Figure 9 and Figure 10, depending on the size of the γ' precipitates and spacing, the dislocation-precipitate interaction can be classified as either weak or strong.

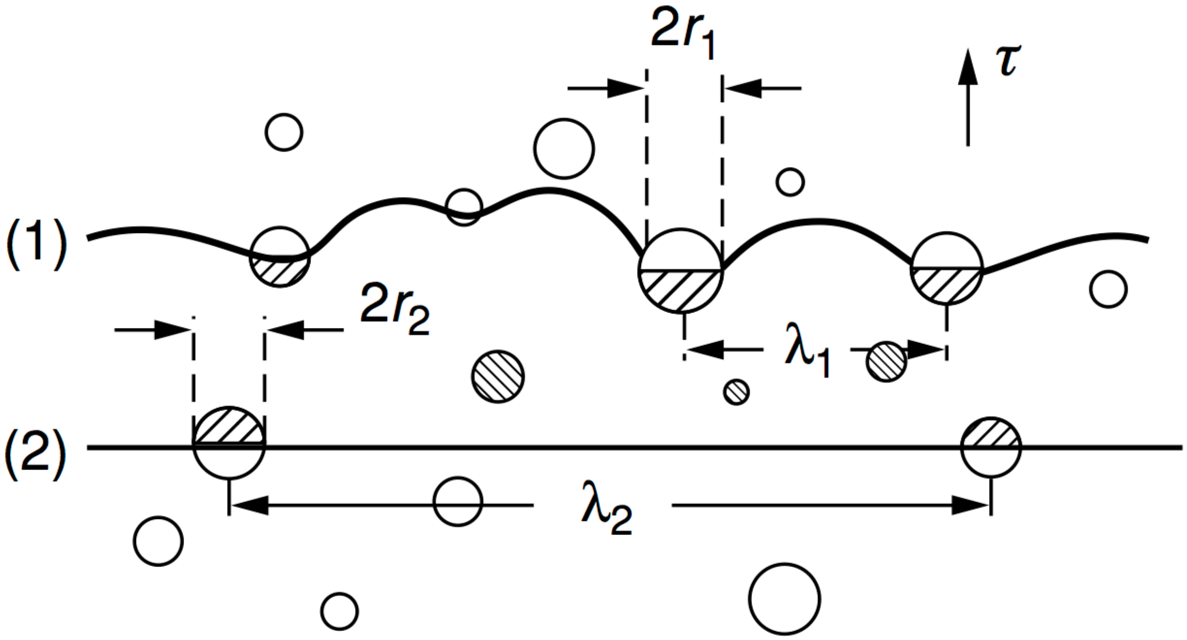

Figure 9: Weak pair-coupling of γ' precipitates sheared by dislocation pairs [7]

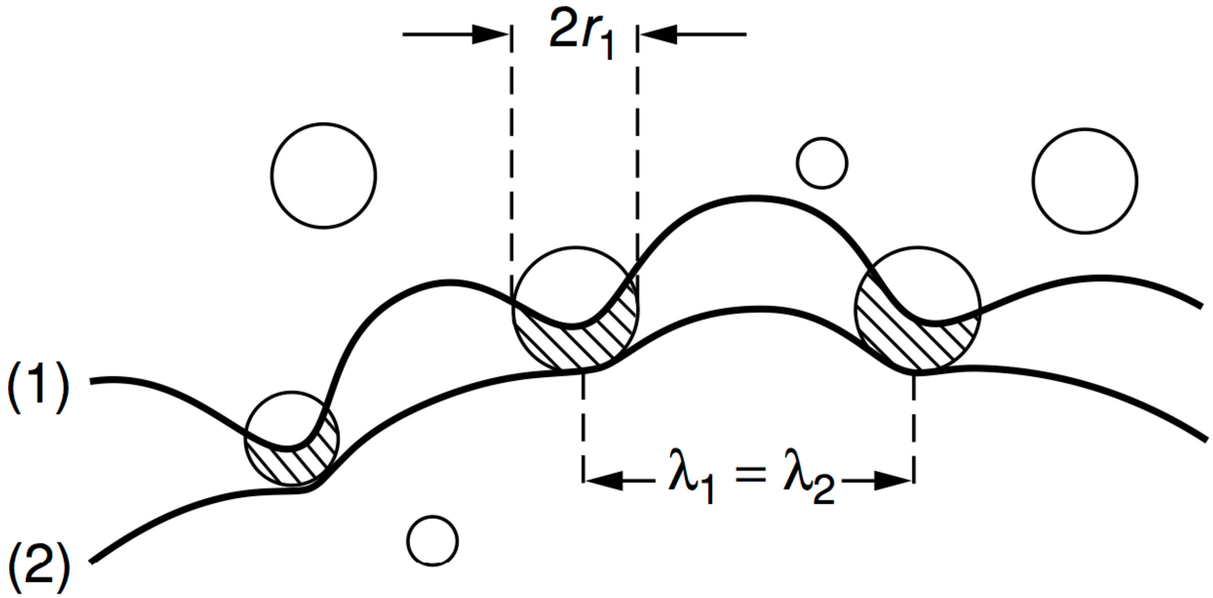

Figure 10: Strong pair-coupling of γ' precipitates sheared by dislocation pairs [7]

Force equilibrium of weakly and strongly coupled dislocations has shown that the right balance between volume fraction and precipitate size can promote hardening by increasing the critically resolved shear stresses on the precipitates [39]. However, it is important to recognize that the microstructures of the superalloys are metastable and that they can evolve with temperature and stress. The equilibrium volume fraction of γ' precipitates depends on temperature and with sustained exposure to high temperatures it can be reduced; for example, a superalloy with 70% γ' at room temperature could experience a reduction to 45% γ' with sustained exposure to 1,100°C [31].

2.4.1.1 Anomalous yield strength of superalloys

In the aged and over-aged states, the γ' dislocation interaction generates a feature of Ni-base superalloys commonly referred to as the anomalous yield strength. Superalloys exhibit an increase of the yield strength with increasing temperatures for temperatures as high as 750°C; at higher temperatures a softening occurs which has been attributed to a preference for slip on the cube planes [7]. A possible explanation to the strengthening of the material with increasing temperature is that at lower temperatures and at sufficiently high stress, precipitates are cut-through and the strengthening is the result of the highly anisotropic energy associated with the APB, as a consequence, cross slip of dislocations from the {111} to {001} slip plane form entanglements which exhaust the population of mobile dislocations, these are known as Kear-Wilsdorf locks (KW), illustrated in Figure 11 [40]. Screw superdislocations that travel in the {111} plane cross-slip onto the cube slip systems forming complex jogs (CJ) and macrokinks (MK), these lie in the cube and octahedral planes, respectively. As temperature increases, thermally activated cross-slip reduces the number of mobile dislocations. As more dislocations continue to cross slip, they become locked and do not propagate until there is enough thermal energy to overcome the Peierls stress and then glide. Depending on the stress level and the amplitude of the cross-slip onto the cube plane, locking can take place over various distances leading to incomplete Kear Wilsdorf (IKW) locks [41]. This situation is schematically illustrated in Figure 11 (c) through (e).

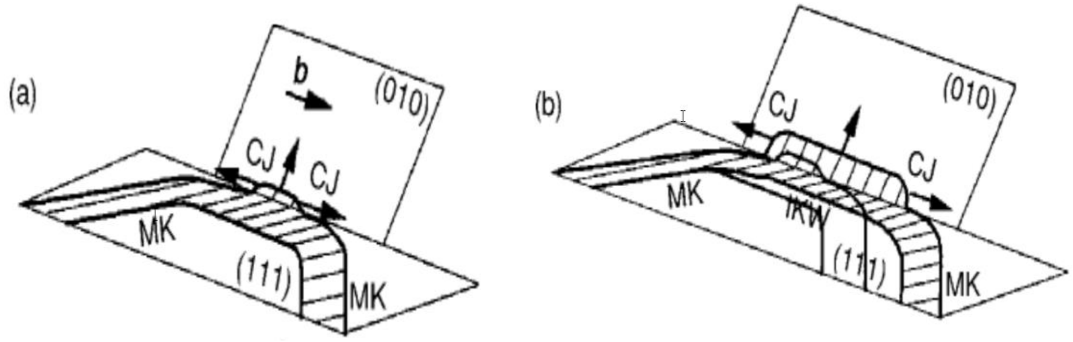

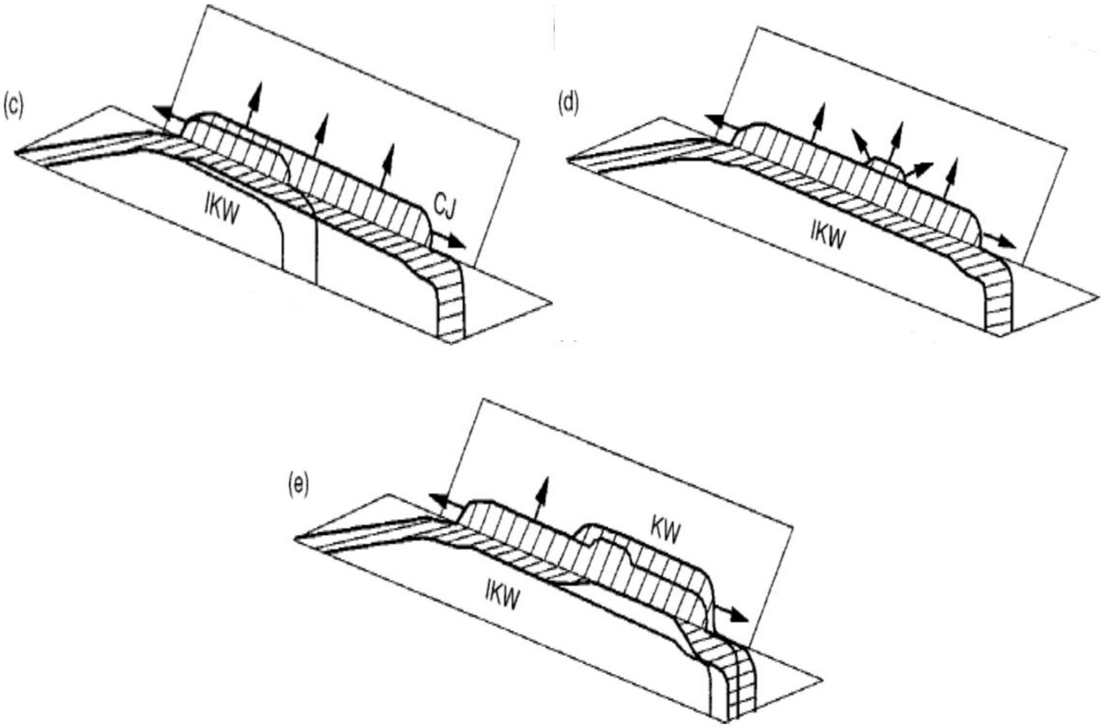

Figure 11: Formation of Kear-Wilsdorf locks (KW): a) screw superdislocations, complex jogs (CJ) and macrokinks (MK) b) lateral spreading of a pair of CJs in opposite directions c) incomplete Kear-Wilsdorf lock and CJ entanglements d) IKW and lateral spreading e) cross-slip of KW, IKW and CJ [42]

2.4.1.2 Creep and fatigue deformation mechanisms

While subject to high homologous temperatures, superalloys can experience rafting, primary creep, secondary or steady state creep, and tertiary creep. As shown in Figure 12, in single-crystals, the creep response is highly dependent on temperature and stress [5, 7, 43, 44],

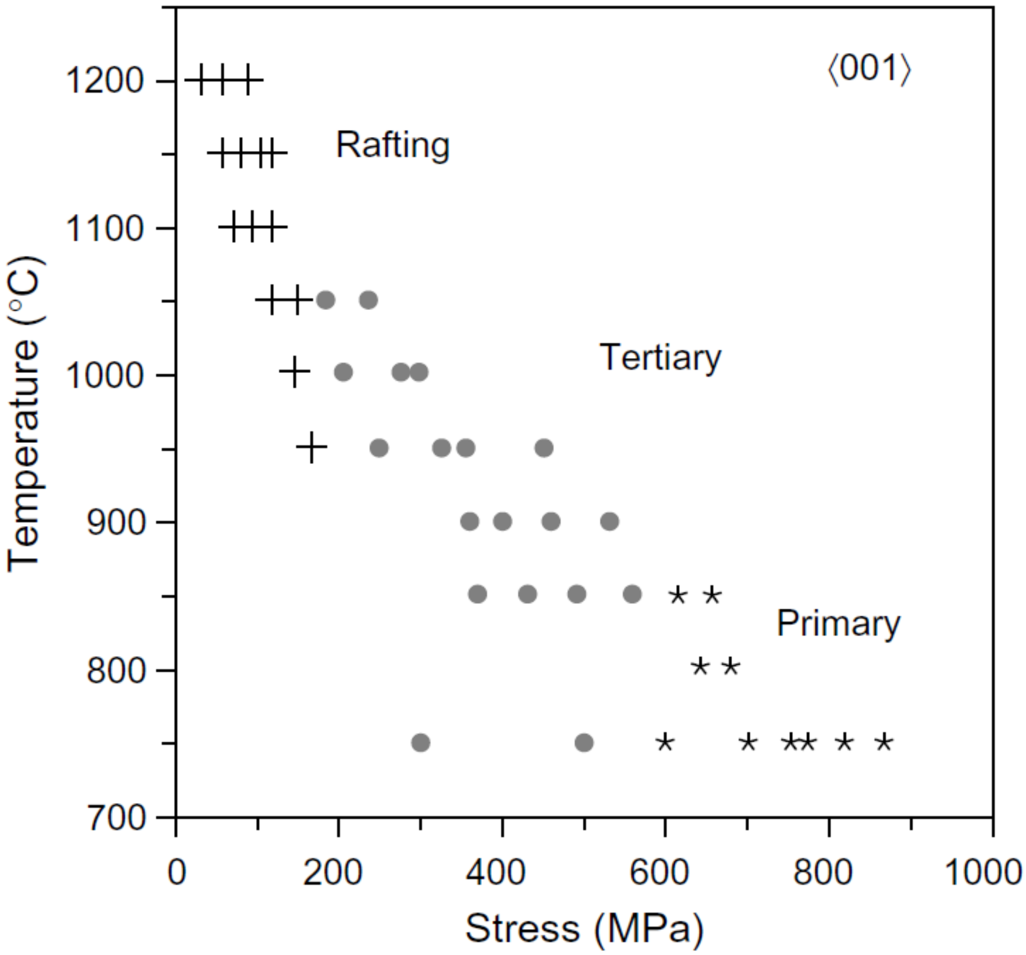

Figure 12: Temperature and stress regimes under which primary, tertiary creep or rafting are the dominant deformation mechanisms on CMSX-4 [7]

Rafting is an evolution of the γ/γ' microstructure resulting in the widening of either the vertical or the horizontal γ channels. This mechanism is seen at very high homologous temperatures. The shape of the resulting microstructure depends on the lattice misfit of the γ/γ' microstructure as well as on the direction of the load [45]. For example, for a negative misfit alloy, in the case of a tensile creep load, matter from the γ channel phase in the vertical channels transports to the horizontal channels forming a microstructure termed N-rafted, shown in Figure 13. In this case the precipitates in the microstructure evolve such that the long side is perpendicular to the loading direction. Shown in Figure 14, is the converse case where a negative creep load is imposed on a negative misfit alloy. This results on a microstructure termed P-rafted, and the long side of the precipitates is along the direction of the loading.

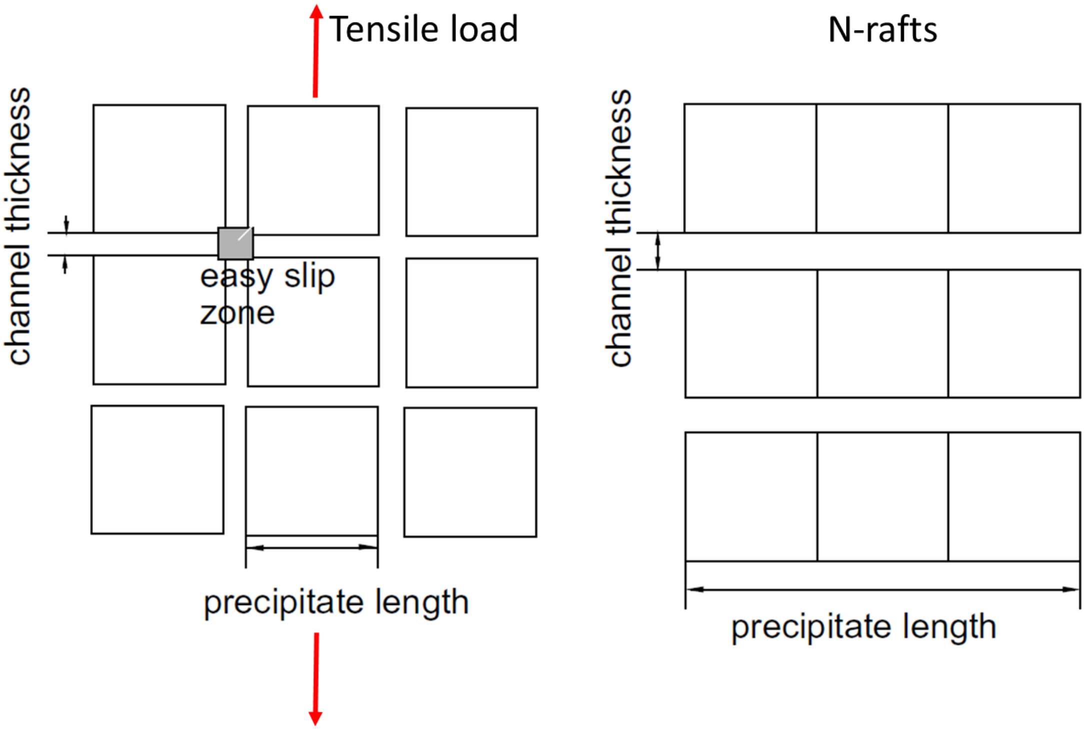

Figure 13: N-rafted microstructure on a negative misfit superalloy due to positive creep load. Adapted from Ma et al. [43].

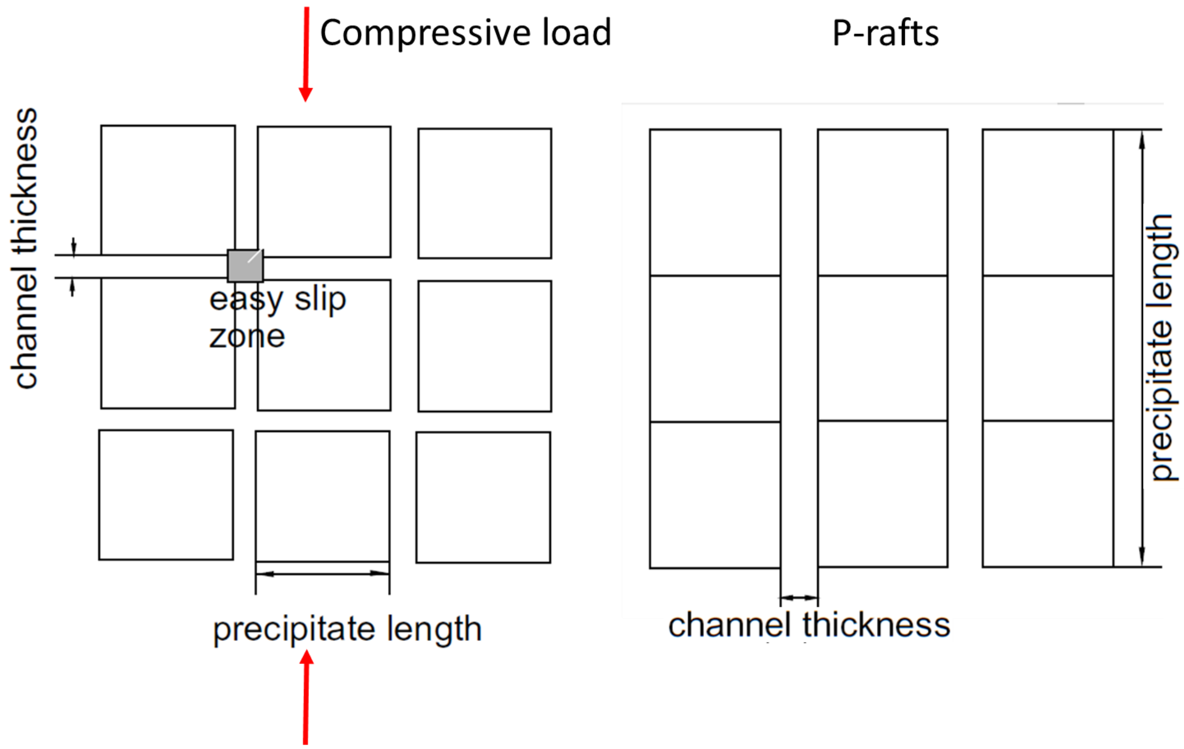

Figure 14: P-rafted microstructure on a negative misfit superalloy due to positive creep load. Adapted from Ma et al. [43]

In Figure 15, a single-crystal turbine blade with different stages of rafting along its span is shown. In this blade both N-raft and P-rafts have formed since there are regions of the turbine that experience positive loads and others that only experience negative loads [46]. Rafting is a topic of on-going research and conflicting accounts on its effect on the constitutive response are often reported. However, rafting has been shown to reduce the life of specimens by up to a factor of 5 [19, 46, 47].

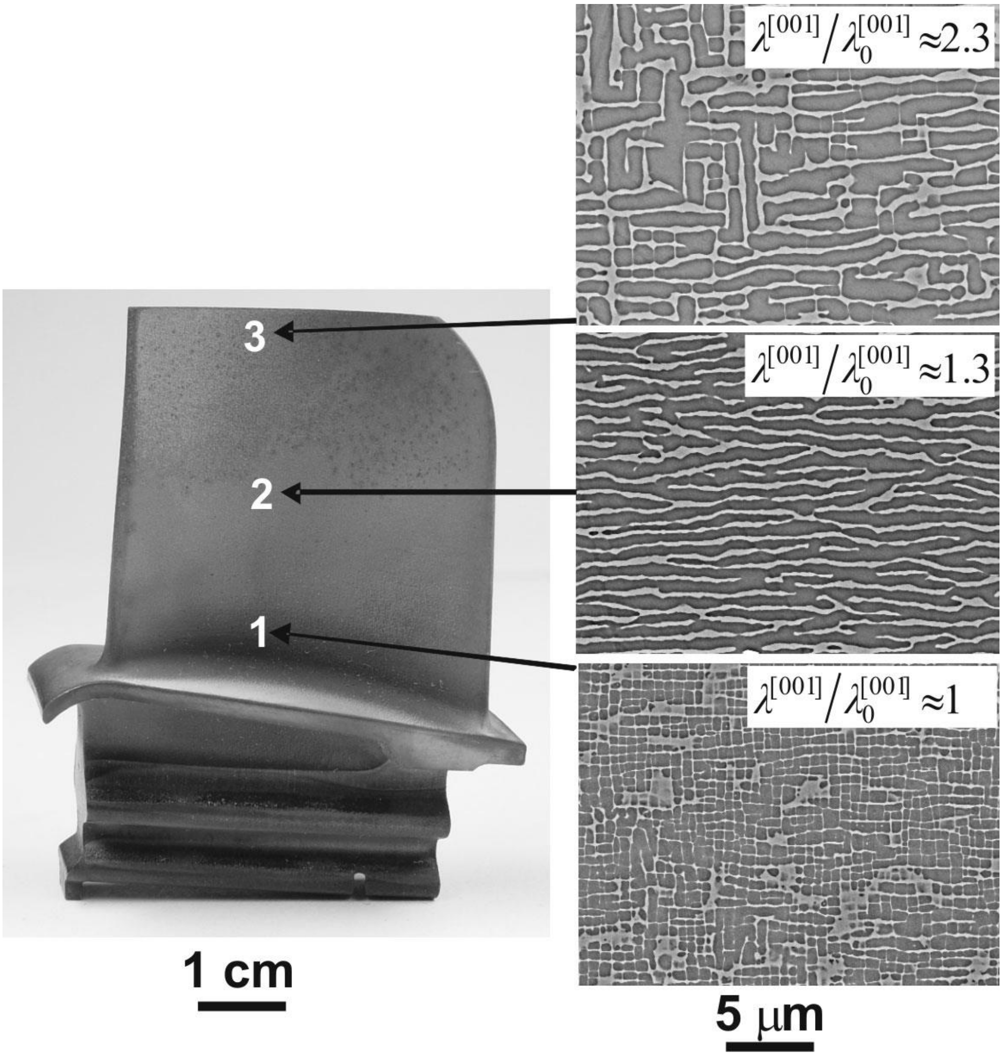

Figure 15: CMSX-4 after service and its microstructure evolution: 1) nearly cuboidal microstructure at the root of the blade 2) N-rafted microstructure 3) P-rafted microstructure [48]

At low temperatures and high stresses, primary creep becomes a very dominant deformation mechanism. As shown in Figure 16, during primary creep, the γ' particles are sheared by dislocations ribbons of overall Burgers vector $a\langle 11\bar{2}\rangle$ dissociated into superlattice partial dislocations separated by a stacking fault [7].

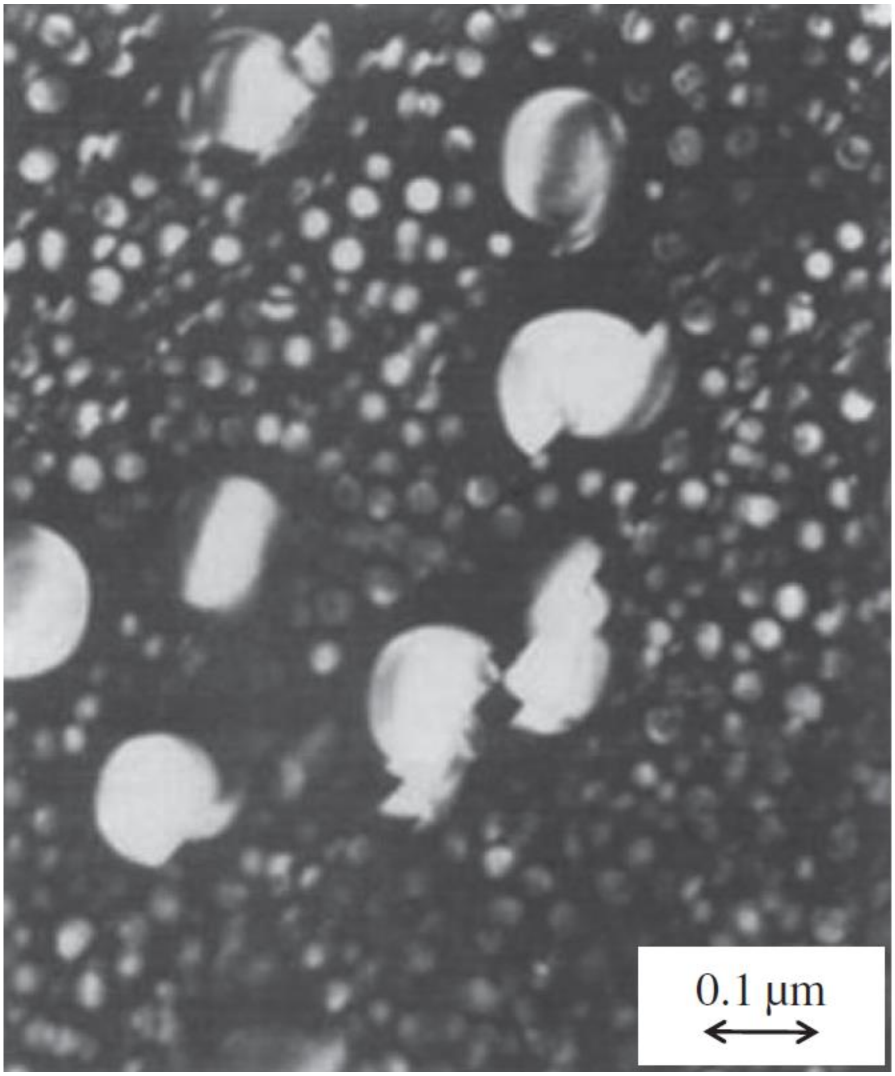

Figure 16: Dark-field TEM image of Waspaloy fatigued at $\Delta\varepsilon_p = 4\text{x}10^{-3}$ at 25°C. The spherical precipitates have been sheared by dislocations [49].

When this mechanism operates the creep curve exhibits primary creep. Primary creep is a complex process involving nucleation, propagation and termination of mobile $a\langle 11\bar{2}\rangle$ dislocation ribbons requiring sufficient densities of at least two $a/2\,\langle 1\bar{1}0\rangle\{111\}$ families of dislocations in the γ channels to enable the nucleation of the dislocations and the sufficient resolved shear stress for propagation of the $a\langle 11\bar{2}\rangle$ ribbon. Because of the very high anti-phase boundary energy

(APBE) associated with the ordered $L1_2$ precipitate, as shown in Figure 17, dislocations have been shown to travel in pairs. The leading edge dislocation forms an antiphase boundary as it shears the precipitate while the trailing edge dislocation removes it.

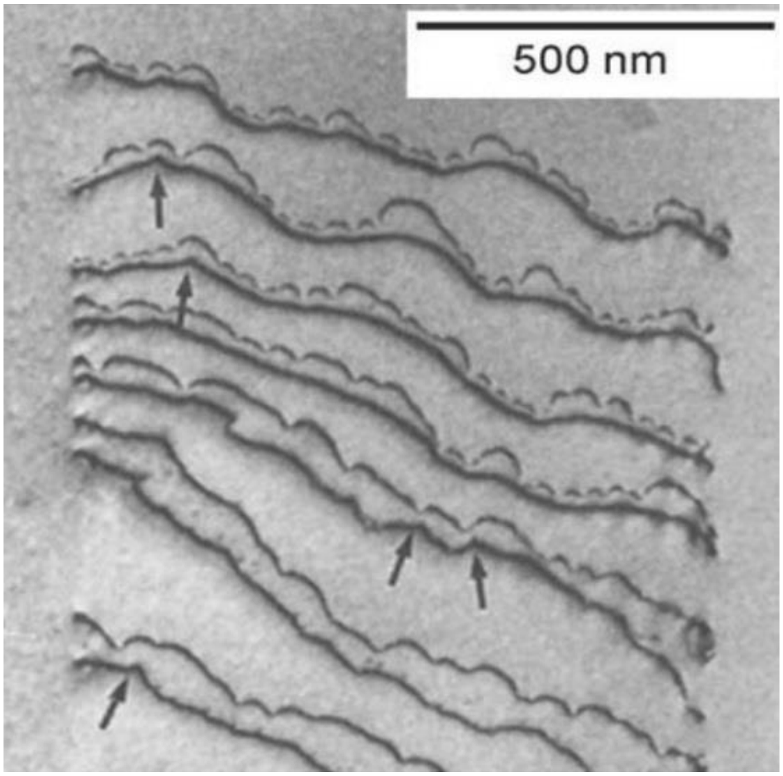

Figure 17: Pair of edge dislocations in Nimonic PE16 [39].

The amount of primary creep is sensitive to the alloy composition. In particular, it is sensitive to additions of the refractory solid solution strengtheners and γ' hardeners and any influences on lattice misfit, Stacking Fault Energy (SFE), and APB energy. In fact, an unintended consequence of optimizing the alloys for resisting greater tertiary creep at higher temperatures is increased amounts of primary creep due to the addition refractory elements [50].

In SX superalloys, secondary creep or steady state creep appears at the saturation point when the γ channels have been saturated with and extensive amount of dislocations. As shown in Figure 18, during steady state creep, multiple slip systems have been activated which generates a build-up of a three-dimensional nodal network of dislocations which fill the γ channels and generates a quasi-stationary structure in time [44].

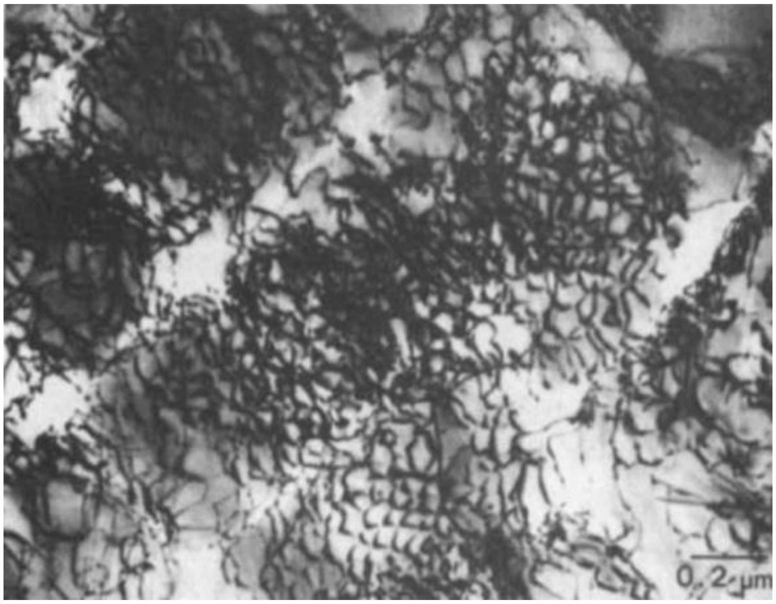

Figure 18: Matrix dislocation networks during secondary creep in CMSX-3. Dislocations pile-up at the γ/γ' interface [44]

At higher temperatures and lower stresses tertiary creep starts to become the dominant mode of deformation, this is not to say that primary creep cannot occur but rather that during deformation most of the creep strain comes from tertiary creep. The dislocations are restricted to the octahedral slip systems in the γ channels; at this lower stress level, the dislocations at the γ/γ' interface cannot push through the γ' precipitates due to the high energy associated with the APB in the γ', and as a result the dislocations must loop around the precipitates [51, 52]. In the tertiary creep regime, the dominant dislocation mechanism is $a/2\,\langle 1\bar{1}0\rangle\{111\}$ with these dislocations primarily being screw in nature. Further, the deformation that occurs is homogeneous, generally with more than two slip systems active [44, 53].

The deformation mechanisms that activate during fatigue are also dependent on temperature. At low temperatures, generally below 750 °C, the deformation is generally dominated by the γ' precipitates shearing. The dislocation motion is very heterogeneous and restricts itself to the $a/2\,\langle 110\rangle\{111\}$ systems with limited cross-slip. Due to the localized deformation, permanent slip bands appear on the surface of fatigued specimens [54]. However in the case of large plastic deformation the dislocation motion becomes more homogeneous thus decreasing the formation of the slip bands [55]. As the temperature increases a deformation induced coarsening takes place leading to dislocation looping. Also, cross-slip is enhanced due to thermal activation making dislocations more mobile in the γ channels. Additionally, the dislocation activity becomes more homogeneous but a small number of slip bands can still be observed [56].

CHAPTER 3

EXPERIMENTAL MEASURE OF CREEP-FATIGUE BEHAVIOR

Four different types of mechanical experiments were conducted: constant stress creep, isothermal strain-controlled creep-fatigue with dwells (CF), isothermal strain-controlled low-cycle fatigue (LCF), and strain-controlled thermomechanical fatigue (TMF). There are three objectives to performing these experiments. First, the data is used to further understand the macroscopic behavior of CMSX-8 in comparison with other superalloys. CMSX-8 is a new alloy for which very few experimental data has been reported in the literature. Second, the experimental data obtained in this research will be used to identify key life data, and mechanical behavior traits that the model must be able to explain and replicate, i.e. temperature dependency of material parameters such as moduli, coefficient of thermal expansion (CTE), and yield strength. Third, the data collected in this section will be used to calibrate the material parameters in the constitutive model. Often, material properties cannot be directly measured or calculated and must be calibrated from macroscopic data. These material parameters include hardening parameters (i.e. parameters associated to the viscoplasticity terms in the flow rule and in the evolution equations), and elastic parameters (i.e. moduli as a function of temperature and orientation, and the coefficient of thermal expansion).

3.1 Material description

In this work CMSX-8[B/C] was tested. This alloy was preferred over other candidates because of its reduced content of Re which makes it cheaper in comparison to other superalloys.

CMSX-8[B/C] contains intentional additions of boron and carbon to improve castability and machinability [23]. The detailed composition of this alloy is proprietary, however the nominal composition of CMSX-8, which does not contain any carbon or boron, can be found in Wahl et al. [6]. The material was cast by PCC Airfoils, LLC in the form of bars in the <001> crystallographic orientation and slabs in the <111> crystallographic orientation. These bars and slabs were solution and double aged treated using proprietary conditions typical for blade components.

The virgin γ/γ' microstructure of CMSX-8[B/C], taken from the dendritic region, is shown in Figure 19. The etchant used to reveal the microstructure was PW#17 etchant, composed of 100 ml HNO_3, 100 ml HCl, 100 ml H_2O and 3.0 g $MoO_3.H_2O$.

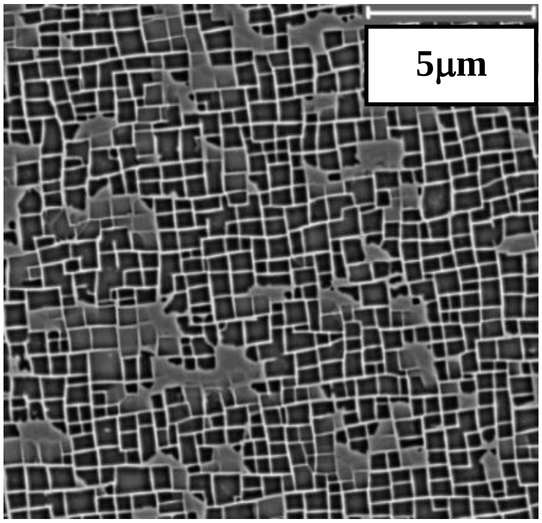

Figure 19: SEM image of as-received microstructure of CMSX-8[B/C] in the dendritic region shows the γ' precipitates (black), and the γ channels (white)

The volume fractions of the γ and γ' phases were estimated to 0.30 and 0.70, respectively. The average γ channel width and γ', were estimated to $0.11\mu m$ and $0.80\mu m$, correspondingly. These estimations of the mean spacing were obtained using two-point spatial statistics analysis [46, 57, 58].

3.2 Experimental procedure

3.2.1 Servohydraulic testing system

Isothermal strain-controlled CF, isothermal LCF and in-phase (IP) and out-of-phase (OP) TMF experiments were conducted in laboratory air using servohydraulic tests systems located at the Georgia Institute of Technology Mechanical Properties Research Laboratory (MPRL). Two MTS servohydraulic load frames were used for testing. One of these systems was an axial servohydraulic frame rated at 44.5kN (10.0 kip) with a load cell resolution of ±0.5 kN (±100 lbf). The other was an MTS frame axial-torsion servohydraulic testing system with a load cell resolution of ±1.25 kN (±250 lbf). Both of these load frames were equipped with water-cooled MTS model 646 collet grips. The nominal hydraulic pressure applied by the collet grips to the specimen’s shoulder was 41.4 MPa (6000 psi); at least 12.7mm (0.5 in) of the specimen’s shoulder was inserted into the collet to assure firm gripping. The frames were controlled using FlexTest40 digital controllers and test scripts were developed using MTS TestSuite Multipurpose Elite Software.

Temperature was controlled and monitored using K-type thermocouples spot-welded to the gage section of the specimen. An analog temperature command signal was output by the FlexTest40 to a Eurotherm model 3204 PID temperature controller. The input analog signal coming from the K-type thermocouple into the Eurotherm controller served as a remote set-point which was used to determine the error signal for the PID control. The specimens were heated to their test temperature by means of electromagnetic induction using Ameritherm 2kW induction heaters. The induction coils, shown in Figure 20, were made from 4.7 mm (3/16 in) diameter copper tubing. The induction coil had 5 complete turns with an inner diameter of 19.05mm (3/4 in), and 12.7mm (1/2 in) spacing between each turn. Moreover, to be able to reach uniform temperature at 1100°C, concentric outer turns of 30.48 mm (1.2 in) were included at both ends of the coils.

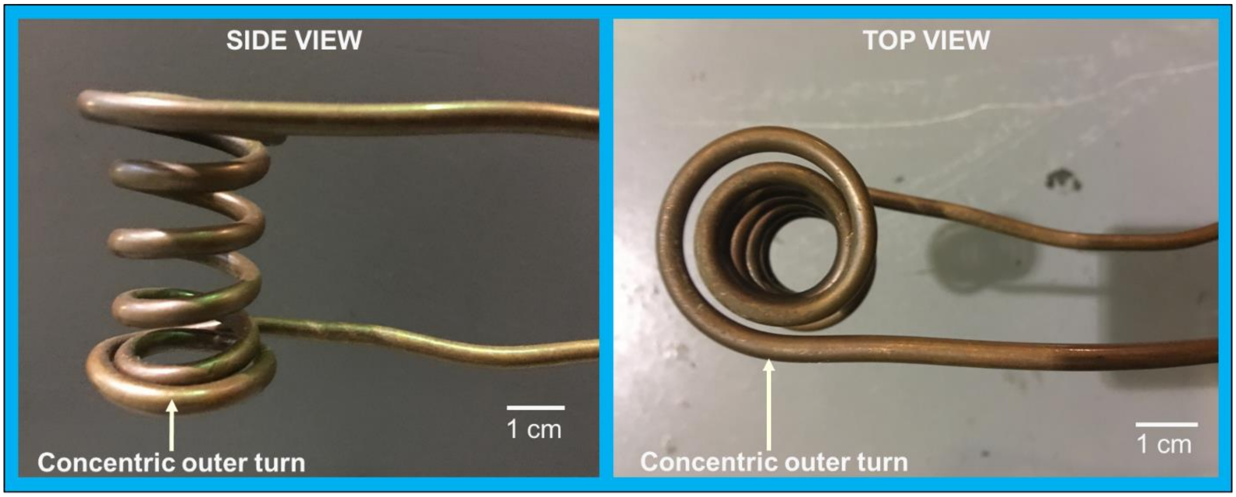

Figure 20: Induction coils design used in the servohydraulic test frames

The axial displacement within the gage section of the specimen was measured using an MTS model 632.52E-14 high-temperature extensometer. The extensometer’s nominal gage length between the tips was 12.7mm (1/2 in). The legs of the extensometer were made from ceramic alumina rods with v-chisel points extended from the extensometer. The extensometer is passed between the middle turns of the induction coil and is pressed against the gage section using a spring mount which also serves as a heat shield for the extensometer. The complete setting including the extensometer, induction coils, and collet grips is shown in Figure 21.

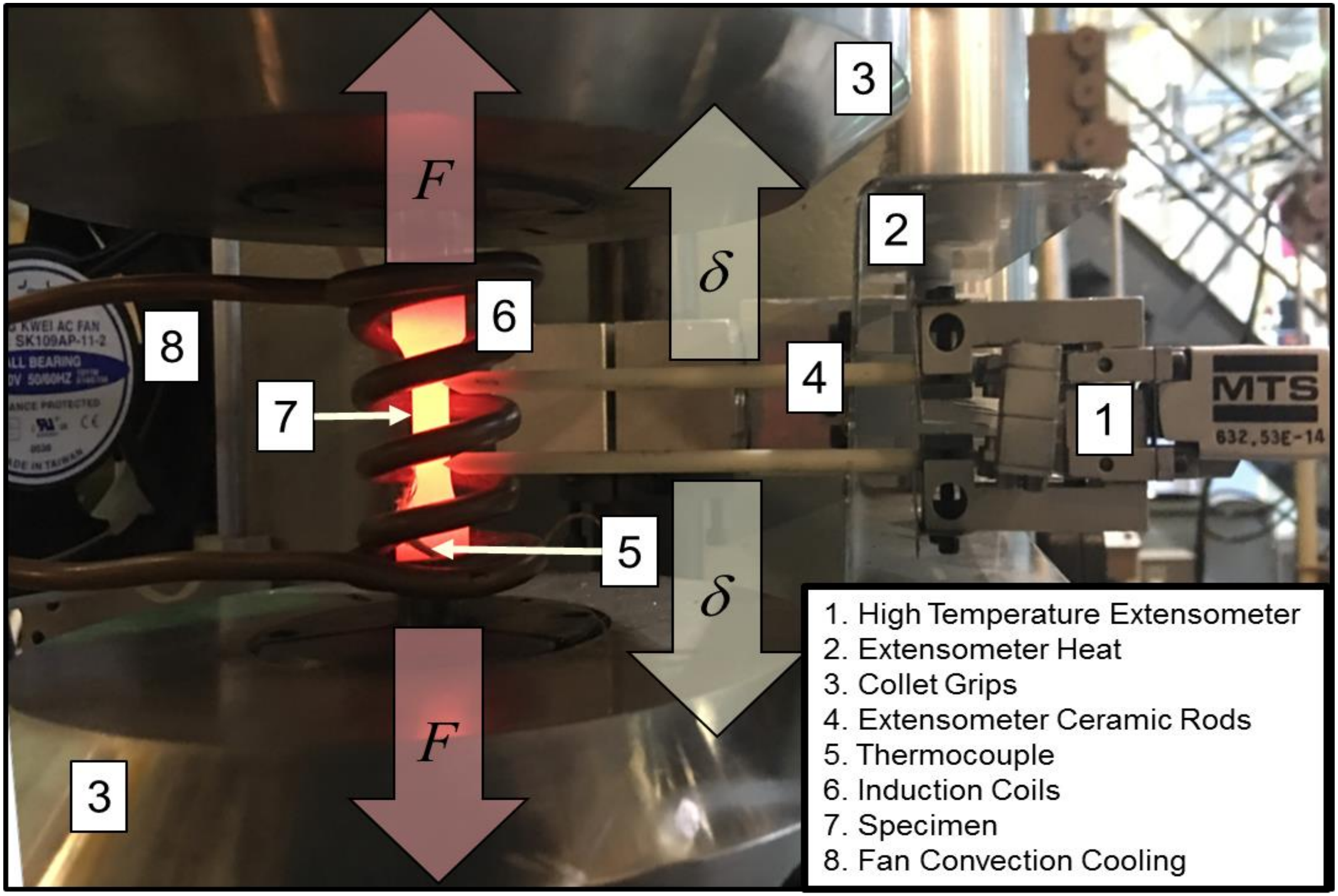

Figure 21: Servohydraulic set-up for strain-controlled testing

During TMF testing, the temperature and the mechanical strain are commanded separately. In-phase (IP) and out-of-phase (OP) TMF test were both considered in this work. The IP and OP TMF command waveform signals are shown schematically in Figure 22. IP TMF tests have a phase angle between the temperature and the mechanical strain command signals of 0 while OP TMF have 180-degree phase angle. Hence, during an IP test, both command signals (strain and temperature) reach their respective minimum and maximum points at the same time. For OP tests, when one signal reaches its maximum the other reaches its minimum.

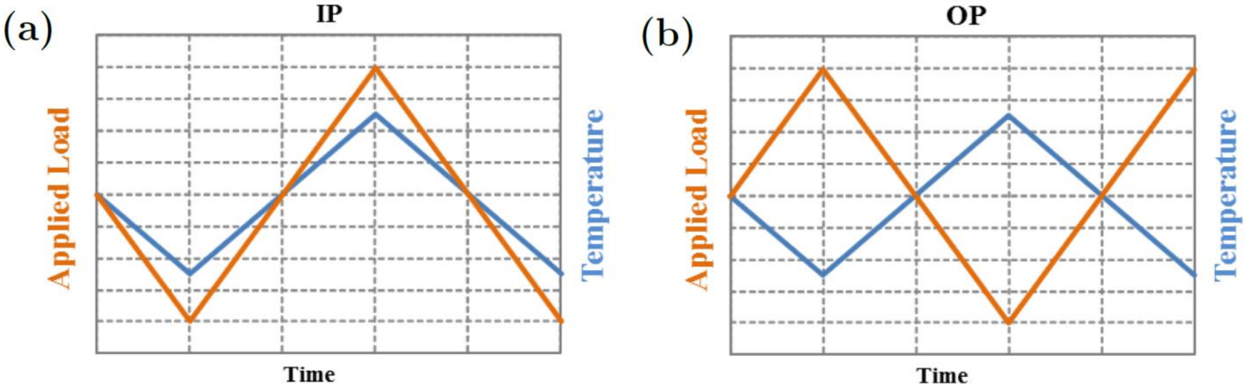

Figure 22: Thermomechanical fatigue waveforms for (a) Out-of-phase (OP) (b) and In-phase (IP) [59]

During TMF testing, the total strain that is measured by the extensometer is comprised of a thermal and a mechanical component,

$$\varepsilon_{total} = \varepsilon_{thermal} + \varepsilon_{mechanical} \tag{8}$$

therefore, to be able to command the required mechanical strain at any given time, the thermal strain that rises form the thermal expansion of the material must be known as well. The thermal strain can be calculated either as a function of temperature or as a function of time. Typically, a polynomial fit is used to model the thermal strain as a function of temperature. The downside of this method is that is does not accurately model the thermal expansion hysteresis induced by the thermal cycle. This hysteresis emerges from experimental errors such as the differences between the heating and cooling of the material, and time lags in the electronic signals used to command both the strain and temperature outputs. Thermal strains can also be calculated as a function of time using periodic functions. A clear advantage of this method is that it can account for the thermal hysteresis in the test. Therefore, time-base thermal expansion compensation is used in this work, as shown in Figure 23. Due to the periodicity of the command signal, periodic Fourier series are used to fit the thermal strains as a function of time,

$$\varepsilon_{thermal} = \frac{1}{2}a_0 + \sum_{n=1}^{N}\left(a_n \sin(nt) + b_n \cos(nt)\right) \tag{9}$$

As shown in Figure 23, between 30 to 40 Fourier coefficients were needed to accurately describe the experimental hysteresis.

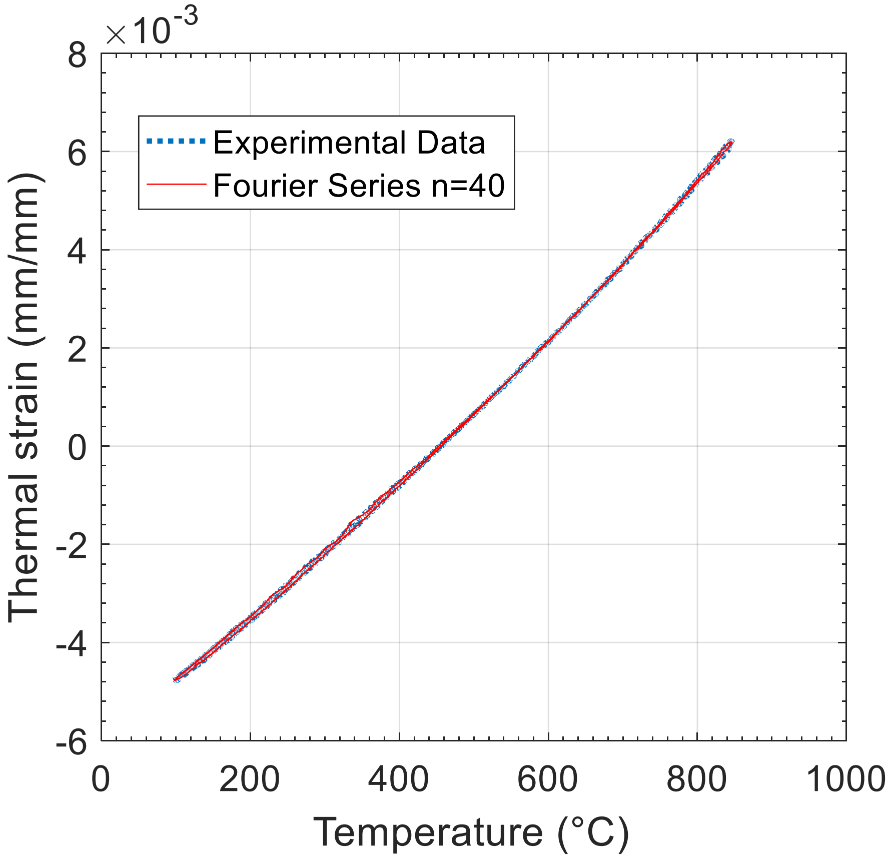

Figure 23: Free expansion thermal strain and time-base thermal strain fit using Fourier Series

3.2.2 Dead-weight testing system

A SATEC model C lever-type dead-weight machine - with a lever ratio of 20:1- was used to load the specimens under constant load and constant temperature. A detail setting of this frame is shown in Figure 24, and Figure 25. A three-zone electric resistance furnace was used to heat the specimens to reach test temperature. The temperature was held within a tolerance of ±1°C using an Omega model CN3251 controller. The temperature in the gage section of the specimen was controlled and monitored using K-type thermocouples which were spot-welded onto the specimen. The creep strain was measured using a high-temperature creep extensometer which was securely mounted at the shoulders of the specimens via machined grooves. The displacement of the extensometer was measured outside the furnace using a clip gage attached through a specially designed gauging platform. The displacement of this platform was converted to strain in accordance to ASTM standard E139-11.

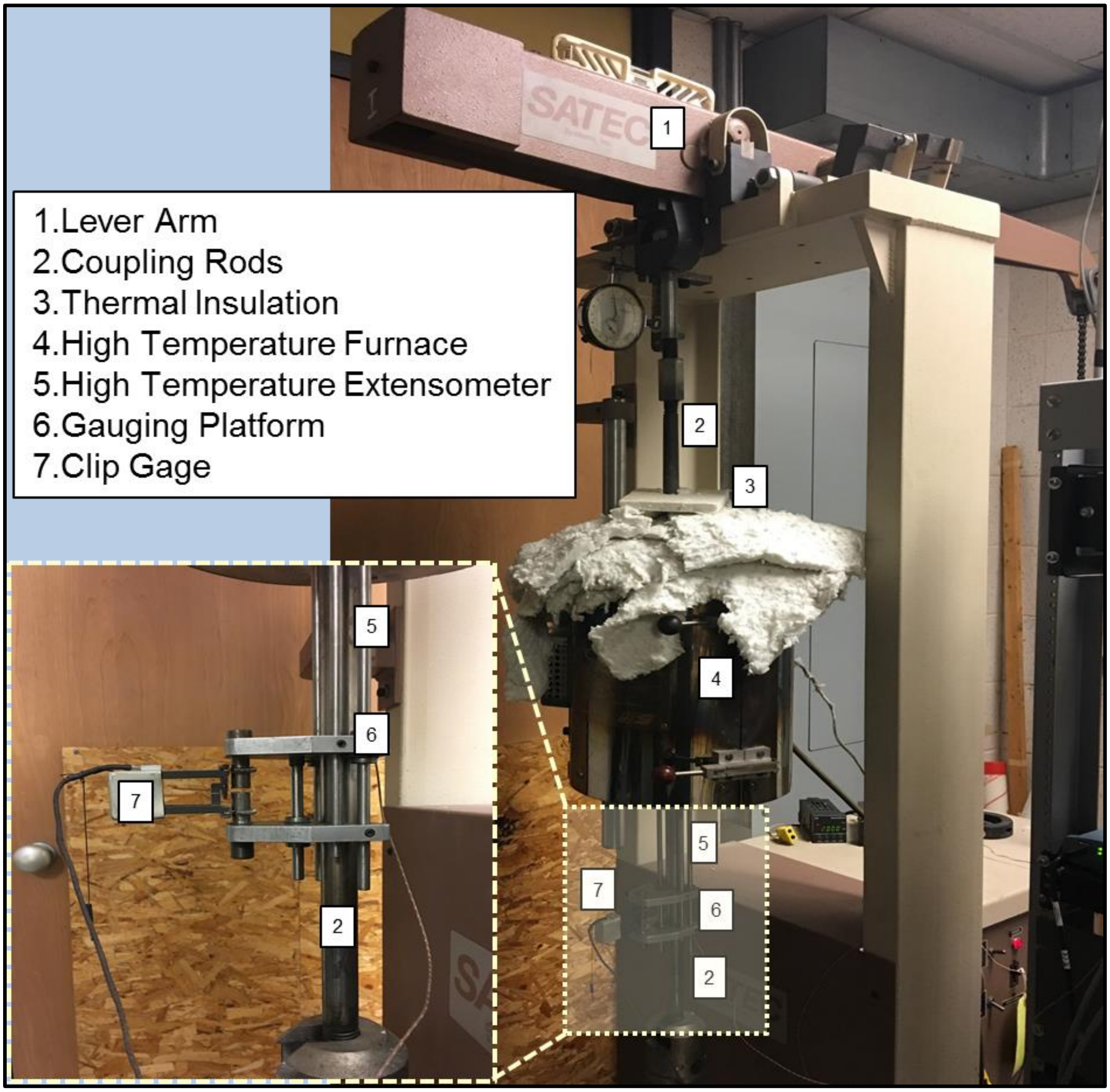

Figure 24: SATEC dead-weight creep machine

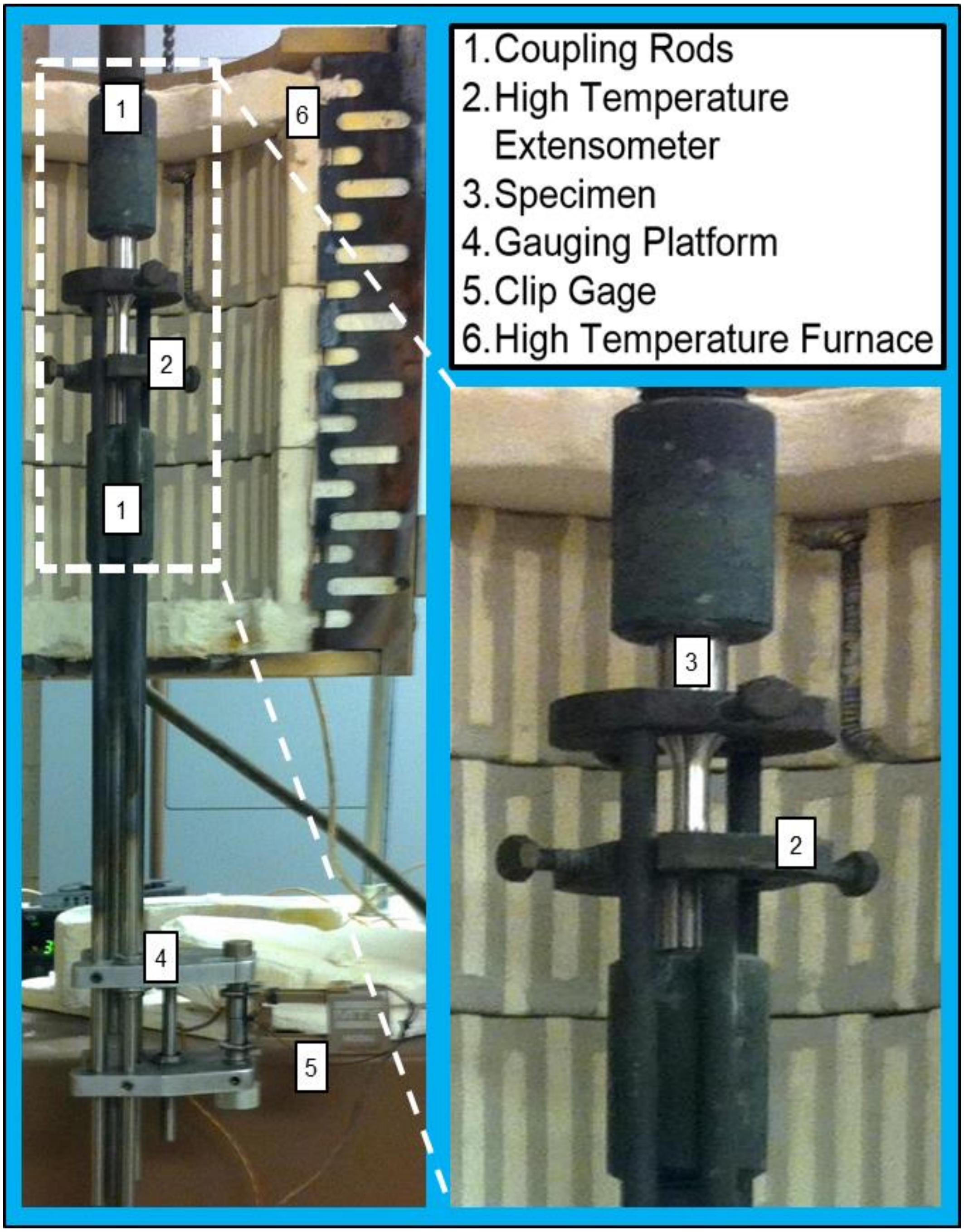

Figure 25: Loading train creep experiment set-up

3.2.3 Strain-controlled experiments

The purpose of these experiments is to generate calibration, verification, and validation data for the creep-fatigue interactions in the constitutive model. Three types of strain-controlled experiments were conducted: isothermal creep-fatigue with strain dwells, isothermal strain-controlled low-cycle fatigue (LCF), and strain-controlled thermomechanical fatigue (TMF). The creep and the CF experiments are used for calibration and verification of the model. The CF experiments contain strain dwells that provide information regarding the coupling of creep and fatigue. The LCF and TMF experiments do not have strain dwells, these tests are used to validate the constitutive model. Out of these two conditions, the TMF tests are the most challenging test conditions to model, and most closely represent the conditions in a hot section component. Hence successful prediction of these conditions means that the model is predictive. Due to the limited availability of specimens, monotonic tests at different orientations and temperatures were not be performed. To compensate for this, the data from the first cycle of the CF and LCF experiments is used to characterize as much of the monotonic response of CMSX-8[B/C] as possible.

All tests were conducted in accordance to ASTM standards. Strain-controlled CF tests with strain dwells were conducted following ASTM standard E2714-13. Strain-controlled LCF tests followed ASTM standard E606/E606M-12. Strain-controlled TMF was performed in accordance to ASTM standard E2369-10. The specimen geometry shown in Figure 26 was used for all the strain-controlled tests and care was taken that the geometry was compatible with all ASTM testing standards. The raw CMSX-8[B/C] rods and slabs were sent to Element Materials Technology, Cincinnati, OH who by grinding manufactured the specimens.

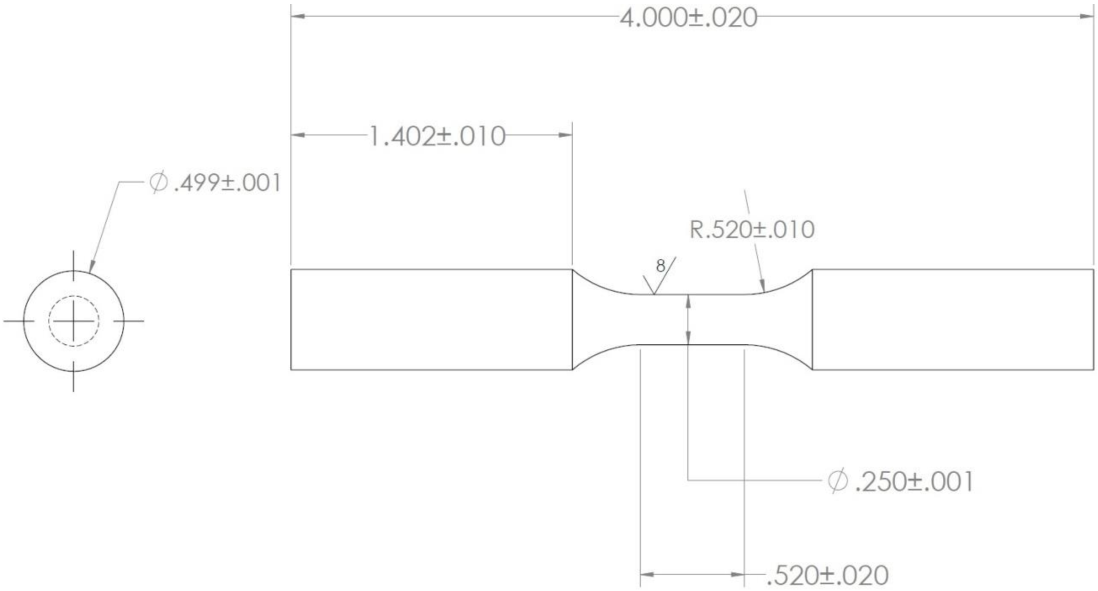

Figure 26: Creep-fatigue, low-cycle fatigue, and thermomechanical fatigue specimen

3.2.4 Stress-controlled experiments

Constant stress creep experiments were conducted in accordance to ASTM standard E139-11. The Cannon Muskegon Corporation, Muskegon, MI, and Siemens Energy Inc., Orlando FL, kindly shared data from twelve tests performed on nominal CMSX-8. Very limited number of CMSX-8[B/C] specimens were available, therefore only two creep tests could be conducted to support the research in this work. Since no literature is available on CMSX-8[B/C], these two test were used to verify that the creep performance of both alloys is relatively close to each other. If their performance were similar, then the nominal CMSX-8 data can be used to calibrate material parameters in the CVP model. The creep specimen geometry is shown in Figure 27 and was designed in accordance with ASTM standards E139-11 and E8/E8M-11. Raw CMSX-8[B/C] rods were sent to Element Materials Technology, Cincinnati, OH for manufacturing.

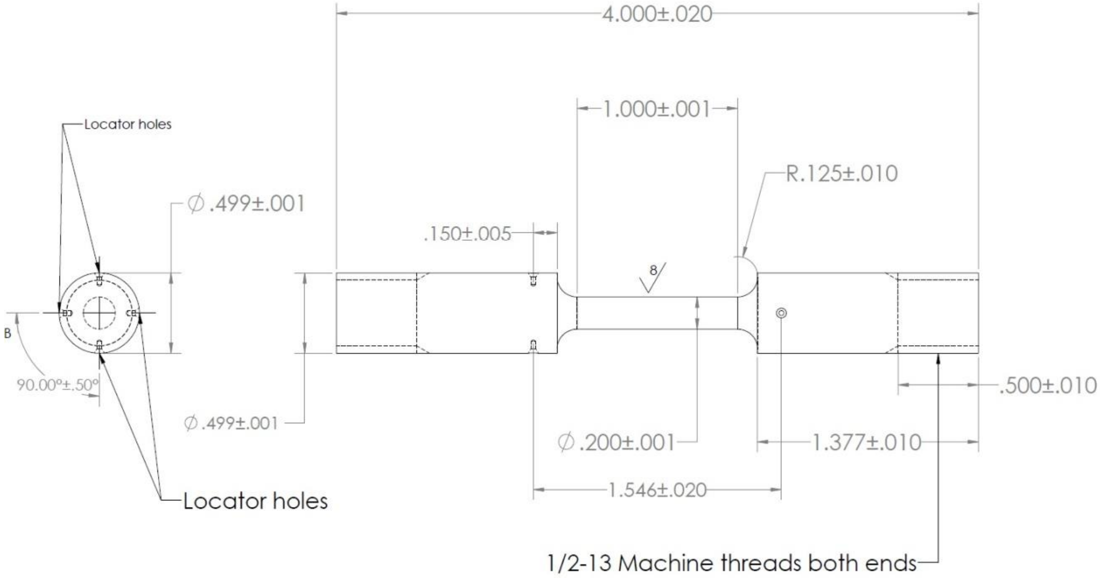

Figure 27: Creep specimen

3.3 Experimental Results

3.3.1 Monotonic response and coefficient of thermal expansion

The data from the first cycle of the CF and LCF experiments was used to characterize as much of the monotonic response of CMSX-8[B/C] as possible. All the CF and LCF test conditions used to infer the monotonic response can be found in the next two sections in Table 4, Table 5, and Table 6 .The monotonic data is used to calibrate the crystallographic elastic tensor components defined by equations (5), (6), and (7). The yield strength is also obtained to calibrate the bulk strength of the material as a function of temperature. In Figure 28, the monotonic behavior of CMSX-8[B/C] in the <001> and <111> orientation as a function of temperature is summarized. An important aspect to note from the monotonic behavior curves is that unlike most superalloys which exhibit yield strength tension and compression asymmetry [60, 61], CMSX-8[B/C] does not experience this behavior.

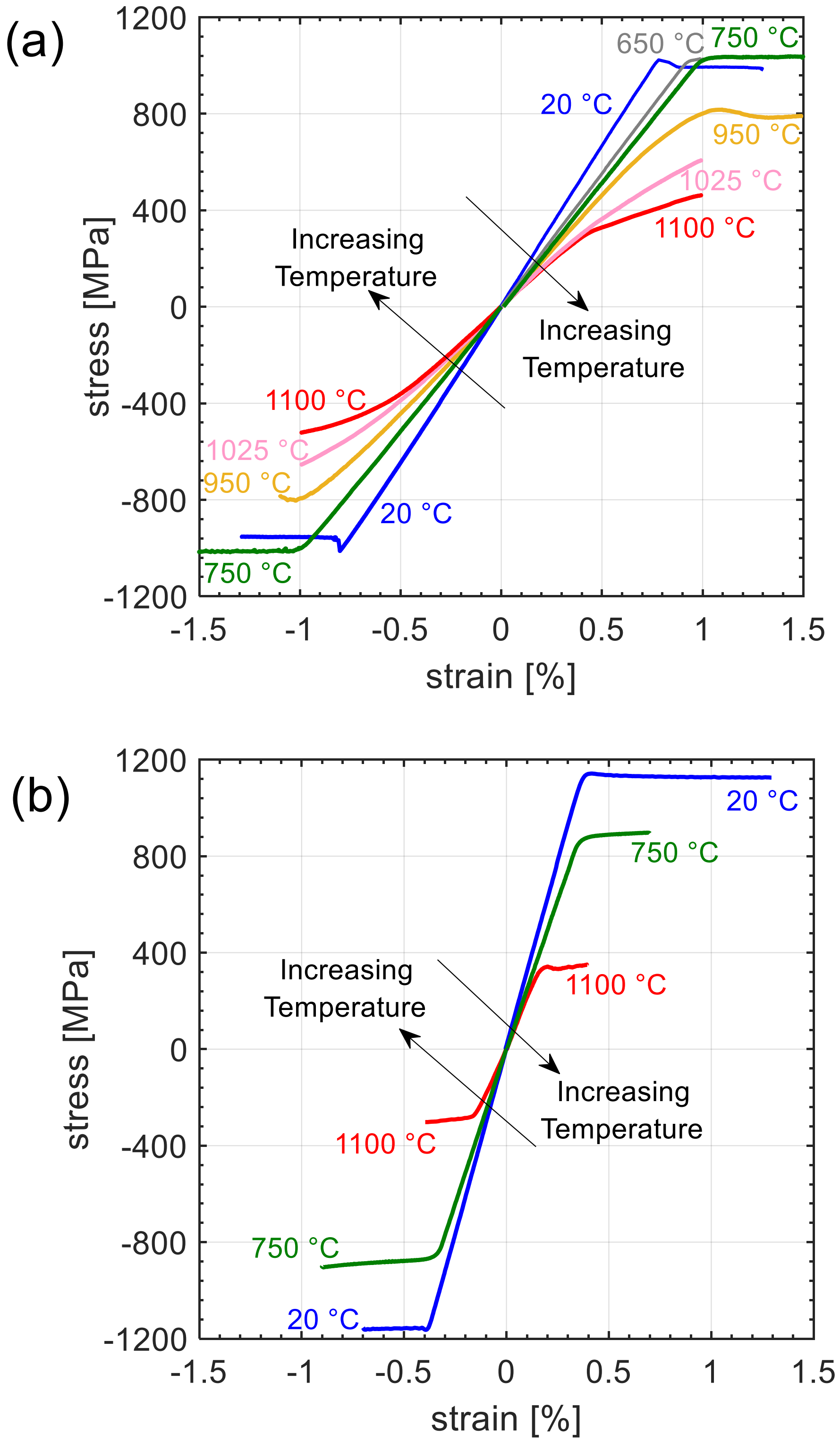

Figure 28: Monotonic behavior of CMSX-8[B/C] at $\dot{\varepsilon}$ of $1x10^{-3}$ [1/s]: (a) in the <001> crystallographic orientation. (b) in the <111> crystallographic orientation

The elastic modulus data is shown in Figure 29 and is calculated by fitting a first order polynomial using linear regression over the elastic region of the monotonic curves. Several CF and LCF tests were conducted at each temperature; hence several moduli measurements were possible per temperature. The variance in the moduli in the <111> orientation data in Figure 29 is due to the small variations in the crystallographic orientation of the specimens. Note that in Figure 7, the gradient of the moduli as a function of orientation is steeper for directions close to the *<111>*, subsequently slight variations in orientation have a more noticeable effect on the moduli in that direction.

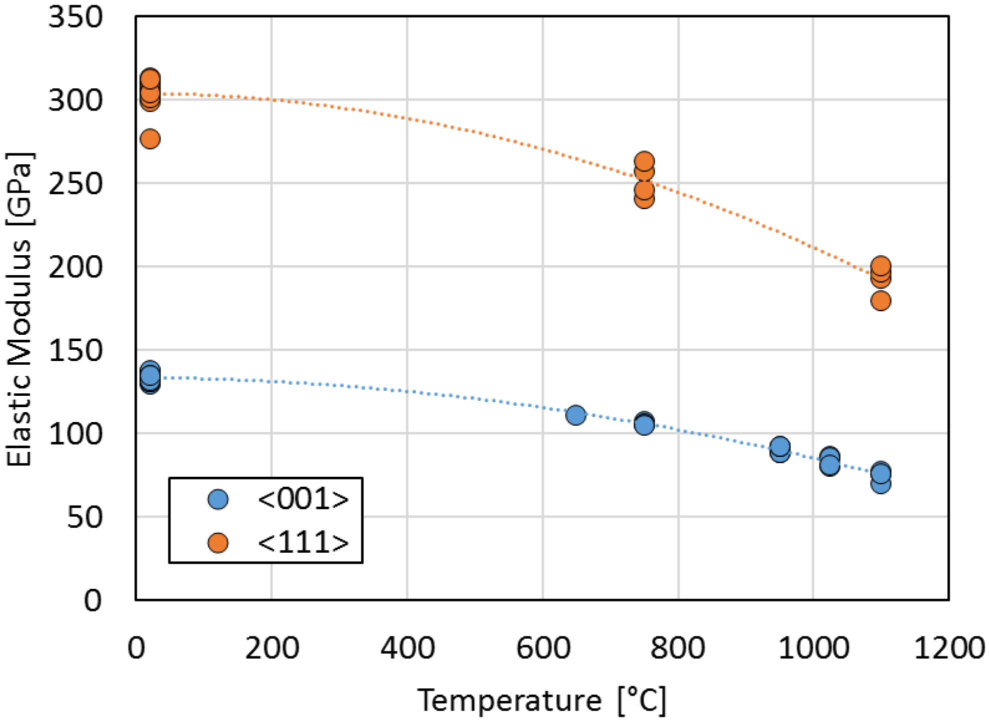

Figure 29: Elastic modulus of CMSX-8[B/C] in the <001> and the <111> crystallographic orientation.

Figure 30 and Figure 31 show the 0.2% and 0.02% yield offset as a function of orientation on CMSX-8[B/C], while Figure 32 shows the 0.2% yield offset on nominal CMSX-8.

The offsets for CMSX-8[B/C] were calculated from the first cycle of those CF and LCF tests that exhibited measurable plastic deformation. By comparing these results to the reported values of yield strength on nominal CMSX-8 in Figure 32, it is seen that CMSX-8[B/C] exhibits a 15% increment in strength at room temperature with respect to CMSX-8, while at higher temperatures the yield strengths of both alloys are comparable. A possibility could be that the presence of carbides might impede the movement of dislocations at lower temperature.

As shown in Figure 30 and Figure 31, the anomalous yield strength is observable in the *<001>* orientation, while in the *<111>* orientation these behavior is not present. This is still explained by the thermally activated cross-slip of dislocations. When tested along the *<111>* crystallographic orientation, entire dislocation segments cross-slip and shear the precipitates due to the very high level of resolved shear stresses in the cube planes. Therefore, the entanglement of dislocations in the energetically unfavorable planes does not take place [62, 63].

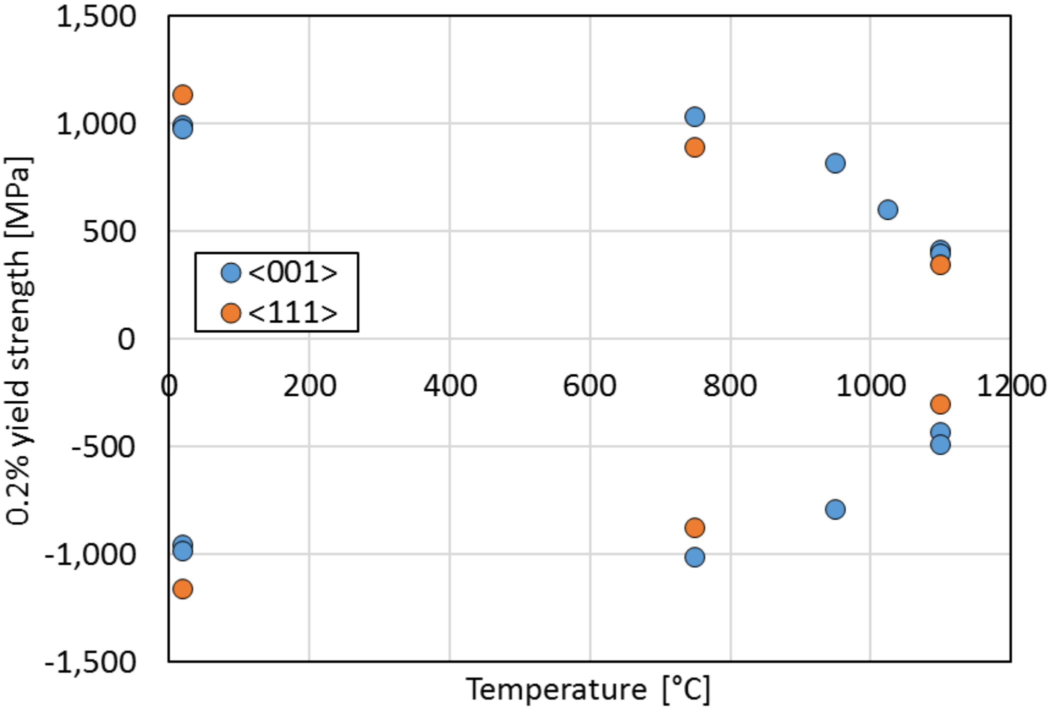

Figure 30: 0.2% offset yield strength of CMSX-8[B/C]

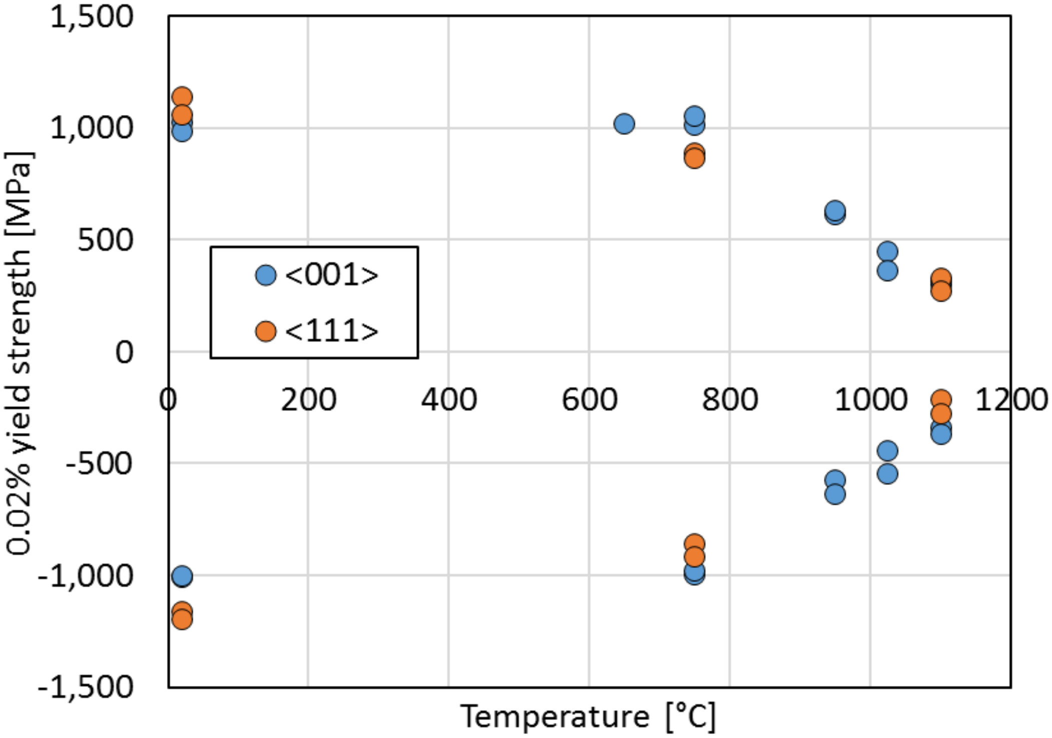

Figure 31: 0.02% offset yield strength of CMSX-8[B/C]

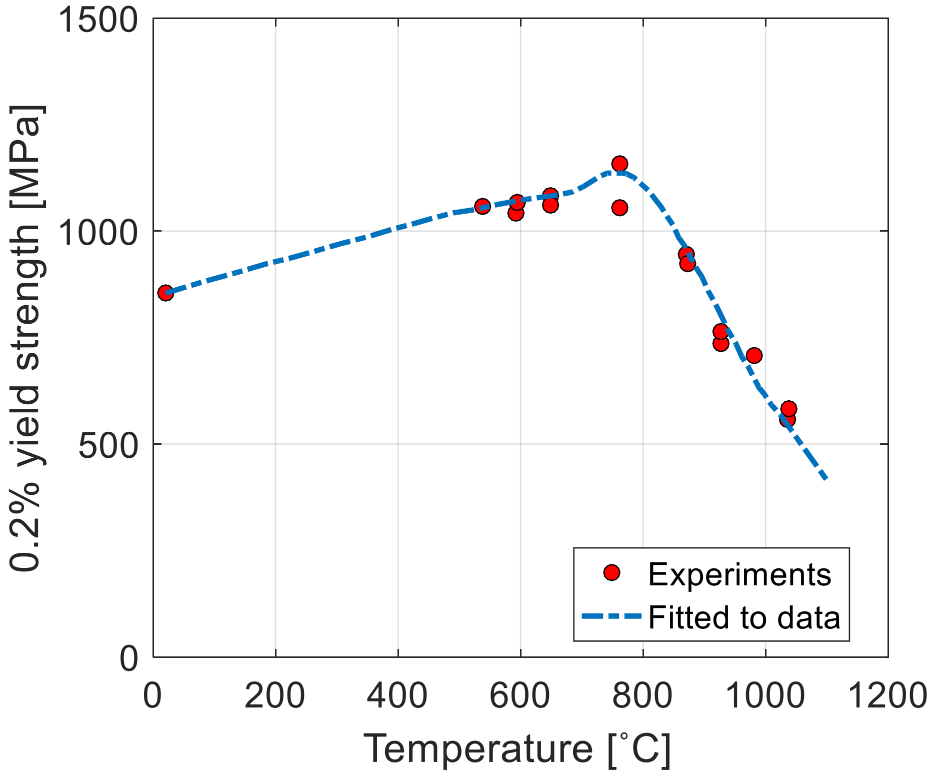

Figure 32: 0.2% offset yield strength of nominal CMSX-8 [6]

The coefficient of thermal expansion (CTE) is obtained as a function of temperature from the data that is acquired while heating the specimens to reach the desired test temperature. This CTE data becomes important in modeling TMF since the CTE is used to calculate the thermal part of the deformation gradient. The thermal strain as a function of temperature is shown in Figure 33. For every creep-fatigue, LCF test, and TMF test, during the heating ramp (10˚C/s) to reach the test temperature, the thermal strain was measured. This measurement was done using the high temperature extensometer while commanding a zero load through the servo-hydraulic system which ensures free expansion of the specimen. By fitting a second order polynomial to the thermal strain vs. temperature data, the coefficient of thermal expansion is obtained as,

$$\alpha = \frac{\partial \varepsilon_{thermal}}{\partial T} \tag{10}$$

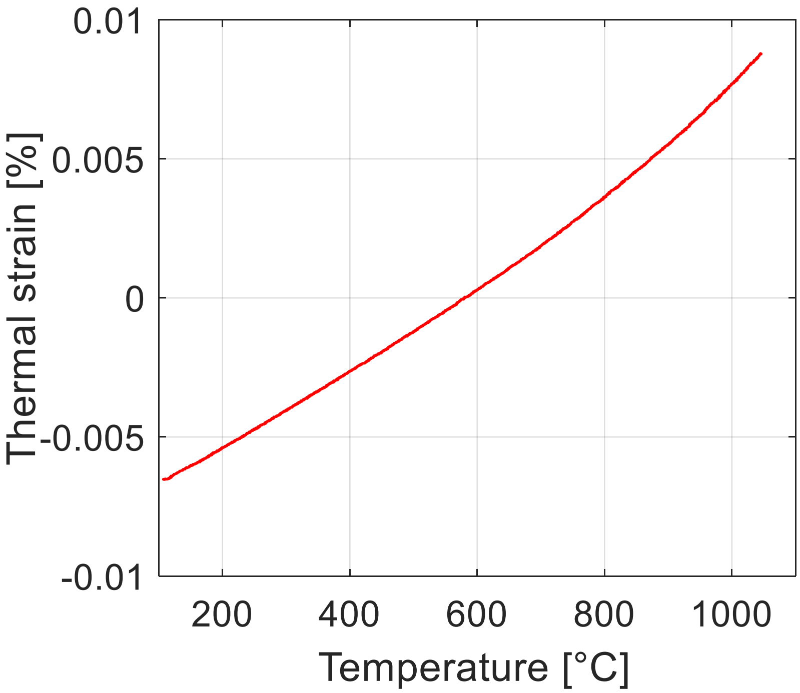

Figure 33: Thermal strain [%] as a function of temperature

3.3.2 Isothermal creep-fatigue with strain dwells

The life data collected from all the CF experiments is plotted in Figure 34 and Figure 35. A 30% load drop is used as a life criterion in this work. It can be seen that in both crystallographic orientations, for an equal strain range, whether the strain ratio (*R*) was zero or negative infinity affected the life of the specimens. Specifically, *R* of negative infinity tends to result in shorter lives than tests performed at *R* of zero. Hence, applied strain ($\Delta\varepsilon$) alone cannot be used to predict life and other variables, including crystallographic orientation, are likely affecting the life.

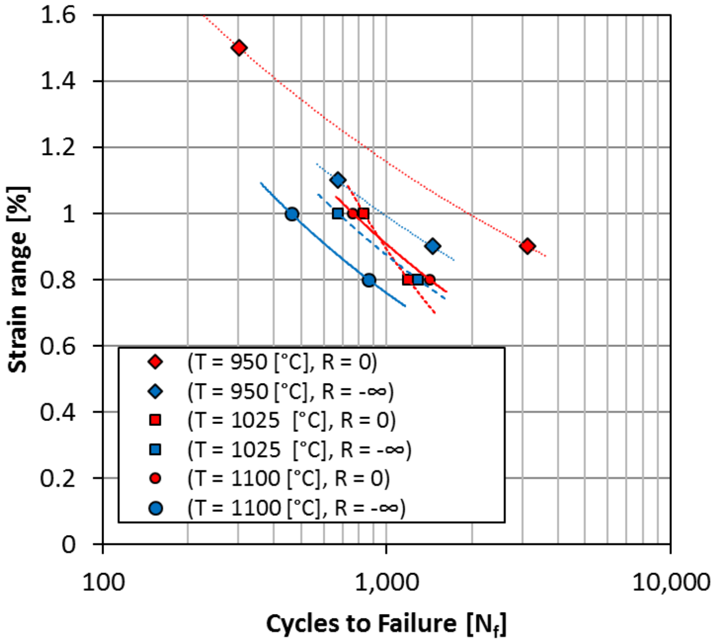

Figure 34: Creep-fatigue life data <001> crystallographic orientation with 3 minute holds using 30% load drop as a life criterion

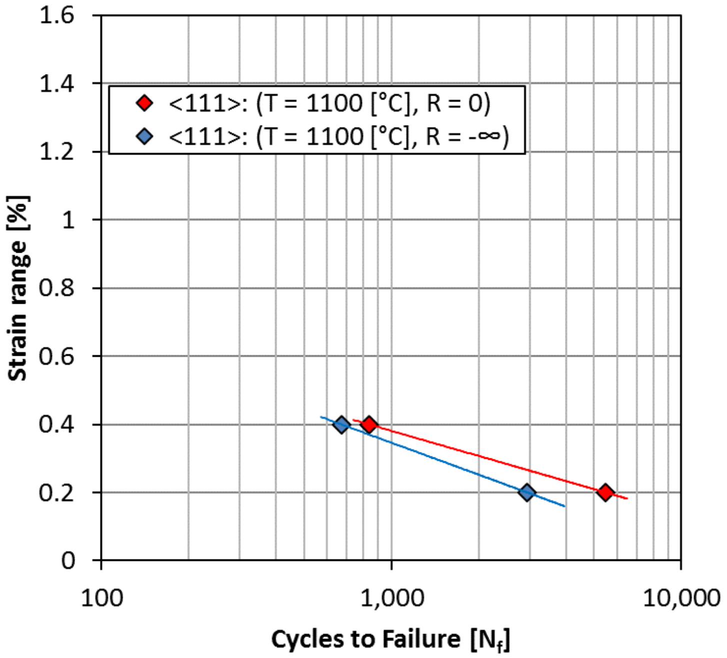

Figure 35: Creep-fatigue life data in the <111> crystallographic orientation with 3 minute holds using 30% load drop as a life criterion

The CF test conditions used to obtain the life results for specimens oriented in the <001> crystallographic orientation are shown in Table 4, while the CF conditions for specimens in the <111> orientation are shown in Table 5.

Table 4: Test conditions for strain-controlled creep-fatigue experiments with strain dwells in the <001> crystallographic orientation

strain rate 1×10^{-3} [1/s]					
Temperature [°C]	**Dwell time [s]**	**Dwell type**	***R***	**$\Delta\varepsilon$ [%]**	**N_f [cycles]**
650	1200	Tensile and Compressive	0	2	15
750	1200	Tensile and Compressive	0	2	15
950	180	Compressive	$-\infty$	0.9	1,447
950	180	Compressive	$-\infty$	1.1	671
950	180	Tensile	0	0.9	3,138
950	180	Tensile	0	1.5	250
1025	180	Compressive	$-\infty$	0.8	1,293
1025	180	Compressive	$-\infty$	1	676
1025	180	Tensile	0	0.8	1,192
1025	180	Tensile	0	1	832
1100	180	Compressive	$-\infty$	0.8	980
1100	180	Compressive	$-\infty$	1	461
1100	180	Tensile	0	0.8	1,420
1100	180	Tensile	0	1	762

Table 5: Test conditions for strain-controlled creep-fatigue experiments with strain dwells in the <111> crystallographic orientation

strain rate 1x10^{-3} [1/s]					
Temperature [°C]	**Dwell time [s]**	**Dwell type**	***R***	**$\Delta\varepsilon$ [%]**	**N_f [cycles]**
1100	180	Compressive	$-\infty$	0.2	2,940
1100	180	Compressive	$-\infty$	0.4	671
1100	180	Tensile	0	0.2	5,477
1100	180	Tensile	0	0.4	836

The strain rate selected for testing is typical of values used to characterize the mechanical behavior of superalloys. Temperatures of 650˚C and 1100˚C will be used for calibrating the model because at these temperatures either the γ phase or the γ' phase deformation mechanisms is dominant. The remaining temperatures will be used for verification. The dwell times are added to calibrate for material parameters that are related to the coupling of creep and fatigue. For 1100˚C, the strain dwells were imposed at either maximum tension or compression in accordance to the strain ratio. To prevent very long testing time, these dwells were set to 3 minutes (180 seconds). At lower temperatures, it was expected for the stress relaxation to take longer, hence the dwell time for the experiments at 650°C and at 750°C was 20 minutes. As shown in Figure 36, the strain dwell time selected is sufficient for the stress relaxation to quasi stabilize. Beyond this time, the material does not exhibit any significant amount of additional stress relaxation. For all the tests with strain dwells, it was verified that similar results were observed.

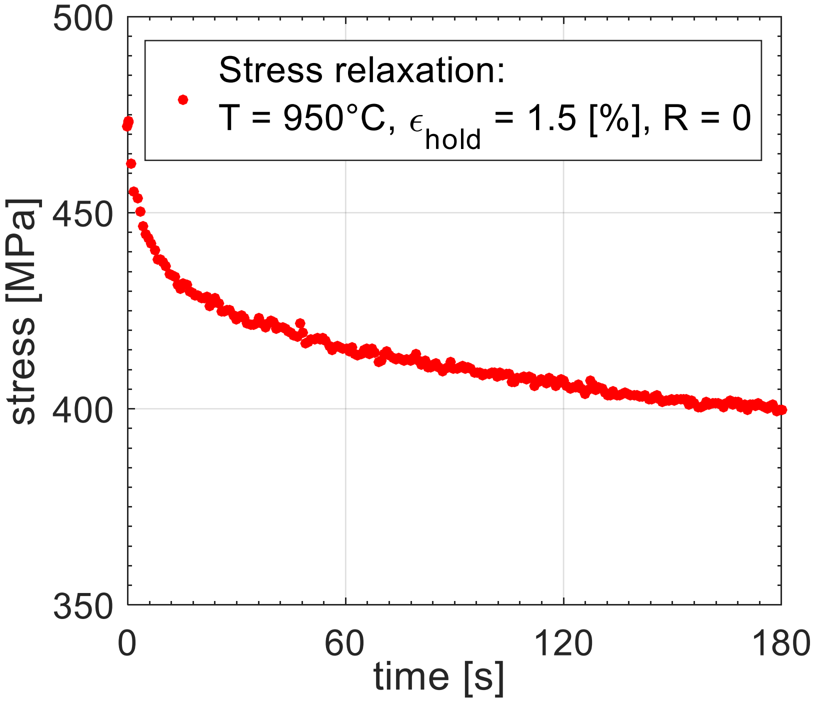

Figure 36: Typical strain dwell relaxation during the stabilized cycle of creep-fatigue test

Turbines blades have regions where they experience either all negative or all positive loads, therefore the tests in this work were conducted for strain ratios (*R*) of 1 and -∞. However, it was observed that CMXS-8[B/C] does not experience visible tension/compression asymmetry. Consequently, for the tests at 650°C and at 750°C, it was considered more effective to use a strain ratio (*R*) of 0 with dwells at maximum tension and at maximum compression in the same test. Finally, the strain ranges in Table 5 and Table 4 were selected such that enough plasticity would be present in the stabilized hysteresis loops, without plasticity only the elastic material parameters could be calibrated.

To understand better understand the life results of Figure 34 and Figure 35, and to extract data useful for the calibration of the model, the hysteresis data obtained from the CF tests was post-processed to make plots of the first ten hysteresis loops and of the stabilized hysteresis loop.

These data provide information regarding the cyclic creep for non-symmetric R ratios, and with information regarding the elastic modulus at the test temperature in the tested crystallographic orientations. The plots of the first ten hysteresis for test matrices detailed in Table 4 and Table 5 can be seen in Figure 37 throughout Figure 42.

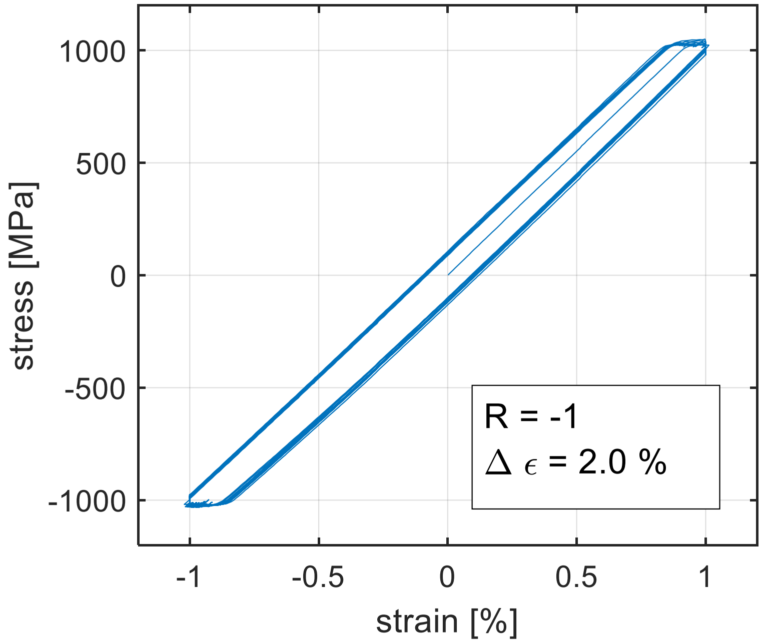

Figure 37: First ten cycles of creep-fatigue experiments at 650°C in the <001> crystallographic orientation: R = -1 and Δε = 2.0%

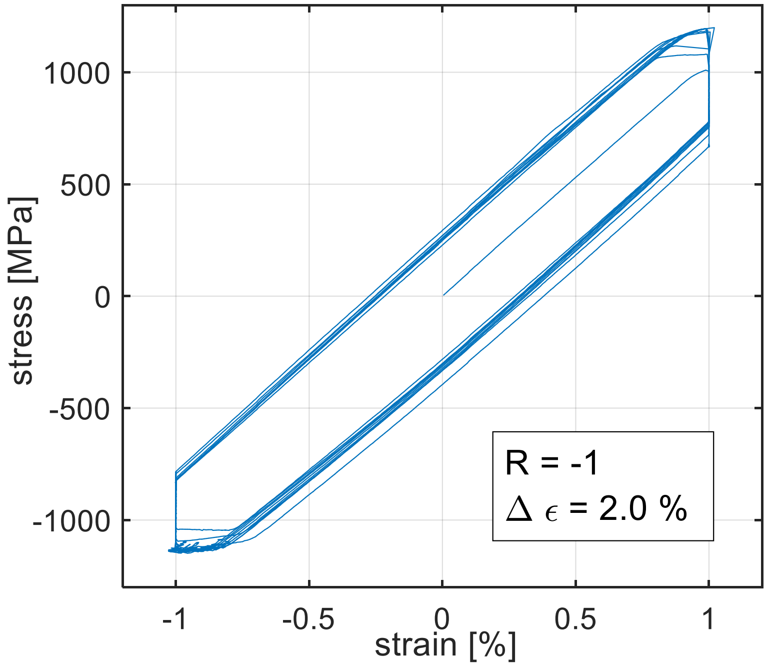

Figure 38: First ten cycles of creep-fatigue experiments at 750°C in the <001> crystallographic orientation: R = -1 and Δε = 2.0%

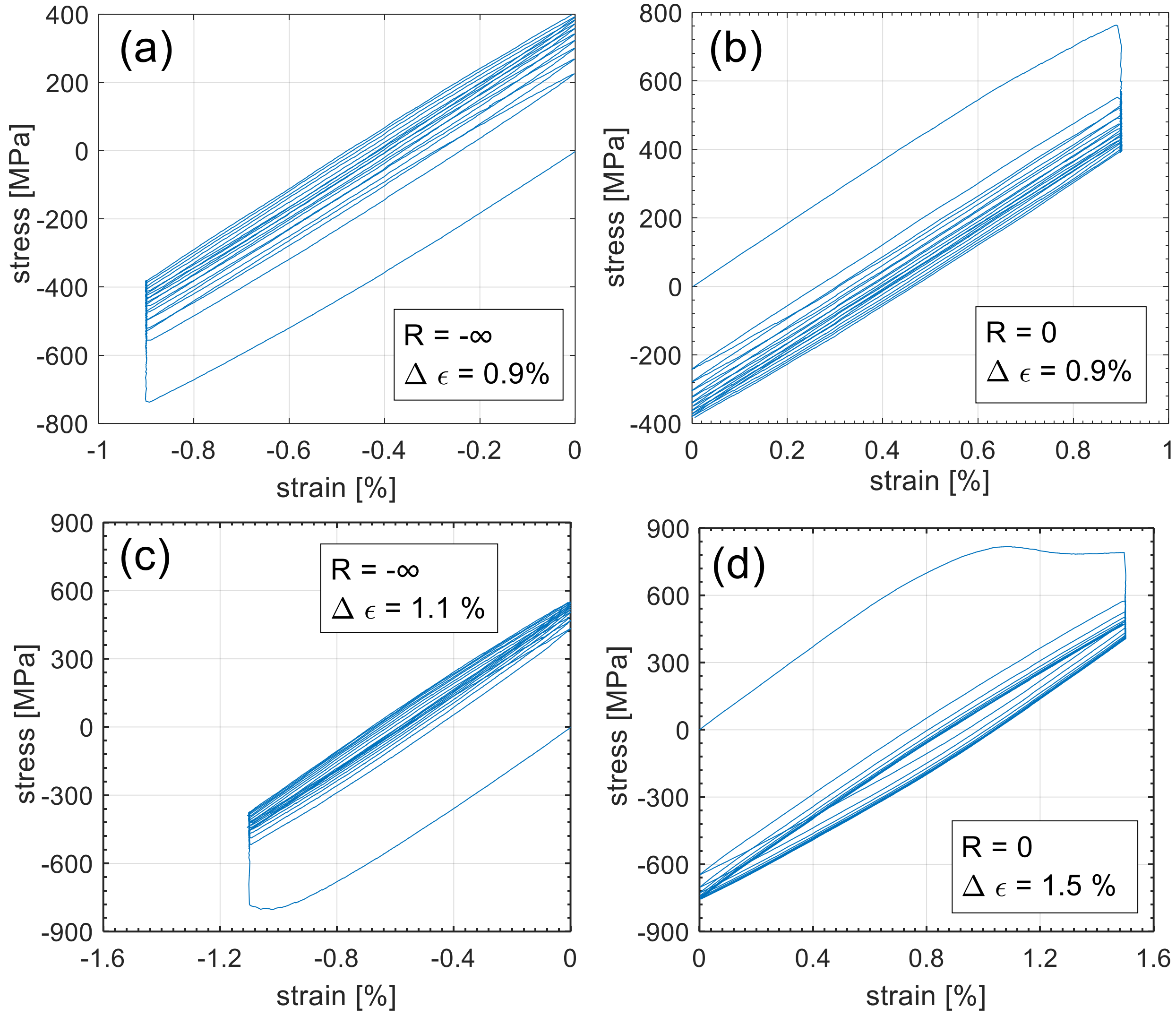

Figure 39: First ten cycles of creep-fatigue experiments at 950°C in the <001> crystallographic orientation: (a) R = -∞ and Δε = 0.9%. (b) R = 0 and Δε = 0.9% (c) R = -∞ and Δε = 1.1% (d) R = 0 and Δε = 1.5%

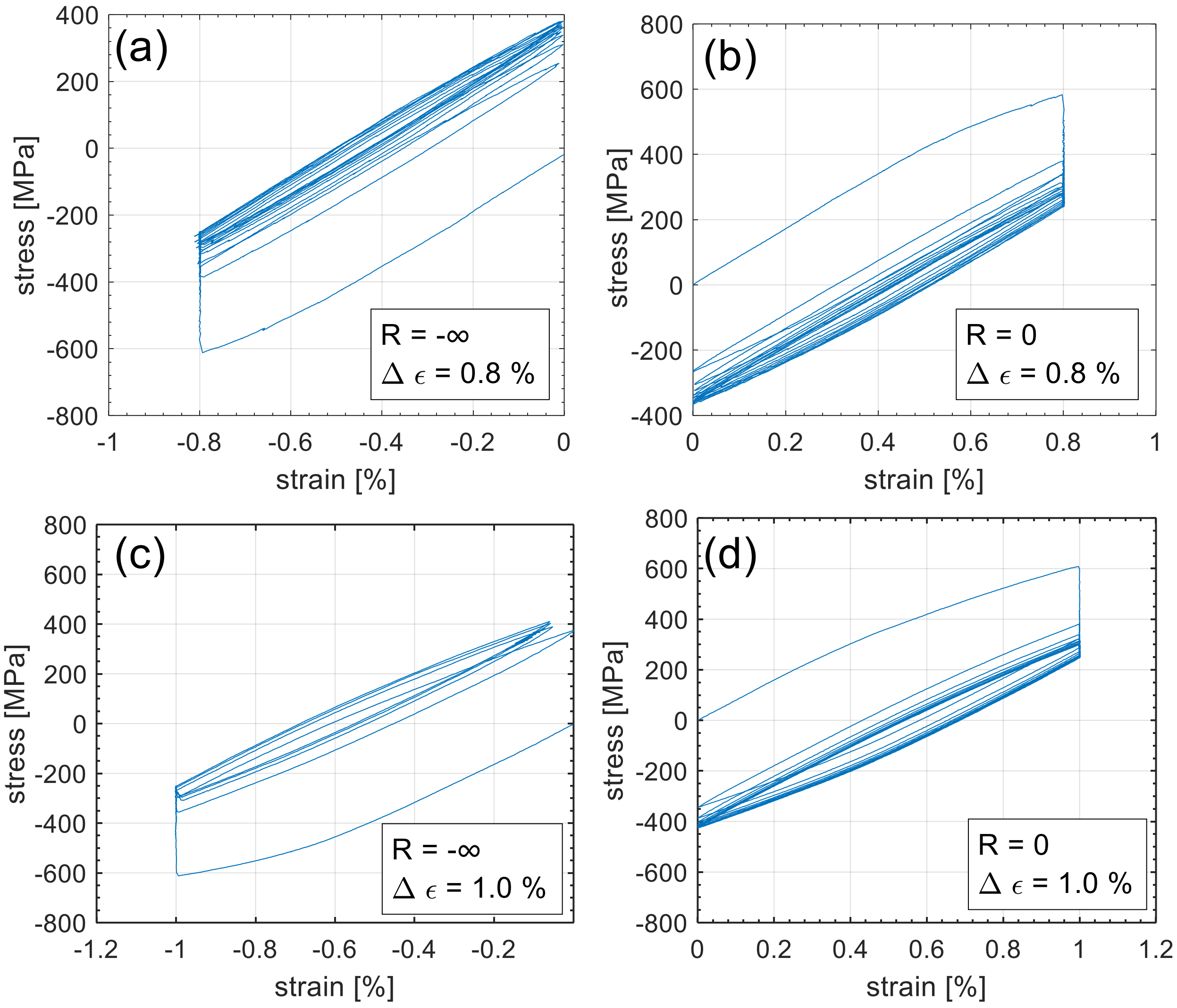

Figure 40: First ten cycles of creep-fatigue experiments at 1025°C in the <001> crystallographic orientation: (a) R = -∞ and Δε = 0.8%. (b) R = 0 and Δε = 0.8% (c) R = -∞ and Δε = 1.0% (d) R = 0 and Δε = 1.0%

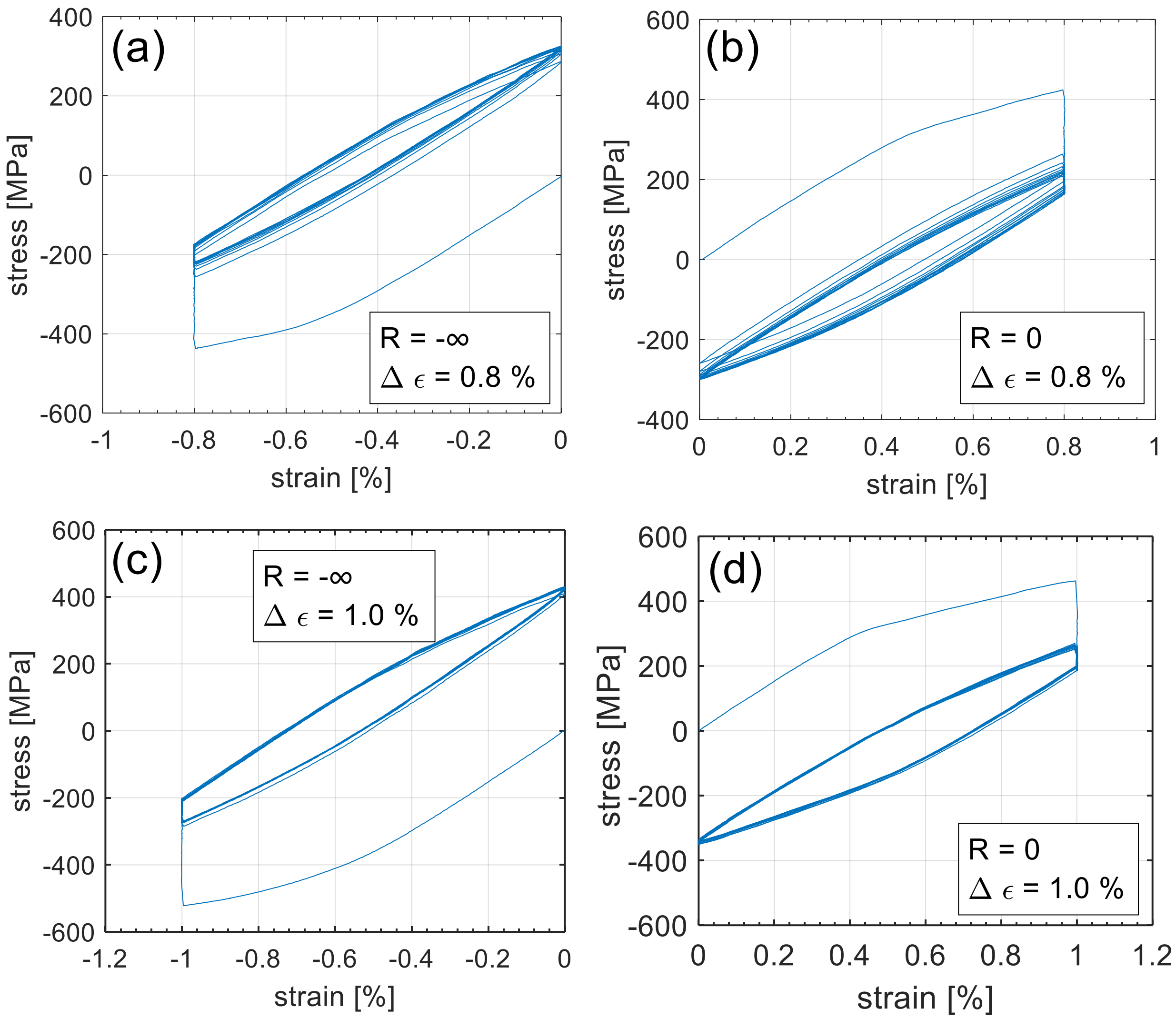

Figure 41: First ten cycles of creep-fatigue experiments at 1100°C in the <001> crystallographic orientation: (a) R = -∞ and Δε = 0.8%. (b) R = 0 and Δε = 0.8% (c) R = -∞ and Δε = 1.0% (d) R = 0 and Δε = 1.0%

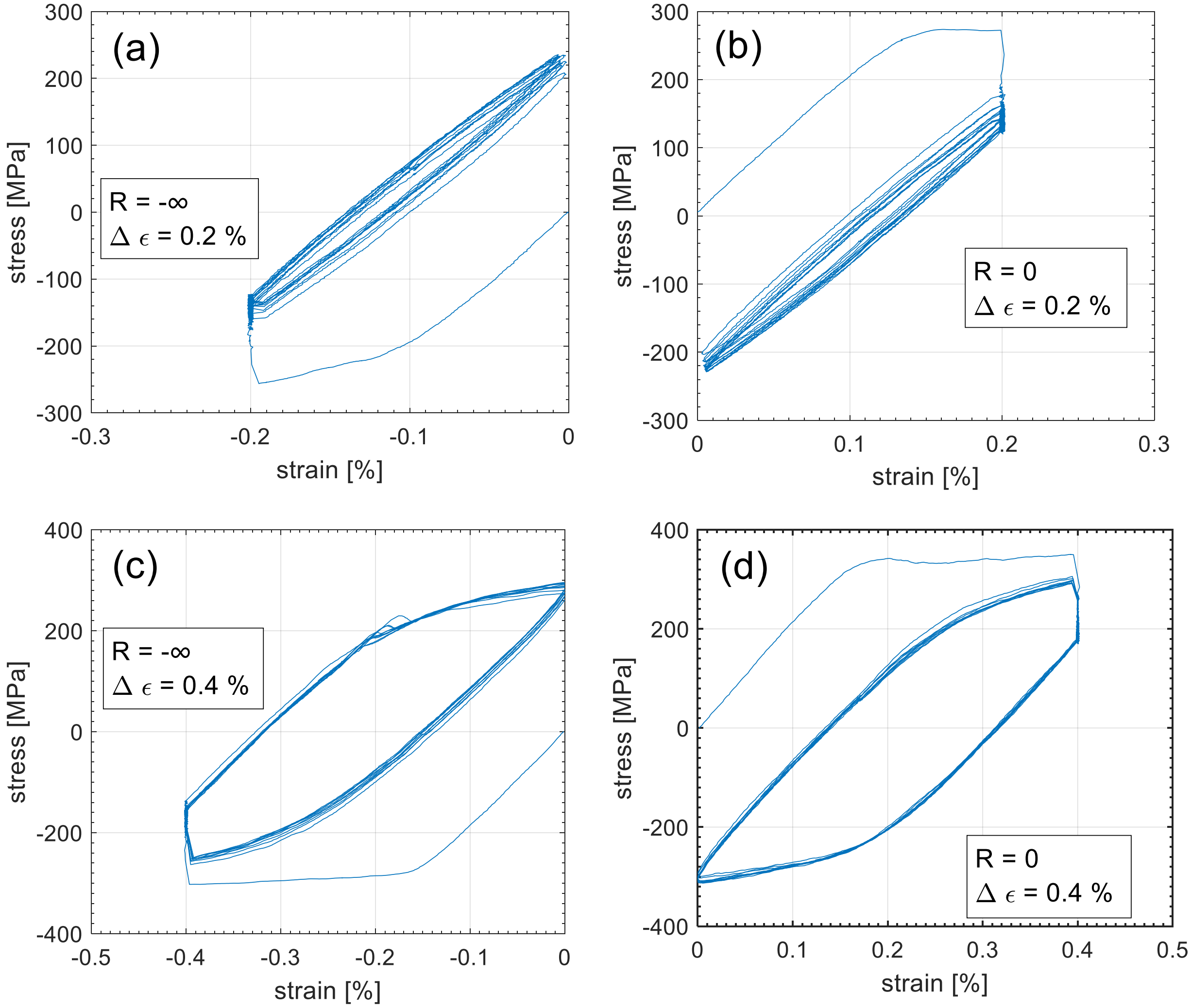

Figure 42: First ten cycles of creep-fatigue experiments at 1100°C in the <111> crystallographic orientation: (a) R = -∞ and Δε = 0.2%. (b) R = 0 and Δε = 0.2% (c) R = -∞ and Δε = 0.4% (d) R = 0 and Δε = 0.4%

From this data, it is observed that the amount of cyclic creep decreases with increasing temperature. The cyclic creep in tests conducted at 1100°C stabilizes very quickly. After the first cycle no cyclic creep is experienced. Another observation from these plots is that at temperatures of 1025°C and 1100°C there is noticeable hardening during the first cycle. Conversely, at lower temperatures very small amount of hardening or none is observed. Also, in the <111> crystallographic orientation, for lower levels of strain range, larger plastic strains are achieved due to the very high stress induced by the larger modulus in this orientation.

The stabilized responses are shown in Figure 43 through Figure 48. Most superalloys reach their stabilized hysteresis loops after the first 10 cycles [46]. The stabilized hysteresis data will be used to calibrate and verify the model parameters related to saturation of the mechanical response.

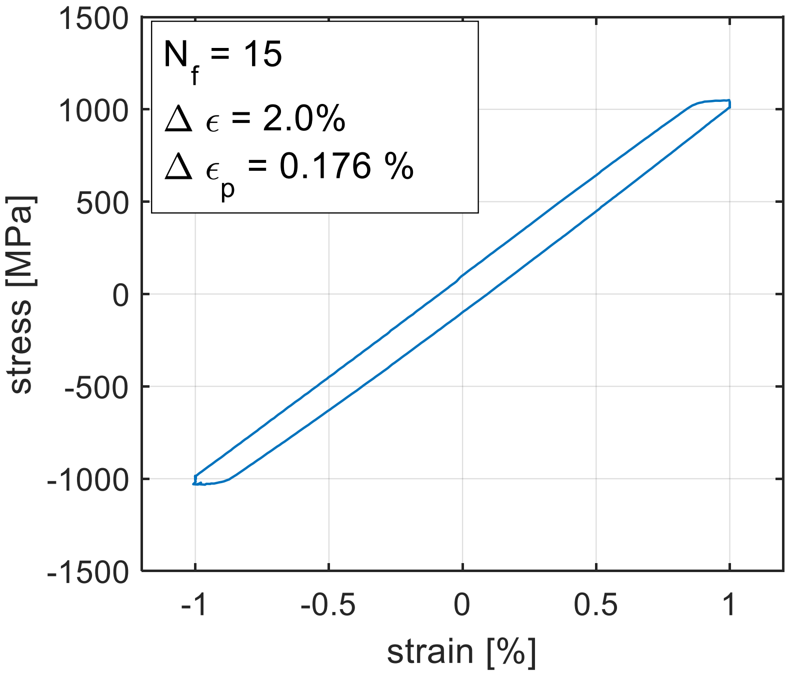

Figure 43: Stabilized hysteresis of creep-fatigue experiments at 650°C in the <001> crystallographic orientation: (a) R = -1 and Δε = 2.0%.

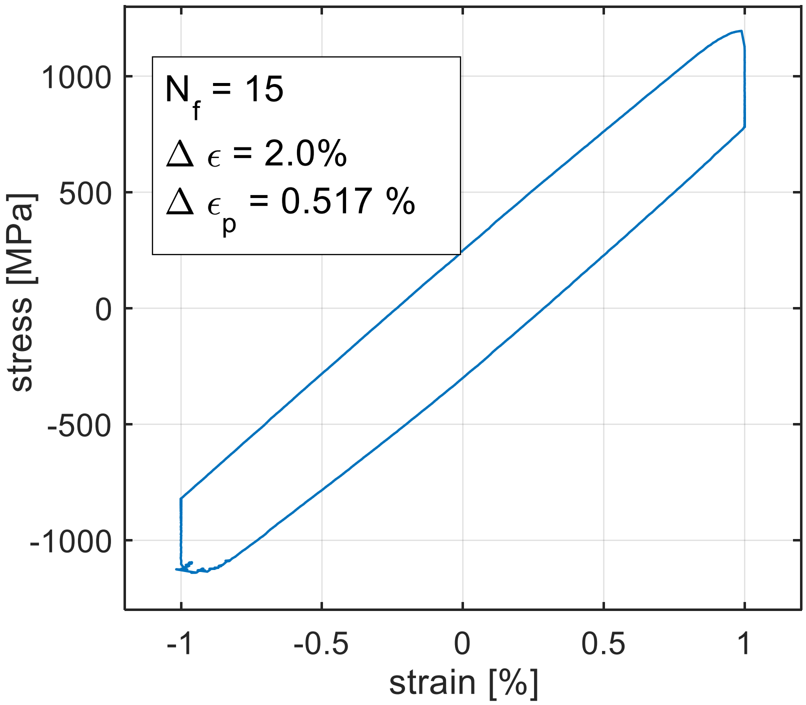

Figure 44: Stabilized hysteresis of creep-fatigue experiments at 750°C in the <001> crystallographic orientation: (a) R = -1 and Δε = 2.0%.

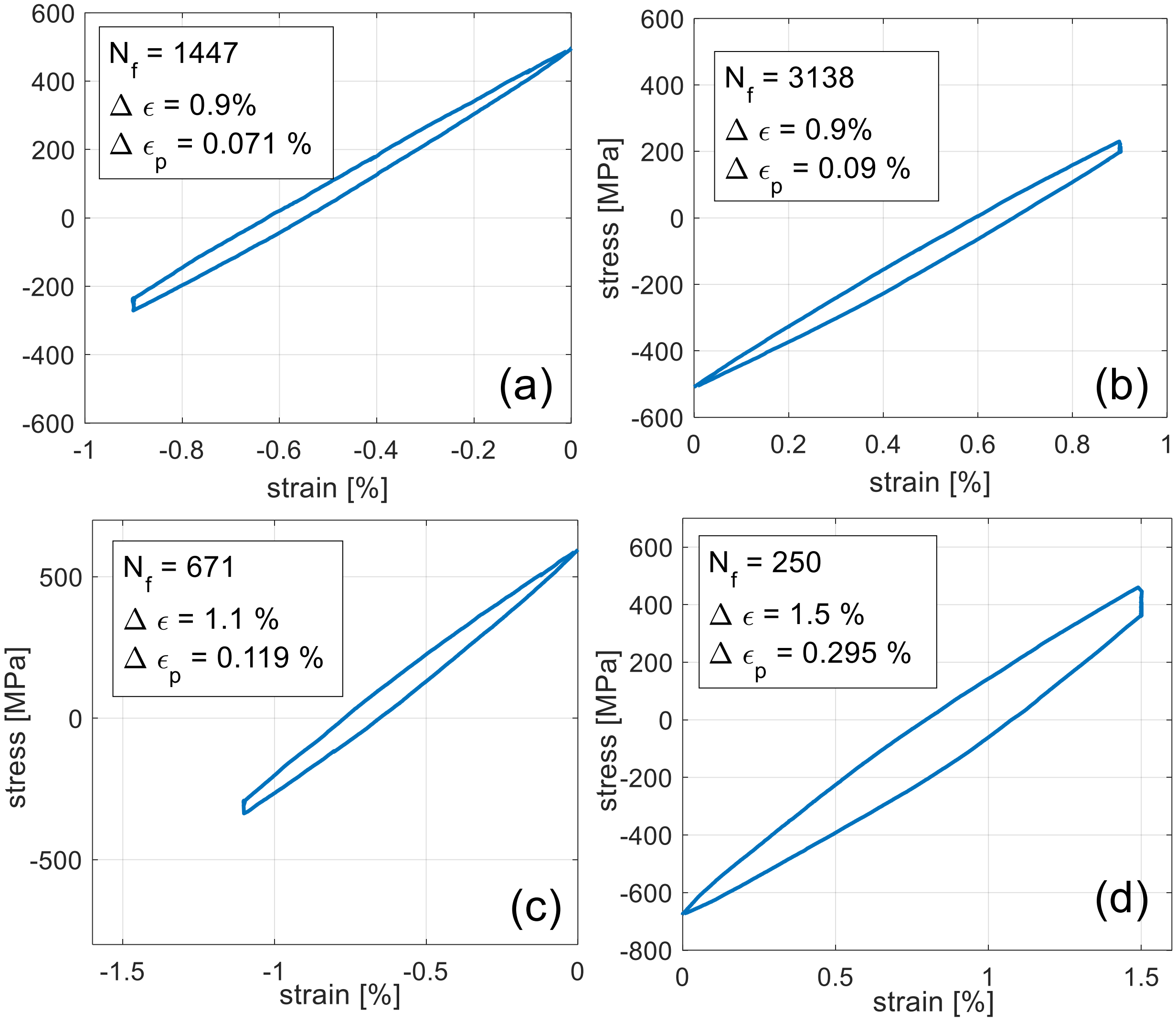

Figure 45: Stabilized hysteresis of creep-fatigue experiments at 950°C in the <001> crystallographic orientation: (a) R = -∞ and Δε = 0.9%. (b) R = 0 and Δε = 0.9% (c) R = -∞ and Δε = 1.1% (d) R = 0 and Δε = 1.5%

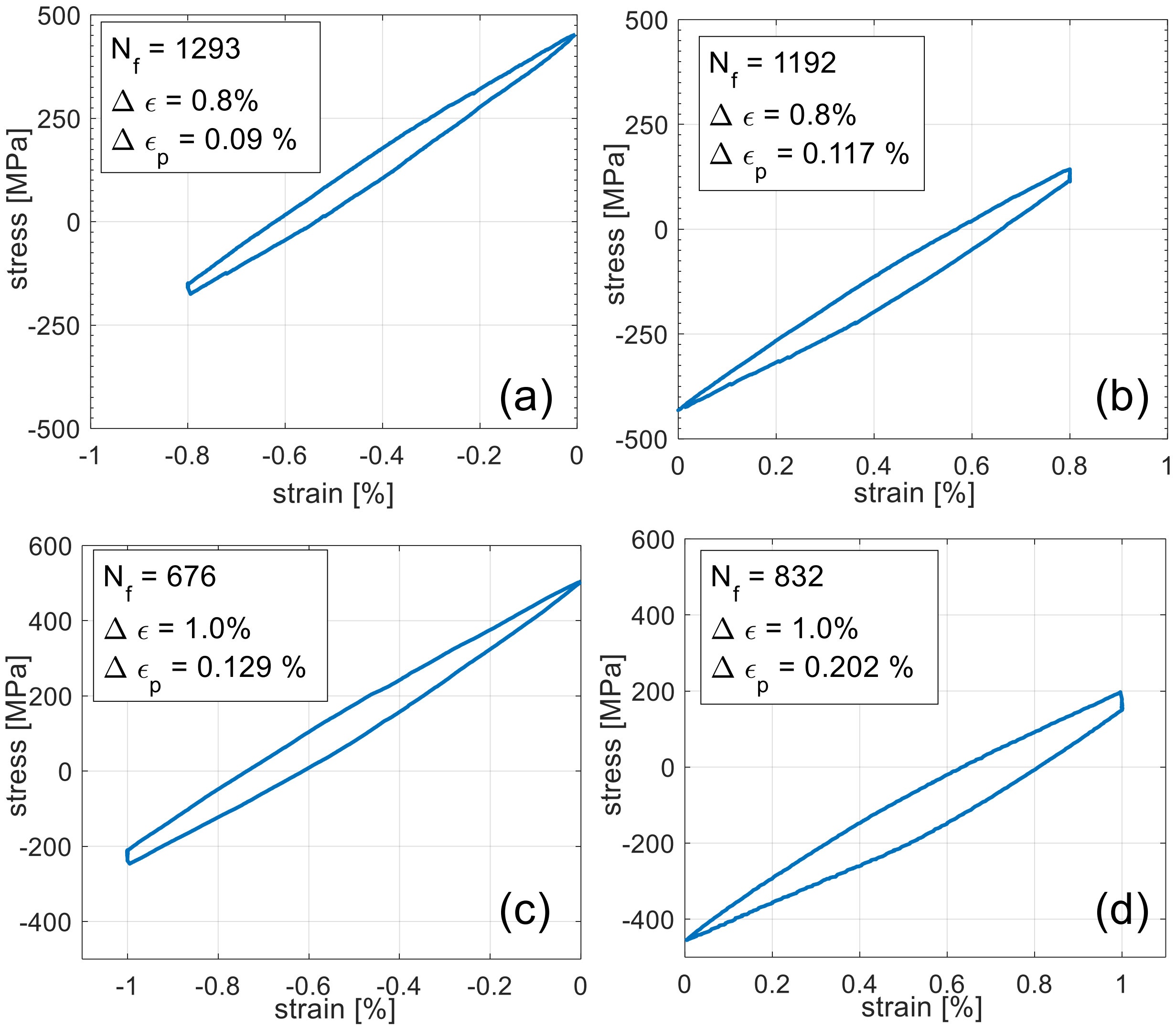

Figure 46: Stabilized hysteresis of creep-fatigue experiments at 1025°C in the <001> crystallographic orientation: (a) R = -∞ and Δε = 0.8%. (b) R = 0 and Δε = 0.8% (c) R = -∞ and Δε = 1.0% (d) R = 0 and Δε = 1.0%

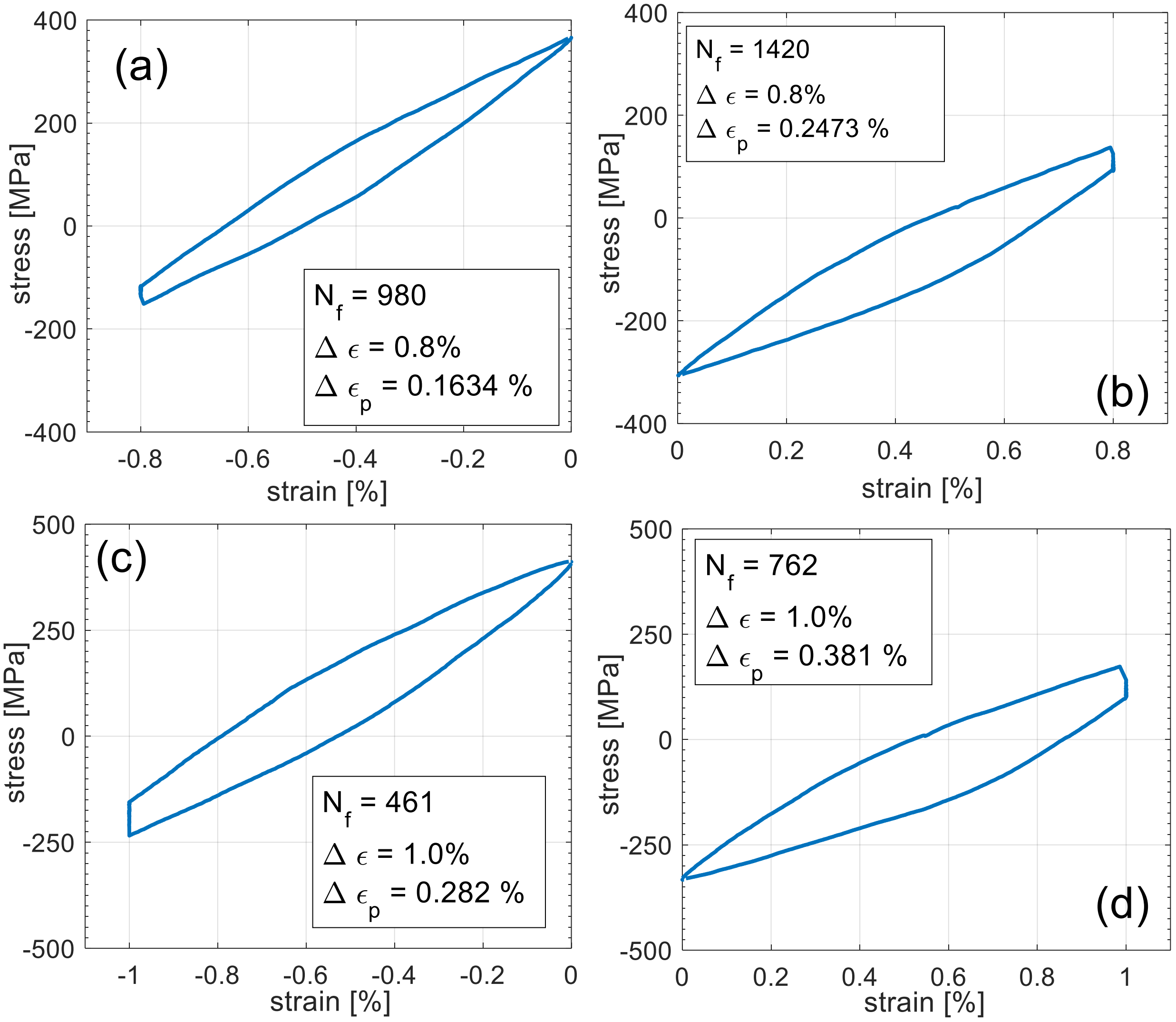

Figure 47: Stabilized hysteresis of creep-fatigue experiments at 1100°C in the <001> crystallographic orientation: (a) R = -∞ and Δε = 0.8%. (b) R = 0 and Δε = 0.8% (c) R = -∞ and Δε = 1.0% (d) R = 0 and Δε = 1.0%

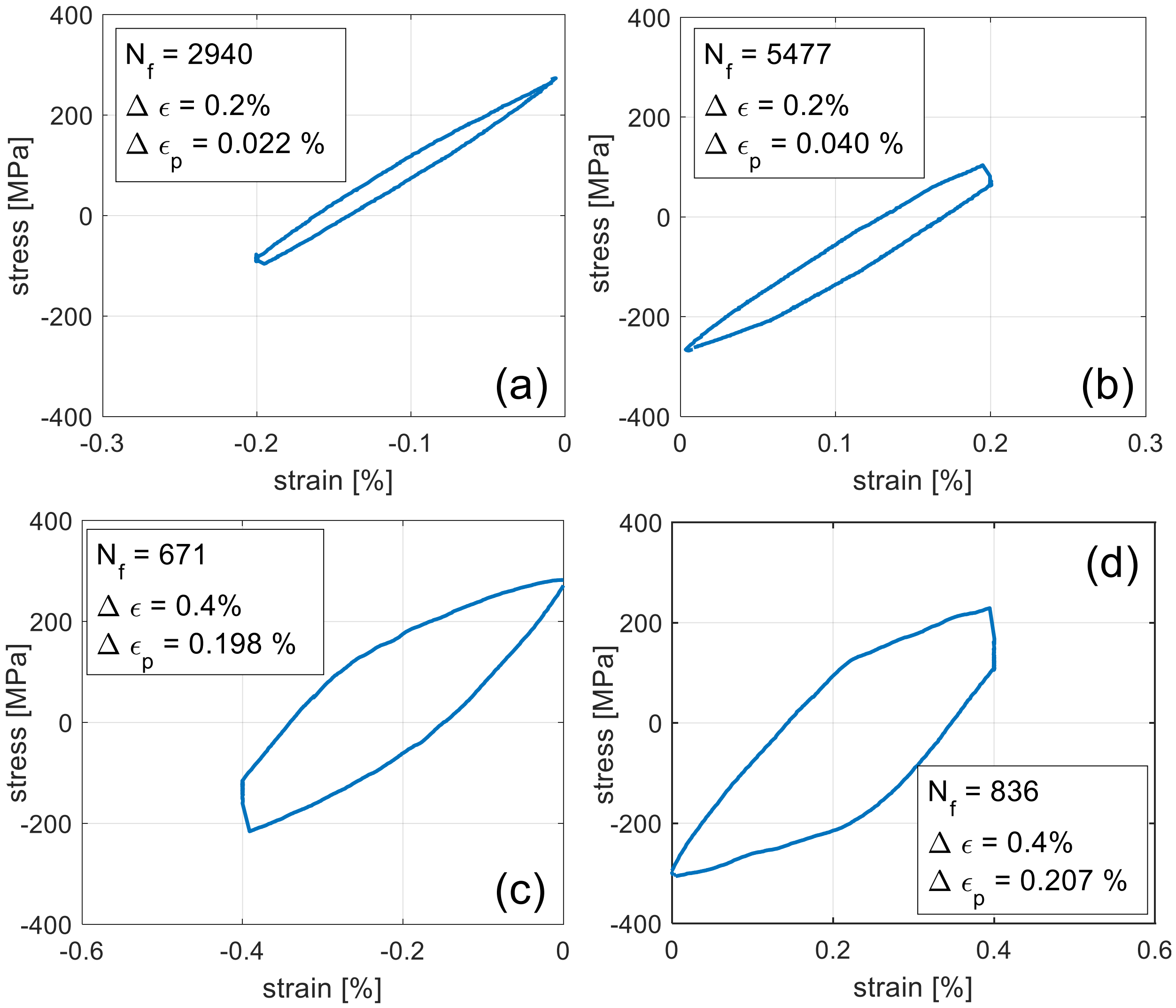

Figure 48: Stabilized hysteresis of creep-fatigue experiments at 1100°C in the <111> crystallographic orientation: (a) R = -∞ and Δε = 0.2%. (b) R = 0 and Δε = 0.2% (c) R = -∞ and Δε = 0.4% (d) R = 0 and Δε = 0.4%

The life data in Figure 34 and Figure 35, can be explained by these hysteresis plots and by the stress evolution over all cycles. From Figure 45 through Figure 48, it can be seen that the mean stress developed over cycling varies with applied strain ratio. This is more apparent in the evolution of the stress during cycling, shown in Figure 51 through Figure 54. The evolution of stress can be explained by the asymmetric nature of the loading conditions. For R equal to 0, the strain dwells are at the maximum tensile strain. During these dwells, the tensile stress relaxes toward a negative stress, thus helping develop a compressive mean stress. Conversely, when R is $-\infty$ the compressive stress reached at the dwells relaxes toward a tensile mean stress. Several empirical life models for Ni-base superalloys use a combination of the mean stress or the maximum stress and the plastic strain range to predict life [64]. Consequently, for the model to be also useful for life prediction applications, it needs to be able to accurately predict not only the stabilized hysteresis characteristics but also the initial amount of stress relaxation during the first cycle and the subsequent stress evolution. A significant contribution to the evolution of stress is from the initial cycling. In Figure 51 through Figure 54, the steep reduction in stress range during the initial cycling is due to the large stress relaxation experienced during the first dwell in comparison with the remaining cycles. This large stress relaxation widens the stress range leading to a larger residual stress upon the load reversal.

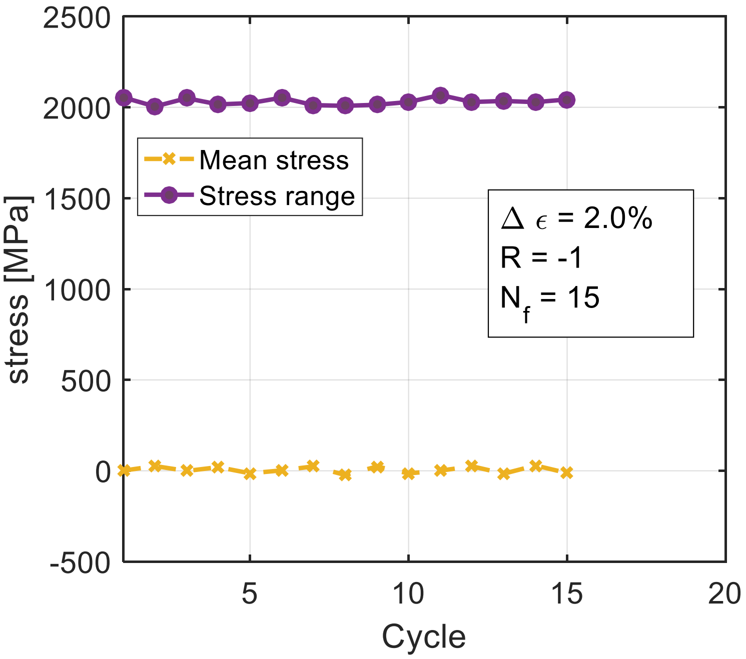

Figure 49: Stress evolution of creep-fatigue experiments at 650°C in the <001> crystallographic orientation: (a) R = -1 and Δε = 2.0 %.

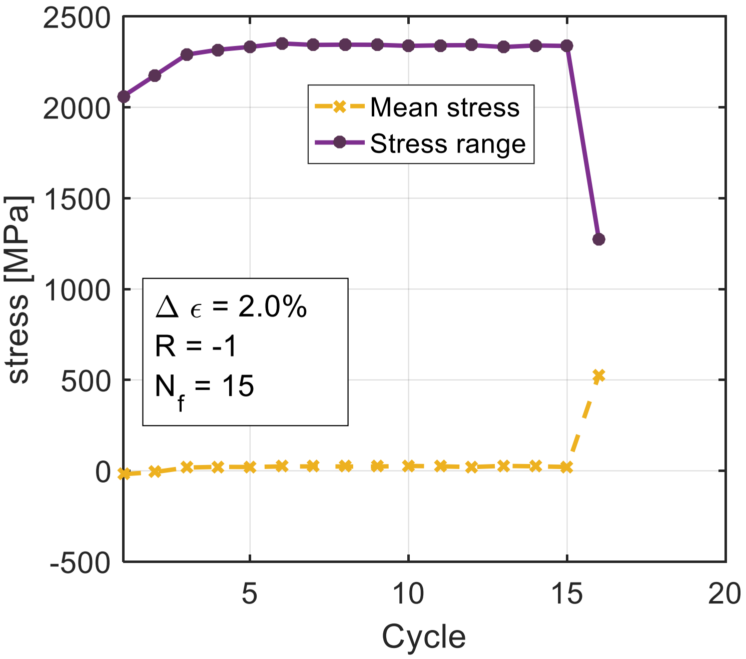

Figure 50: Stress evolution of creep-fatigue experiments at 750°C in the <001> crystallographic orientation: (a) R = -1 and Δε = 2.0 %.

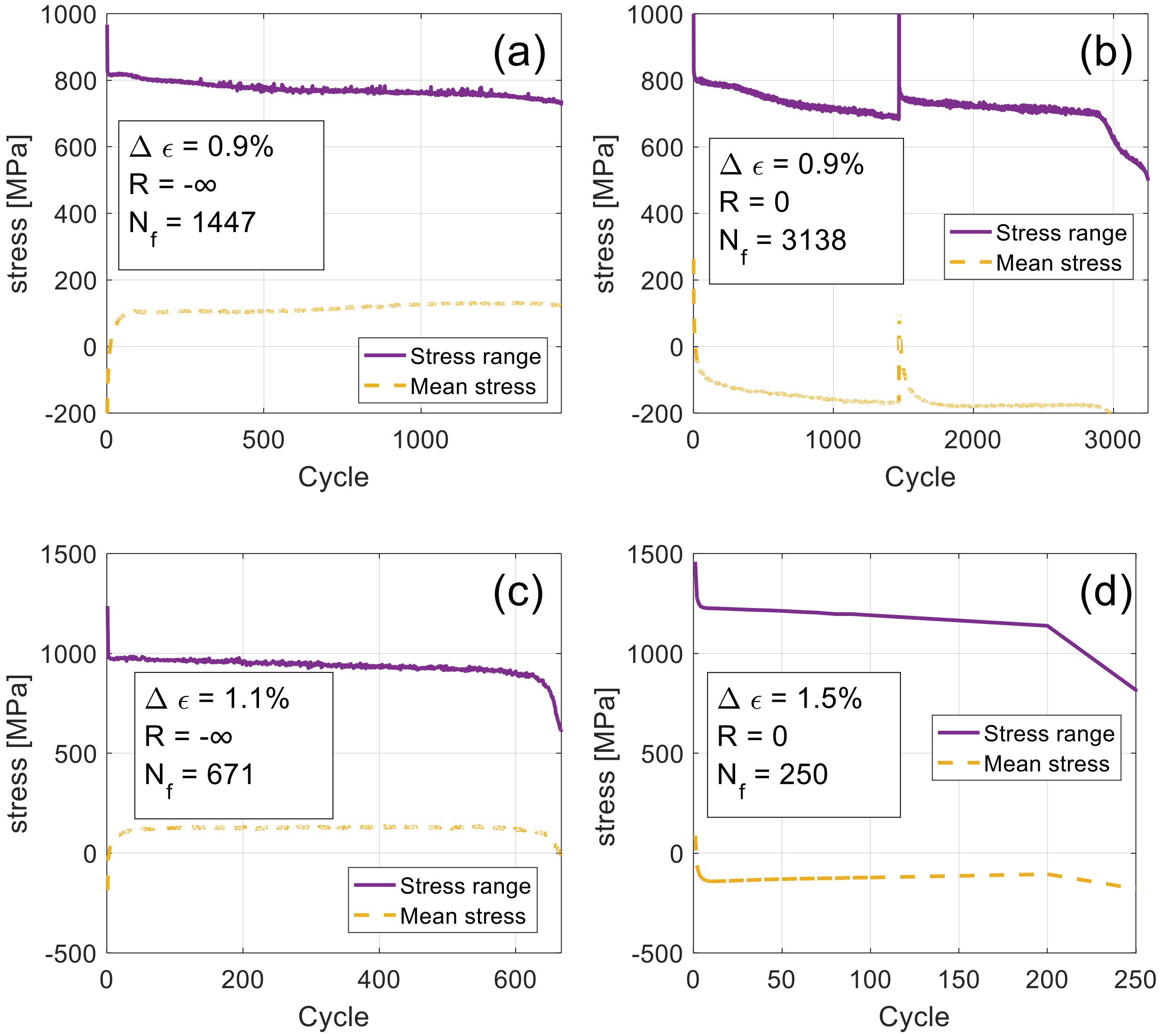

Figure 51: Stress evolution of creep-fatigue experiments at 950°C in the <001> crystallographic orientation: (a) R = -∞ and Δε = 0.9%. (b) R = 0 and Δε = 0.9% (c) R = -∞ and Δε = 1.1% (d) R = 0 and Δε = 1.5%

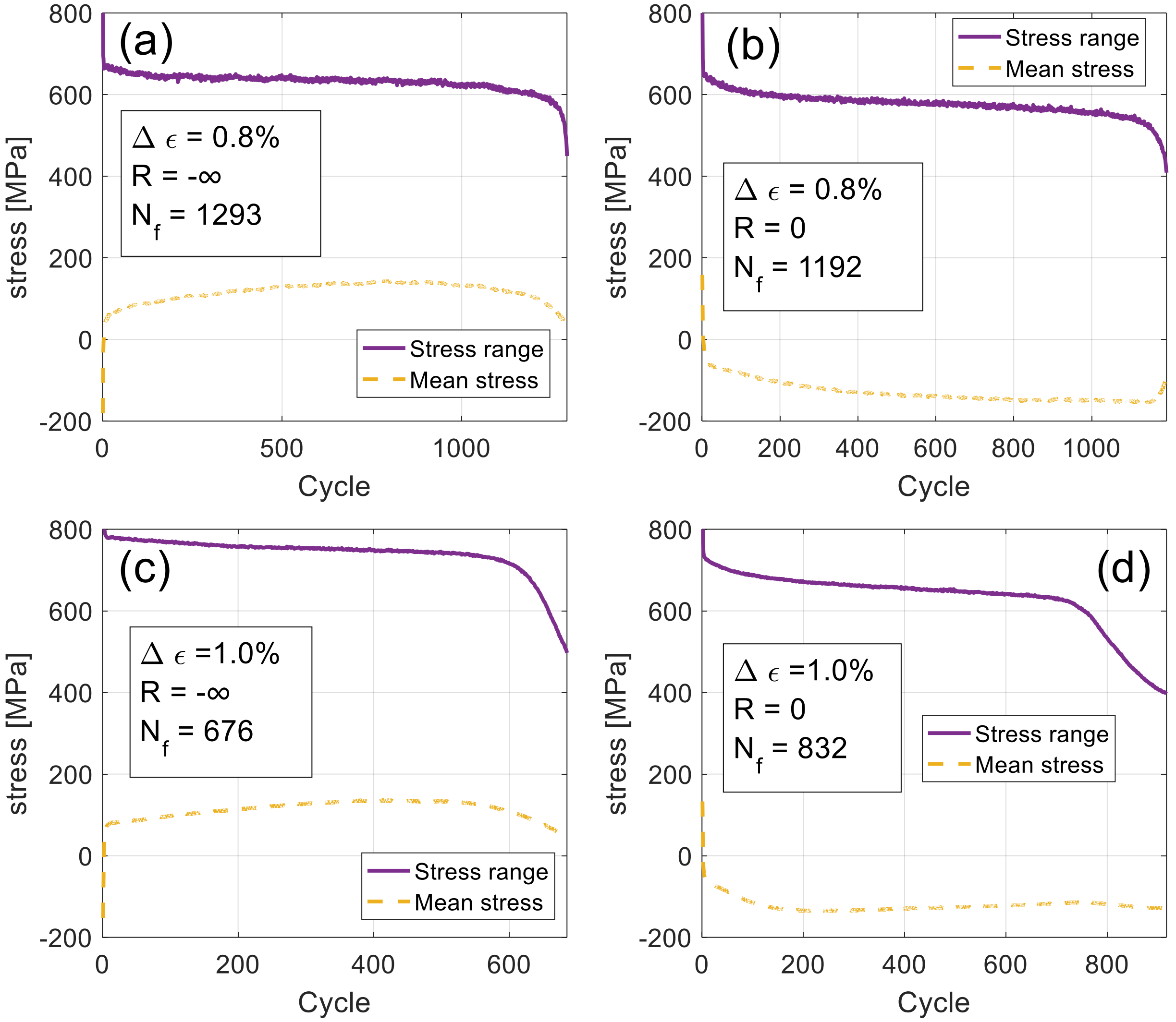

Figure 52: Stress evolution of creep-fatigue experiments at 1025°C in the <001> crystallographic orientation: (a) R = -∞ and Δε = 0.8%. (b) R = 0 and Δε = 0.8% (c) R = -∞ and Δε = 1.0% (d) R = 0 and Δε = 1.0%

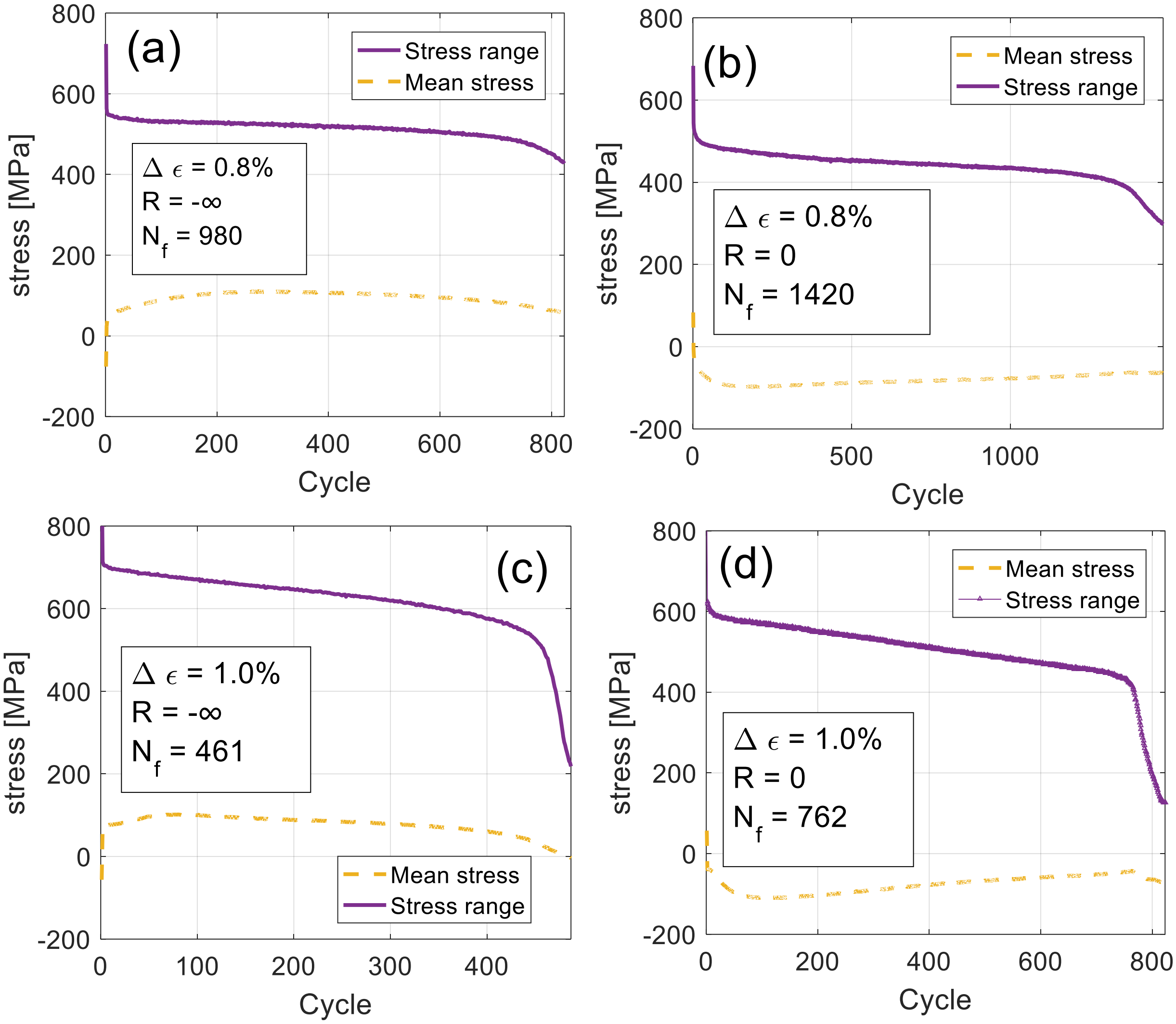

Figure 53: Stress evolution of creep-fatigue experiments at 1100°C in the <001> crystallographic orientation: (a) R = -∞ and Δε = 0.8%. (b) R = 0 and Δε = 0.8% (c) R = -∞ and Δε = 1.0% (d) R = 0 and Δε = 1.0%

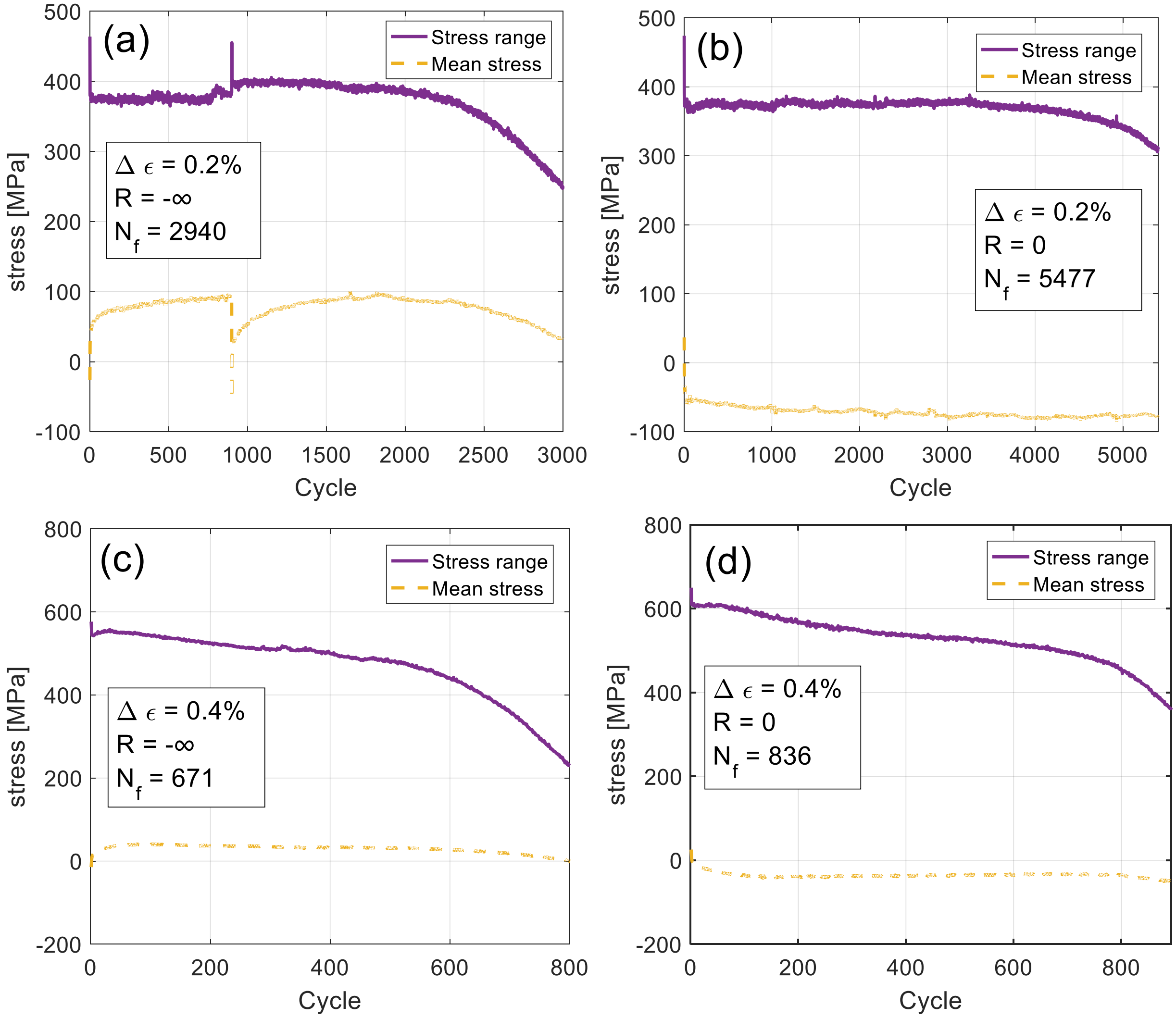

Figure 54: Stress evolution of creep-fatigue experiments at 1100°C in the <001> crystallographic orientation: (a) R = -∞ and Δε = 0.8%. (b) R = 0 and Δε = 0.8% (c) R = -∞ and Δε = 1.0% (d) R = 0 and Δε = 1.0%

3.3.3 Low-cycle isothermal fatigue

The life data from the LCF tests is summarized graphically in Figure 55. As opposed to the CF results of Figure 34 and Figure 35, in LCF *R* of negative infinity tends to result in larger lives, whereas strain ratios of zero lead to shorter specimen lives.

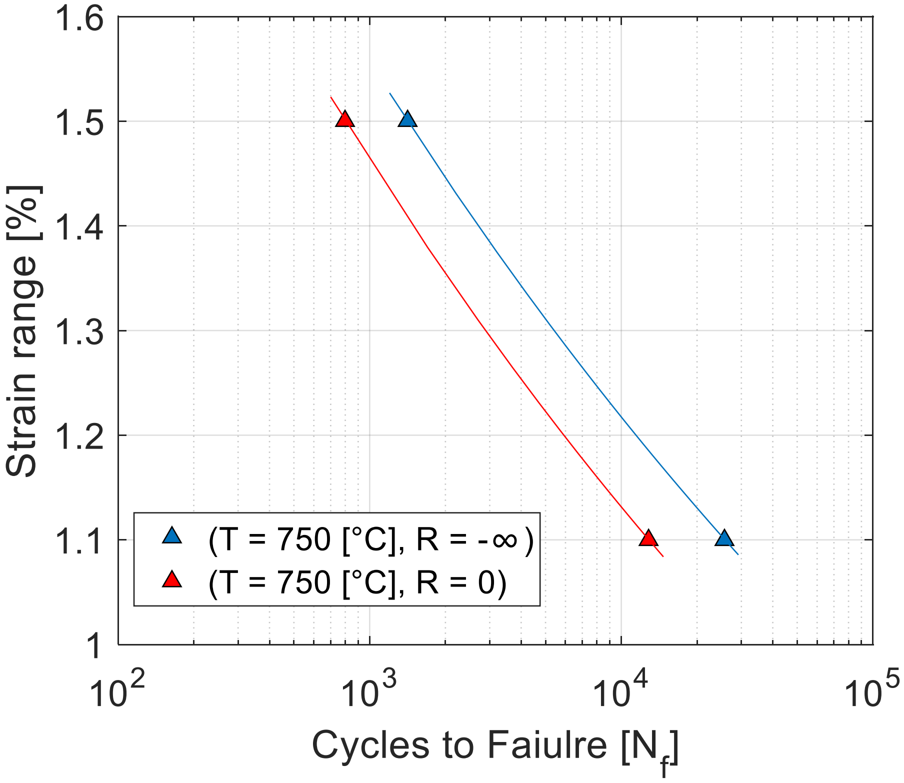

Figure 55: LCF life data using 30% load drop as a life criterion

No additional LCF experiments are available at other temperatures to make any further observations. LCF is the case where only fatigue is present, unlike the CF experiments, the LCF experiments do not contain any strain dwells. Therefore, this set of data can be used as validation that the crystal viscoplasticity model can also predict the deformation of the alloy under pure fatigue. The test conditions used for the LCF experiments are listed in Table 6,

Table 6: Test conditions for strain-controlled low-cycle fatigue experiments in the <001> crystallographic orientation

strain rate $1\text{x}10^{-3}$ [1/s]			
Temperature [°C]	***R***	**$\Delta\varepsilon$ [%]**	**N_f [cycles]**
750	$-\infty$	1.5	1,418
750	$-\infty$	1.1	25,829
750	0	1.5	803
750	0	1.1	12,873

The test temperature was chosen such that the alloy would exhibit its maximum yield strength. The strain ratios (*R*) were selected as $-\infty$ and 0 for the same reasons explained in the CF experiments. Finally, the strain ranges in the LCF are selected such that a larger maximum strain is reached in comparison to the CF calibration experiments. Hence, this data will also be used for validating that the model can predict the plastic response for high levels of plastic strain. The strain ranges in the TMF test are typical of strain ranges commonly used for Ni-base superalloys [46].

Insights into the life results of Figure 55 can be obtained by examining the first ten cycles, shown in Figure 56, for the tested conditions.

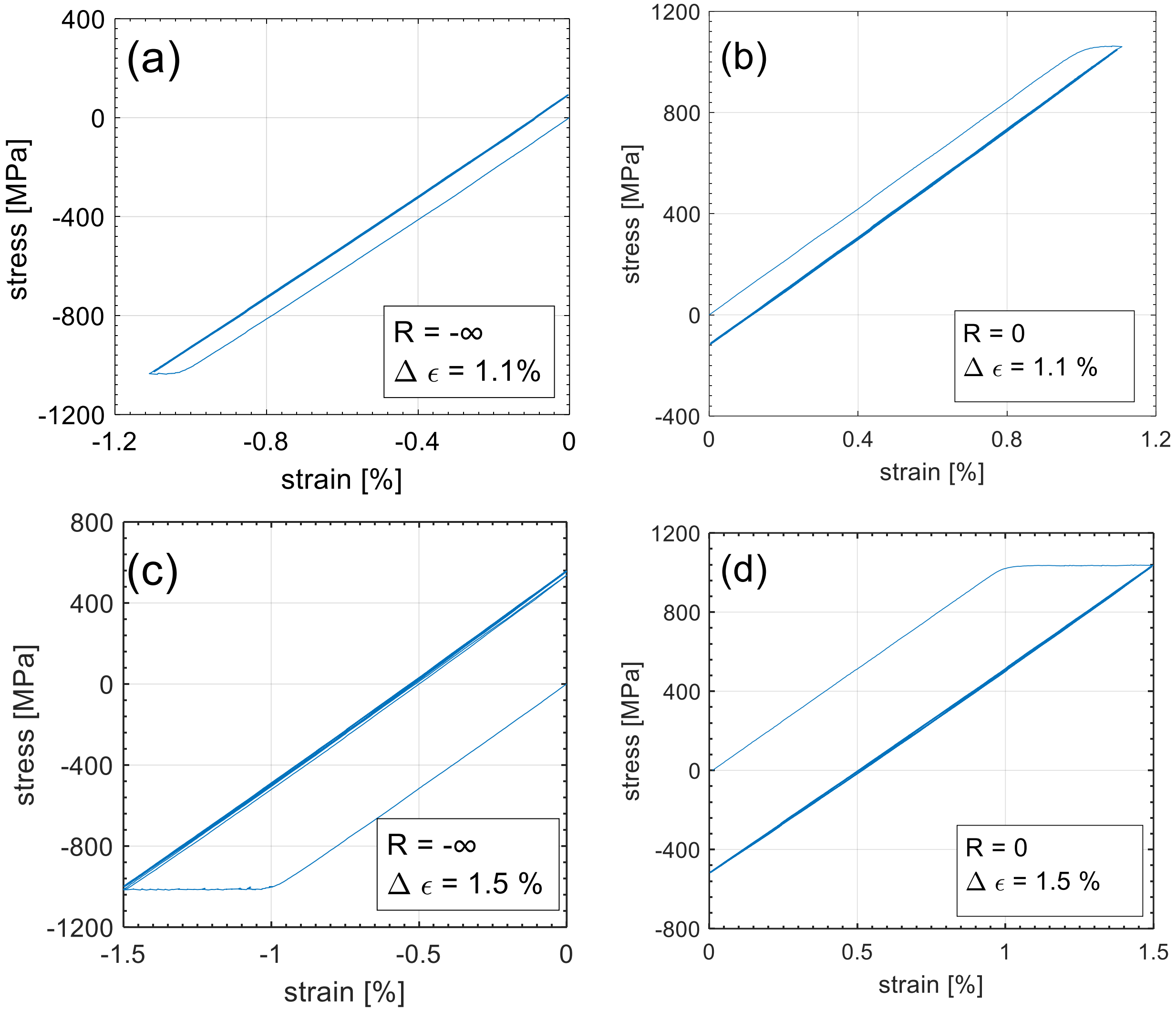

Figure 56: First ten cycles of low-cycle fatigue experiments at 750°C in the <001> crystallographic orientation: (a) R = -∞ and Δε = 1.1%. (b) R = 0 and Δε = 1.1% (c) R = -∞ and Δε = 1.5% (d) R = 0 and Δε = 1.5%

From Figure 56, it can be seen that without the strain dwell the negative strain ratios retain a negative mean stress, while tests at strain ratio of zero they retain a positive mean stress. Moreover, note that the material yields during the first cycle and goes well into the plastic regime. Hence, this is a very interesting case to test and simulate since the CVP model should replicate the plastic flow during the first cycle, as opposed to the hardening seen at 1025 ˚C and at 1100˚C, followed by an almost elastic response during the subsequent loading.

The stabilized hysteresis for each LCF condition are plotted in Figure 57. Note that very little plasticity is seen in the stabilized hysteresis. The lack of plasticity in the hysteresis is characteristic of SX superalloys at this temperature, which typically reach their maximum strength around 750˚C due to the anomalous yield strength behavior.

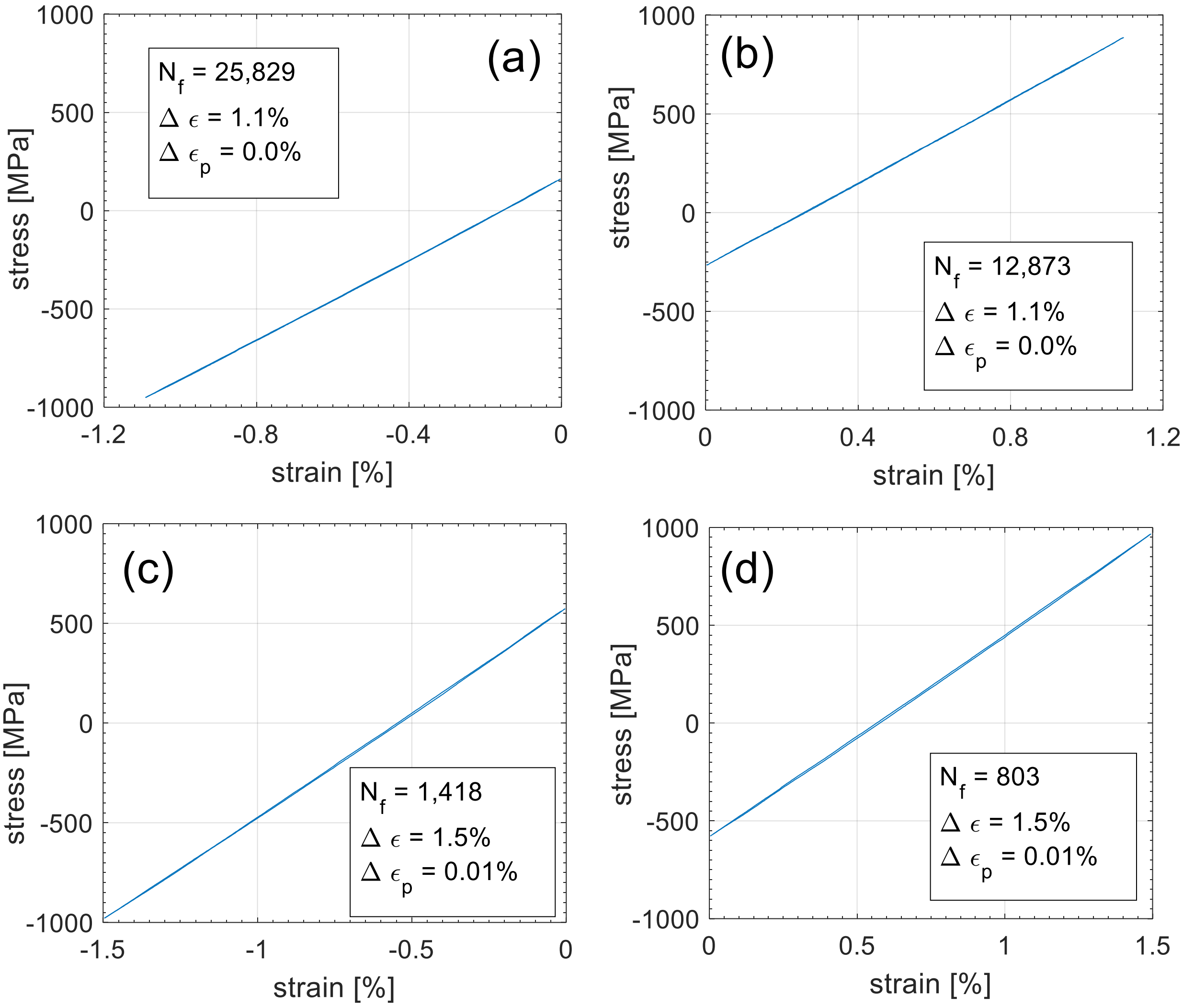

Figure 57: Stabilized hysteresis of low-cycle fatigue experiments at 750°C in the <001> crystallographic orientation: (a) R = -∞ and Δε = 1.1%. (b) R = 0 and Δε = 1.1% (c) R = -∞ and Δε = 1.5% (d) R = 0 and Δε = 1.5%

The stress evolutions are reported in Figure 58. Examination of these data shows that the effect of the *R* ratio on the mean stress evolution appears to have flipped with respect to the CF tests. Without the stress relaxation induced by the strain dwells, the asymmetry of the cycles in the fatigue experiments dominates, and therefore the positive strain loading leads to positive mean stress while the negative strain loading leads to negative mean stress. These findings suggest that the evolution of stress, specifically the sign of the mean stress, is an important variable controlling life for both LCF and CF cycles.

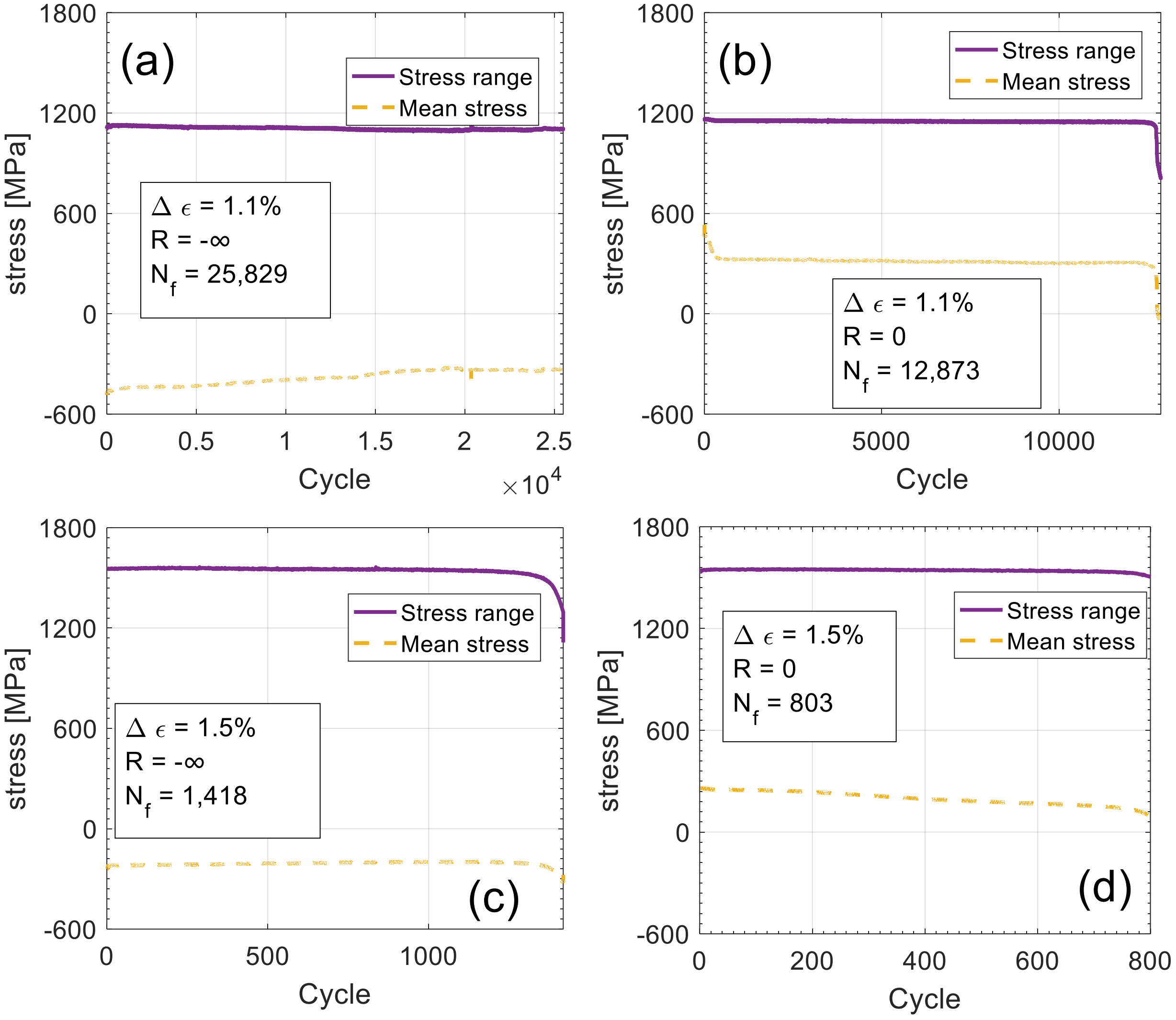

Figure 58: Stress evolution of low-cycle fatigue experiments at 750°C in the <001> crystallographic orientation: (a) $R = -\infty$ and $\Delta\varepsilon = 1.1\%$. (b) $R = 0$ and $\Delta\varepsilon = 1.1\%$ (c) $R = -\infty$ and $\Delta\varepsilon = 1.5\%$ (d) $R = 0$ and $\Delta\varepsilon = 1.5\%$

3.3.4 Thermomechanical fatigue

TMF is the case when both the thermal and the mechanical strain components of the total strain change concurrently. The life of the TMF specimens is reported in Figure 59. The role of strain ratio and phasing on TMF life is not clear from this figure.

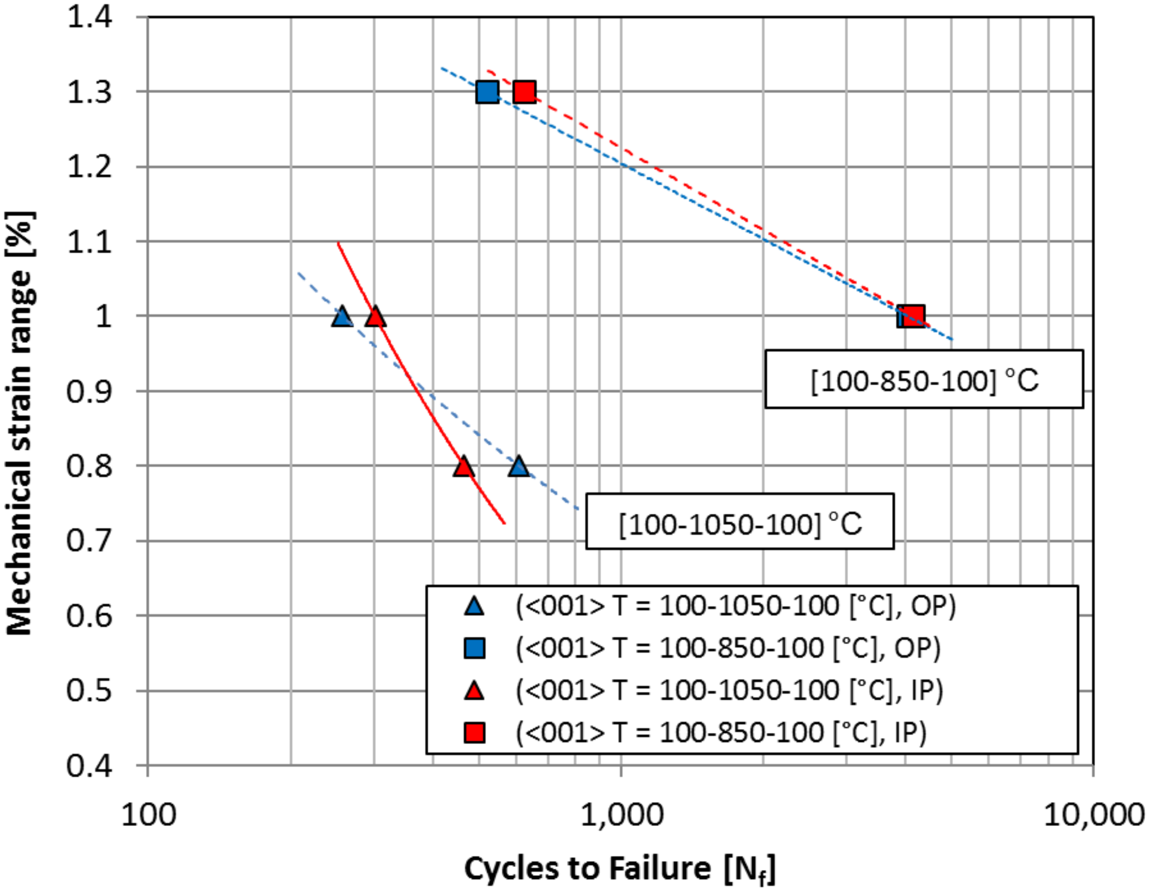

Figure 59: TMF life data using 30% load drop as a life criterion

The experimental conditions selected for these set of experiments are listed in Table 7,

Table 7: Test conditions for strain-controlled thermomechanical fatigue experiments in the <001> crystallographic orientation

Cooling/Heating Rate 2.83 [ºC /s]					
Minimum Temperature [ºC]	**Maximum Temperature [ºC]**	**R**	**Phasing**	**$\Delta\varepsilon_{mechanical}$ [%]**	**N_f [cycles]**
100	850	0	IP	1.0	4,141
100	850	0	IP	1.3	623
100	850	-∞	OP	1.0	4,048
100	850	-∞	OP	1.3	519
100	1050	0	IP	0.8	466
100	1050	0	IP	1.0	302
100	1050	-∞	OP	0.8	609
100	1050	-∞	OP	1.0	258

The strain ranges in the TMF test are typical of strain ranges commonly used for Ni-base superalloys [46]. Also, the very wide temperature range used in the TMF experiments serves to validate the model predictions. For the same reasons as before, the strain ratios (*R*) were selected as –∞ and 0. IP TMF was used for tests with strain ratio of 0, and OP TMF for strain ratios of -∞. This is because these combinations of phase angles and strain ratios are representative of the complete start-up and shut-down cycle experienced by turbine components.

The first ten cycles for these TMF conditions are shown in Figure 60 and Figure 61. It can be seen from these figures that the material reaches its stabilized hysteresis very quickly.

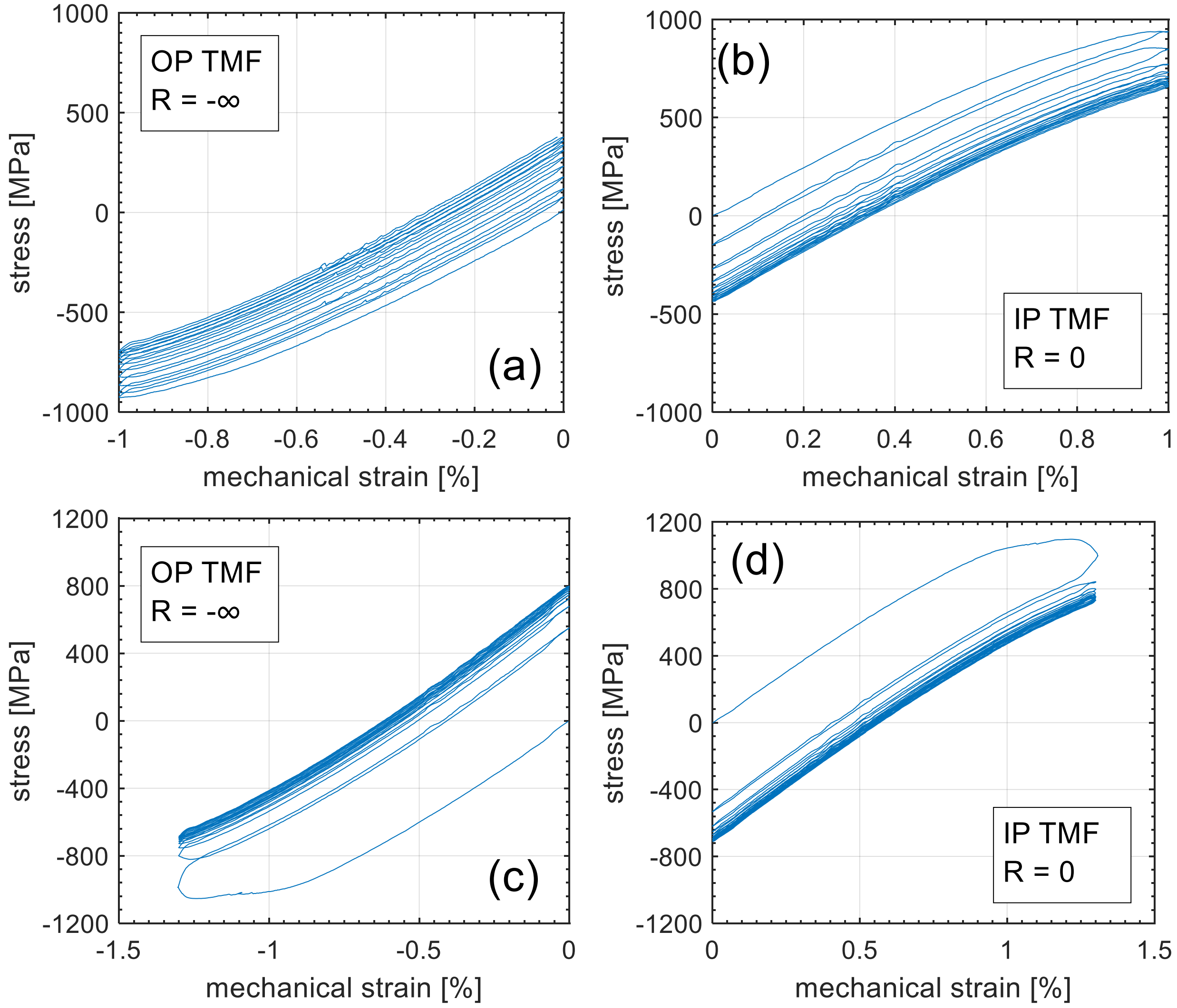

Figure 60: First ten cycles of TMF experiments with temperature path 100-850-100 [°C] in the <001> crystallographic orientation: (a) R = -∞ and Δε = 1.0 %. (b) R = 0 and Δε = 1.0 % (c) R = -∞ and Δε = 1.3% (d) R = 0 and Δε = 1.3%

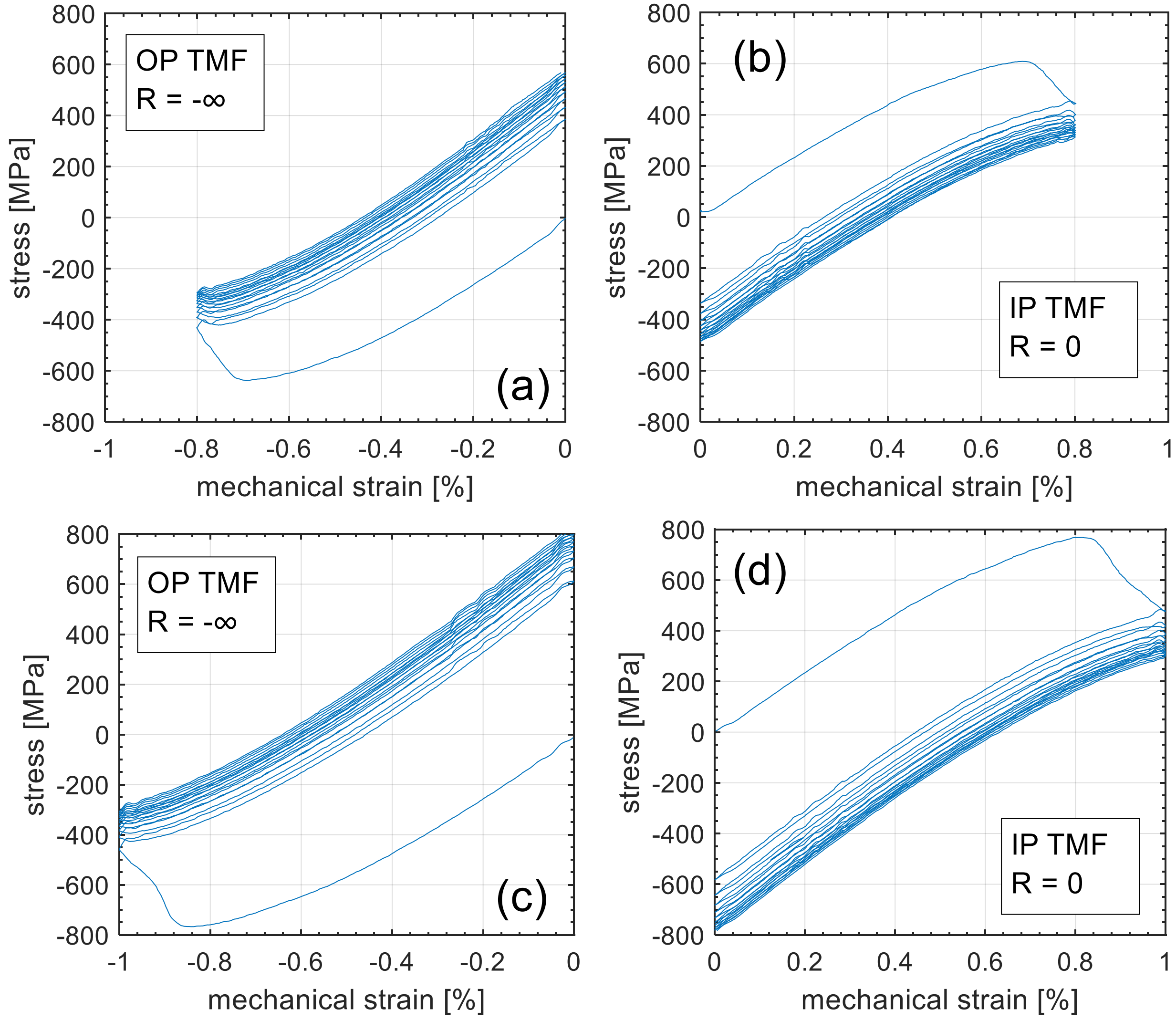

Figure 61: First ten cycles of TMF experiments with temperature path 100-1050-100 [°C] in the <001> crystallographic orientation: (a) R = -∞ and Δε = 0.8 %. (b) R = 0 and Δε = 0.8 % (c) R = -∞ and Δε = 1.0% (d) R = 0 and Δε = 1.0%

The stabilized hysteresis plots for the TMF experiments are shown in Figure 62 and Figure 63. In these results, as it was the case for the CF and LCF tests, the asymmetric strain loading has an effect in determining the sign of the mean stress. A positive mean stress is seen for strain ratios of –∞ and negative mean stress for strain ratios of zero.

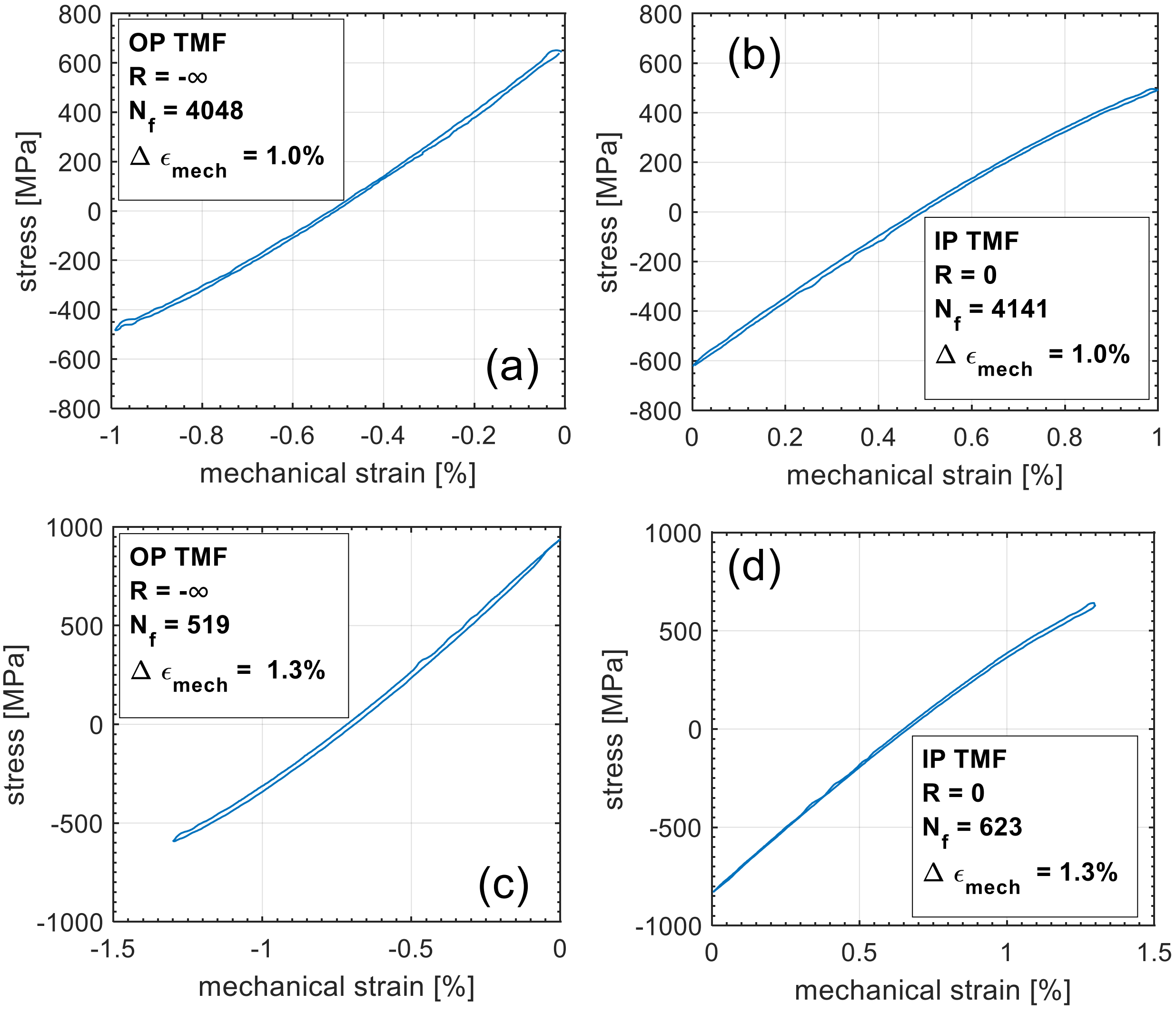

Figure 62: Stabilized hysteresis of TMF experiments with temperature path 100-850-100 [°C] in the <001> crystallographic orientation: (a) R = -∞ and Δε = 1.0 %. (b) R = 0 and Δε = 1.0 % (c) R = -∞ and Δε = 1.3% (d) R = 0 and Δε = 1.3%

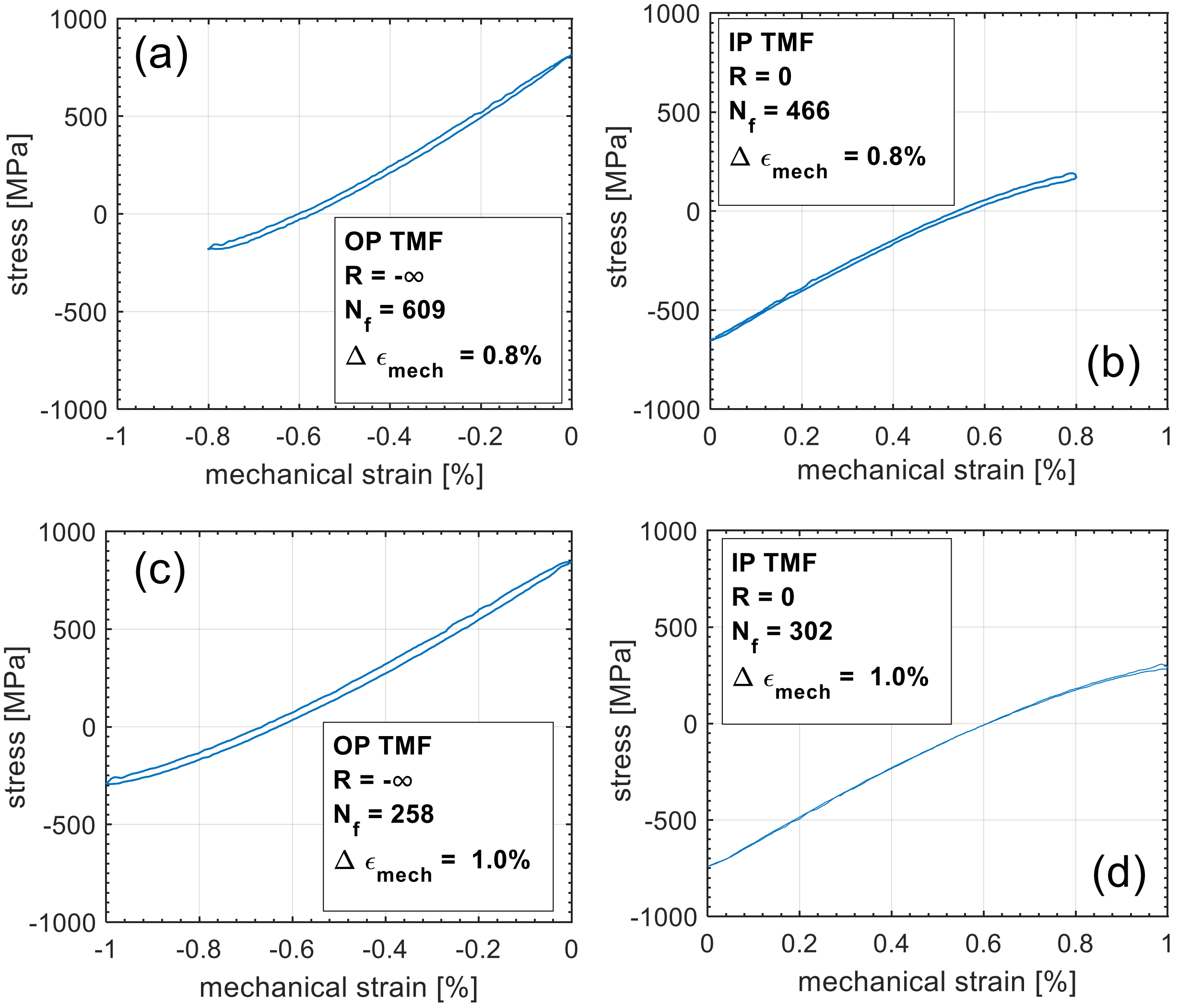

Figure 63: Stabilized hysteresis of TMF experiments with temperature path 100-1050-100 [°C] in the <001> crystallographic orientation: (a) R = -∞ and Δε = 0.8 %. (b) R = 0 and Δε = 0.8 % (c) R = -∞ and Δε = 1.0% (d) R = 0 and Δε = 1.0%

The mean stress evolutions are presented in Figure 64 and Figure 65. The OP tests all had a strain ratio of –∞. Hence, the maximum compressive strain was reached when the temperature was the highest, subsequently while on compression, creep effects act to relax the mean stress in the positive direction. The opposite situation takes place for the IP test, with a strain ratio of 0, the maximum temperature and the maximum tensile strain happen concurrently, therefore the stress relaxes toward the negative direction.

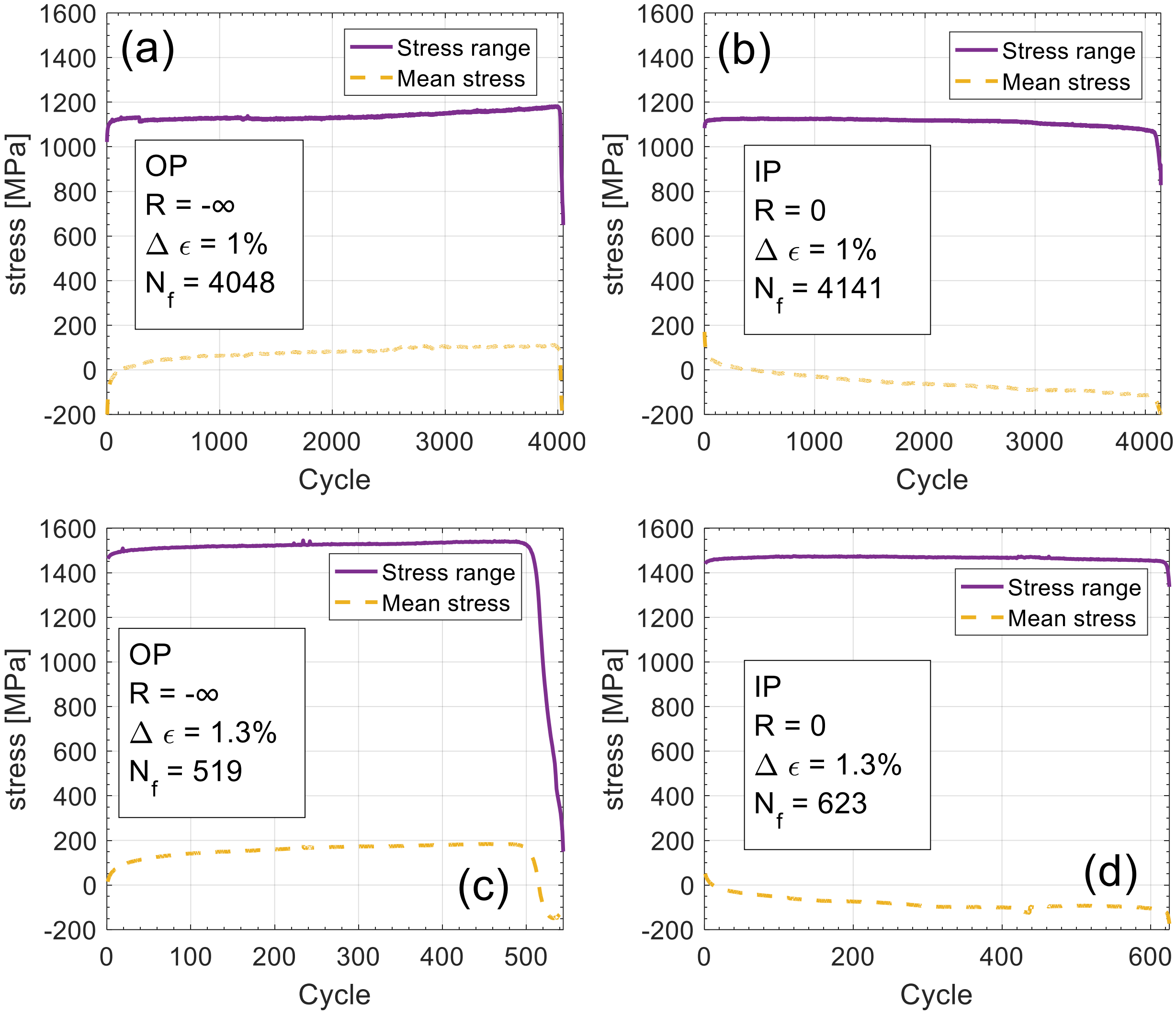

Figure 64: Stress evolution of TMF experiments with temperature path 100-850-100 [°C] in the <001> crystallographic orientation: (a) R = -∞ and Δε = 1.0 %. (b) R = 0 and Δε = 1.0 % (c) R = -∞ and Δε = 1.3% (d) R = 0 and Δε = 1.3%

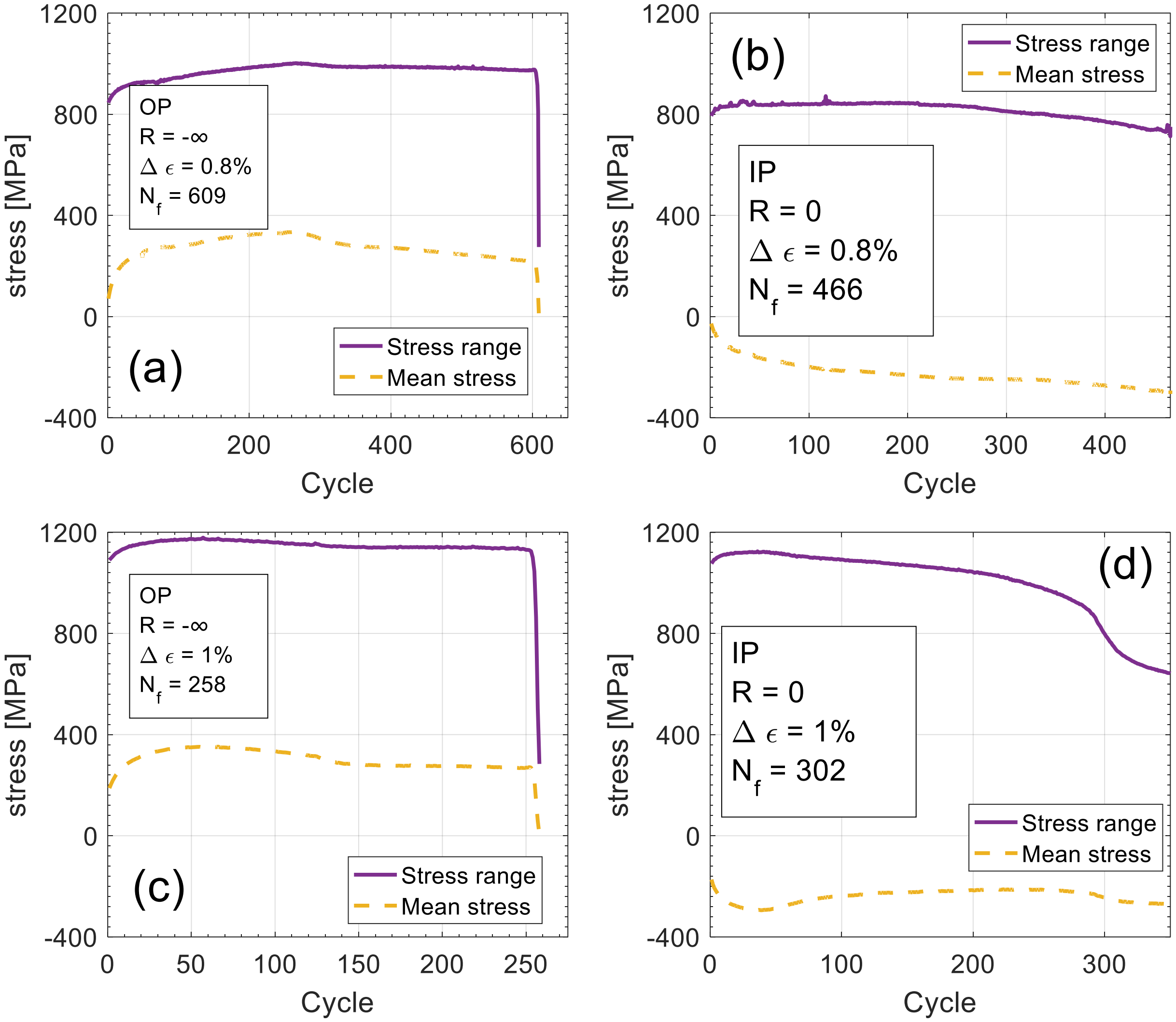

Figure 65: Stress evolution of TMF experiments with temperature path 100-1050-100 [°C] in the <001> crystallographic orientation: (a) R = -∞ and Δε = 0.8 %. (b) R = 0 and Δε = 0.8 % (c) R = -∞ and Δε = 1.0% (d) R = 0 and Δε = 1.0%

For the TMF experiments, the role of the mean stress in the life of the specimens is not clear, with positive mean stresses sometimes leading to less life and with negative mean stress sometimes prolonging life. This suggests that additional variables beyond the mean stress are responsible for life during TMF. Due to the very limited number specimens available for TMF tests in this work, no further observations could be made.

3.3.5 Creep

A Larson-Miller parameter plot of CMSX-8, CMSX-8[B/C], and CMSX-4 is shown in Figure 66.

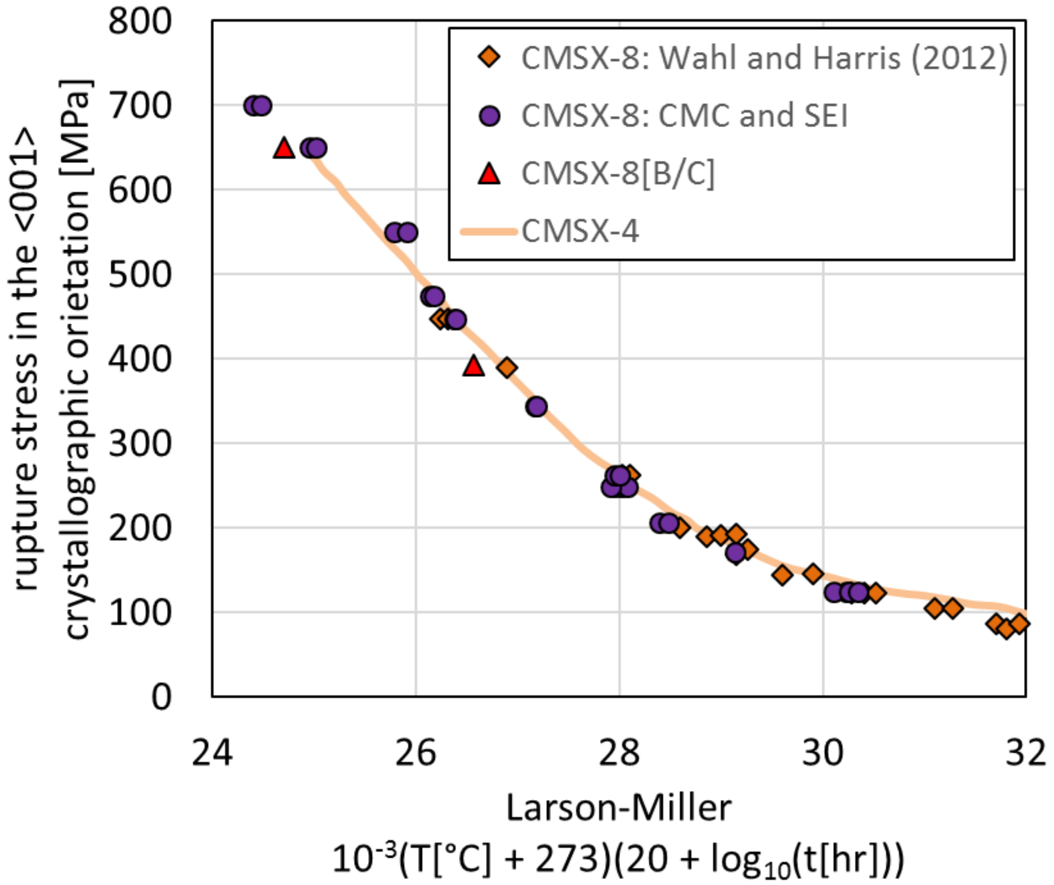

Figure 66: Larson-Miller of rupture life of CMSX-8[B/C], CMSX-8, and CMSX-4 in the <001> crystallographic orientation. CMSX-8, and CMSX-4 data taken from Wahl and Harris [6]

CMSX-8's performance, in comparison to CMSX-4's, is lower at higher values of Larson-Miller parameter. This corresponds to situations where the temperature is high. This is consistent with the reduced amount of Re in this alloy. Also, note from the plot that the two CMSX-8[B/C] specimens closely follow the Larson-Miller curve of nominal CMSX-8 published by Wahl and Harris [6].

These test conditions tested to generate the Larson-Miller plots are listed in Table 8 and in Table 9.

Table 8: Constant creep experimental conditions on CMSX-8 data provided by Cannon Muskegon Corporation, Muskegon, MI, and Siemens Energy Inc., Orlando FL

Applied temperature [°C]	Applied creep stress [MPa]	Time to rupture [hours]
750	700	7075
850	475	1899
850	651	167
871	448	1128
927	345	451
950	250	748
982	207	421
982	248	210
1010	262	61
1038	172	171

Table 9: Tested constant stress creep conditions tested on CMSX-8[B/C]

Applied temperature [°C]	Applied creep stress [MPa]	Time to rupture [hours]
850	650	99
900	390	440

The test conditions at 1038˚C and 750˚C will be used to calibrate the material parameters for pure creep, while the remaining conditions will be used to verify that the calibrated model can perform well at intermediate temperatures. At temperatures of 1038˚C and 750˚C either the γ phase or the γ' phase deformation mechanisms are dominant which permits calibrating the material parameters associated to each phase from these experimental conditions.

Shown in Figure 67, are the experimental results of the test condition in Table 9 at 850°C and 650MPa. It can be seen that the experimental results obtained using CMSX-8[B/C] compared well to data on CMSX-8,

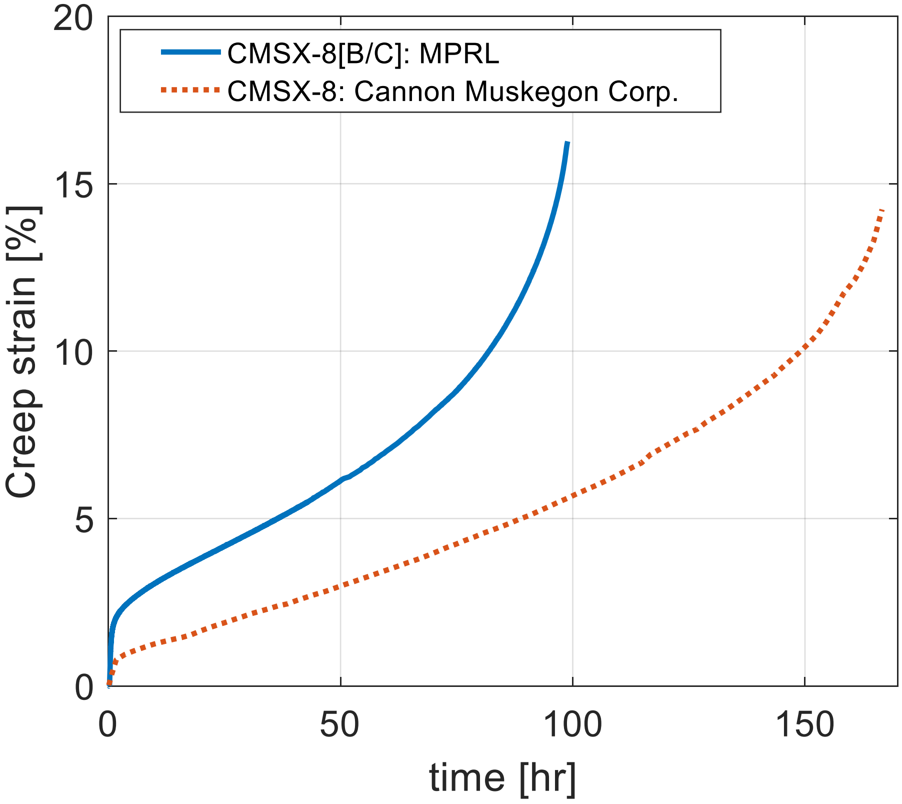

Figure 67: Creep response of CMSX-8[B/C] at stress of 650 MPa and temperature of 850°C

The differences between the curves are within the expected variability for creep curves tested for identical conditions. Creep is very sensitive to material small variations in crystallographic orientation, even small misalignments can cause visible variability for same experimental conditions. Also note that for this applied stress and temperature, primary creep is very noticeable, and can be responsible for up to 25% of the total creep deformation.

The experimental results for test condition in Table 9 at 900°C and 390MPa are shown in Figure 68. This test condition was also tested on CMSX-4 by Tsuno et al. [61]. The results show that CMSX-8[B/C] follows the reported creep response on CMSX-4 closely,

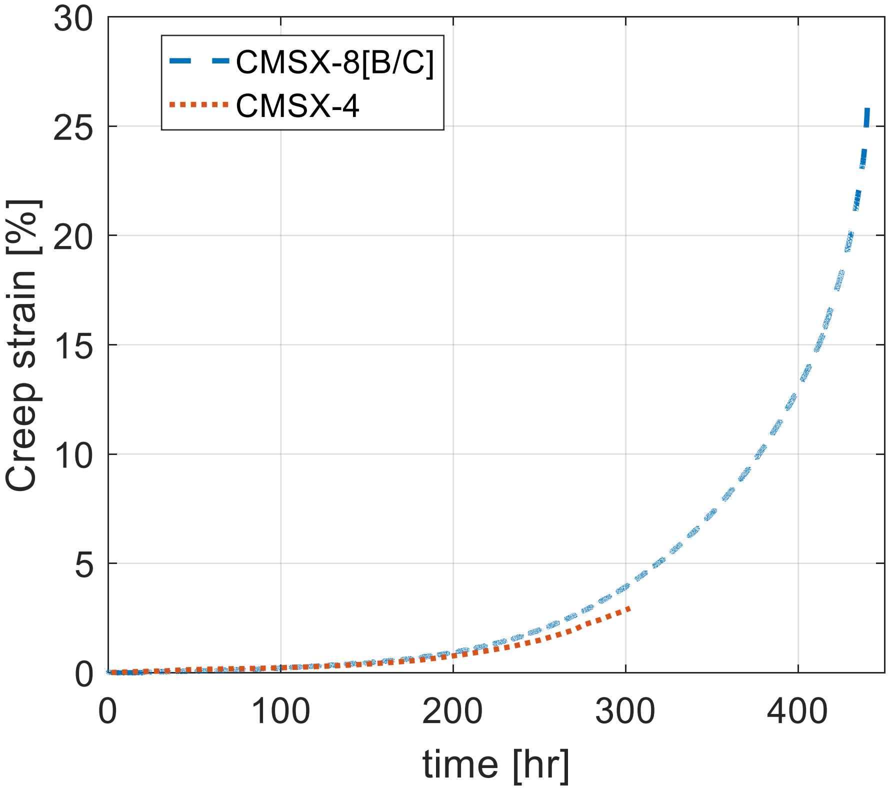

Figure 68: Creep response of CMSX-8[B/C] compared to CMSX-4 at stress of 390 MPa and temperature of 900°C. CMSX-4 data taken from Tsuno et al. [61]

For this test condition, most of the creep strain is due to tertiary creep and no primary creep is visible for both CMSX-4 and CMSX-8[B/C]. These creep responses and the Larson-Miller plot indicate that CMSX-8[B/C] follows the behavior of nominal CMSX-8 very closely, therefore it is possible to use nominal CMSX-8 creep curves to calibrate the crystal viscoplasticity model to CMSX-8[B/C]. From this point on, no distinction will be made between CMSX-8 and CMSX-8[B/C].

As it was done for Figure 67 and Figure 68, all of the available data on CMSX-8 was plotted and inspected to assess whether primary or tertiary creep was present. In Figure 69, the results of the previous analysis were used to extend the findings presented in Figure 12 to include CMSX-8,

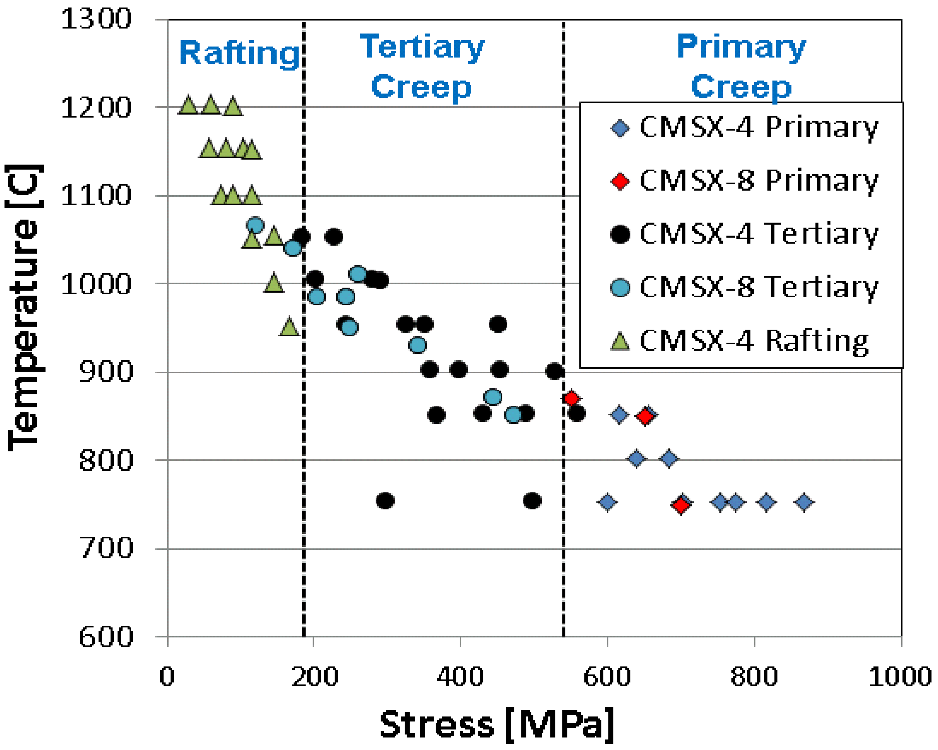

Figure 69: Temperature and stress regimes under which primary, tertiary creep or rafting are the dominant deformation mechanisms. CMSX-4 data taken form Reed [7]

CMSX-8 follows the behavior of CMSX-4 and it would be expected that other single-crystal superalloys would exhibit similar thresholds. The experimental results in Figure 69 are consistent with the superalloys having different active deformation mechanisms which depend on temperature and applied loading. An applied stress in the order of 550 MPa is necessary for primary creep to be present, hence for the precipitates to be shear by dislocation ribbons in the $a/2\,\langle 112\rangle\{111\}$ slip system. These data further demonstrate that for the model to be accurate over a wide range of loading conditions, it needs to be sensitive to the stresses and temperature level regimes which are driven by the different deformation mechanism at the microstructure level.

3.4 Summary of key experimental observations

A summary of important experimental observations includes:

1. The elastic properties of CMSX-8 are a function of temperature, and the yield strength of this alloy exhibits the anomalous behavior.
2. The yield strength of CMSX-8 does not exhibit tension/compression yield asymmetry.
3. The 0.2% yield strength of CMSX-8[B/C] at room temperature is 15% higher than nominal CMSX-8, while yield strengths at higher temperatures are comparable.
4. In the <001> orientation, hardening and cyclic creep are a function of temperature, with higher temperatures leading to more hardening and less cyclic creep and with lower temperatures resulting in less hardening and more cyclic creep. In the <111> orientation neither cyclic creep or hardening was observed at the highest temperature tested.
5. For CF tests with three-minute strain dwells and R of negative infinity, a positive mean stress is evolved over cycling, while for R of zero, a negative mean stress is obtained.

6. Asymmetric loading conditions without strain dwells of *R* negative infinity retain negative mean stress, while those of *R* equal to zero result in positive mean stress.
7. CF and LCF life -conducted in laboratory air- is a function of strain range, maximum stress range or mean stress, and of crystallographic orientation.
8. The creep response and the creep rupture behavior of CMSX-8 and CMSX-8[B/C] are similar to each other.
9. The primary creep and tertiary creep behavior of CMSX-8 is stress and temperature dependent. An applied stress in the order of 550 MPa is necessary for primary creep to be present, hence for the precipitates to be shear by dislocation ribbons.

Given these experimental observations, constitutive modeling using the framework of crystal plasticity is a reasonable approach for this type of material since this method permits capturing the highly anisotropic inelastic behavior of single-crystal alloys.

CHAPTER 4

MICROSTUCTURE-SENSITIVE CRYSTAL-VISCOPLASTICITY MODEL

In this chapter, a crystal-viscoplasticity model is proposed for the creep and fatigue deformation of Ni-base superalloys single-crystals. The model will follow the traditional framework of crystal plasticity. However, significant enhancements are developed that improve the constitutive modeling by taking a physically-based approach which will closely model the alloy’s microstructure and the distinctly different deformation mechanisms of the γ and γ' phase. In the model, dislocation densities in the γ and γ' phases are used as the internal state variables (ISVs) which more adequately capture the heterogeneous deformation of both phases over a wide range of temperatures and stresses. The fundamentals of crystal plasticity will be presented in the next section. After the fundamentals are discussed, the basic crystal plasticity framework will be modified to develop the microstructure-sensitive CVP model for Ni-base superalloys.

4.1 Fundamentals of single-crystal deformation

Crystal plasticity was first established in the early part of last century by the distinguish contributions of authors such as Erwin and Rosenhain, Bragg, Taylor and Schmid among others authors of that time [65-70]. During the earlier days of this discipline it was observed that the major source of plastic deformation was the movement of dislocations through the crystalline lattice structure which occurred on specific directions and planes. From the first experimental observations at room temperature, several mathematical representations of these movement of dislocations have advanced from the early work of Taylor to modern formulations presented by

Asaro, Rice and Hill [71-74]. In this section, some of the basic premises of crystal plasticity as they are pertinent in the context of the enhanced crystal plasticity framework proposed in this thesis will be presented.

4.1.1 Schmid's Law

During early studies on single-crystals, it was observed that the yield strength varied from one experiment to the next. This variation was attributed to the relative orientation of the crystal lattice with respect to the loading direction. After testing aluminum and zinc single-crystals, it was postulated by Schmid in 1924 and by Taylor and Elam in 1925 that the shear component resolving on a slip direction and on a slip plane was responsible for initiating plastic deformation on a single crystal [70, 75]. This result is now known as Schmid's law and mathematically is expressed as,

$$\tau^{(\alpha)} = \sigma_{ij} : \left(s_i^{(\alpha)} \otimes m_i^{(\alpha)} \right) \tag{11}$$

were $\boldsymbol{s}^{(\alpha)}$ and $\boldsymbol{m}^{(\alpha)}$ are the slip direction and slip plane normal in the α^{th} slip system, respectively, and σ_{ij} is the applied stress. This law has been shown to adequately explain the variations of critically resolved shear stress with respect to changes in orientation, however there exist non-Schmid effects, such as cross-slip of screw dislocations, that could result in deviations from Schmid's law [71].

4.1.2 Lattice rotation

The lattice of the a single-crystal rotates during large plastic deformation, the loading axis rotates as shown in Figure 70,

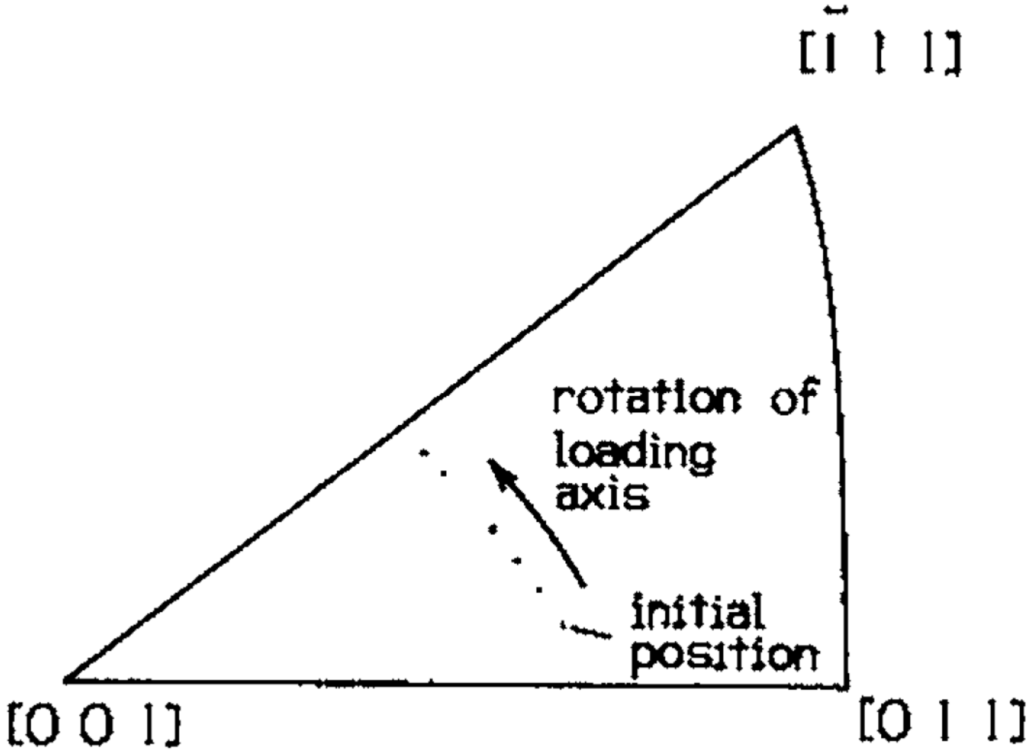

Figure 70: Rotation of the loading axis on a standard stereographic triangle [76]

As schematically illustrated in Figure 71, in reality since the testing frame is rigid, it is the specimen that experiences a rotation of its crystalline lattice. During uniaxial testing, the shoulders of the specimen are held in place by the test frame's gripping system. During plastic deformation, as parts of the single-crystal start to slip, the crystal lattice rotates with respect to the fixed loading direction. As portrayed in Figure 72, if the specimen were free at the shoulders, then the line of action of the force would translate and dislocations would exit the single-crystal at its sides. The rotation of the lattice can happen under tension or under compression with the response in compression in general being reversed to the one in tension [77]. This is because under tension it is the slip direction that rotates toward the loading axis while in compression it is the normal to the slip plane that will rotate.

Figure 71: Lattice rotation due to fixed constraint at the specimen's shoulders [78]

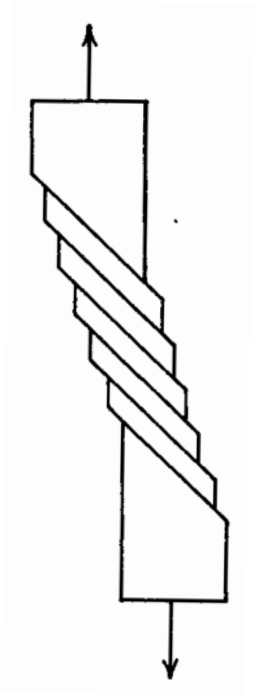

Figure 72: Deformation of single-crystal without constraints at the shoulders [78]

4.1.3 Latent and Self Hardening

It has been observed in several studies that single-crystals exhibit self-hardening and latent hardening [68, 69, 79-81]. During self-hardening an active slip system hardens by slip on itself. This is the simplest form of hardening and is often termed after Taylor who first reported it in 1934 [68]. For most applications, except when severe levels of plasticity are expected such as in rolling operations, Taylor hardening is sufficient to model the hardening behavior of single crystals. During latent-hardening, a slip system hardens by slip on other systems, even if the slip system is inactive. Including latent-hardening in the modeling adds a significant level of complication. Consider for example a simple hardening rule for the critically resolved shear stress on the α^{th} slip system,

$$\dot{\tau}_{cr}^{(\alpha)} = \sum_{\beta=1}^{Nslip} h^{(\alpha)(\beta)} \left| \dot{\gamma}_{in}^{(\alpha)} \right| \tag{12}$$

The components of $h^{(\alpha)(\beta)}$ represent the hardening moduli on slip system α due to slipping on slip system β. When only self-hardening is considered, the off-axis elements of $h^{(\alpha)(\beta)}$ are zero, which greatly simplifies the computations. For instance, the number of components in the hardening modulus of a face-centered cubic (FCC) material with 12 slip systems would be reduced from 144 to 12. In this work Taylor hardening will be used since in-service nickel-base superalloys do not experience extreme levels of inelastic deformation. Moreover, this simpler hardening theory is favored because there is no consensus on how to model and characterize hardening behavior of single-crystals [34].

4.2 Kinematics of plastic deformation in single-crystals

Crystal plasticity relates the macroscopic behavior of metals to the fundamental mechanisms of deformation at the grain level. This multiscale theory acknowledges dislocation motion through the crystal lattice as the main source of plastic deformation in metals. During plastic deformation, it is assumed that the lattice retains its shape while during elastic deformation the lattice is distorted elastically [72, 76, 82-85]. The total deformation is assumed to occur in two independent steps, one for the reversible elastic distortion of the lattice and another one for the irreversible plastic deformation due to the dislocation motion. Mathematically this is represented by a multiplicative decomposition of the total deformation gradient,

$$\mathbf{F} = \mathbf{F^e} \bullet \mathbf{F^{in}} \tag{13}$$

where $\mathbf{F^e}$ represents the rigid body rotation and elastic deformation of the lattice and $\mathbf{F^{in}}$ is the plastic deformation of the crystal or the crystal’s inelastic deformation in the most general case.

Since during inelastic deformation the lattice retains its shape, then the slip direction and slip normal vectors associated to the lattice in the initial configuration, $\mathbf{s_0}$ and $\mathbf{m_0}$ respectively, are not altered by the movement of dislocations, and therefore after applying the transformation $\mathbf{F^{in}}$ they remain the same. The lattice vectors only rotate and stretch or compress after applying the elastic deformation gradient $\mathbf{F^e}$.

The slip direction at the current state in the α^{th} slip system is given by the following transformation rule,

$$\mathbf{s}^{(\boldsymbol{\alpha})} = \mathbf{F^e} \bullet \mathbf{s}_{\mathbf{0}}^{(\boldsymbol{\alpha})} \tag{14}$$

Moreover, it can be shown that in order to ensure that the slip plane normal is always orthogonal to the slip plane the following relation has been introduced,

$$\mathbf{n}^{(\boldsymbol{\alpha})} = \mathbf{n}_{\mathbf{0}}^{(\boldsymbol{\alpha})} \bullet \left(\mathbf{F^e}\right)^{\mathbf{-1}} \tag{15}$$

These equations describing deformation of the lattice within a single-crystal are portrayed graphically in Figure 73, similar illustrations can be found in the literature [82, 83, 86, 87],

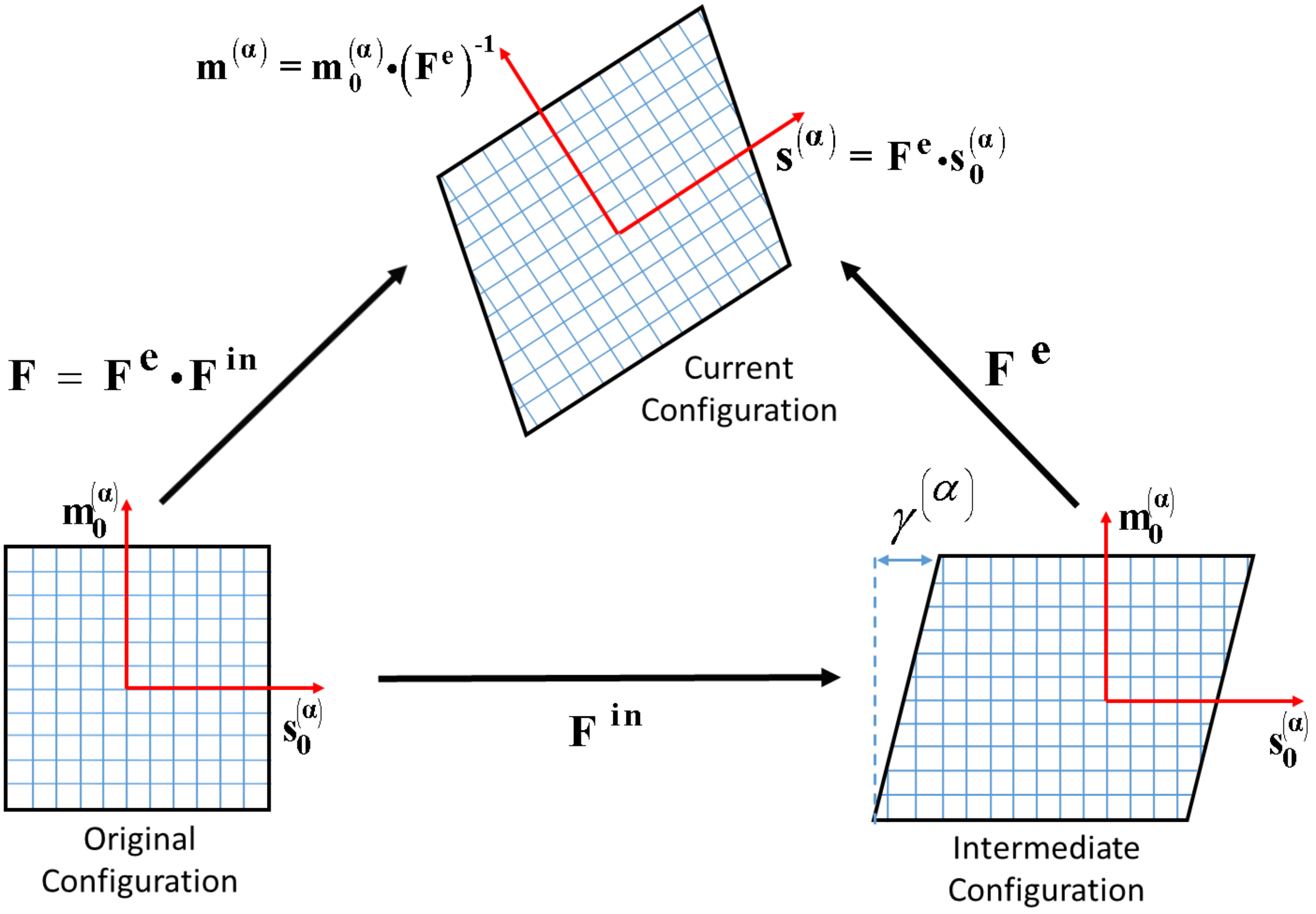

Figure 73: Graphical representation of the elastic-plastic decomposition in crystal plasticity

The kinematics of deformation in crystal plasticity have been extended for the case when the thermal deformation of the lattice cannot be neglected, such as in TMF. In this case, an additional step is added to the deformation gradient which is related to the reversible thermal expansion or contraction of the lattice and assumes that the lattice will only stretch or contract the bonds between the atoms in the original configuration [88, 89],

$$\mathbf{F} = \mathbf{F^e} \bullet \mathbf{F^{in}} \bullet \mathbf{F^{\theta}} \tag{16}$$

The total deformation gradient, **F**, is in general an asymmetric tensor and is a very important input in displacement-based finite element analysis codes. The deformation gradient is used to bridge the macroscopic component deformation to the crystal lattice deformation.

The thermal deformation gradient is obtained by integrating the following expression,

$$\dot{\mathbf{F}}^{\boldsymbol{\theta}} = \mathbf{L}_{\mathbf{0}}^{\boldsymbol{\theta}} \bullet \mathbf{F}^{\boldsymbol{\theta}} \tag{17}$$

where $\boldsymbol{L_0^{\theta}}$ assumes isotropic expansion and is a function of the coefficient of thermal expansion — itself a function of temperature — and of temperature rate.

$$\mathbf{L}_{\mathbf{0}}^{\boldsymbol{\theta}} = (\alpha \dot{T})\mathbf{I} \tag{18}$$

Likewise, the inelastic component of the deformation gradient is obtained by integrating,

$$\dot{\mathbf{F}}^{\mathbf{in}} = \mathbf{L}_{\mathbf{0}}^{\mathbf{in}} \bullet \mathbf{F}^{\mathbf{in}} \tag{19}$$

where $\boldsymbol{L_0^{in}}$ is the inelastic velocity gradient which accounts for the effect of the flow of dislocations on all slip systems in the reference configuration. This tensor has been shown to be related to the shearing rates on all slip system by [71],

$$\mathbf{L}_{\mathbf{0}}^{\mathbf{in}} = \sum_{\alpha=1}^{N_{slip}} \dot{\gamma}^{(\alpha)} \mathbf{s}_{\mathbf{0}}^{(\boldsymbol{\alpha})} \mathbf{n}_{\mathbf{0}}^{(\boldsymbol{\alpha})} \tag{20}$$

where $\dot{\gamma}^{(\alpha)}$ is the shearing rate on the α^{th} slip system which is commonly referred to as the flow rule. Flow rules follow modifications of the Orowan equation [90],

$$\dot{\gamma}^{(\alpha)} = \rho_m b v^{(\alpha)} \tag{21}$$

where different types of expressions are often assumed by various authors for mobile dislocation density (ρ_m), burgers vector (b), and for average velocity of dislocations through a field of obstacles ($v^{(\alpha)}$). Finally, the elastic deformation is obtained by iteratively solving equation (16) using Newton-Raphson numerical integration schemes [87].

4.3 Limitations of Crystal Plasticity

Crystal plasticity is more physically representative of the deformation of metals in comparison with other classical plasticity approaches because it acknowledges the motion of dislocations as the main driver for inelastic deformation of the crystallographic lattice. Its continuum mechanics based formulation allows for relatively easy implementation in commercially available Finite Element packages and for accounting the anisotropy of the material. Moreover, numerous authors have extended its application to cases with high homologous temperatures over a variety of materials. These features make crystal plasticity a very attractive option for modeling nickel-base superalloys.

However, crystal plasticity is still limiting in that it does not explicitly account for the microstructure of the γ, γ' and γ/γ' interface. The theory assumes a uniform lattice across the solid which is not the case for nickel-base superalloy single-crystals; consider for instance the lattice mismatch. Moreover, the formulations do not account for the distinct mechanisms through which dislocations move on the alloy's material phases, for example shearing of the precipitates versus climb and glide in the matrix. Additionally, the occurrence of each mechanism is subject to specific temperature and stress regimes. In the next section, we will place great emphasis into extending the crystal plasticity framework to be able to account for the microstructure and for the deformation mechanisms that take place in superalloys. Some authors have approach this limitation by explicitly meshing the γ matrix, γ' precipitates and γ/ γ' interface and then assigning different constitutive crystal plasticity models for each region [91-95]. This introduces significant complexity to the analysis and creates an additional homogenization step that prevents direct application of the constitutive model to macroscopic components. In this work we will address this limitation with a novel integration algorithm that will be presented in detail in CHAPTER 6. It is also important to close this section by stating that although the content of this thesis is aimed toward single-crystals, the model can be extended to polycrystalline superalloys using traditional polycrystalline plasticity theory methods [46, 76, 87]. Additionally, modifications of crystal plasticity to account for the tension and compression asymmetry are available in the literature which allow for the incorporation of this behavior for SX superalloys that display it [96-98]

4.4 Microstructure-sensitive crystal viscoplasticity model

The physically-based model proposed in this work has basis on a crystal-viscoplasticity and damage formulation originally developed by Ma, Dye, and Reed [43]. In their work, they assumed an additive contribution of the material phases (γ and γ') to deformation in the velocity gradient. Traditionally when modeling superalloys using crystal plasticity, only one functional form of the shearing rates on all slip systems is assumed for the two phases in the unit cell which, when calibrated with macroscopic data, forcefully limits the model to give an average measure of deformation,

$$\mathbf{L}^{in} = \dot{\mathbf{F}}^{in}\,\mathbf{F}^{in^{-1}} = \sum_{\alpha=1}^{N_{slip}} \dot{\gamma}^{in(\alpha)} \left(\hat{\mathbf{d}}_o^{(\alpha)} \otimes \hat{\mathbf{n}}_o^{(\alpha)}\right) \qquad (22)$$

where $\widehat{\boldsymbol{d}}_{\mathbf{0}}^{(\boldsymbol{\alpha})}$ and $\widehat{\boldsymbol{n}}_{\mathbf{0}}^{(\boldsymbol{\alpha})}$are the slip direction and slip plane normal unit vectors respectively, defined in the reference configuration for each slip system, and N_{slip} is the number of possibly active slip systems. A more appropriate description should consider the distinct deformation mechanisms of the two phases. As discussed earlier, in some literature this concern has been addressed by meshing a microstructure unit cell with two distinct constitutive relations for the γ and γ' phases, then either dislocation dynamics or traditional crystal-plasticity finite element method is used to connect the microstructure behavior to the macroscale through diverse homogenization techniques [5, 99, 100]. A downside of this approach is that it does not allow immediate application to macroscopic components. Two major assumptions in the model proposed by Ma, Dye, and Reed [43] is that isostress can be assumed between the matrix and the precipitate phase, and that the contribution to the overall deformation of the γ and γ' phase can be additively separated in the plastic velocity gradient,

$$\mathbf{L}^{in} = f_{\gamma}\left(\sum_{\alpha=1}^{12} \dot{\gamma}_{\gamma}^{in(\alpha)} \left(\hat{\mathbf{d}}^{(\alpha)} \otimes \hat{\mathbf{n}}^{(\alpha)}\right)\right) + f_{\gamma'}\left(\sum_{\alpha=13}^{24} \dot{\gamma}_{L1_2}^{in(\alpha)} \left(\hat{\mathbf{d}}^{(\alpha)} \otimes \hat{\mathbf{n}}^{(\alpha)}\right)\right) \qquad (23)$$

where f_{γ} and $f_{\gamma'}$ are the volume fractions of the γ and γ' phases respectively. This equation admits distinctly different flow rules for both material phases and weights their contributions to the total deformation by their volume fraction. Moreover, this additive decomposition is assumed over all material elements. Therefore, deformation on the γ and γ' phases can be modeled without having to mesh the basic microstructure unit. This offers a major advantage over traditional models because it allows for immediate application to macroscopic components since no additional homogenization steps are needed between the microstructure and component level.

Deformation is assumed to occur in the <111> plane for both material phases as shown in Figure 74,

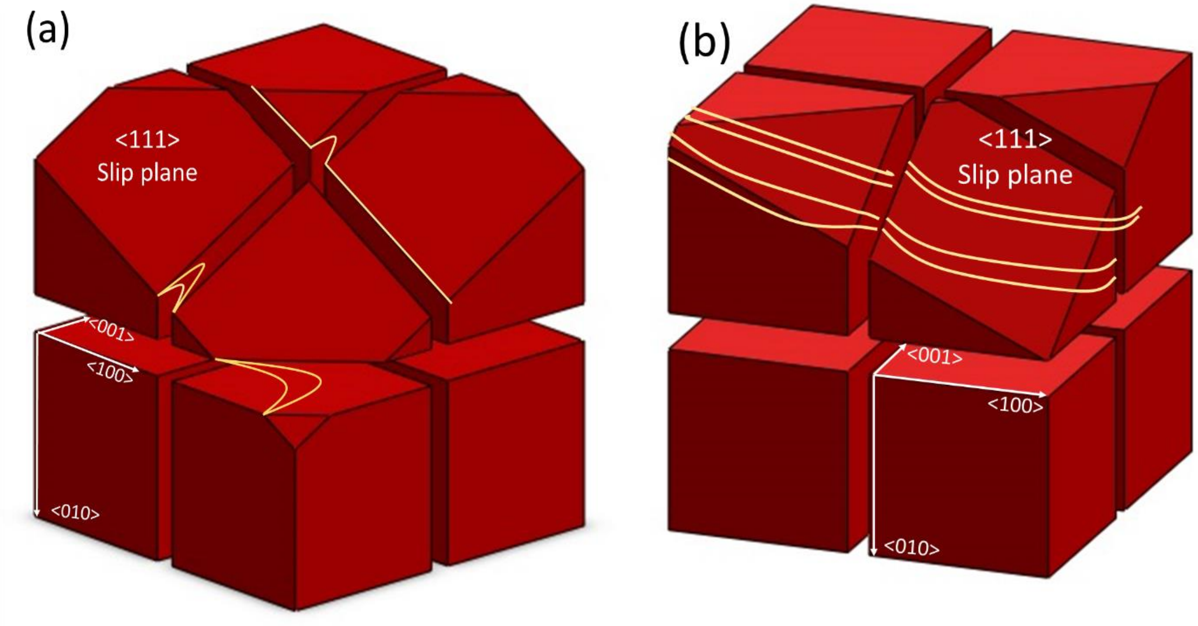

Figure 74: (a) Dislocations of mean spacing $\boldsymbol{\lambda_{\gamma}^{(\alpha)}}$ gliding and climbing in the γ channels in the <111> slip plane (b) Cutting of the γ' precipitates in the <111> slip plane by dislocations of mean spacing $\boldsymbol{\lambda_{L1_2}^{(\alpha)}}$

In Figure 74 (a), in the γ channels climb and glide of dislocations is considered; while in Figure 74 (b), shearing of the precipitates through dislocation ribbons is modeled in the γ' phase. The slip planes are assumed to be octahedral for all slip systems; i.e., $\hat{n}^{(\alpha)}||\{111\}$. However, in the γ', the primary octahedral slip systems operate, $\hat{d}^{(\alpha)}||\langle 111\rangle$, while dislocations cutting through γ' depend on shear stress acting on partial dislocations necessary to cut through the ordered structure that manifests as ribbon shearing; hence, $\hat{d}^{(\alpha)} || \langle 112 \rangle$ for $13 \leq \alpha \leq 24$. In Figure 75, these slip systems are schematically illustrated on one of the {111} planes for an FCC material,

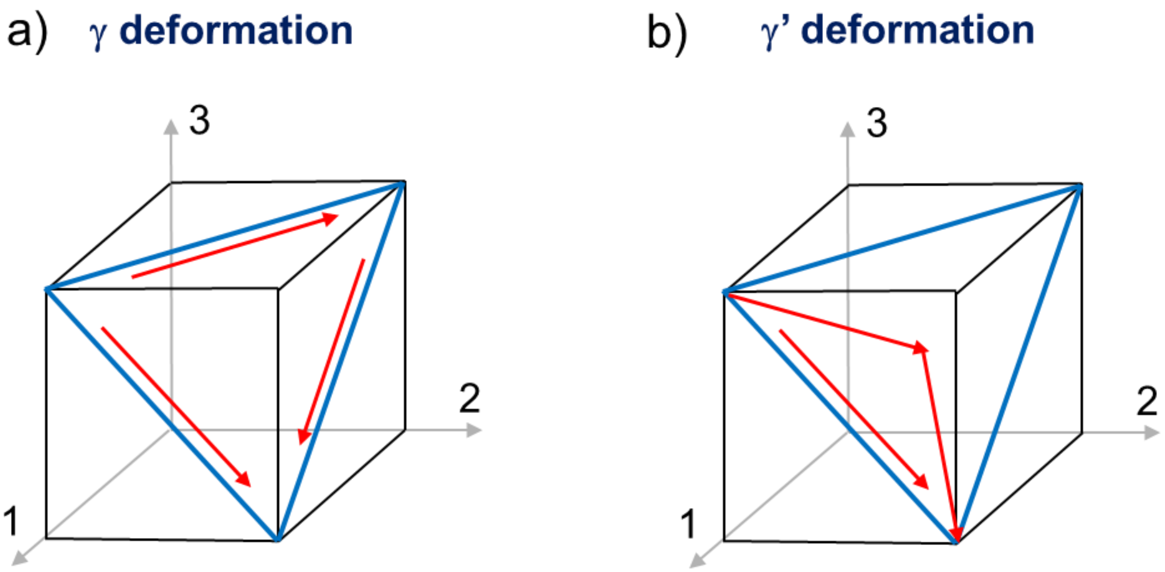

Figure 75: (a) Octahedral slip systems in γ (b) Dislocation ribbon slip systems in γ'

Despite not meshing the basic microstructure unit, this formulation is microstructure-sensitive for three reasons. First, the volume fraction of each phase serves as a weight reflecting the phase contributing the most to the overall deformation. Second, the Schmidt tensors for each phase are distinct. Third, and perhaps more importantly, separating the plastic velocity gradient for the phases also allows for explicitly incorporating two distinct flow rules and distinct evolution equations for the dislocation densities for each material phase which more closely resembles the deformation mechanisms of superalloys. Next, we describe in detail the proposed flow rules for the γ and γ' phase.

4.5 Inelastic shear strain relation and evolution equations

In the flow rules proposed in this work, the relationship between the inelastic strain rates on each slip system and the velocity of mobile dislocations is assumed to follow modifications of the Orowan equation (equation (21)) for both phases. A suitable expression for the velocity of mobile dislocation has been assumed, and in the γ phase the flow rule for each primary slip system is described by,

$$\dot{\gamma}_{\gamma}^{in(\alpha)} = \rho_{\gamma}^{(\alpha)} b \lambda_{\gamma}^{(\alpha)} F_{attack} \Theta(T, \xi) \left(\frac{\tau_{eff_{\gamma}}^{(\alpha)}}{\kappa_{\gamma}^{(\alpha)}} \right)^{n} \exp\left(\frac{-Q_{slip}^{110} + \left(\left| \tau_{eff_{\gamma}}^{(\alpha)} \right| - \kappa_{\gamma}^{(\alpha)} \right) V_{c1}^{(\alpha)}}{kT} \right) sign\left(\tau_{eff_{\gamma}}^{(\alpha)} \right) \quad (24)$$

This flow rule includes a diffusivity parameter, the backstress, and a *sign* function. The diffusivity parameter is composition sensitive and is calibrated to the alloy's rhenium content using thermodynamics and kinetic software Thermo-Calc and DICTRA. The diffusivity parameter is assumed to be of the form,

$$\Theta(T) = C_1 \left(\frac{T}{T_{melt}} \right)^{C_2} \exp\left(-\frac{Q_o}{kT} \right) \qquad (25)$$

The pre-exponential coefficient is calibrated using macroscopic creep test data while the activation energy for diffusion is composition sensitive and is calculated using Thermo-Calc and DICTRA using the procedure outlined by Gorgannejad et al. [101] and, by Estrada Rodas et al. [102]. The backstress accounts for the Bauschinger effect which is important to describe the reversibility of slip for creep-fatigue loading. The sign function reverses the shearing rates in the direction of the applied loading effectively modeling load reversals. The power-law with a strain rate sensitivity exponent is needed in the flow rule to successful model the rate-dependent and rate-independent regimes. During calibration of the model, it was found that an inadequate relationship between yield strength and creep relaxation is observed when this term is absent. This observation will be further discussed in CHAPTER 6. The activation energy Q_{slip}^{110} represents the thermal component for overcoming the obstacles in absence of stress. The exponential term in the flow rule describes the probability of dislocations moving. The pre-exponential coefficient accounts for the speed of the mobile dislocations and is dependent on the mobile dislocation density on that slip system, the Burger's vector, the dislocation vibration frequency, and the dislocation mean free path which is defined as [43],

$$\lambda_{\gamma}^{(\alpha)} = c_{jump1}\left(\frac{1}{L_{\gamma}} + \frac{1}{L_{\rho}^{(\alpha)}}\right)^{-1} \tag{26}$$

The dislocation mean free path (jump distance) is an average measure of the distance travelled by dislocations between the source and storage points and is proportional to the dislocation pinning spacing. In here, the mean free path is assumed proportional to the harmonic mean of the channel size and the forest dislocations. The harmonic mean is preferred over the traditional mean since it better represents quantities which can differ by orders of magnitude. The components due to pinning at the γ/γ' interfaces and the average spacing of forest dislocations is assumed to be [43],

$$L_{\rho}^{(\alpha)} = \frac{c_{Fdis}}{\sqrt{\rho_F^{(\alpha)}}} \tag{27}$$

The effective resolved shear stress is considered as the contributions of the applied loading, the misfit stresses and the backstress:

$$\tau_{eff_{\gamma}}^{(\alpha)} = \tau_{\gamma}^{(\alpha)} + \tau_{mis}^{(\alpha)} - \chi_{\gamma}^{(\alpha)} \tag{28}$$

In this expression the misfit stresses are assumed to relax due to the γ dislocations becoming captured in the γ/γ' interface which causes loss in elastic coherency [43, 44],

$$\tau_{mis}^{(\alpha)}\left(T,\gamma_{\gamma}^{(\alpha)}\right)=\tau_{mis0}^{(\alpha)}\left\{1-\exp\left(\left(\frac{\sum_{\alpha=1}^{12}\rho_{pb}^{(\alpha)}}{-\rho_{pb}^{ref}}\right)^{c_{icb}}\right)\right\} \tag{29}$$

The threshold stress is assumed to rise from the hardening generated by the parallel dislocation density within the γ phase (Taylor self-hardening) [103],

$$\kappa_{\gamma}^{(\alpha)}=\tau_{\gamma pass}^{(\alpha)}=c_{pass11}Gb\sqrt{\rho_{P_{\gamma}}^{(\alpha)}} \tag{30}$$

The forest and parallel dislocations used to characterize the resistance of mobile dislocations are defined by projecting the total dislocation density to the slip systems as [104],

$$\rho_{F}^{(\alpha)}=\sum_{\beta=1}^{N_{slip}}\rho_{I}^{(\beta)}\left|\cos\left(\hat{\mathbf{n}}^{(\alpha)},\hat{\mathbf{n}}^{(\beta)}\times\hat{\mathbf{d}}^{(\beta)}\right)\right| \tag{31}$$

$$\rho_{P}^{(\alpha)}=\sum_{\beta=1}^{N_{slip}}\rho_{I}^{(\beta)}\left|\sin\left(\hat{\mathbf{n}}^{(\alpha)},\hat{\mathbf{n}}^{(\beta)}\times\hat{\mathbf{d}}^{(\beta)}\right)\right| \tag{32}$$

These projections are schematically described in Figure 76.

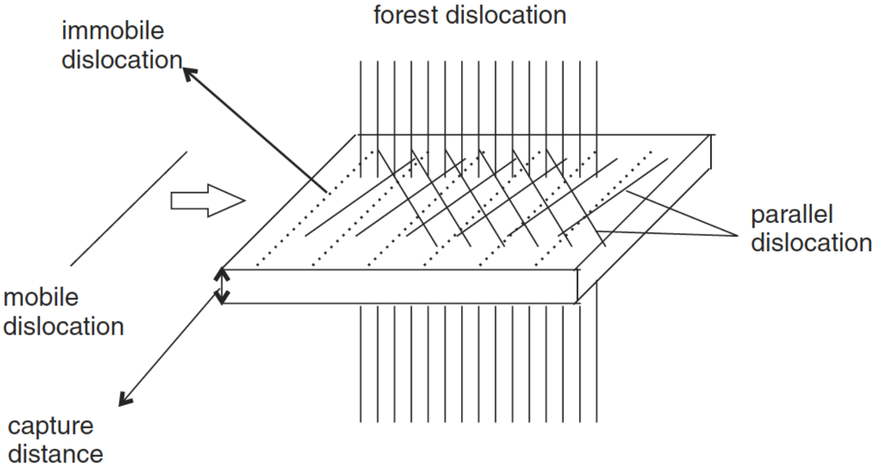

Figure 76: Graphical representation of forest and parallel dislocations [105]

It is assumed that these dislocation densities depend only on the immobile dislocation density $\rho_I^{(\alpha)}$ on each slip system since the mobile dislocation density is lower by at least one order of magnitude.

The activation volume is the volume that is physically swept by dislocations from a ground equilibrium state to an activated state after deformation [43, 106],

$$V_{c1}^{(\alpha)} = c_{vc1} b^2 \lambda_{\gamma}^{(\alpha)} \tag{33}$$

In the γ' phase, the flow rule defines the rate of dislocation shearing through the γ' precipitates in a ribbon fashion on the secondary slip systems,

$$\dot{\gamma}_{L1_2}^{in(\alpha)} = \rho_{L1_2}^{(\alpha)} b \lambda_{L1_2}^{(\alpha)} F_{attack} \exp\left(\frac{-Q_{slip}^{112} + \left(\left| \tau_{eff_{\gamma}'}^{(\alpha)} \right| - \kappa_{L1_2}^{(\alpha)} \right) V_{c2}^{(\alpha)}}{kT} \right) sign\left(\tau_{eff_{\gamma}'}^{(\alpha)} \right) \tag{34}$$

Unlike the γ channels, in the γ' phase, the dislocation mean free path (jump distance) is calculated using the size of the γ′ particles $L_{\gamma'}$ as a parameter, this is because dislocation in the precipitates can be separated by a distance as large as the precipitate size,

$$\lambda_{L1_2}^{(\alpha)} = c_{jump2}\left(\frac{1}{L_{\gamma'}} + \frac{1}{L_{\rho}^{(\alpha)}}\right)^{-1} \tag{35}$$

Since dislocation in the precipitates travel in pairs, it is assumed that the dislocation spacing in the γ' precipitates can never be less than [7],

$$\lambda_{mim} = \frac{Gb^2}{2\pi\gamma_{APB}} \tag{36}$$

This expression is derived from force balance of two dislocations cutting through a precipitate. This is implemented to ensure that, as dislocation density increases, the alloy does not become artificially strengthened when dislocations come infinitely close to each other.

Different from the case in the γ channels, the threshold stress in the γ' precipitates has two components, one is due to the hardening generated by the passing of dislocations in this phase and the other is a result of the resistance from the APB created when a pair of dislocations enter the precipitate,

$$\kappa_{L1_2}^{(\alpha)} = \tau_{L1_2 pass}^{(\alpha)} + \tau_{APB} \tag{37}$$

moreover, the passing stress in this phase, $\tau_{L1_2 pass}^{(\alpha)}$, has an additional term which accounts for the hardening associated with the increased incoherency at the γ/γ' interface. The otherwise coherent boundary between the γ and γ' phases becomes incoherent as dislocations that generated in the channels travel and accumulate in the γ/γ' boundary, these increased incoherency strains the lattices and induces stresses which have a strengthening effect;

$$\tau_{L1_2 pass}^{(\alpha)} = Gb\left(c_{pass21}\sqrt{\rho_{P}^{(\alpha)}} + c_{pass22}\sqrt{\rho_{P_{pb}}^{(\alpha)}}\right) \tag{38}$$

finally, the APB resistance in the threshold stress is described by the APBE as [7],

$$\tau_{APB} = \frac{\gamma_{APB}}{b} \tag{39}$$

The effective stress in the precipitates is comprised only of the applied stress resolved onto the secondary slip systems,

$$\tau_{eff_{\gamma'}}^{(\alpha)} = \tau_{\gamma'}^{(\alpha)} \tag{40}$$

After reaching the critical stress level for precipitate shearing, the precipitate offers very little resistance to dislocation motion and therefore the backstress is not included in the γ' phase. Moreover, the effect of the misfit stress is strongest at the γ/γ' interface and before shearing has taken place, therefore it is only accounted for in the γ phase.

Separating the flow rules has made it possible to propose distinct equations describing the deformation mechanisms of each material phase. The mechanisms that cause glide and climb of dislocations in the channels versus the shearing of precipitates by dislocation pairs are properly differentiated and their contributions to the overall deformation adequately accounted for. Additionally, the morphology of the microstructure is also considered by the volume fraction and size of the γ channels and the γ' precipitates. These foundations allow the model to become microstructure-sensitive and to explicitly model the relevant features of the deformation of superalloys. Next we define the set of evolution equations for the hardening variables and for the backstress.

4.6 Evolution equations

An important aspect of the state of the microstructure of this alloy is its dislocation density and how it evolves in the individual phases and near their interface. Therefore, these three dislocation densities are used as the ISVs. The dislocation density in the γ channels, in the γ' particles and in the γ/γ' interface will be controlled by unique sets of evolution equations since their values are often distinctly different, particularly under conditions when looping of the precipitates occurs, and hence the microstructure attributes that control their evolutions are distinct. In the γ channels, the dislocation density assumes a Kocks-Mecking form [107],

$$\dot{\rho}_{\gamma}^{(\alpha)} = \frac{c_{mult1}}{b\lambda_{\gamma}^{(\alpha)}}\left|\dot{\gamma}_{\gamma}^{in(\alpha)}\right| - c_{annh1}\rho_{\gamma}^{(\alpha)}\left|\dot{\gamma}_{\gamma}^{in(\alpha)}\right| \tag{41}$$

This equation assumes that the evolution solely depends on self-hardening, however this can be easily extended if needed to include cross-hardening. The evolution equations for dislocations gathered at the interface also use the Kocks-Mecking form and are dependent on the rates in the γ channels. This is because the population of dislocations at the interface would have been initially generated in the channels and travel along the slip systems to meet the γ/γ' interface:

$$\dot{\rho}_{pb}^{(\alpha)} = \frac{c_{mult}^{pb}}{bL_{\gamma}}\left|\dot{\gamma}_{\gamma}^{in(\alpha)}\right| - c_{annh}^{pb}\rho_{pb}^{(\alpha)}\left|\dot{\gamma}_{\gamma}^{in(\alpha)}\right| \tag{42}$$

In the γ' particles, the evolution equations include one more multiplication term that captures the ease of dislocations in the γ/γ' interface entering a γ' precipitate, this additional term is controlled by a thermally activated process [43]. Enough dislocations need to gather at the interface before they can start cutting the precipitates,

$$\dot{\rho}_{L1_2}^{(\alpha)} = c_{mult21}\rho_{pb}^{(\alpha)}\Gamma + \frac{c_{mult22}}{b\lambda_{\gamma'}^{(\alpha)}}\left|\dot{\gamma}_{\gamma'}^{(\alpha)}\right| - c_{annh2}\rho_{\gamma'}^{(\alpha)}\left|\dot{\gamma}_{\gamma'}^{(\alpha)}\right| \tag{43}$$

where,

$$\begin{cases} \Gamma = F_{attack} \exp\left(\dfrac{-Q^{pb} + \left(\left| \tau^{(\alpha)} \right| - \tau^{(\alpha)}_{pb_{pass}} \right) V^{(\alpha)}_{c2}}{kT} \right) sign\left(\left| \tau^{(\alpha)} \right| - \tau^{(\alpha)}_{pb_{pass}} \right) \\ Q^{pb} = c_{misfit} G b^3 \left| \delta \right| \\ \tau^{(\alpha)}_{pb_{pass}} = c^{pb}_{pass} G b \sqrt{\rho^{(\alpha)}_{P_{pb}}} \end{cases} \tag{44}$$

It is important to notice that the dislocation density in the precipitates, $\rho^{(\alpha)}_{L1_2}$, is a function of dislocation density at the interface and consequently is also a function of dislocation density at the γ channels. The stress and temperature conditions should be such that enough dislocations generate at the interphase to overcome the thermally activated term associated to precipitate shearing. Moreover, note that an increase in $\rho^{(\alpha)}_{L1_2}$ does not lead to additional hardening. The hardening in the precipitates is mostly due to the APBE but it also has contributions from dislocation networks that form at the γ/γ' interface.

In classical plasticity, the Backstress is used in kinematic hardening models and represents the center of the yield surface in stress space. The backstress and its corresponding evolution with plastic deformation is often necessary to model behaviors such as the Bauschinger effect. The evolution equation of the backstress reflects a competition between the extra hardening due to the increasing polarity of dislocations after yielding and the associated diffusion-assisted recovery of defect trails [103]. Some authors refer to these two behaviors as saturation hardening and recovery, respectively. In this research, we adopted evolution equations of the backstress which depended on dislocation density as an ISV and which have saturation and recovery terms. The evolution of the backstress has the form used by Shenoy et al. [108], these evolution equations have been successfully used previously in modeling of polycrystalline IN100 Nickel-base superalloys,

$$\dot{\chi}_{\gamma}^{(\alpha)} = C_{\chi}\left\{\eta C_{44} b\sqrt{\rho_{\gamma}^{(\alpha)}}\,\mathrm{sgn}\left(\tau_{\gamma}^{(\alpha)} - \chi_{\gamma}^{(\alpha)}\right) - \chi_{\gamma}^{(\alpha)}\right\}\left|\dot{\gamma}_{\gamma}^{(\alpha)}\right| \tag{45}$$

$$\eta = \frac{\eta_o \dfrac{c_{mult1}}{b\lambda_{\gamma}^{(\alpha)}}}{\dfrac{c_{mult1}}{b\lambda_{\gamma}^{(\alpha)}} + \kappa\sqrt{\rho_{\gamma}^{(\alpha)}}} \tag{46}$$

The backstress is used to capture the Bauschinger effect associated with the resistance of dislocations glide in the matrix. Also, it is assumed that the backstress captures the contribution of the Orowan stress, which relates to the bowing of the dislocations in the γ channels between the precipitate interfaces and is dependent on the dislocation mean free path and therefore is a function of dislocation density in the channels [103].

4.7 Damage parameter

Not many formulations in the literature can incorporate the effect of damage in crystal-plasticity. In this work, the damage is modeled by assuming a damage parameter acting on the resolved shear stresses [43],

$$\tau^{(\alpha)} = \frac{\tau_{applied}^{(\alpha)}}{1-D} \tag{47}$$

The damage parameter at any time *t* is defined as,

$$D = \left(\int_{t=0}^{t=t}\left(\sum_{\alpha=1}^{12}\dot{R}_{\gamma}^{(\alpha)} + \sum_{\alpha=1}^{12}\dot{R}_{pb}^{(\alpha)} + \sum_{\alpha=13}^{24}\dot{R}_{\gamma'}^{(\alpha)}\right)d\tau\right)^{\frac{2}{3}} \tag{48}$$

Damage in this model is assumed to be only due to void condensation; therefore, the damage parameter is made a function of the average void radii ($R^{(\alpha)}$) in each material phase. For each time step, the contributions to the damage parameter made by each material phase are summed. Subsequently these contributions are integrated over time because the average void size will grow as more dislocations continue to annihilate. The 2/3 exponent in the definition of the damage converts the volume ratio to the effective cross-sectional area of shearing.

The evolution of the void radii in each material phase is made proportional to the contributions of void condensation that results when dislocations with burgers vector of opposing sign meet in the γ, γ' phase and in the γ/γ' interface. Consequently, the void radii can be related to the activity of the annihilation of dislocation densities [43]:

$$\dot{R}_{\gamma}^{(\alpha)} = c_{void} \frac{c_{annh1} \rho_{\gamma}^{(\alpha)} \left| \dot{\gamma}_{\gamma}^{in(\alpha)} \right| b^2}{2} \tag{49}$$

$$\dot{R}_{pb}^{(\alpha)} = c_{void} \frac{c_{annh1} \rho_{pb}^{(\alpha)} \left| \dot{\gamma}_{\gamma}^{in(\alpha)} \right| b^2}{2} \tag{50}$$

$$\dot{R}_{\gamma'}^{(\alpha)} = c_{void} \frac{c_{annh2} \rho_{\gamma'}^{(\alpha)} \left| \dot{\gamma}_{\gamma'}^{in(\alpha)} \right| b^2}{2} \tag{51}$$

4.8 Summary

In this chapter, we have presented the theoretical development of the microstructure-sensitive crystal-viscoplasticity model for modeling the deformation of Ni-base superalloys. The equations proposed in this chapter explicitly model the relevant aspects of the microstructures and of the deformation mechanism that take place on each material phase. Dislocation densities were used as ISVs for all material phases. Moreover, the dislocations that form at the γ/γ' interface are modeled and are used to connect the deformation in the channels and in the precipitates which more closely represents the deformation of the alloy. Finally, damage was also modeled though incorporating void condensation as a damage mechanism which was directly applied to the resolved shear stress in the form of a dimensionless damage parameter. In the next Chapters, the model will be implemented as a 1-dimensional (1-D) stress-based routine and as a 3-dimensional (3-D) displacement-based routine and several applications of the models will be described in the context of alloy design.

CHAPTER 5

REDUCED ORDER ONE-DIMENSIONAL STRESS-BASED MODEL IMPLEMENTATION

In this chapter the microstructure-sensitive CVP model is implemented in a 1-dimensional (1-D) stress-based MATLAB® routine that can be used to perform quick trade studies on the creep response of superalloys. The implementation technique will be presented first, followed by the model calibration and by numerical explorations of the model focused on the effect of microstructure parameters on the creep response of superalloys.

5.1 One-dimensional stress-based creep model implementation

During a traditional ASTM standard creep test the load is constant. In this case, integration of the constitutive equations is relatively simple if one ignores the lattice rotation and the contribution of the elastic strain that rises from the initial loading. The current time step and the shearing rates, equations (24) and (34), can be input directly into the plastic velocity gradient (equation (23)) to obtain the deformation gradient and subsequently the green strain tensor as follows,

$$\mathbf{F} = \left(\mathbf{I} + \mathbf{L_p} dt\right)\mathbf{F_0} \tag{52}$$

$$\mathbf{E} = \frac{1}{2}(\mathbf{F^T F} - \mathbf{I}) \tag{53}$$

This ease of implementation makes the one-dimensional stress-based creep application very attractive for alloy design since one can very rapidly evaluate the effect on the creep response of the material due to variations of the microstructure parameters. This stress-based creep case can also be implemented in 3-D. However, the extension of this model to three-dimensional simulations is not trivial and will be discussed in detail in the next chapter. In the following section, we use macroscopic creep test data to calibrate the material parameters of the model to the stress-based creep cases.

5.2 Creep model parameter estimation and model verification

The creep tests conducted at the maximum and minimum temperatures tested, 750°C and 1037°C respectively, were used to calibrate the material parameters. Material parameters most associated to the γ channel deformation were calibrated using the data at 1037 °C while the data at 750 °C was used to calibrate material parameters most relevant to the γ' phase. The remaining experimental conditions were used to verify the goodness of the calibration. In Figure 77, the calibration and the verification data sets are shown along with the model predictions,

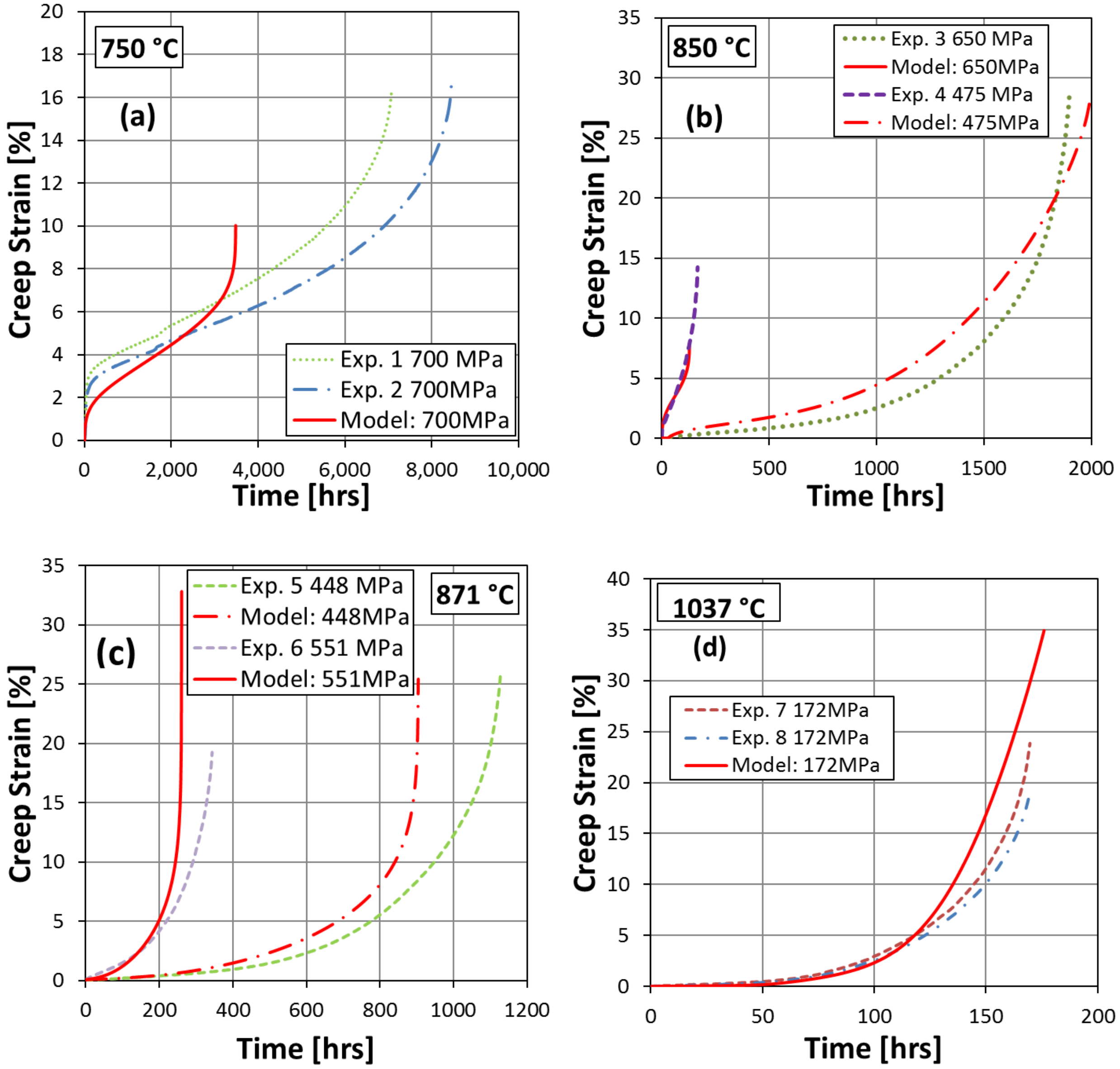

Figure 77: Creep response for different loading conditions: Plots (a) and (d) are calibration sets, while plots (b) and (c) are verification sets

As shown in Figure 77, the model readily captures all regimes of creep for CMSX-8. In Figure 77 (a) and (b) it accurately estimates that the deformation will show significant primary creep; which agrees well with the experimental data from Figure 69. At this higher stress level, there is enough force for dislocations to cut through the γ' precipitates thus promoting primary creep. Furthermore, note that in Figure 77 (b), and Figure 77 (c) the deformation shows some primary creep but is largely dominated by tertiary creep, this is also consistent with the experimental results. As temperature increases, there is no visible primary creep and the deformation is completely dominated by tertiary creep as seen in Figure 77 (d). The physical parameters used in this model are given in Table 10. These are parameters that can be calculated by first principles or are known via independent experiments [7, 14, 31, 43, 109, 110]. The remaining material parameters are shown in and Table 11, these are determined by calibrating the model to the available creep data.

Table 10: Fundamental microstructure parameters

Fundamental parameters		**Microstructure parameters**	
b	2.49 (Å)	Virgin microstructure:	
F_{attack}	$1x10^{12}$ [1/s]	f_{γ}	*0.3*
γ_{APB}	0.111 [J/m^2]	$f_{\gamma'}$	*0.7*
δ	-0.002	L_{γ}	$0.1x10^{-6}$ [m]
T_{melt}	1726 [K]	$L_{\gamma'}$	$0.8x10^{-6}$ [m]

Table 11: Parameters fit to creep deformation data

c_{annh1}	20.0	c_{pass11}	1.4
c_{annh}^{pbd}	10.0	c_{pass22}	1.5x10^{-2}
c_{annh2}	10.0	c_{pass21}	1.5x10^{-2}
c_{Fdis}	0.1	c_{vc1}	1.0
c^{icb}	5.0	c_{vc2}	7.5x10^{-1}
c_{jump1}	9x10^{-2}	c_{void11}	1.5x10^{3}
c_{jump2}	6x10^{-2}	c_{void22}	1x10^{5}
c_{misfit}	275 [*1/mol*]	c_{void21}	1.5x10^{3}
c_{mult1}	3x10^{-4}	n	0
c_{mult}^{pbd}	1x10^{-3}	Q_{slip}^{110}	300 [*kJ/mol*]
c_{mult2}	9x10^{-3}	Q_{slip}^{112}	180 [*kJ/mol*]
$\mathrm{c}_{\mathrm{mult21}}$	5x10^{-15}	$\left.\rho_{\gamma}^{(\alpha)}\right\|_{t=0}$	1x10^{11} [*1/m*^{2}]
c_{oro}	0.816	$\left.\rho_{L1_2}^{(\alpha)}\right\|_{t=0}$	0 [*1/m*^{2}]
		ρ_{γ}^{ref}	1.0x10^{13}

While calibrating the 1-D stress-based creep model, it was observed that the evolution of the backstress (equation (45)) prevented tertiary creep from taking place. This is because as dislocation density stabilizes, a constant value of the backstress is also experienced. Because the effective stress (equation (28)) in the flow rule is obtained by subtracting the backstress from the applied resolved shear stress, the constant backstress that emerges during dislocation density stabilization serves to reduce the effect of the applied stress. The resulting constant dislocation density structure prevents tertiary creep from taking place. To correct for this, the backstress is suppressed from the 1-D model and the Orowan stress due to the bowing of dislocation is instead considered a threshold stress in the γ phase as was done by Ma et al. [43],

$$\chi_{\gamma}^{(\alpha)} = 0 \tag{54}$$

$$\kappa_{\gamma}^{(\alpha)} = \tau_{\gamma pass}^{(\alpha)} + \tau_{oro}^{(\alpha)} = c_{pass11} G b \sqrt{\rho_{P_{\gamma}}^{(\alpha)}} + c_{oro} \frac{Gb}{L_{\gamma}} \tag{55}$$

This suggests that the relationship between the backstress and the Orowan bowing is rather complex. Hence assuming that backstress due to saturation hardening and dynamic recovery alone can completely account for the bowing of dislocations in the channels during creep is not sufficient. An alternate form of backstress formulation is still needed. However, very limited literature is available that investigates the mechanics of the backstress in superalloys, and to the author’s best knowledge an alternative approach to the one proposed in this thesis could not be found.

5.3 Alloy design: sensitivity to changes in the microstructure morphology and anti-phase boundary energy

In this section the channel size (L_{γ}) and correspondingly the volume fraction ($f_{\gamma'}$) and size of the precipitates ($L_{\gamma'}$) will be varied to study the effect changes in the morphology have in the creep response. Superalloys have been developed for many decades and currently there exists several types and generations of superalloys with various volume fraction of γ and γ'. It has been shown in multiple studies that there is a direct correlation between γ' particle size and hardening and that there is an optimum strength in superalloys takes place at the transition from weak to strong coupling [37, 38]. In Figure 78, the γ channel size has been increased while keeping the volume fraction of γ' precipitate constant and varying the size of the precipitates according to the constraint [43]:

$$f_{\gamma'} = \frac{L_{\gamma'}^3}{\left(L_\gamma + L_{\gamma'}\right)^3} \tag{56}$$

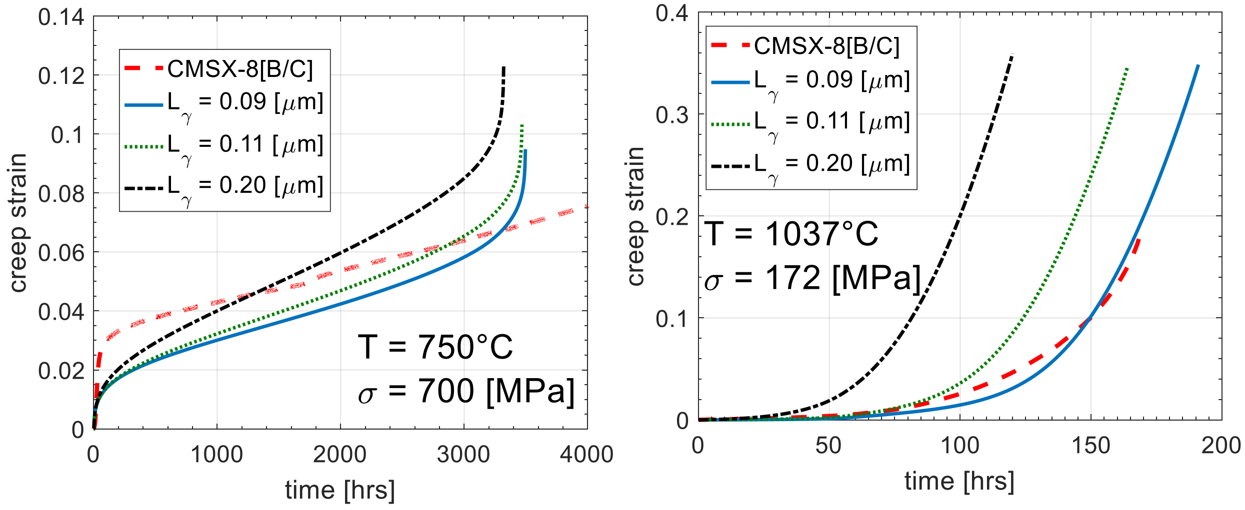

Figure 78: Effect of channel size on creep response

This analysis shows that increasing the channel size accelerates the steady state creep rate. Note that primary creep is also affected and the microstructure with the smaller precipitate size exhibits greater amount of primary creep. Also, the onset of tertiary creep is accelerated. This behavior is due to the reduced coupling of dislocations. As the precipitates become smaller, the coupling between dislocations becomes weak which in turn softens the material. Finally note that the effect of increasing the channel size is not linear and at very high temperatures slight variations in channel width can have a significant impact in the creep performance of the alloy.

The APBE was also varied. Changing this parameter did not have any visible effect on the creep behavior at higher temperatures, however a strong effect was observed at lower temperatures as shown in Figure 79,

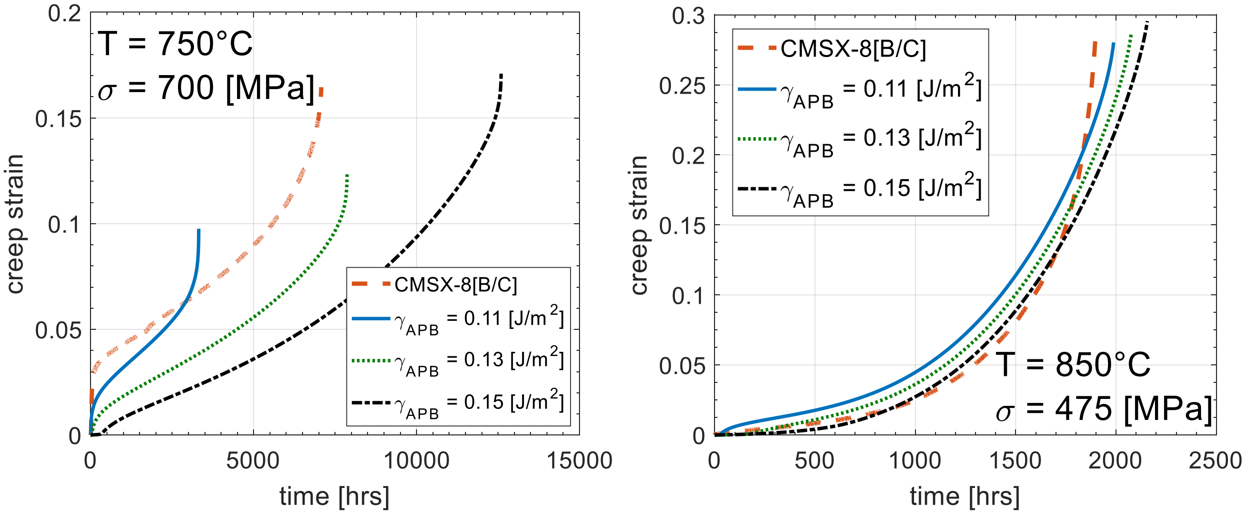

Figure 79: Effect of anti-phase boundary energy on creep response

These results are consistent with the deformation mechanisms of these superalloys at lower temperatures and higher stresses. A higher value of APBE directly affects the precipitates and prevents dislocations from cutting them thus reducing the amount of primary creep. Also, note that the simulations with higher anti-phase boundary energies also show longer creep rupture lives which suggests that the initial shearing of the precipitates has a very adverse effect on the creep life and thus it would be desirable to reduce the amount of primary creep that the alloy experiences. However, this could prove to be a very difficult task since the addition of refractory elements needed to resist tertiary creep at higher temperatures also increases the amount of primary creep.

5.4 Effect of crystallographic orientation on creep

Although creep tests in material orientations other than the <001> were not available for this work, several material orientations were simulated and qualitatively assessed. In Figure 80, the creep response for CMSX-8 is examined and compared to results obtained by McKay and Maier on MAR-M247 and MAR-M200 at 750 °C [111]

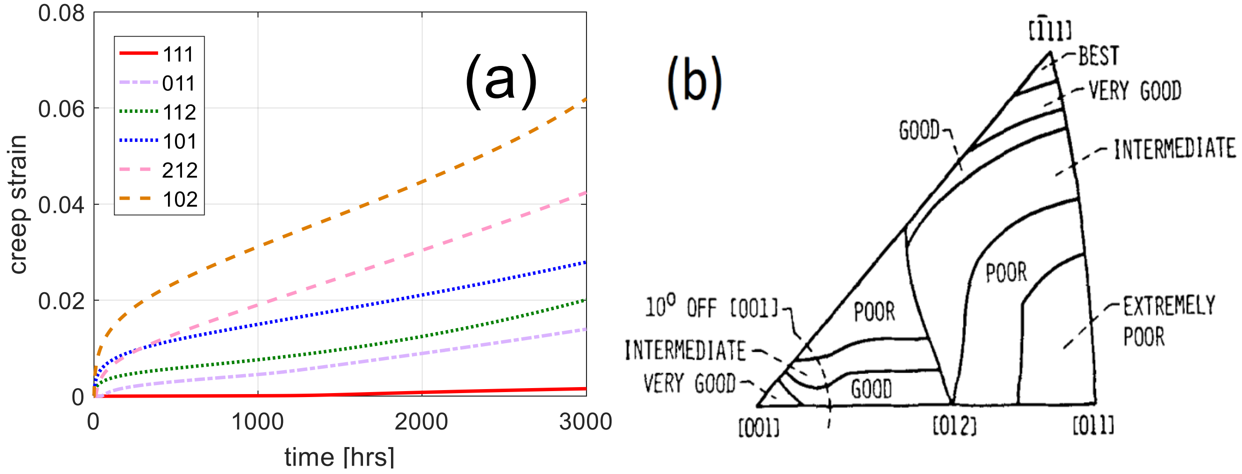

Figure 80: (a) Creep simulations tested for several crystallographic orientations at 700 MPa and 750°C (b) Suggested performance of superalloys as a function of orientation at 750°C [111]

The simulations are consistent with the orientation regimes estimated by McKay and Maier, the best performance at this temperature is obtained for orientations close to <111>, while the worse performance is for orientations closer to the <011> and the <012>.

5.5 1-dimensional model limitations

One clear limitation of the model as presented in this chapter is that it is a1-D stress-based model for creep only. This simplification forces the CVP model to ignore effects such as the lattice rotation which can only be implemented using a full three-dimensional formulation. These simplifications prevent the 1-D model from being able to predict creep-fatigue, low-cycle fatigue and thermomechanical fatigue. In the next section, the model is implemented to three-dimensions and the backstress is activated to enable predictions on the creep-fatigue behavior of nickel-base superalloy single-crystals.

The evolution of the microstructure was not exercised in the 1-D model implementation due to unavailability of experimental data on CMSX-8. However, is not clear whether this behavior needs to be modeled in constitutive models. In aging studies of superalloys, rafting became observable for temperatures of 950 ºC and above [19, 112]. Rafting has been shown to play some role in the response of creep, however it is important to note that conflicting accounts on its effect are often reported in the literature. More research is needed to fully understand this behavior and to assess whether the incorporation of this behavior in constitutive models is necessary. A possibility is that as designers continue pushing to increase the temperatures in the hot gas path, modeling of the evolution of the microstructure during rafting could become necessary to completely account for the deformation and for life of components at higher temperatures. If modeling microstructure evolution became necessary, the model developed in this thesis could be easily modified by utilizing evolution equations for the morphology of the microstructure. In this 1-D implementation, we only considered a cuboidal microstructure. However, the model can be implemented under rafting conditions by using an approach similar to the one proposed by several other authors [19, 46, 53] in which the kinetics of rafting are determined a priori in order to characterize the state of the microstructure as a function of exposure time.

CHAPTER 6

DISPLACEMENT-BASED 3-DIMENSIONAL MODEL IMPLEMENTATION

The microstructure-sensitive crystal-viscoplasticity model is implemented in a 3-dimensional (3-D) displacement-based routine that can be used in commercially available finite element software. Implementation of the model in 3-D is not trivial and a novel numerical technique is developed to enable the model extension to 3-D. The model is implemented in commercial finite element analysis package ABAQUS, however the method presented in this chapter is applicable to any other software, commercial or research-based, that uses displacement-based elements. Following the numerical implementation, the model is validated using LCF, and TMF data. Finally, the model is exercised in the context of alloy design and several sensitivity studies of relevant microstructure parameters are explored.

6.1 ABAQUS and user material subroutine (UMAT) interface

ABAQUS allows users to input their own constitutive models through the User MATerial Subroutine (UMAT) capability. The process under which ABAQUS interacts with the UMAT is shown schematically in Figure 81. At each time step, the constitutive equations are solved through the UMAT which ultimately allows for the calculation of the deformation gradient of next time step.

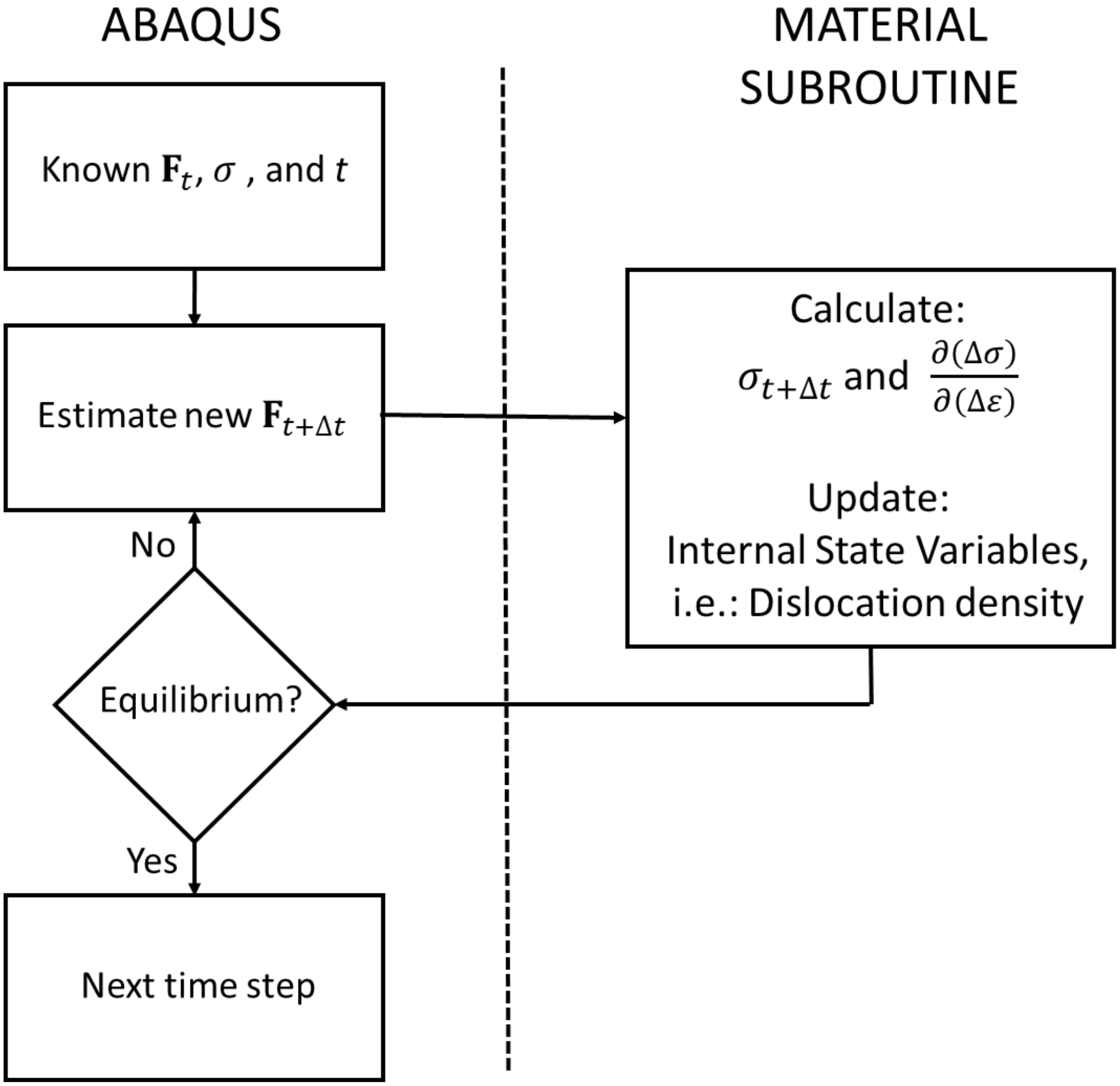

Figure 81: Flow diagram displaying the interaction between the UMAT and the ABAQUS solver. Adapted from McGuinty [87].

Within the UMAT the values of the shearing rates (flow rules) for the current time step are solved iteratively by using the shearing rates and ISVs of the current time step as an initial guess for the Newton-Raphson method. The iterations stop when an acceptable error between the current guess and the next iteration is reached. This process is graphically shown in Figure 82,

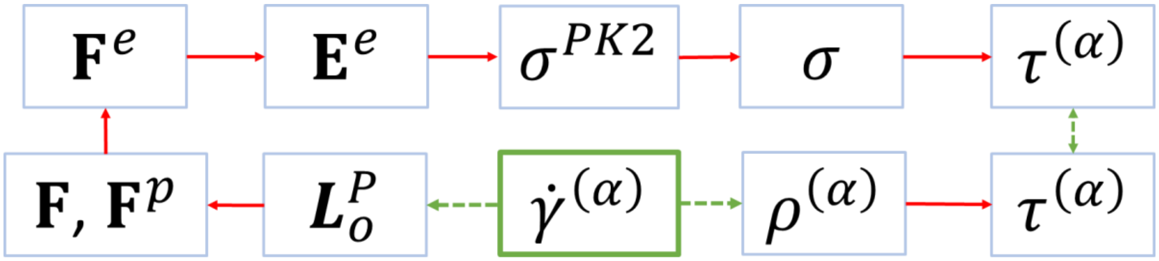

Figure 82: Iterative procedure used by the UMAT to calculate the resolved shear stress

The set of flow rules (equations (24) and (34)) and evolution equations proposed in this research (equations (41), (42) and (43)) to describe the deformation of the γ, γ' and the γ/γ' phases are implicit and highly coupled to each other through the resolved shear stresses, and through the dislocation densities of the γ and γ' phases and the γ/ γ' interface. In the following section, we develop a novel Newton-Raphson algorithm that will enable time integration of the CVP on each time step.

6.2 Challenges in numerical implementation

By separating $\mathbf{L}^{in}$ into a γ and a γ' contribution in equation (23) we were able to incorporate distinctly different deformation mechanisms in a one-unit cell. This greatly enhances crystal-viscoplasticity in that physically-based equations can be incorporated to describe the deformation of a two-material phase alloy. However, this introduces a significant level of complexity in the solution of the equations because the shearing rates, equations (24) and (34), become greatly coupled through the resolved shear stresses. To overcome this challenge, a new Newton-Raphson algorithm is developed.

6.2.1 Quasi Newton-Raphson with Line Search Algorithm

The Newton-Raphson (NR) integration scheme coupled with line search algorithms has been the preferred method for incorporating constitutive models into commercially available Finite Element packages due to its rapid convergence, and numerical stability allowing for the usage of larger time steps in comparison with other methods [87, 105, 113]. A complication of using NR is that a fully implicit integration algorithm is required. Plasticity models proposed to this date have all assumed one functional form flow rule in the inelastic velocity gradient as in shown in equation (22). In this case, the NR procedure is relatively straight forward. Essentially, the NR scheme evaluates the shearing rates based upon quantities at the end of the time step. To accomplish this, the method requires a level function $f^{(\alpha)}$ over which to minimize a weighted error function, and an initial guess vector for all the shearing rates [87]. The increment on the shearing rates is then calculated as,

$$\Delta\dot{\gamma}^{(\beta)} = -\mathbf{J}^{-1} f^{(\alpha)} \tag{57}$$

$$J_{\alpha\beta} = \frac{\partial f^{(\alpha)}}{\partial\dot{\gamma}^{(\beta)}} \tag{58}$$

where **J** is the Jacobian matrix and indicates the rate of change in the level function due to changes in the shearing rates thus providing the direction of minimum error for the next guess. There are several types of error functions that can be used, however a weighted least-squares error function is typically employed since it is a scalar that can be readily compared to a user defined error criterion. This allows easy implementation on multivariate problems and is also continuous and differentiable,

$$\mathrm{E} = \frac{1}{N_{slip}} \sqrt{\sum_{\alpha=1}^{N_{slip}} \left(\frac{\dot{\gamma}^{(\alpha)}}{\dot{\gamma}_{\max}} f^{(\alpha)} \right)^2} \tag{59}$$

In the case of two flow rules in $\mathbf{L}^{in}$ as in equation (23), the equations of the level function and the NR Jacobian become greatly coupled due to the dependency on the resolved shear stresses of both flow rules, i.e.:

$$\begin{cases} L^p_{ij_{guess}} = f_\gamma \sum_{\alpha=1}^{12} \dot{\gamma}^{(\alpha)}_{\gamma_{guess}} \left(\hat{\mathbf{d}}^{(\alpha)} \otimes \hat{\mathbf{n}}^{(\alpha)} \right)_{t=t_0} + f_{\gamma'} \sum_{\alpha=13}^{24} \dot{\gamma}^{(\alpha)}_{\gamma_{L12_{guess}}} \left(\hat{\mathbf{d}}^{(\alpha)} \otimes \hat{\mathbf{n}}^{(\alpha)} \right)_{t=t_0} \\ F^e_{ij} = F_{ij} \cdot \left(e^{L^p_{ij_{guess}}} \cdot \left(F^p_{ij} \right)_{t=t_0} \right)^{-1} \\ \tau^{(\alpha)} = \sigma^{PK2}_{ij} : \left(F^e_{ij} \cdot s^{(\alpha)}_j \otimes m^{(\alpha)}_j F^{e^{-1}}_{ji} \right) \end{cases} \tag{60}$$

therefore, the next guess for the resolved shear stress on slip system α is a function of the guesses of both of the flow rules over all the remaining slip systems. This adds two significant complications to the NR procedure. First, to ensure convergence one cannot impose arbitrary guesses on the shearing rates of one phase without having a proper estimate of the shearing rates of the other phase at hand. Since the shearing rates of both material phases depend on the resolved shear stresses, then the guess on one slip system on a given material phase must be constrained by some function of the remaining slip systems of both materials. Second, the Jacobian of the NR scheme cannot be easily derived. The flow rules depend on each other because of the resolved shears stresses but also because of the evolution of dislocation densities at the γ/γ' interfaces which affect the deformation of the γ' phase. Due to this coupling, the level function $f^{(\alpha)}$ will have cross-derivatives of the shearing rates of both flow rules which are not easy to obtain, i.e.:

$$\frac{\partial\dot{\gamma}_{\gamma}^{in(\alpha)}}{\partial\dot{\gamma}_{L1_2}^{in(\beta)}} \text{ and } \frac{\partial\dot{\gamma}_{L1_2}^{in(\alpha)}}{\partial\dot{\gamma}_{\gamma}^{in(\beta)}} \tag{61}$$

To overcome these challenges, we propose a new quasi-Newton method that uses a sub-set of the Jacobian matrix and constrains the guesses on each iteration based on a flip-flop logic that can adequately account for the coupling in all these equations.

Let $f^{(\alpha)}$ be a level function for the α^{th} slip system such that $f^{(\alpha)}$ is derivable by $\dot{\gamma}_{\gamma}^{in(\alpha)}$ and $\dot{\gamma}_{L1_2}^{in(\alpha)}$. Then a row in the NR system of equations for the α^{th} system is of the form:

$$\frac{\partial f^{(\alpha)}}{\partial\dot{\gamma}_{\gamma}^{in(1)}}\Delta\dot{\gamma}_{\gamma}^{in(1)}+\ldots+\frac{\partial f^{(\alpha)}}{\partial\dot{\gamma}_{\gamma}^{in(12)}}\Delta\dot{\gamma}_{\gamma}^{in(12)}+\frac{\partial f^{(\alpha)}}{\partial\dot{\gamma}_{L1_2}^{in(13)}}\Delta\dot{\gamma}_{L1_2}^{in(13)}+\ldots+\frac{\partial f^{(\alpha)}}{\partial\dot{\gamma}_{L1_2}^{in(24)}}\Delta\dot{\gamma}_{L1_2}^{in(24)} = f^{(\alpha)} \tag{62}$$

From this equation, it can be seen that the system of equations of the Newton-Raphson scheme can be partitioned into the following sub-matrices,

$$-\begin{bmatrix} \left[\dfrac{\partial f^{(\alpha)}}{\partial\dot{\gamma}_{\gamma}^{in(\beta)}}\right] & \left[\dfrac{\partial f^{(\alpha)}}{\partial\dot{\gamma}_{L1_2}^{in(\zeta)}}\right] \\ \left[\dfrac{\partial f^{(\omega)}}{\partial\dot{\gamma}_{\gamma}^{in(\beta)}}\right] & \left[\dfrac{\partial f^{(\omega)}}{\partial\dot{\gamma}_{L1_2}^{in(\zeta)}}\right] \end{bmatrix} \begin{Bmatrix} \left[\Delta\dot{\gamma}_{\gamma}^{in(\beta)}\right] \\ \\ \left[\Delta\dot{\gamma}_{L1_2}^{in(\zeta)}\right] \end{Bmatrix} = \begin{Bmatrix} \left[f^{(\alpha)}\right] \\ \\ \left[f^{(\omega)}\right] \end{Bmatrix} \quad \text{with} \quad \begin{matrix} \alpha = 1\ldots12 \\ \omega = 13\ldots24 \\ \beta = 1\ldots12 \\ \zeta = 13\ldots24 \end{matrix} \tag{63}$$

In this partitioned matrix, the α rows are associated to the level functions of the γ phase, while the ω rows with the level functions for the γ'. This distinction in notation helps visualizing what terms of the formulation can be associated to each material phase. In this formulation, there exists one error function of the form of equation (59) which will have the added errors on the guesses of both material phases.

$$\mathrm{E} = \frac{1}{24}\sqrt{\sum_{\alpha=1}^{12}\left(\frac{\dot{\gamma}_{\gamma}^{in(\alpha)}}{\max\left(\left|\dot{\gamma}_{\gamma}^{in(\alpha)}\right|\right)} f_{\gamma}^{(\alpha)}\right)^2 + \sum_{\omega=13}^{24}\left(\frac{\dot{\gamma}_{L1_2}^{in(\alpha)}}{\max\left(\left|\dot{\gamma}_{L1_2}^{in(\alpha)}\right|\right)} f_{\gamma'}^{(\omega)}\right)^2} \tag{64}$$

If the cross-derivatives in the Jacobian were easy to obtain, then the process would follow a regular NR method. However, due to the tensorial form of the resolved shear stresses and the intricate dependency on the dislocation densities, determining these derivatives becomes a formidable task. The essence of our algorithm consists of splitting the problem into two distinct parts constrained by a flip-flop logic on two different error surfaces, one for each material phase instead of one. If an error surface diverges then the NR step is flopped from one material phase to the other. We start by proposing two sets of systems of equations in which there exist two types of error functions and two types of level functions, one for each material phase, and in which the cross-derivatives are ignored,

$$-\sum_{\beta=1}^{12}\frac{\partial f^{(\alpha)}}{\partial\dot{\gamma}_{\gamma}^{in(\beta)}}\Delta\dot{\gamma}_{\gamma}^{in(\beta)}=f^{(\alpha)}\left(\dot{\gamma}_{\gamma}^{in(\alpha)},\tau^{(\alpha)}\right),\ \text{with}\ \alpha=1...12 \tag{65}$$

$$-\sum_{\beta=13}^{24}\frac{\partial f^{(\omega)}}{\partial\dot{\gamma}_{L1_2}^{in(\beta)}}\Delta\dot{\gamma}_{L1_2}^{in(\beta)}=f^{(\omega)}\left(\dot{\gamma}_{\gamma}^{in(\omega)},\tau^{(\omega)}\right),\ \text{with}\ \omega=13...24 \tag{66}$$

The role of the Jacobian in the NR method is to provide the direction of the minimum error and therefore its precision only determines the rate of convergence of the iterative process and does not affect the accuracy a NR step. Therefore, it is possible to propose an approximation of the Jacobian without sacrificing the accuracy of the solution.

Like is done for the level functions, it is assumed that there are two distinct error functions for each material phase,

$$\mathrm{E}_{\gamma}=\frac{1}{12}\sqrt{\sum_{\alpha=1}^{12}\left(\frac{\dot{\gamma}_{\gamma}^{in(\alpha)}}{\max\left(\left|\dot{\gamma}_{\gamma}^{in(\alpha)}\right|\right)}f_{\gamma}^{(\alpha)}\right)^{2}} \tag{67}$$

$$\mathrm{E}_{L1_2} = \frac{1}{12}\sqrt{\sum_{\omega=13}^{24}\left(\frac{\dot{\gamma}_{L1_2}^{in(\alpha)}}{\max\left(\left|\dot{\gamma}_{L1_2}^{in(\alpha)}\right|\right)}\, f_{\gamma'}^{(\omega)}\right)^2} \tag{68}$$

Under these assumptions, these systems of equations remain coupled because of the level functions' dependency on the resolved shear stresses and dislocation densities. It is very important that no approximations are made on the level functions because the level functions need to converge to a unique and accurate solution space. By splitting the problem into two parts, we have greatly simplified the mathematics but have lost significant amount of information regarding the direction that will take the next iteration to the minimum error, this loss will often impede convergence. To complement for this a flip-flop logic is adhered to the error functions. A flow diagram of this logic applied to our problem is presented in Figure 83,

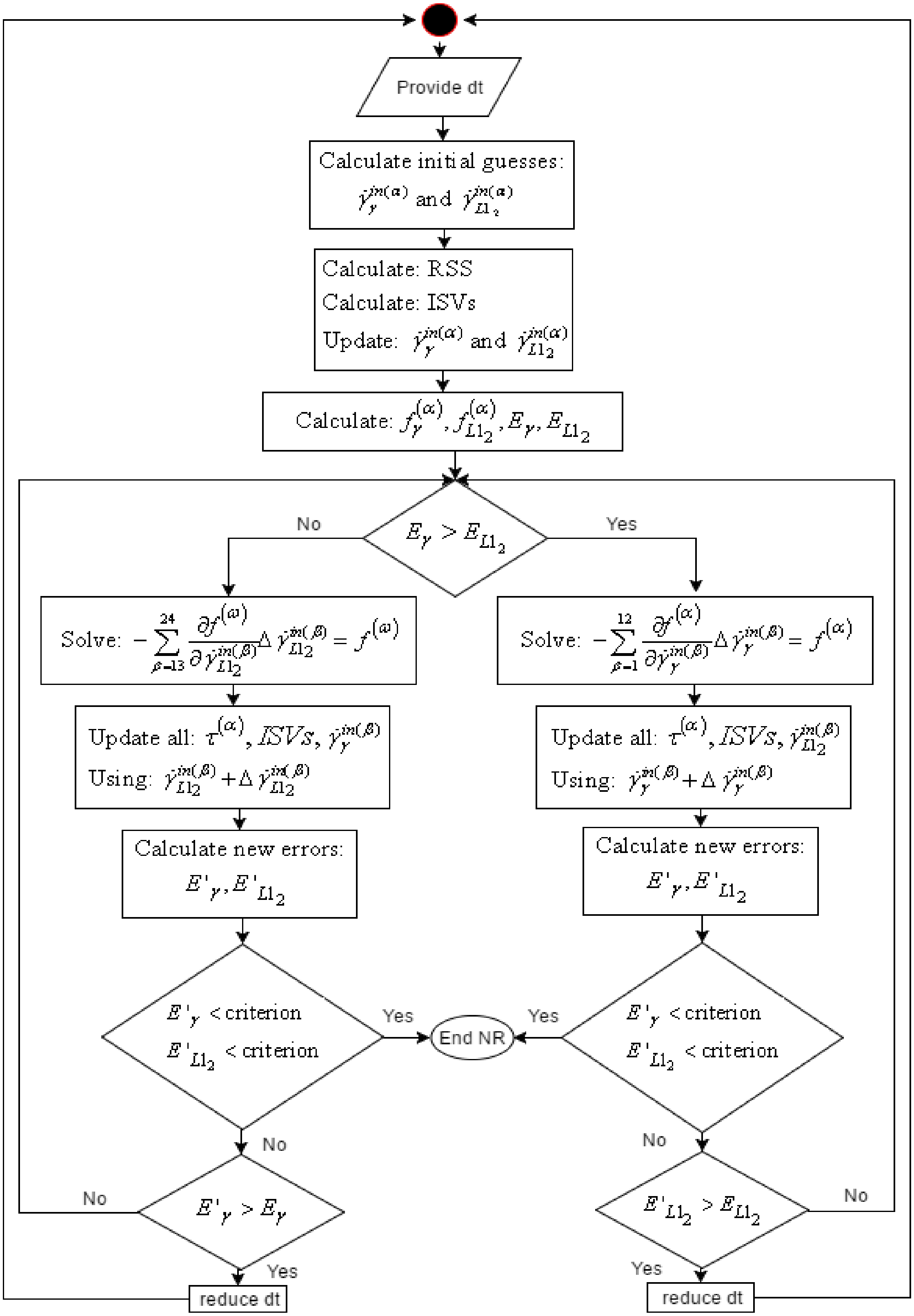

Figure 83: Flow diagram of the quasi-Newton Raphson method

We start by evaluating both shearing rates for the current time step and we use those values as the initial guesses of the NR iterations. Equation (60) is then used to update the resolved shear stresses (RSS) and the ISVs with the corresponding time increment. Then both shearing rates are updated using these values and equations (67) and (68) are used to calculate the error on both phases. Subsequently a NR step, either equation (65) or (66), is taken on the phase that resulted with the greatest error. The results of each NR iteration are used to update all ISVs and RSS and flow rules, which in turn determine the new errors for both material phases, then the NR step is performed again on the phase with the largest error.

Line search algorithms are used to reduce the number of NR iterations thus achieving greater computational speed [87]. Therefore, a line search algorithm is also incorporated to the model by halving the values of the current iteration of the current NR vector, $\Delta\dot{\gamma}_{\gamma}^{in(\beta)}$ or $\Delta\dot{\gamma}_{L1_2}^{in(\zeta)}$, this procedure is repeated while the error of both material phases keeps decreasing. After each line search iteration, as it is done in the NR iterations, all ISVs, RSS and flow rules are updated and the errors are recalculated to decide on which material phase the next NR step will be performed.

Although the solution space of equations (65) and (66) is 24th dimensional -since there are 12 slip systems for each material phase- the method with the line search algorithm can be exemplified graphically. Let us assume two guesses from the initial time step estimation, we can illustrate these guesses using 2-dimensional subsets of the solution spaces for the $\Delta\dot{\gamma}_{\gamma}^{in(\beta)}$ and $\Delta\dot{\gamma}_{L1_2}^{in(\beta)}$ that result from each Newton-Raphson steps, where the contours are of the error function that is minimized,

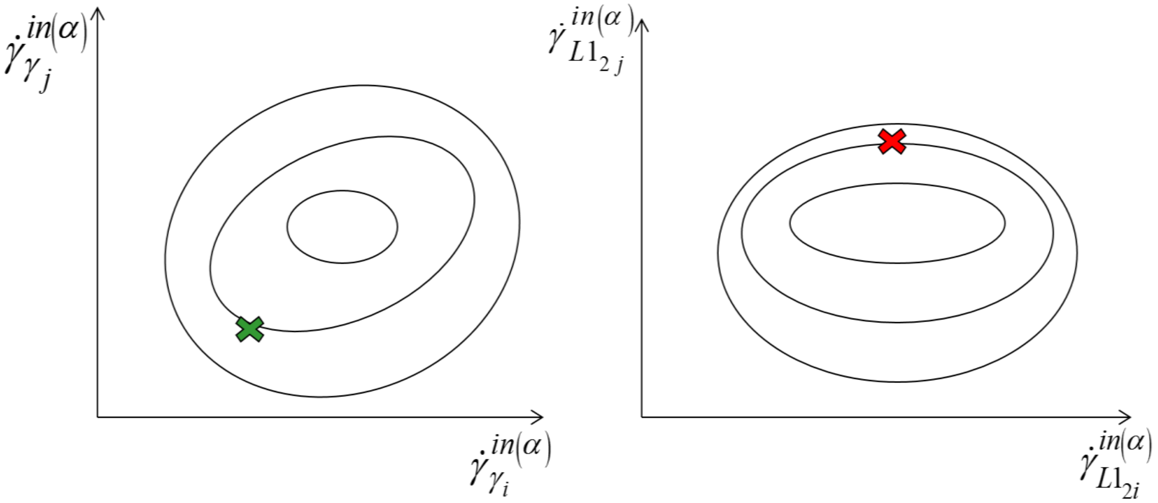

Figure 84: Left: initial guess on the γ phase. Right: initial guess on the γ' phase

with these guesses at hand, we now apply a NR step on the material phase with the greatest error, the γ phase in this case since is farthest away from the minimum contour. The NR method will provide with a vector on the $\dot{\gamma}_{\gamma}^{in(\alpha)}$ solution space that points to the minimum error as shown on Figure 85; after the new values for $\dot{\gamma}_{\gamma}^{in(\alpha)}$ are obtained, all ISVs, RSS and errors are updated. Note that in this schematic, the updates on the γ' phase move the solutions closer to the minimum error, therefore this NR step is acceptable and a line search step is taken next.

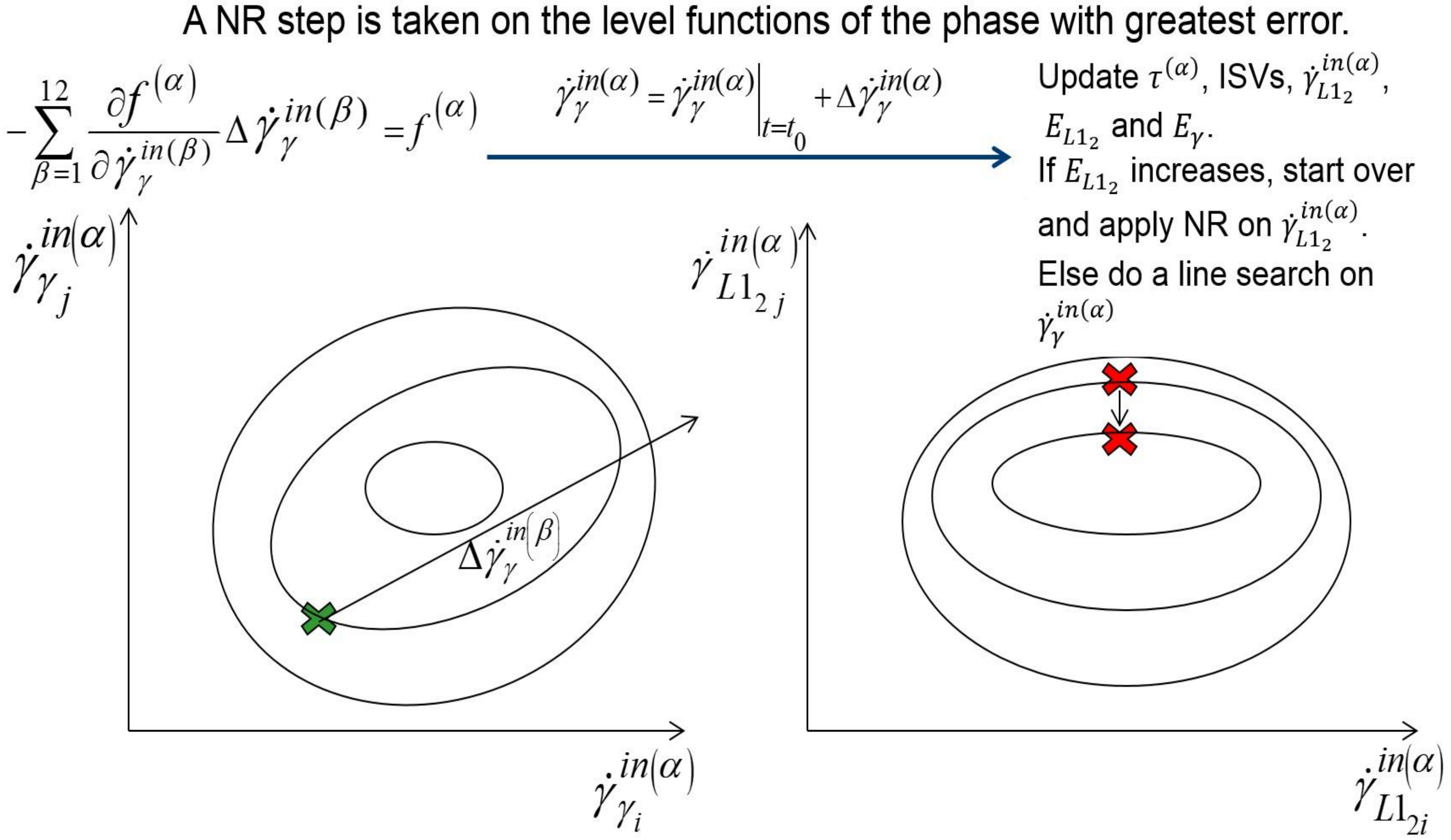

A NR step is taken on the level functions of the phase with greatest error.

$$-\sum_{\beta=1}^{12} \frac{\partial f^{(\alpha)}}{\partial \dot{\gamma}_{\gamma}^{in(\beta)}} \Delta \dot{\gamma}_{\gamma}^{in(\beta)} = f^{(\alpha)}$$

$$\dot{\gamma}_{\gamma}^{in(\alpha)} = \dot{\gamma}_{\gamma}^{in(\alpha)}\Big|_{t=t_0} + \Delta\dot{\gamma}_{\gamma}^{in(\alpha)}$$

Update $\tau^{(\alpha)}$, ISVs, $\dot{\gamma}_{L1_2}^{in(\alpha)}$, E_{L1_2} and E_{γ}.

If E_{L1_2} increases, start over and apply NR on $\dot{\gamma}_{L1_2}^{in(\alpha)}$.

Else do a line search on $\dot{\gamma}_{\gamma}^{in(\alpha)}$

Figure 85: Left: a Newton-Raphson step has been taken on the level function of the γ phase. Right: updated error

By careful inspection of Figure 85, it can be seen that the NR step has overestimated the magnitude of the vector that takes the solution to the minimum error, in fact a value closer to half the magnitude depicted in the figure is closer to the minimum. The line search algorithm proposed by McGuinty [87] halves the current Newton-Raphson vector several times until it becomes of such length that the its end point is the closest to the minimum error as shown in Figure 86. All ISVs, RSS, flow rules and errors must be updated after every time the Newton-Raphson vector is halved. After each update, the errors of both material phases could remain the same, decrease or increase. The line search is carried out on the current Newton-Raphson step, in this case in the γ phase, for as long as the error in the current step keeps decreasing and while each update does not increase the error on one or both of the material phases. If any of the errors increases, as shown in Figure 86, the current NR or line search iteration is reversed and a new NR step is taken on the material phase with the greatest error as shown in Figure 87.

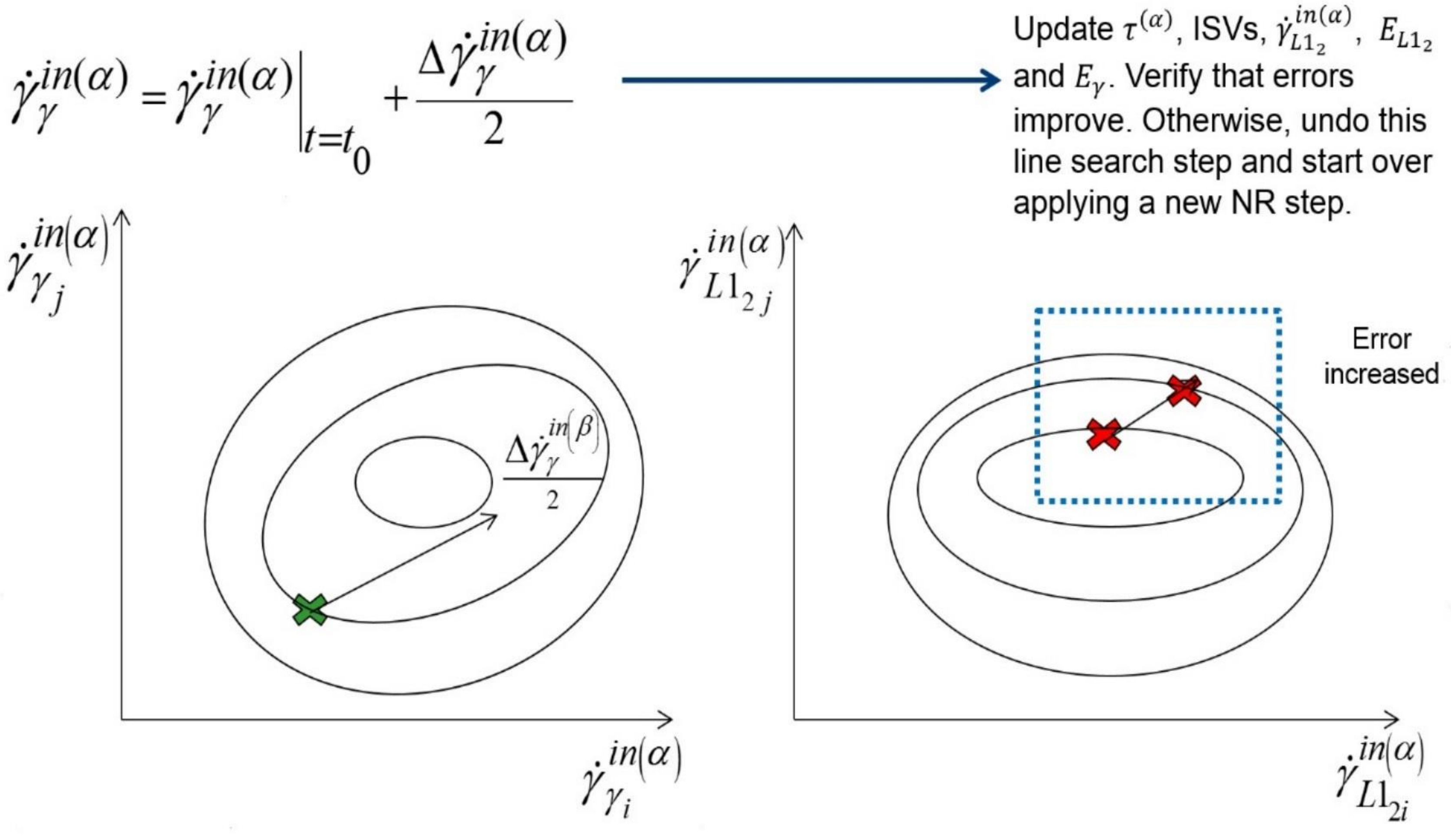

$$\dot{\gamma}_{\gamma}^{in(\alpha)} = \dot{\gamma}_{\gamma}^{in(\alpha)}\Big|_{t=t_0} + \frac{\Delta\dot{\gamma}_{\gamma}^{in(\alpha)}}{2}$$

Update $\tau^{(\alpha)}$, ISVs, $\dot{\gamma}_{L1_2}^{in(\alpha)}$, E_{L1_2} and E_{γ}. Verify that errors improve. Otherwise, undo this line search step and start over applying a new NR step.

Figure 86: Left: a line search step has been taken on the current NR of the γ phase. Right: updated error

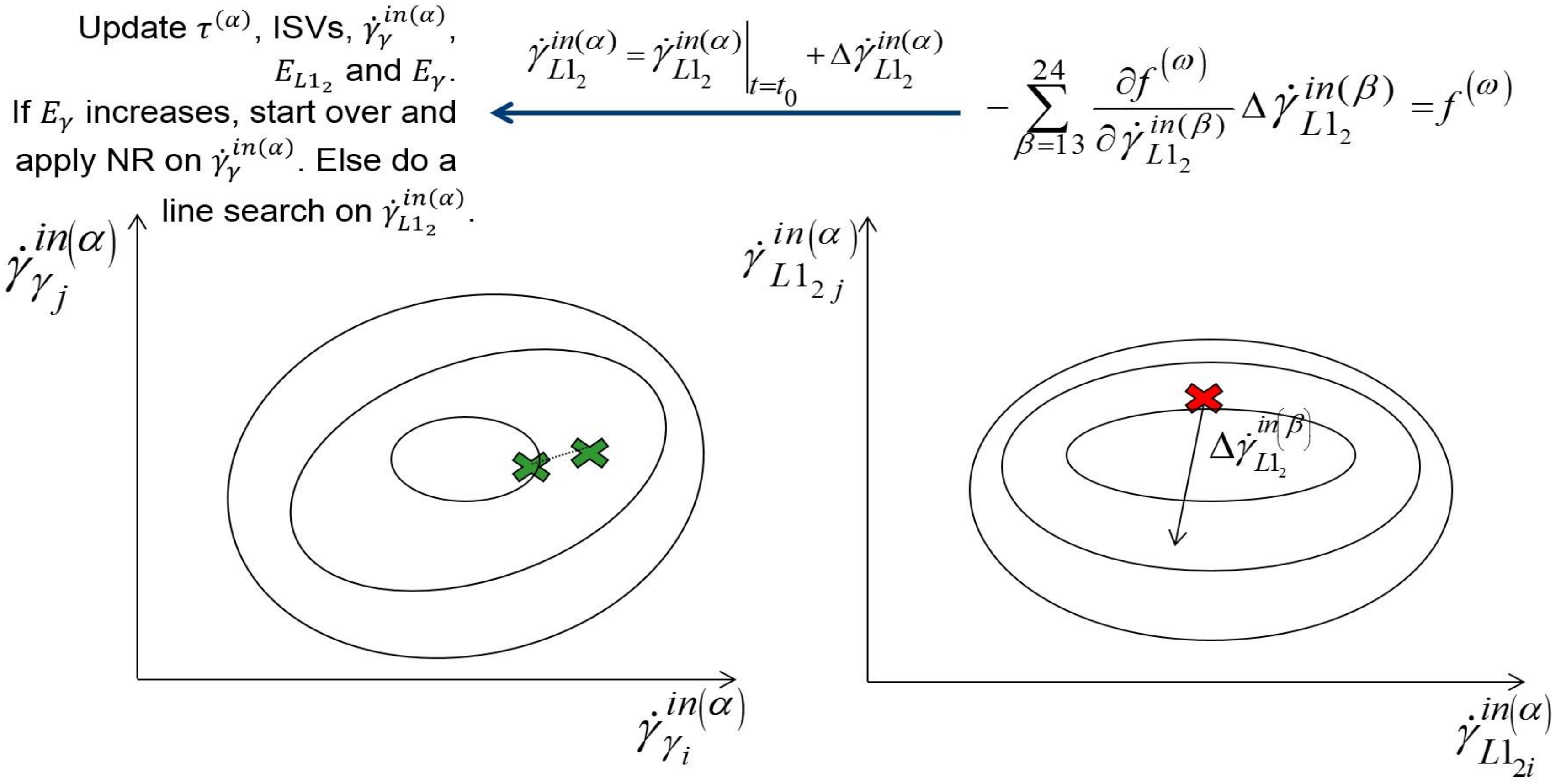

Figure 87: A new NR step is taken on the phase farthest away from the minimum error, in this case the γ' phase. Right: a Newton-Raphson step has been taken on the γ' phase. Left: updated error

In essence, the proposed Quasi-Newton method with line search algorithm can be summarized in three broader directives:

- A NR step is always performed on the set of level functions with the greatest error.
- A NR step on the level functions of material phase *"A"* is flopped to a NR step on levels of material phase *"B"* every time a NR step or line search step applied on level function *"A"* increases the error on level function *"B"*.
- If a NR step or line search increases the error on one or both material phases, then the process is restarted with a decreased time increment.

6.2.2 Verification of the quasi Newton-Raphson algorithm

In order to verify the accuracy of the proposed quasi Newton-Raphson algorithm, the 1-D stress-based model implementation was adapted as a 3-dimensional displacement-based model in ABAQUS. A UMAT of the constitutive model using material parameters in Table 10 and Table 11 was developed. In this displacement-base routine, a single element with reduced-order integration (shown in Figure 88) was employed to prevent the lattice rotation from taking place. The boundary conditions and loading applied to the single element are shown in Figure 89, where a uniform distributed pressure is applied on the top surface of the element. With this setting, ABAQUS calculates the required nodal forces at the top nodes for the top surface of the element to experience a uniform pressure. These conditions become equivalent to prescribing a constant applied stress and makes the set-up comparable to the 1-D stress-based simulation.

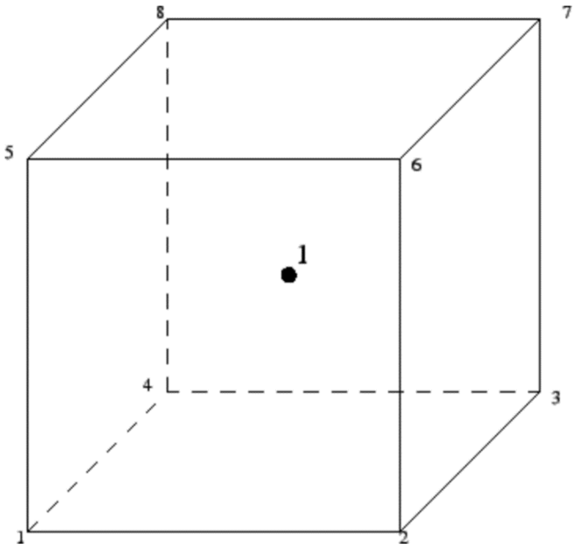

Figure 88: 1x1x1 integration point hexahedral element [114]

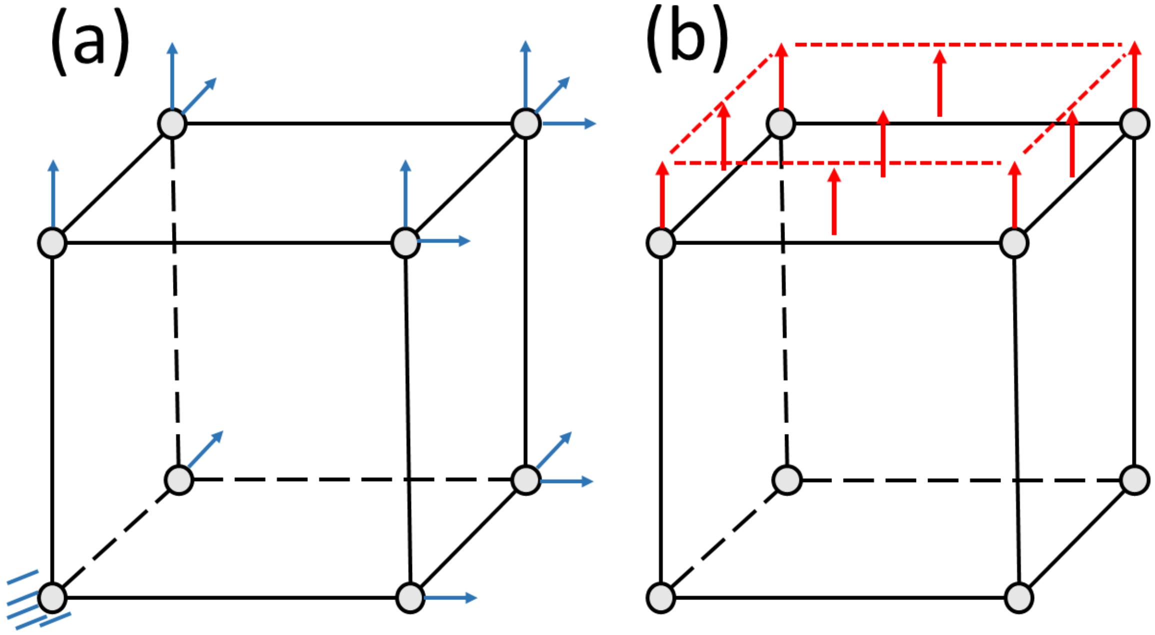

Figure 89: Boundary conditions used in a single-element representative volume element:

(a) allowed nodal displacements (b) uniformly distributed pressure

The creep cases that were run using the 1-D stress-based formulation were re-simulated using the displacement-based UMAT. As seen in sample plots in Figure 90, no visible difference was observed between the 1-D stress-based implementation and the 3-D displacement-based implementation which serves to show that the algorithm arrives an accurate and unique solution.

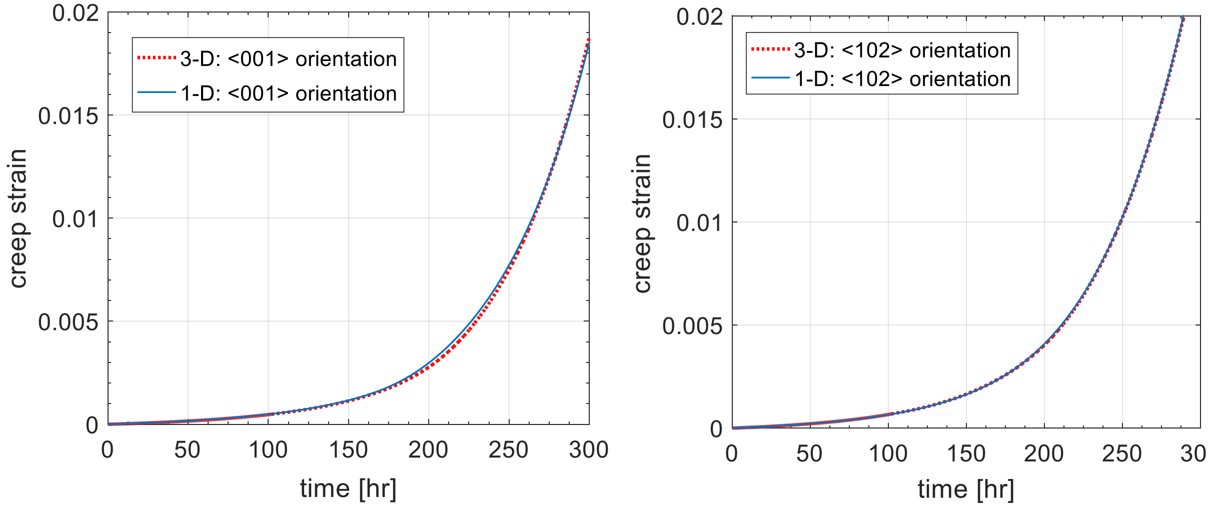

Figure 90: Verification of displacement based Newton-Raphson algorithm solution with respect to 1-D stress-based implementation: creep simulations at 950°C and 250 MPa on different crystallographic orientations

Knowing that the quasi Newton-Raphson provides accurate solutions, the displacement-based formulation can be used to assess whether ignoring the lattice rotation in the 1-D simulations introduces significant error. This assessment exercise is particularly important if one considers the additional computational expense of running the 3-D model in comparison with its 1-D counterpart. Whereas the 1-D model provides practically instantaneous results using one 2.41GHz processor, the 3-D routine, using the same processor and a single element in ABAQUS, can use up to three hours of computation, depending on the loading conditions. Moreover, due to its simplicity, the 1-D model is easier to implement and to modify if needed because it uses explicit integration schemes. Conversely in the 3-D model, changes in the flow rules or in the evolution equations require updating the equations used in the NR Jacobian which are not simple to derive and debug. Therefore, provided that the 3-D effects do not affect the solutions significantly, there is enough incentives to use the 1-D creep model for rapid exploration of changes in the creep performance due to changes in the microstructure.

A solid displacement-based element with eight integration points is used to simulate creep using boundary conditions shown in Figure 89,

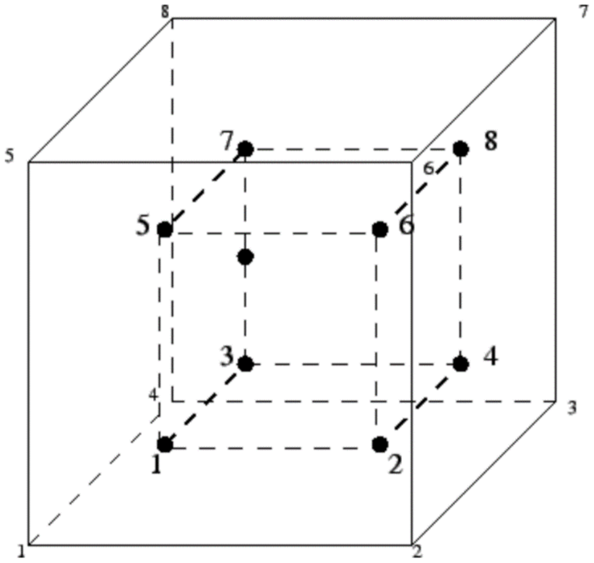

Figure 91: 2x2x2 integration point hexahedral element [114]

Two loading conditions were tested at four different crystallographic orientations. One loading condition was at low temperature with significant primary creep and another one at higher temperature where tertiary creep is dominant, these conditions are plotted in Figure 92 and Figure 93,

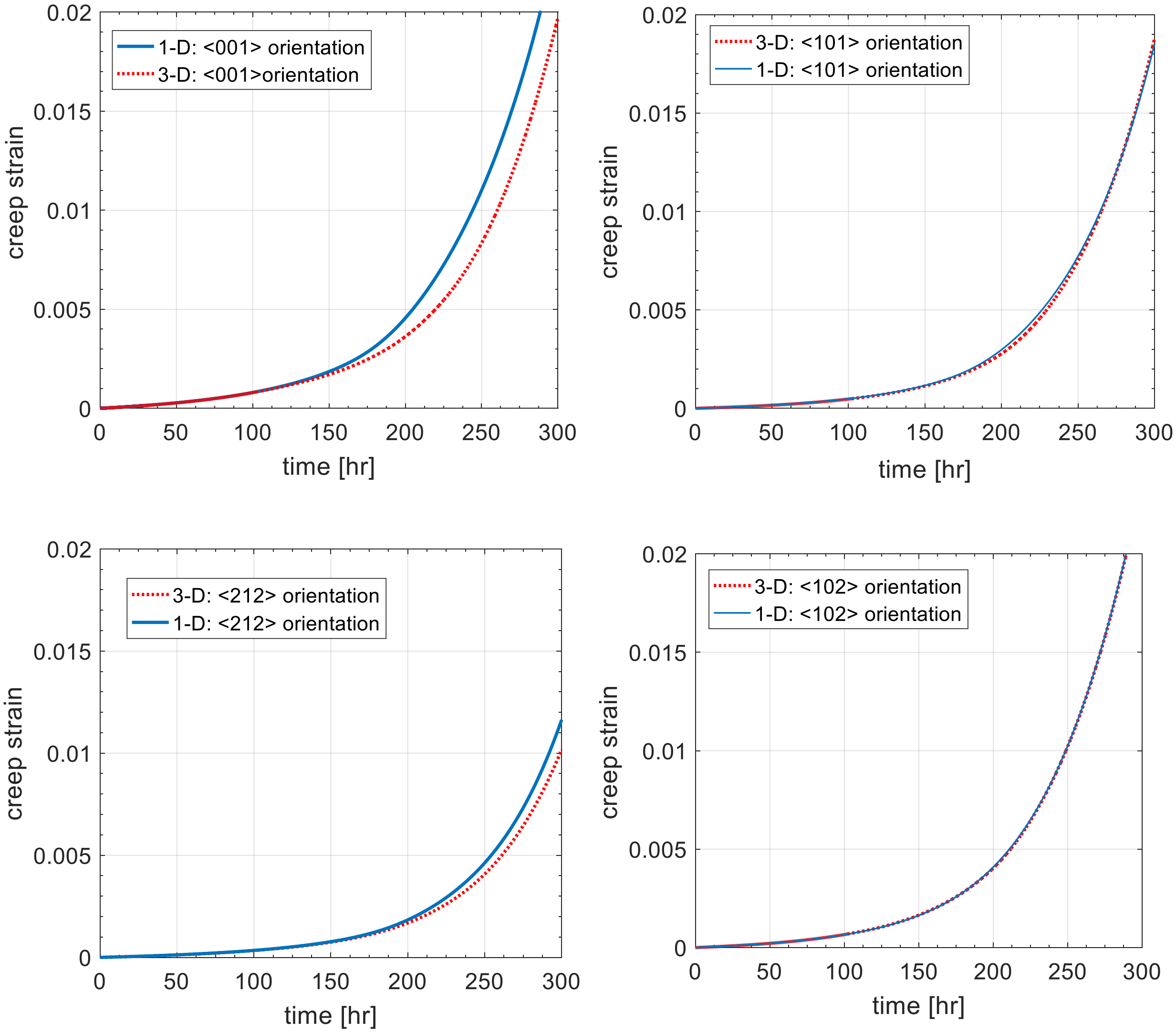

Figure 92: Influence of 3-dimensional effects on creep simulations at 950°C and 250 MPa

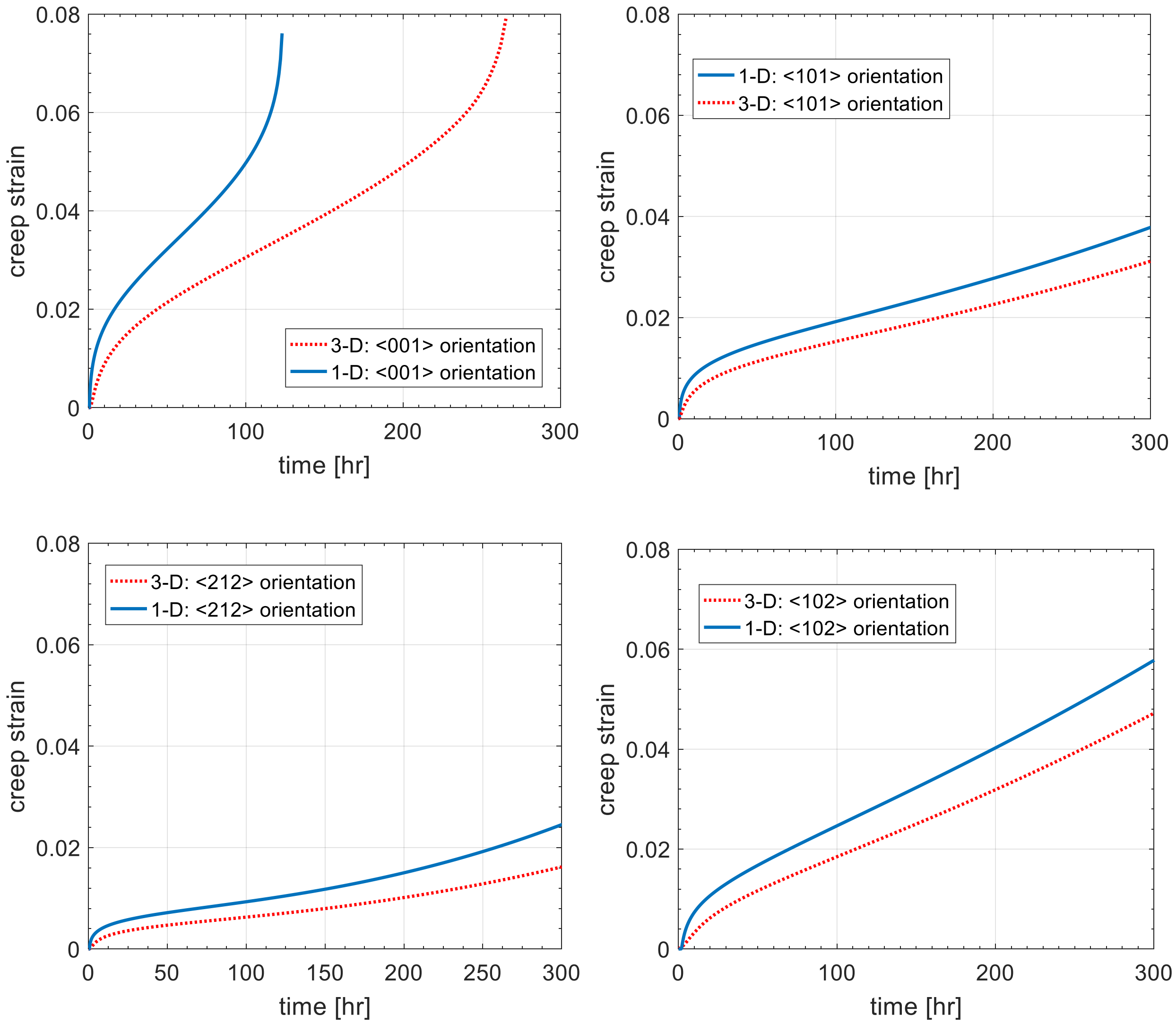

Figure 93: Influence of 3-dimensional effects on creep simulations at 850°C and 650 MPa

It can be seen from these figures that most of the effect is seen at lower temperatures which sustain primary creep. This could be explained by the higher stresses at lower temperatures which induce more lattice rotation. Although there are differences between the models, the extra level of analysis did not provide any insights that could not be derived using the simpler 1-D model. Therefore, 1-D physically-based microstructure-sensitive stress-based creep models like the one presented in this work can become very practical tools for alloy development. These models can rapidly provide important insights on changes in the mechanical response due to changes in microstructure and material parameters.

6.3 Strain rate sensitivity exponent

It was found during the calibration of the 3-D model implementation that a strain rate sensitivity exponent was needed in the flow rule of the γ channels to be able to capture the creep-fatigue interactions. Without this additional term the CVP model is only successful at modeling the rate dependent regime and an inadequate relationship between yield strength and creep relaxation is observed. Several other authors in the literature assume a strain sensitivity exponent in their flow rule when modeling monotonic loading and fatigue cycles [5, 19, 20, 91, 108, 115].

When the strain sensitivity exponent is equal to zero, one cannot independently calibrate for the yield strength and for the creep relaxation. As shown in Figure 94, increasing the yield strength also decreases the amount of creep relaxation,

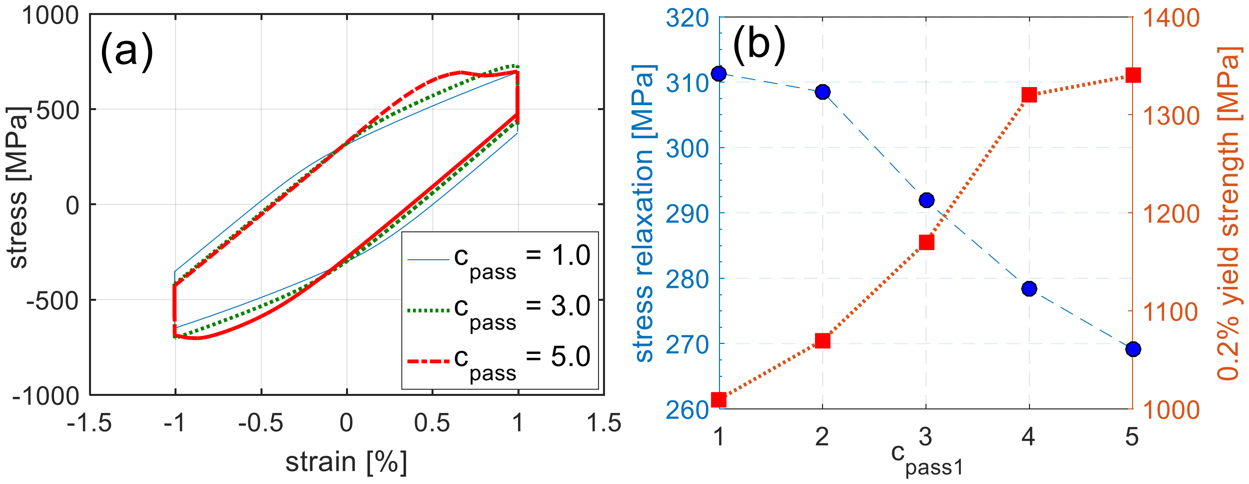

Figure 94. Sensitivity of c_{pass} when n = 0: (a) effect on the hysteresis loop (b) effect on stress relaxation and on yield strength

As a matter of illustration, consider adjusting the strengthening parameters in the flow rule in equation (24) with *n* equal to zero, i.e. there is no strain rate sensitivity term. One can adjust the strengthening in the alloy by directly calibrating the passing stress which is a function of the dislocation density and of c_{pass11}. Because of the relationship dislocation density holds with other material phases, adjusting the material parameters in the dislocation density evolution equations could lead to undesirable results, therefore adjusting c_{pass11} becomes preferred because the effect on the hardening is targeted. In Figure 94 we have plotted the first complete hysteresis for different values of c_{pass11} when *n* is zero at 750°C. Note that increasing c_{pass11} increases both the yield strength and the resistance to creep relaxation reflected by a significant reduction in the amount of relaxed stress. While calibrating the model at higher temperatures, it became challenging to obtain the correct value of yield strength without almost eliminating the stress relaxation, conversely it was also challenging to obtain the correct amount of stress relaxation without severely lowering the resultant yield strength. This is very undesirable since both of these determine the plastic strain range and the mean stress in the hysteresis which is an important metric used in design and in life models. Therefore, a strain-rate sensitivity term is needed in the flow rule. In this work we have adopted Tinga, Brekelmans and Geers power law formulation for the strain sensitivity term [5],

$$\dot{\gamma}_\gamma^{in(\alpha)} = \dot{\gamma}_0 \left(\frac{\tau_{eff_\gamma}^{(\alpha)}}{\kappa_\gamma^{(\alpha)}}\right)^n \left\{1-\exp\left(-\frac{\tau_{eff_\gamma}^{(\alpha)}}{\tau_{oro}^{(\alpha)}}\right)\right\}^m sign\left(\tau_{eff_\gamma}^{(\alpha)}\right) \tag{69}$$

which is adapted to the flow rule in this research as,

$$\begin{aligned}\dot{\gamma}_\gamma^{in(\alpha)} = \rho_\gamma^{(\alpha)} b \lambda_\gamma^{(\alpha)} F_{attack} \Theta\left(T,\xi\right)\left(\frac{\tau_{eff_\gamma}^{(\alpha)}}{\kappa_\gamma^{(\alpha)}}\right)^n \\ \exp\left(\frac{-Q_{slip}^{110}+\left(\left|\tau_{eff_\gamma}^{(\alpha)}\right|-\kappa_\gamma^{(\alpha)}\right)V_{c1}^{(\alpha)}}{kT}\right) sign\left(\tau_{eff_\gamma}^{(\alpha)}\right)\end{aligned} \tag{70}$$

The problem in calibrating without the strain sensitivity exponent raises from to the inability of independently calibrating the flow rule for the strain-rate independent and the strain-rate dependent regime. In Figure 95, the flow rule has been evaluated for a fixed microstructure state over a range of resolved shear stresses at 1100°C and with *n* equal to zero,

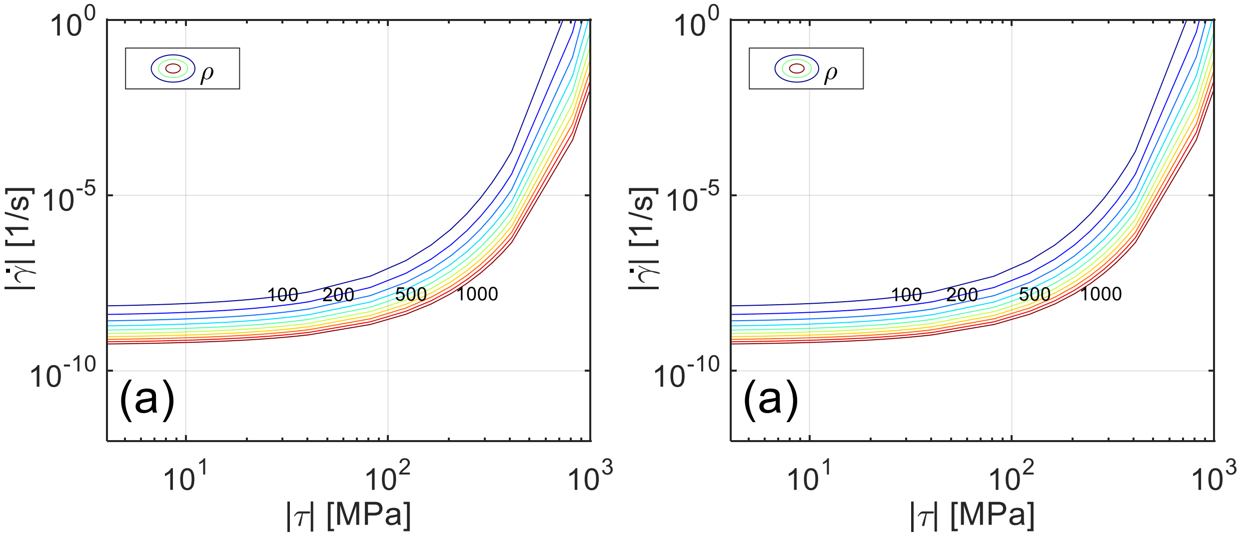

Figure 95. Sensitivity of the flow rule to (a) dislocation density in 1x10^9 [1/m^2] and to (b) c_{pass11} at 1100°C for n = 0

It can be seen that changes in dislocation density and in c_{pass11} only translate the curves but do not change the slope in the curves. The ability to tilt the curve by changing the slopes is necessary to be able to independently adjust for the strain-rate sensitive and strain-rate insensitive regime. As shown in Figure 96, during the calibration it was found that out of all parameters, only the strain-rate sensitivity exponent was able to provide this tilt,

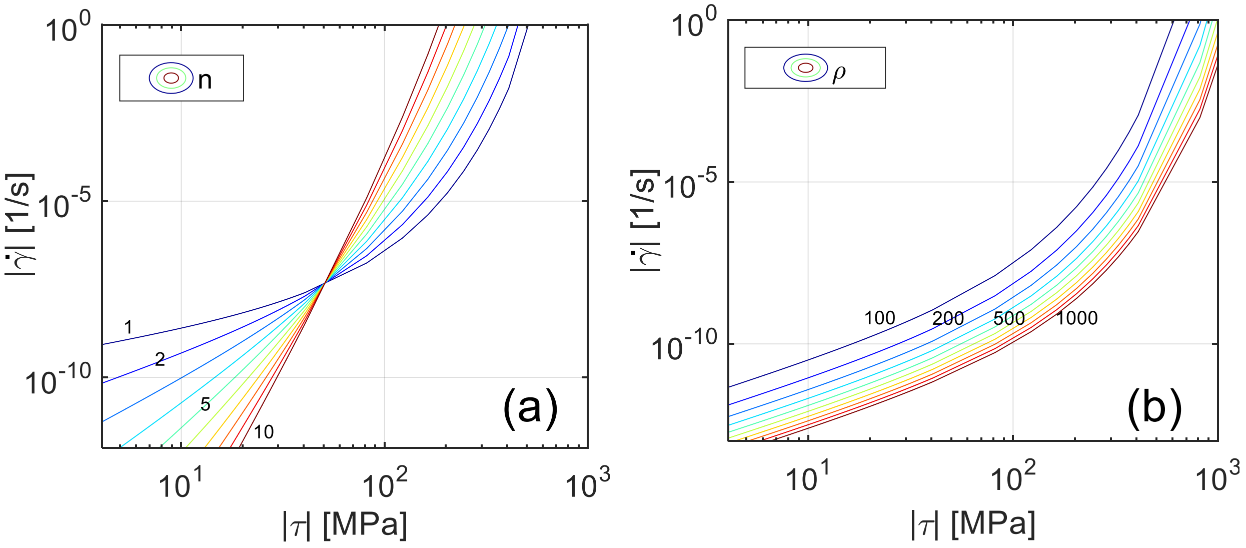

Figure 96 Effect the strain rate sensitivity at 1100°C: (a) Flow rule sensitivity to n and to (b) dislocation density in $1x10^{9}$ [$1/m^{2}$] for n= 2

Once an adequate level of tilt is obtained, the remaining parameters in the model can be adjusted using the calibration procedure outlined in the following section.

6.4 Three-dimensional model parameter adjustment and model verification

The 1-D model implementation is different from the 3-D implementation of the model. In the 1-D implementation the backstress was not exercised since in the studied stress-based creep cases there were no reversals of the load. Moreover, in the 1-D model, in order to simplify the integration procedure and to allow for rapid implementation, the effect of the lattice rotation was not considered since this can only be calculated by implicit time integration of the deformation gradient. Additionally, the material parameters used in the 1-D model implementation presented in Table 11 were obtained using solely creep data. As a result of these simplifications, the parameters in Table 11 need to be adjusted to best describe creep-fatigue and thermomechanical fatigue cycles. In this section, some of the model parameters presented in Table 11 will be adjusted using creep-fatigue cycle experimental data.

The creep-fatigue testing data was used to determine the 3-D model material parameters while the TMF and LCF data was used for validation of the material parameters. Creep-fatigue experiments have been shown to be efficient in providing enough amount of information to calibrate plasticity models [110]. The physical parameters (parameters that can be determined via first principles or via experiments) in the 3-D implementation of the model were not changed with respect to those parameters used in the 1-D model. However, out of a total of twenty-nine material parameters, twelve parameters had to be adjusted; these are shown in Table 12 and are compared to the values obtained for the 1-D model. A set of parameters that universally fitted the 3-D and 1-D models could not be found.

Table 12: Parameters that require adjustment to account for creep-fatigue deformation

1-D model		3-D model	
c_{annh2}	10.0	c_{annh2}	5.0
c_{Fdis}	0.1	c_{Fdis}	1.0
c_{mult1}	$3x10^{-4}$	c_{mult1}	$3x10^{-5}$
c_{pass11}	1.4	c_{pass11}	3.0
C_{χ}	Not used: 0	C_{χ}	$1x10^{2}$
c_{pass21}	$1.5x10^{-2}$	c_{pass21}	$3\ x10^{-3}$
c_{vc2}	$7.5x10^{-1}$	c_{vc2}	$8.4x10^{-1}$
κ	Not used: 0	κ	$1x10^{6}$
N	Not used: 0	n	2
η_0	Not used: 0	η_0	20.0
Q_{slip}^{110}	300 [*kJ/mol*]	Q_{slip}^{110}	295 [*kJ/mol*]
Q_{slip}^{112}	180 [*kJ/mol*]	Q_{slip}^{112}	240 [*kJ/mol*]

The changes required in the material parameters for the 3-D model are within an order of magnitude or less from those of the 1-D model implementation. These changes are reflective of terms in the model that are potentially affected by creep-fatigue loading in 3-D. The material parameters in Table 12 were adjusted using creep-fatigue hysteresis data at 1100°C and at 650°C. The remaining creep-fatigue hysteresis at the intermediary temperatures were used to verify that the selected parameters worked well at intermediate temperatures. Although close to

30 parameters are used in this CVP model, only a subset of these is very sensitive to changes thus easing the burden of recalibrating the model to other Ni-base superalloys. As is shown in Figure 97, the calibrated parameters used in this model result in simulations that are in good agreement with the experimental data,

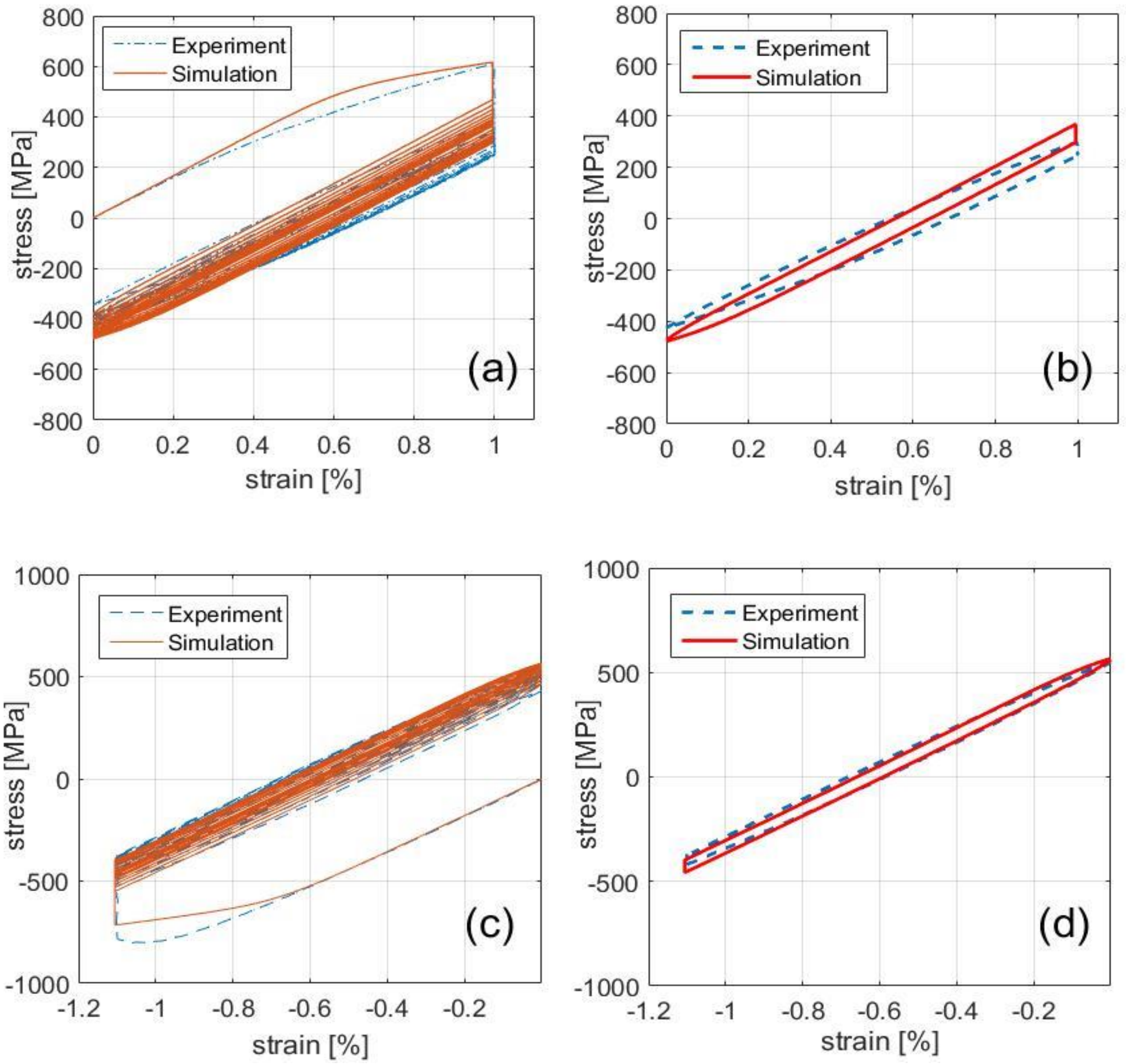

Figure 97. Calibrated model: (a) fist ten cycles (b) stabilized hysteresis of creep-fatigue at 1025°C and strain rate of 1x10^{-3} [1/s] with 3 minute holds at maximum tension. (c) fist ten cycles (d) stabilized hysteresis of creep-fatigue at 950°C and strain rate of 1x10^{-3} [1/s] with 3 minute holds at maximum compression

Note that the model not only readily estimates the stabilized hysteresis but also provides good estimations of important features in the deformation such as the yield strength, amount of stress relaxation and amount of cyclic creep and therefore the stress evolution is also predicted.

6.5 Model validation and damage parameter verification

The model was exercised to validate its application outside of the creep-fatigue conditions that were used to calibrate it. The model predicts very well for isothermal strain-controlled LCF and TMF test conditions; the validation plots are seen in Figure 98,

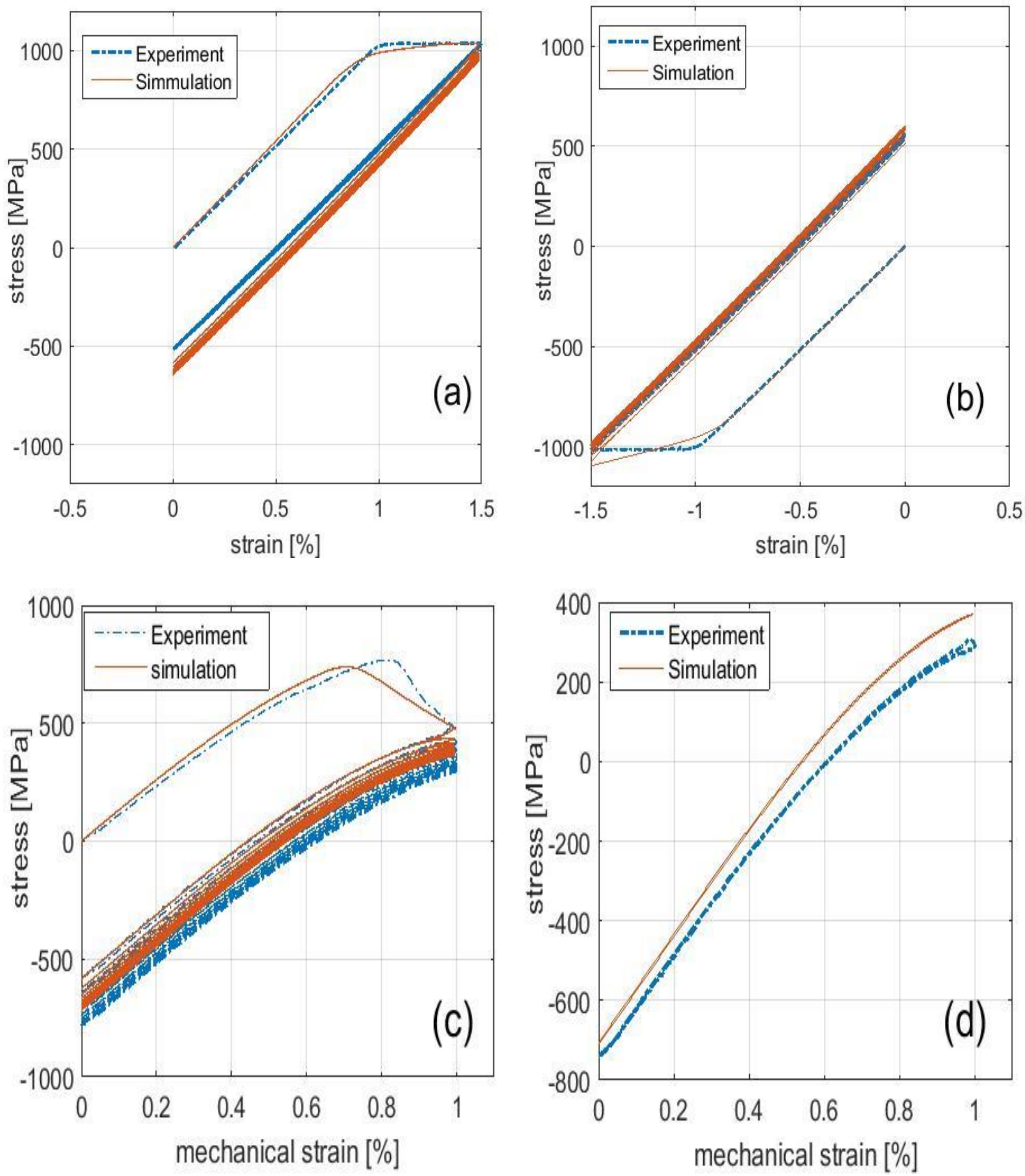

Figure 98. Calibrated model: (a) and (b) isothermal fatigue at 750°C with strain rate of $1x10^{-3}$ [1/s]. (c) and (d) Cycles 1 through 10 and stabilized hysteresis respectively of in-phase TMF test from 100°C to 1050°C with heating rate of 2.83 [°K/s]

Note that this model can predict the cyclic creep that takes place during the first few cycles of TMF and lack of thereof during the first few cycles of the isothermal fatigue at lower temperatures. Another important feature of this model is the damage parameter, which is verified using the 3-dimensional UMAT simulation against experimental creep-fatigue response and life data.

As the damage parameter increases there is significant non-linearity introduced in the equations thus the computational demand increases. To avoid a long simulation, the creep-fatigue in Table 4 conducted at 750°C with 20 minute holds both at maximum tension and compression with a strain range of 2%, a strain rate of $1x10^{-3}$ (1/s) and strain ratio (R) of -1 a was used. This specimen had a life of 16 cycles. This test condition was simulated and the damage parameter was used as a failure criterion. The simulation was requested to stop if the damage parameter for the next iteration reached a critical level of 50% or if the non-linearity of the current iteration prevented convergence thus stopping the simulation from moving to the next time step. The life calculated with our model under these assumptions was of 10 cycles. In Figure 99, we plot the experimental and simulated hysteresis and in Figure 100 we plot the evolution of damage.

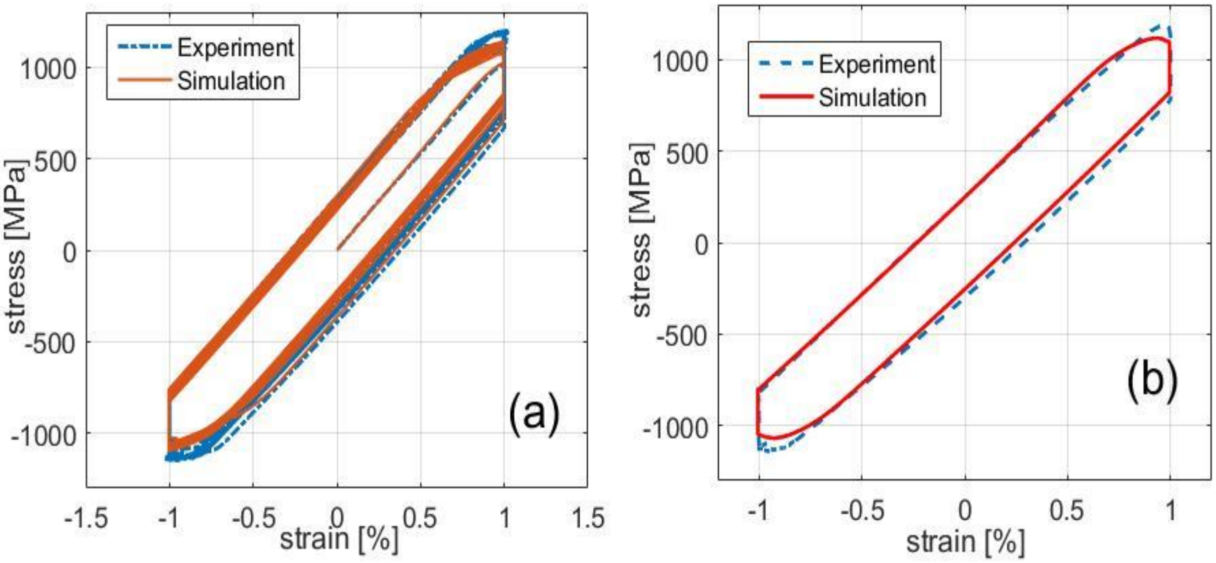

Figure 99: Creep-fatigue at 750°C and strain rate of 1x10^{-3} [1/s] with 20 minute holds at maximum tension and compression: (a) fist ten cycles (b) stabilized hysteresis

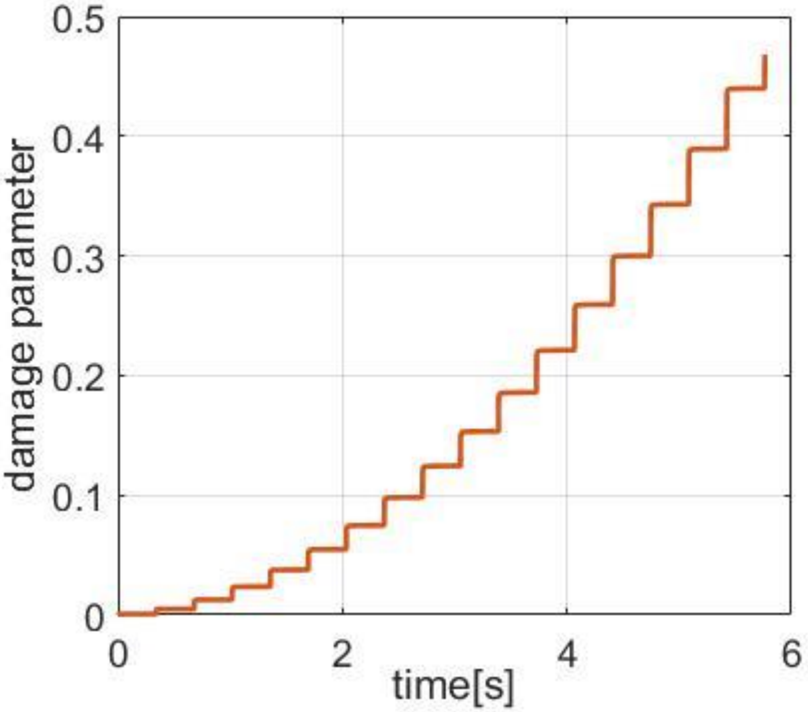

Figure 100: Evolution of damage for creep-fatigue at 750°C and strain rate of 1x10^{-3} [1/s] with 20 minute holds at maximum tension and compression

Note that the model correctly replicates the very large levels of plasticity under these conditions. Moreover, the model provides with a good estimate of the life while allowing to make insightful observations through the evolution of damage. For instance, note that Figure 100 suggests that most of the damage occurred during the loading ramps and, that in comparison, little damage was accumulated during the strain dwells. This type of analysis allows the incorporation of failure into crystal-plasticity frameworks and may help identifying the most damaging loading conditions in the load history of a component which could deliver better turbine blade designs.

6.6 Applications of the microstructure-sensitive crystal-viscoplasticity model to alloy design

6.7 Sensitivity study

The model includes several microstructure-sensitive parameters, for instance the volume fraction of the phases, size of the precipitates, and the APBE. A clear advantage of including these in the modeling is that the effect of changes on microstructural features can be studied and quantified which can provide insightful direction when designing alloys. In this section a sensitivity study is performed on the APBE, the γ channel size and the initial value of dislocation densities in the channels. The sensitivity studies are done at high temperatures where the γ dominates the deformation and at lower temperatures where γ' dominates. Isothermal creep-fatigue tests were simulated at 1100°C and at 750°C. Periods of 3 minute holds were used for the higher temperature and of 20 minutes for the lower temperature so as to allow comparisons with the experimental results reported in this work. All the simulations used a strain rate of $1\text{x}10^{-3}$ (1/s).

In Figure 101, the sensitivity of the response to changes in the APBE is plotted.

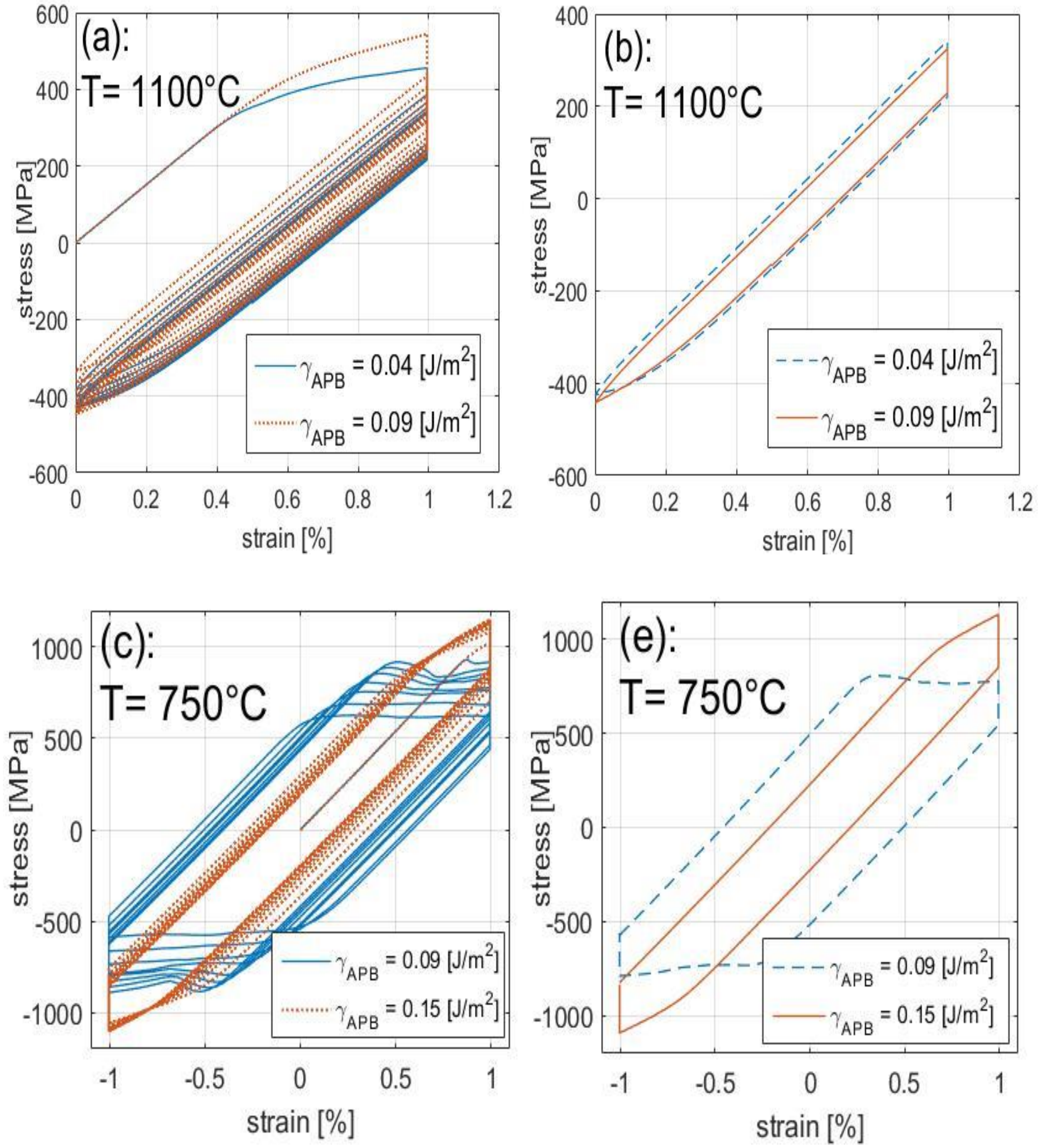

Figure 101. Influence of APBE on mechanical response: (a) fist ten cycles (b) stabilized hysteresis of creep-fatigue at 1100°C and strain rate of 1x10^{-3} [1/s] with 3 minute holds at maximum tension. (c) fist ten cycles (d) stabilized hysteresis of creep-fatigue at 750°C and strain rate of 1x10^{-3} [1/s] with 20 minute holds at maximum tension and compression.

Increasing the APBE has a greater effect at the lower temperatures as shown in Figure 101. This is no surprise considering that at these low temperatures with these high stresses it is the γ' phase that provides the greatest resistance to the movement of dislocations. Reducing the APBE allows for more dislocations to cut through the precipitates. At higher temperatures, changes in APBE affect the initial yield more than they affect the stabilized response. This is attributed to the fact that precipitate shearing takes place during initial loading due to the higher stresses. A cycling is continued, the dislocations begin to stabilize and the material hardens which reduces the effective stress seen by the precipitates.

An interesting observation can be made when analyzing the damage parameter. The damage parameter reveals that a large APBE serves to prolong the life of the specimen which would further justify efforts to try to increase this property. As shown in Figure 102 and Figure 103 when the APBE decreases, more dislocations are able to penetrate and shear the precipitates which also increases the damage parameter thus reducing life.

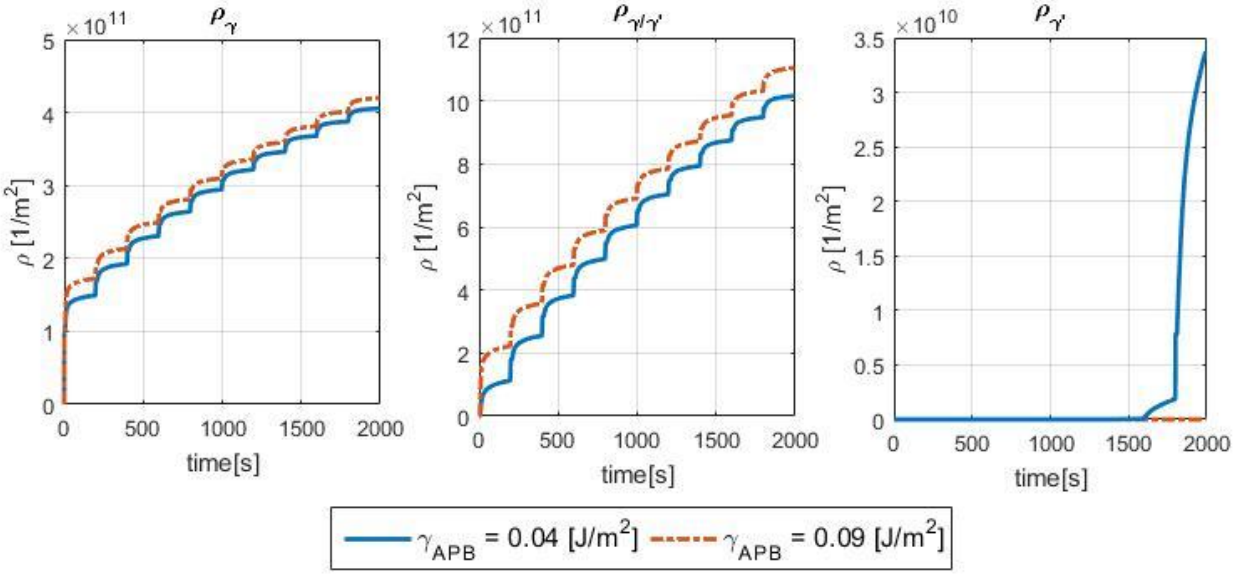

Figure 102. Influence of APBE on dislocation density evolution

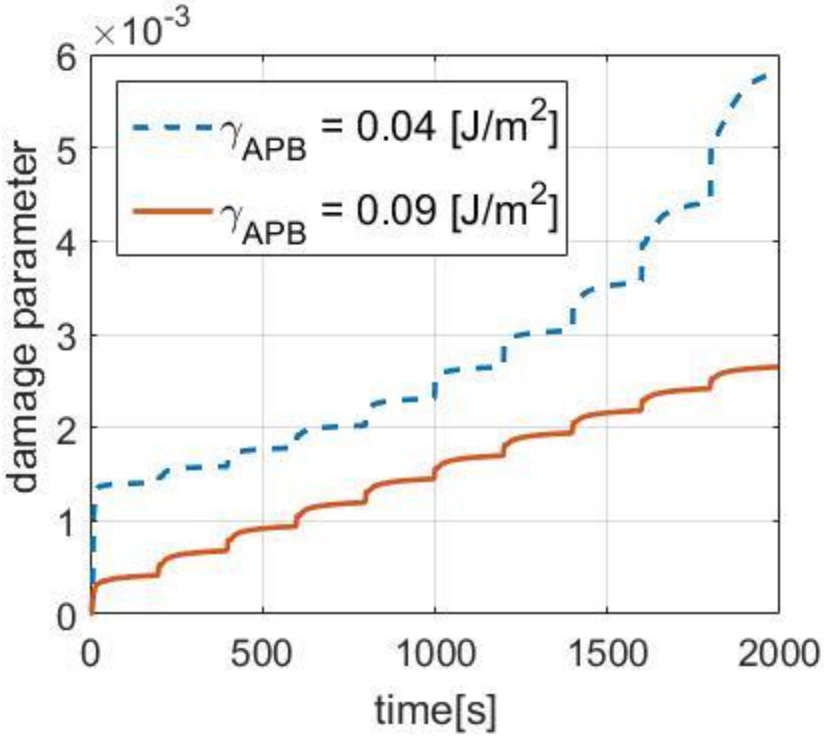

Figure 103. Influence of APBE on damage

Another defining feature of the microstructure in the superalloys is the γ channel size and volume fraction of γ'. As it was done in CHAPTER 4, using equation (56), the γ channel size has been increased while keeping the volume fraction of γ' precipitate constant while adjusting the size of the precipitates accordingly. As it was the case in the creep response, this sensitivity analysis shows that increasing the channel size has and adverse effect on the mechanical response of superalloys, specifically reducing the yield strength, the hardening rate and flow stress during the initial loading and in subsequent loading increasing the plastic strain range and the stress relaxation of the stabilized hysteresis. These adverse effects can be attributed to the reduced coupling of dislocations which in turn reduces the strength of the material.

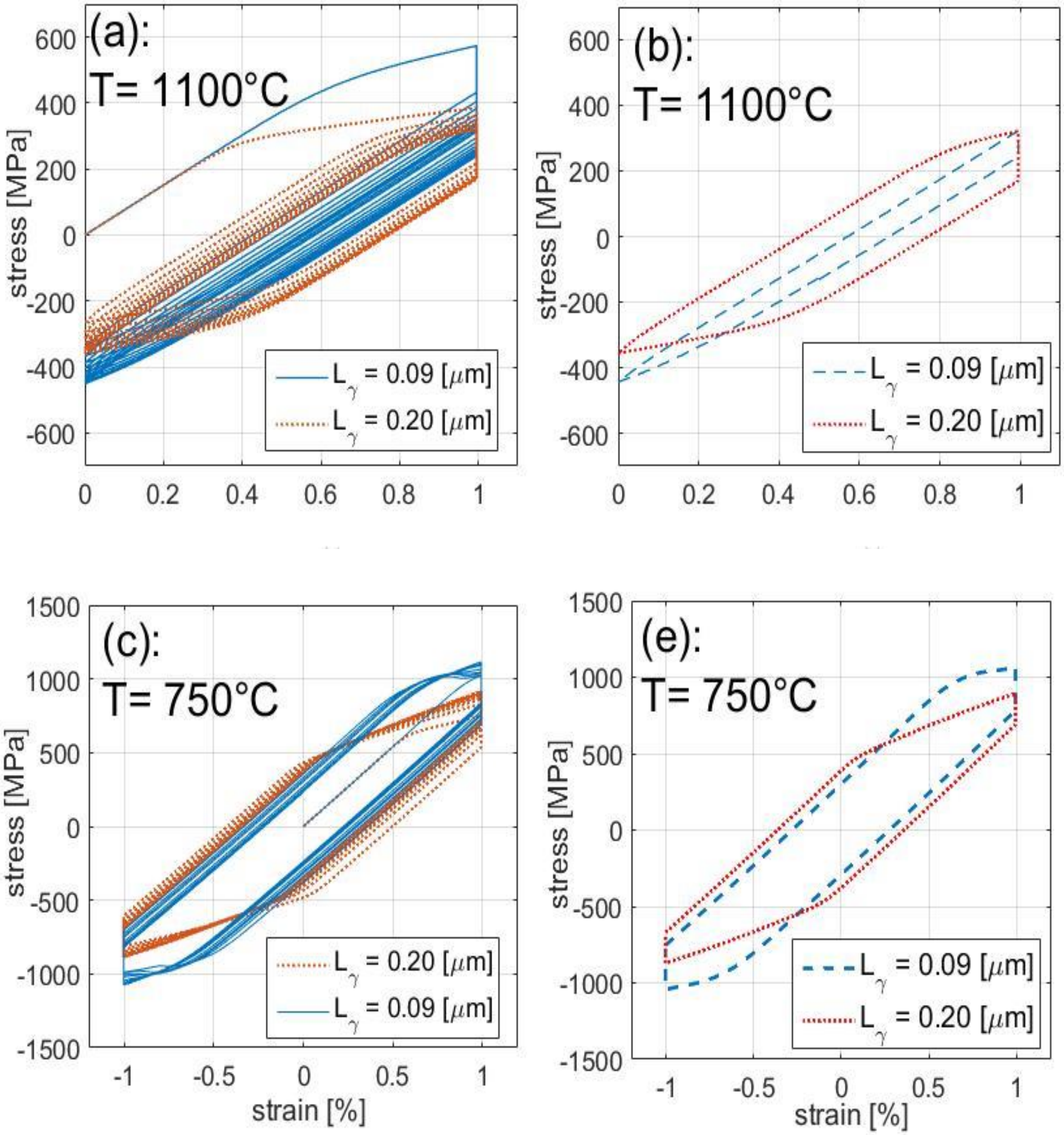

Figure 104. Influence of γ channel size on mechanical response: (a) fist ten cycles (b) stabilized hysteresis of creep-fatigue at 1100°C and strain rate of 1x10^{-3} [1/s] with 3 minute holds at maximum tension. (c) fist ten cycles (d) stabilized hysteresis of creep-fatigue at 750°C and strain rate of 1x10^{-3} [1/s] with 20 minute holds at maximum tension and compression

Finally, the initial amount of dislocations in the γ channels is representative of different aging heat treatments [29, 44]. In Figure 105, the dislocation densities are varied by two orders of magnitude, this variation shows that increasing the initial dislocation density increases the initial strength of the material however little effect is seen in the stabilized hysteresis of the alloys.

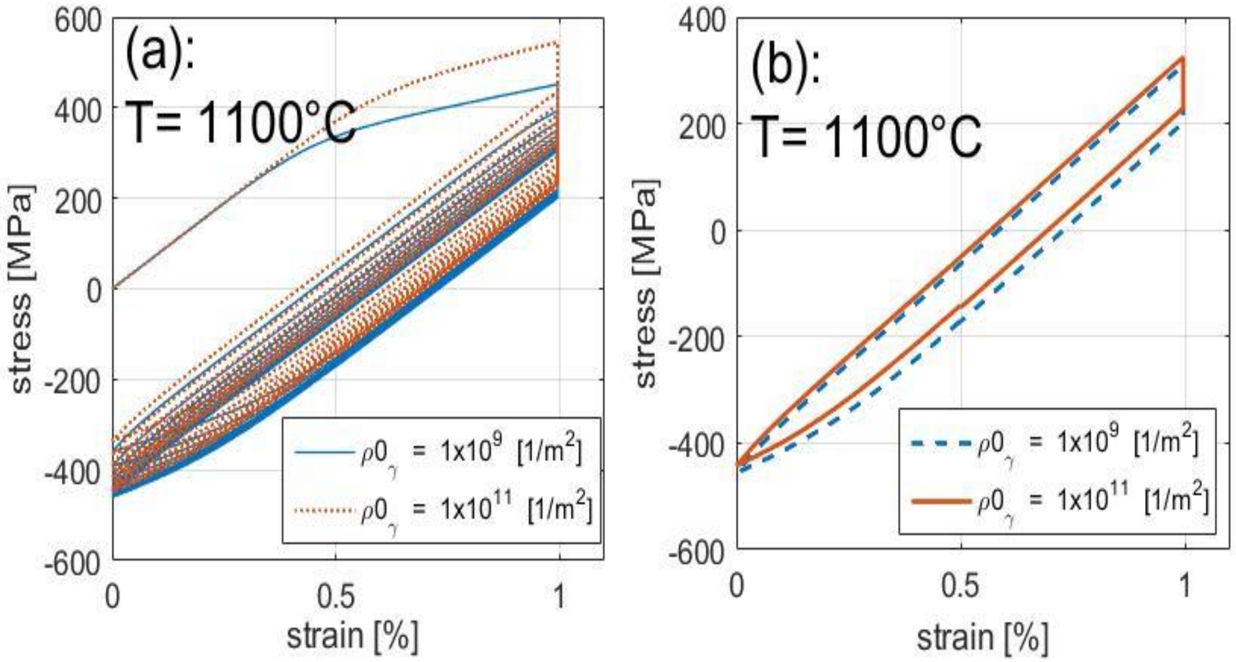

Figure 105: Influence of initial dislocation density in the γ channels on mechanical response: (a) fist ten cycles (b) stabilized hysteresis of creep-fatigue at 1100°C and strain rate of 1x10^{-3} [1/s] with 3 minute holds at maximum tension

6.8 Case study: insights into strengthening behavior of superalloy single-crystals

The model can be used in conjunction with experimental observations to further the understanding of the mechanical behavior of superalloys. In a recent study into the strengthening mechanisms of single-crystal superalloys performed by le Graverend et al. [115], thermal jumps with zero force were imposed at high temperatures. Under this condition a transient increase in strength with respect to the as-heat-treated condition was observed. In the study, it was argued that this transient increase was due to the precipitation of fine γ' particles which pinned dislocations in the channels. It was theorized that after the dissolution of these particles the alloy lost its transient increase in strength. In our model, this mechanism can be simulated by decreasing the mean obstacle spacing in the channels. This provides a first order approximation to the experimental observations made by le Graverend et al. [115]. In Figure 106, we compare these experimental results with model predictions,

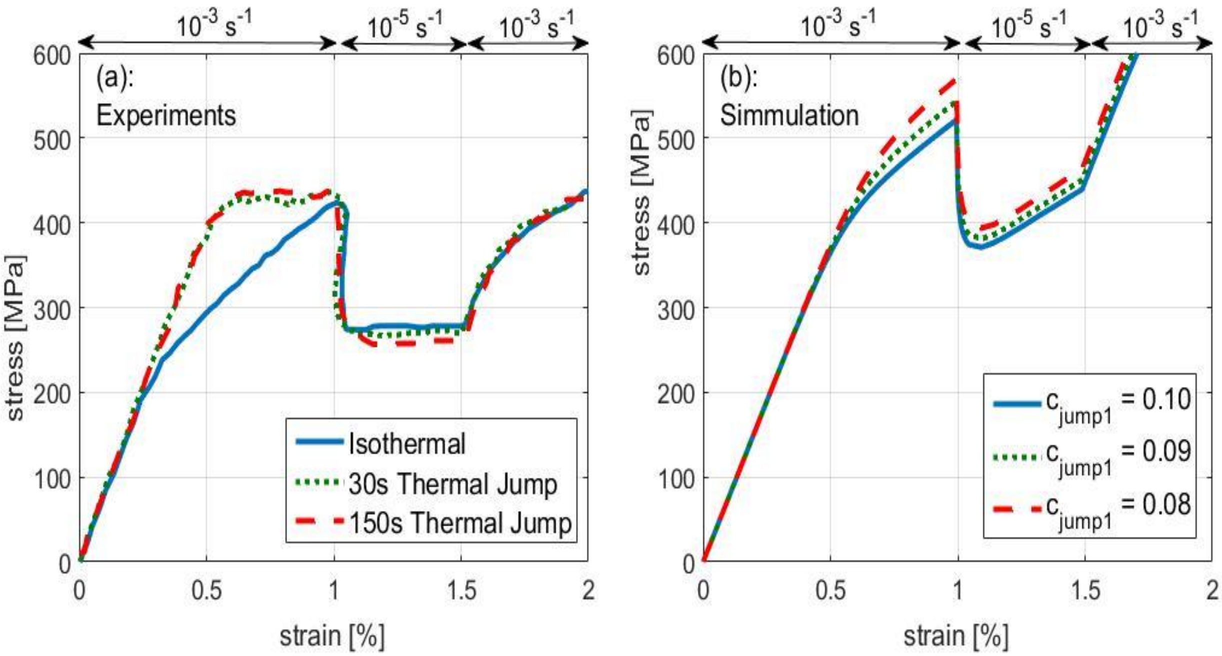

Figure 106. Transient hardening due to temperature jumps: (a): Experimental results on unspecified single-crystal superalloy at 1050°C (b): Simulation of CMSX-8 at 1100°C

In the figure c_{jump1} is varied to simulate the presence of fine γ' in the channels. In the model c_{jump1} is directly proportional to the mean obstacle spacing; therefore, if more γ' prime is present in the channels the value of this constant would be reduced. From Figure 106 it can be seen that the model replicates within reason the observations made by le Graverend et al. [115]. With this example, it is shown that it is possible that the hardening observed in the experiments is due to the formation of pinned dislocations at finer γ' particles. It is worth noting that the model has not been calibrated to the same material used by Graverend et al. [115] and therefore the comparisons on this material are only qualitative. Moreover, the rather simplistic approach that we have proposed would need to be refined if greater level of fidelity was necessary. However, this case serves to demonstrate the capability of the model to extrapolate and help alloy and component designers understand the mechanical behavior of the superalloys to propose better designs.

6.9 Limitations in modeling the effect of crystallographic orientation

The model has shown promise in capturing the mechanical behavior of the superalloys over a wide range of temperatures. However as seen in Figure 107, although the simulation of specimens tested at 1100°C in the <111> orientation correctly predicts the elastic modulus, it does not accurately predict the yield strength, the stress relaxation, and the plastic flow.

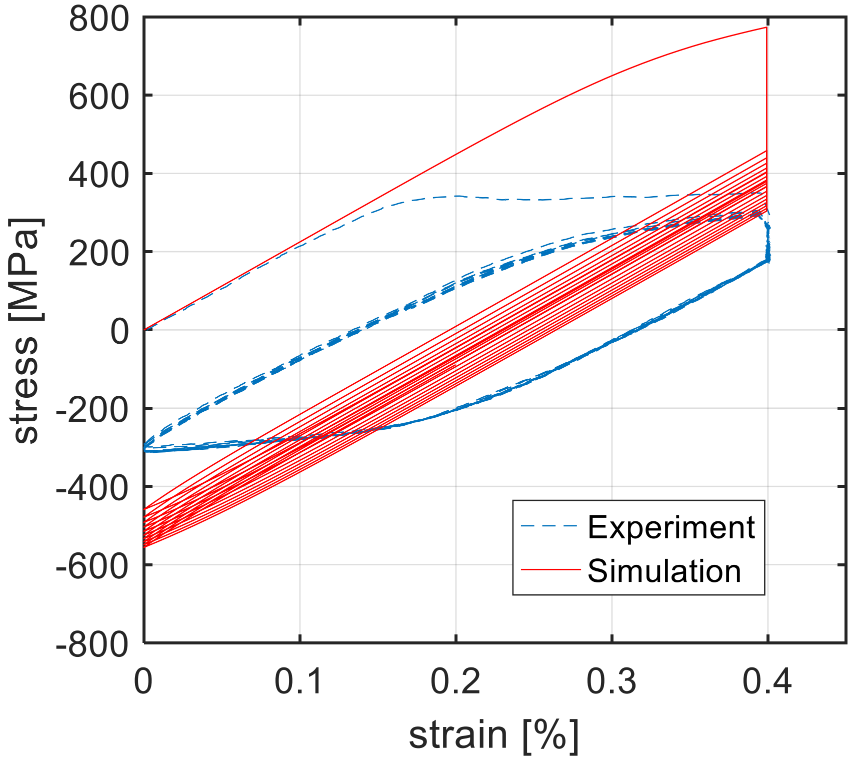

Figure 107: Creep-fatigue in the <111> crystallographic orientation at 1100°C and strain rate of 1x10^{-3} [1/s] with 3 minute holds at maximum tension

A universal set of parameters that worked for all temperatures in the <001>, and the <111> orientation could not be found. To diagnose the problem, the material parameters were varied until reaching better correlation to the <111> results. This exercise helps determine terms in the current formulation of the model that need modifications to account for the effect of orientation. It was found that the dislocation mean obstacle spacing ($\lambda_{\gamma}^{(\alpha)}$), and the threshold stress ($\kappa_{L1_2}^{(\alpha)}$) need further development to properly model the effect of crystallographic orientation.

To approximate the <111> results, parameter c_{jump1} in $\lambda_{\gamma}^{(\alpha)}$ was increased from 9x10^{-2} to 0.3. This suggests that when loaded in the <111> orientation, the dislocation mean obstacle spacing in the γ channels should increase significantly. The increase could be explained by examining the flow rule. In the flow rule, the shearing rates are directly proportional to the velocity of mobile dislocations, which is directly proportional to $\lambda_{\gamma}^{(\alpha)}$. When loaded in the <111> orientation, the Schmid factors are larger than in the <001> orientation, hence promoting larger velocity of dislocations and consequently larger shearing rates which softens the material. The formulation proposed for $\lambda_{\gamma}^{(\alpha)}$and its effect on the velocity of mobile dislocations does not sufficiently capture this softening indicating that further changes to this term and potentially to the flow rule might be necessary to account for the effect of orientation. Additionally, to better correlate to the <111> results, the γ_{APB} parameter in the threshold stress was also changed; decreasing from 0.111 to 0.02 (J/m^2). In the model, it was assumed that only 12 $\{111\}\langle 112\rangle$ slip systems are active in the γ' phase, and therefore the value of APBE should not change with orientation. However, as shown in Table 3 the value of APBE depends on the plane on which the APB resides. It is possible that when loaded at a different orientation and at a high temperature that other slip systems become active on which the APBE is lower. As seen in Figure 108, with these changes in the material parameters, the simulations in the <111> orientation better replicate the yield strength, the plastic flow and the stress relaxation.

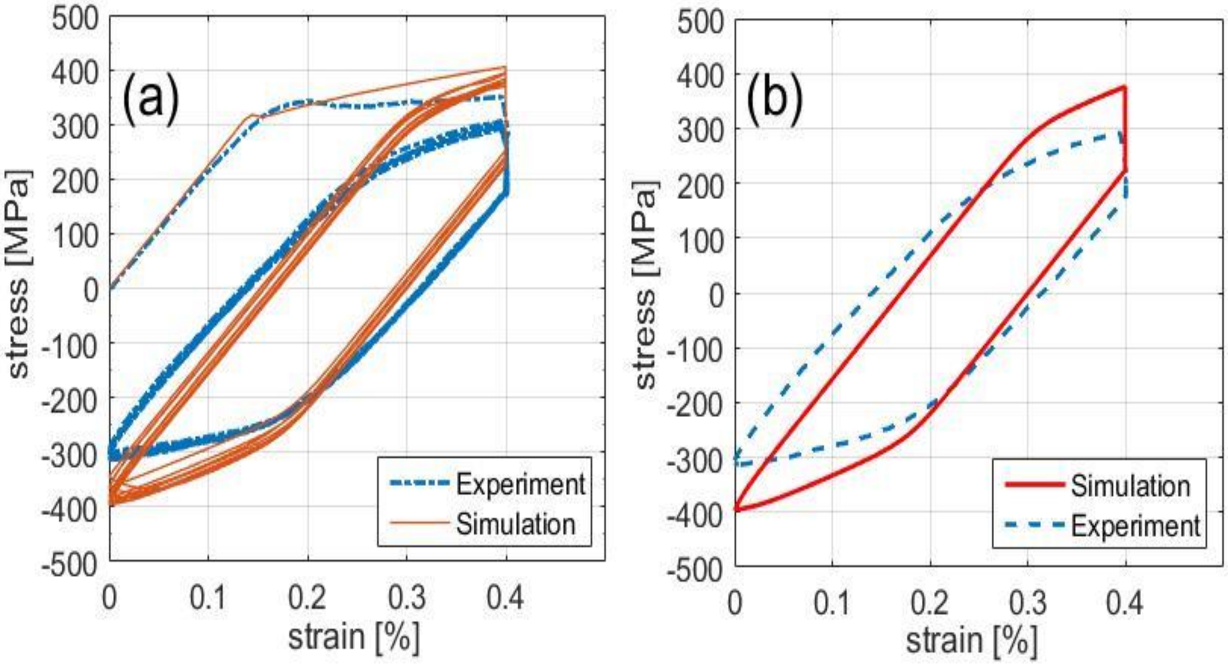

Figure 108: Creep-fatigue at 1100°C and strain rate of 1x10^{-3} [1/s] with 3 minute holds at maximum tension: (a) fist ten cycles (b) stabilized hysteresis

Specimens in different orientations, other than the <001> and the <111>, were not available and hence no further insights or observations could be made to propose changes to the equations. However, the model without any changes still provides the correct trend of deformation. In Figure 109 the mechanical responses for creep-fatigue tests in the *<001>* and in the *<111>* orientation simulated using the calibration obtained solely from experiments in the *<001>* orientation.

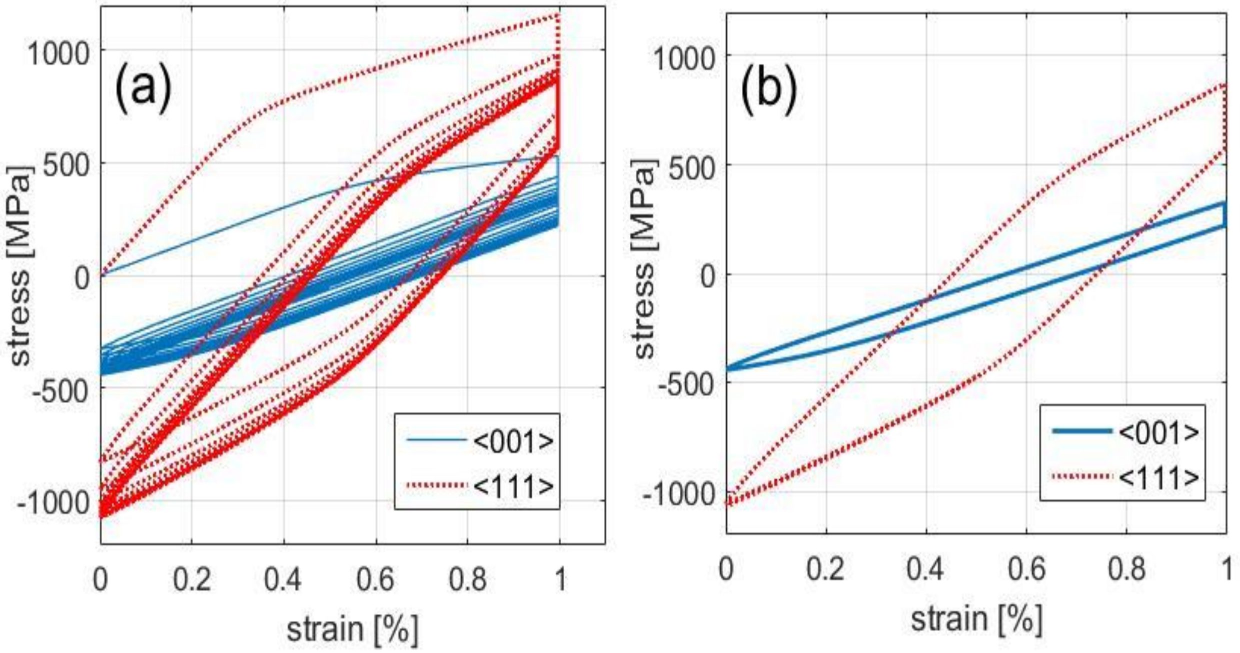

Figure 109. Simulated creep-fatigue response in the <001> and the <111> orientation at 1100°C, strain rate of 1x10^{-3} [1/s] with 3 minute holds at maximum tension

The model correctly predicts the elastic response in the <111>, and provides the correct trend in estimating a larger plastic strain range in the stabilized hysteresis. The influence of orientation on the mechanical response is plotted in Figure 110,

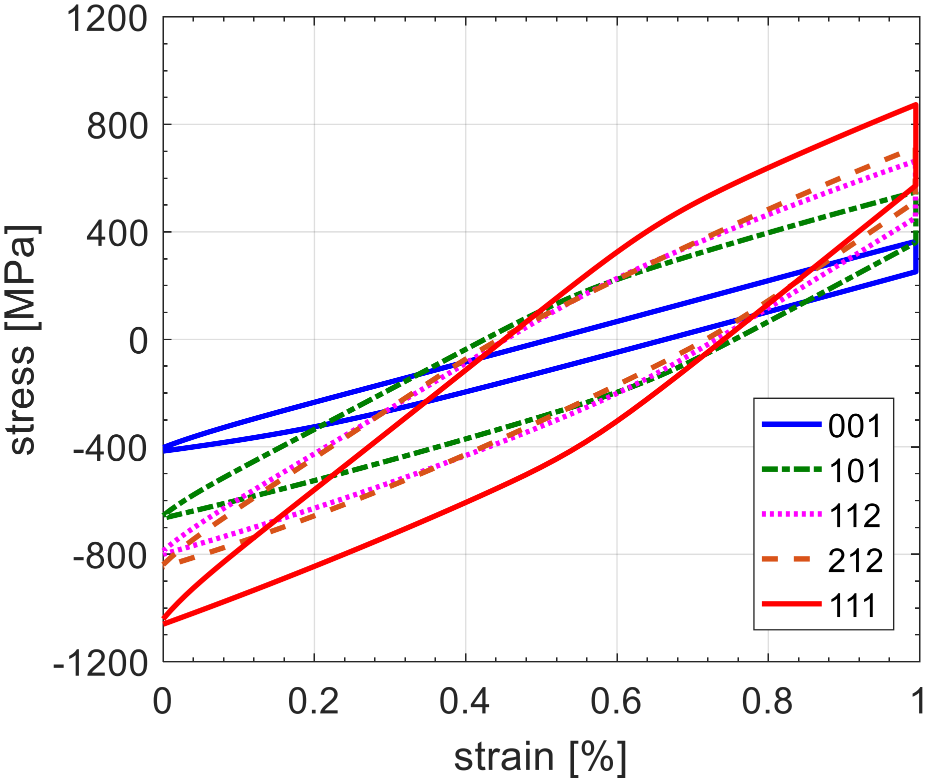

Figure 110: Influence of orientation on strain-controlled constant amplitude response with a 3-minute dwell in tension at 1100°C with strain rate of 1x10^{-3} [1/s]

CHAPTER 7

CONCLUSIONS AND SIGNIFICANCE

A novel microstructure-sensitive crystal-viscoplasticity model targeting the creep-fatigue interactions of single-crystal nickel-base superalloys was developed. The model is unique in that it accounts for the deformation mechanisms in the γ' precipitates and γ matrix separately using two additive shear strain rates which better describes the movement of dislocations in the superalloys. This makes the model able to capture the influence of changes in the γ' precipitate size, morphology, and volume fraction which is necessary to better capture the changes in the creep and fatigue responses at different temperatures. The significance of the work developed in this research falls under three main categories: experimental results of new modified second generation single-crystal superalloy CMSX-8, enhanced material modeling techniques that account for the deformation mechanisms in the γ', γ and γ/γ' interphase, and new numerical methods that enable implementation in the context of 3-dimensional applications of the creep-fatigue interactions.

7.1 Experimental characterization

The experimental work presented has provided a significant amount of mechanical behavior data on the deformation of single-crystal CMSX-8, which was first introduced in the Superalloys 2012 proceedings in Silver Springs, PA. A summary of the experimental findings of this work are:

1. Monotonic response: The temperature-dependent stress-strain response in tension and in compression was measured in the <001> and in the <111> crystallographic orientations. The anomalous yield strength in this alloy was also quantified. An interesting finding is that the yield strength of CMSX-8 does not exhibit discernible tension/compression yield asymmetry. It was also notable that the 0.2% yield strength of CMSX-8[B/C] at room temperature is 15% higher than nominal CMSX-8, while yield strengths at higher temperatures are comparable.
2. Creep response: The primary creep and tertiary creep behavior of CMSX-8 is stress and temperature dependent. For this alloy, at a temperature below 900°C, an applied stress in the order of 550 MPa is necessary for primary creep to be present promoted by the shearing of the precipitates. Conversely, for an applied stress below 550 MPa and at temperatures greater than 900°C, tertiary creep is the dominant mode of deformation and is promoted by climb and glide of dislocations in the channels. Finally, the experimental data in the Larson-Miller plots suggest that the reduction in Re in CMSX-8 affects the creep rupture performance of the alloy at very high temperatures with respect to CMSX-4.
3. Life: The life of creep-fatigue (CF with three-minute dwells) and low-cycle fatigue (LCF) CMSX-8 specimens tested in laboratory air is a function of strain range, crystallographic orientation, and mean stress evolution. The evolution of stress was shown to play an important role in determining life. Specimens that evolved compressive mean stress tend to exhibit longer lives. The role of the environment and crack behavior on life was not studied.

4. Evolution of stress: Stress evolution is affected by the joint effect of the stress relaxation (during strain dwells) and the strain ratio (*R*). CF tests with strain ratio of zero and strain dwells at maximum tension evolved to a compressive mean stress. Conversely, LCF tests with the same strain ratio but with no strain dwells evolved a tensile mean stress. For CF tests with strain ratio of -∞ and strain dwells at maximum compression, the stress relaxation during the strain dwell promoted the evolution of a tensile mean stresses. On the contrary, LCF loaded for the same strain ratio resulted in the mean stress evolving toward a compressive mean. The case for TMF was similar to the creep-fatigue case, with IP TMF leading to negative mean stress.
5. Cyclic creep and hardening behavior: It was observed that for CMSX-8 the cyclic creep experienced under asymmetric cycles was most observable at lower temperatures, while at the highest temperature the hysteresis very quickly stabilizes leaving no visible cyclic creep. Additionally, a considerable amount of hardening is experienced at very high temperatures in the <111> orientation.

7.2 Constitutive relations modeling creep-fatigue interactions in Ni-base superalloys single-crystals

The Ma et al. model [43] allowed two different flow rules to be introduced in the velocity gradient which better resembles the deformation of Ni-base superalloy single-crystals. However, this model could only be used for simple 1-D stress-based creep. The model presented in this work has been extended to 3-D creep, fatigue, creep-fatigue interactions and thermomechanical fatigue. The major changes that allow this constitutive model to be implemented in the context of 3-D creep-fatigue are:

1. The flow rule of the γ channels was modified by including a strain rate sensitivity exponent. It was shown in this work that this term is needed to capture both the strain rate sensitive and the strain rate insensitive regime. The Arrhenius formulation without this term, as used in the literature, can only model creep or fatigue but cannot successfully model the creep-fatigue coupling.
2. A sign function and the backstress have been introduced in the flow rules. The sign function is used to account for the load reversals since during fatigue cycles there will be loading and unloading. The backstress is applied in the γ phase flow rule using a dislocation-based saturation and recovery approach which helps in capturing the Bauschinger effect and dislocation pile-ups.
3. The minimum mean obstacle spacing between dislocations in the precipitates is determined. As dislocations multiply inside the precipitates, they are prevented from becoming infinitely close to each other by imposing a minimum distance between them. This distance, obtained from force balance between two dislocations, prevents artificial hardening of dislocations that become infinitely close to each other.
4. The dislocation density evolution of the γ/γ' interphase was explicitly modeled. Also, this evolution is linked to the evolution of the dislocations within the precipitates which models the process of dislocations forming at the channels and then gathering at the interphase before shearing the precipitates. Finally, the strengthening due to increased incoherency at the interphase is also modeled through the modification of the passing stress in the γ' precipitates.

7.3 Implementation and sensitivity studies

The model was implemented in two forms, first as a 1-D stress-based creep MATLAB® routine and second as a 3-D displacement-based ABAQUS UMAT:

1. The 1-D stress-based implementation showed to be useful for performing quick trade-offs of microstructure and material parameters that could become valuable for alloy designers. Although the model is to a large extent phenomenological, several physically-based parameters were introduced that can allow changes in microstructure attributes such as the size of the γ channels and γ' precipitates, and their volume fraction. It also allows for adjustments in the lattice parameter, the antiphase boundary energy, and the initial dislocation density in the γ channels. Therefore, the effect of changes in these microstructure attributes on the response as a function of temperature, stress, time, and orientation can be explored.
2. A novel quasi Newton-Raphson numerical algorithm was developed to enable implementation of the model in 3-D. The algorithm allows integration of the constitutive relations when the plastic velocity gradient is partitioned between the contributions to the overall deformation of the γ and γ' phases. Although this algorithm was developed to address superalloys and their 2-phase microstructure, it can be readily used with other alloy systems in which deformation contributions of the distinct material phases can individually be modeled and included as separate terms in the plastic velocity gradient.
3. The 3-D implementation of the creep-fatigue interactions were in good agreement with the CF experimental data. Also, the model was validated using TMF data and good agreement across temperatures ranging from 100°C to 1100°C was achieved.

4. Trade-off studies showed that the model correctly predicts known trends of the deformation of superalloys. With further development, the model could be used to quantitatively assess the changes on the creep-fatigue response due to changes in the microstructure. The sensitivity studies suggested that increasing the APBE can lead to less damage and longer life, also small variations in γ channel size have a significant effect in the plastic behavior, with larger channel size leading to larger plastic strain range in the hysteresis loops, lower yield strength, and shorter creep life.

Implementing the model in its full three-dimensional formulation as an ABAQUS user material subroutine shows promise in studying the effect of changes in critical microstructure attributes that spatially vary as a function of processing, heat treatment, and aging on the creep-fatigue or TMF behavior. This increased fidelity is a necessary first step that can allow designers construct sets of virtual experiments and that could lead to alloy-process design and component performance, hence serving as a structure-property tool for Integrated Computational Materials Engineering (ICME) of superalloys.

CHAPTER 8

RECOMENDATIONS

Despite the significant improvement in the modeling of nickel-base superalloy constitutive response achieved by this research, there remain several open issues that will need further development:

1. During service conditions, hot section superalloy components of turbine engines experience an evolution of their microstructure in the form of rafting. The superalloys' microstructure, depending on the magnitude and direction of the loading, can experience coarsening or form N-rafts, or P-rafts. Since the model explicitly accounts for the morphology of the microstructure, it can be easily extended to account for this behavior in the constitutive response. There are two approaches to achieving this. In the first approach, and perhaps as a very simple first approximation, the microstructure could be assumed to be rafted already. In its rafted state, the microstructure parameters such as the $L\gamma$ and $L\gamma'$ can be adapted to account for the orientation dependence of the rafted morphology. The mechanisms for the movement of dislocations in the rafted configuration could be different and thus the evolution equations for the dislocation densities could need changes to reflect that. Evolution kinetics formulations such as the ones proposed by Gorgannejad et al.[101], Epishin et al.[116], and Kirka [46] could be used to infer the state of the microstructure after being in service, which would become an input the CVP model. If more fidelity was needed, a second approach to incorporating the evolution of the microstructure would be to include a time, stress and temperature dependent formulations to the microstructure parameters and to the evolution equations of the dislocation densities. This approach would require adding a significant amount of

complexity to the model. However, the microstructure of the superalloys continues to evolve until it reaches a saturation point, therefore if a superalloy component is expected to reach its saturated microstructure shortly after it is put into service, the additional layer of complexity in the model might not provide with additional insights in comparison with a simpler formulation. Moreover, rafting mostly affects the life of components, and its effect on the constitutive response is not yet apparent, hence it is not clear whether the modeling it in constitutive models is necessary.

2. Although the model successfully predicted the trends of deformation, it would likely require recalibration of the dislocation mean free path constant for different orientations. The usage of crystal plasticity alone was insufficient to accurately model the yield strength, the plastic flow and the stress relaxation on the <111> orientation without having to recalibrate model parameters c_{jump1} and γ_{APB}. It could be theorized that over different crystal orientations, there are geometric effects that directly affect the mean free path and the effect of the APB resistance which the rather simplistic formulations used in equation (26), (35), and (39) cannot not capture. Therefore, more understanding on how dislocations travel when the material is loaded on different orientations is needed to refine the description of the mean free path and of the APB resistance. To this end, testing on additional orientations and additional calibrations might be useful in understanding the functional form of the dislocation mean free path and of the antiphase boundary resistance.
3. Although several case studies useful for alloy design were presented in this work, the approach could be greatly enhanced by incorporating the effect of alloy composition in the material parameter, hence connecting a fundamental linkage of the processing to the

structure of the material. As a first step, data available in the literature for other Ni-base superalloy single-crystals could be used to re-calibrate the model and gain understanding on which material parameters become affected by changes in composition. For instance, the model could be calibrated to CMSX-4, which main difference with respect to CMSX-8 is its %wt. Re. At a later stage, software such as Thermo-Calc and its diffusion model (DICTRA) can be used to further understand the effect of composition on the constitutive response by connecting diffusion controlled reactions to physical terms in the flow rule. Adding this level of detail could enable alloy designers to select the elemental composition and weight fractions that can lead to superior superalloys.

4. The spatial variation of the γ/γ' microstructure is known to vary depending on whether measurements are made in the dendritic region or in the interdendritic region. The dendritic region displays the finest and most uniform distribution of the γ/γ' microstructure, while the interdendritic region shows a coarser and less well defined microstructure. Hence, with the model developed in this work, the dendritic and interdendritic region could be simulated to explore the influence of this heterogeneity at a length scale spanning several dendrites.
5. Additive manufacturing offers exciting opportunities for the development of hot-path components made from superalloys. In recent work, some researchers have been able to manufacture Ni-base superalloy components using additive manufacturing techniques. These techniques can make it possible to propose and manufacture intricate designs that can further push the state of the art of cooling strategies and thermal efficiencies. The U.S. Department of Energy, Los Alamos National Laboratory, Sandia National Laboratory, Oak Ridge National Laboratory, among other private and government

entities are pioneers in additive manufacturing processing and modeling work. In the modeling work, researches have been able to recreate 3-D printed microstructures to which they have attached a very simple flow rule to each grain. The physically-based model presented in this research would better represent the constitutive behavior of additive manufactured parts. Therefore, sensitivity studies could be proposed in which grain size, orientation and layout would be varied which could serve to gain understanding of configurations that yield better performance.

REFERENCES

1. Perepezko, J.H., *Materials science. The hotter the engine, the better.* Science, 2009. **326**(5956): p. 1068-9.

2. Gurrappa, I. and A.S. Rao, *Thermal barrier coatings for enhanced efficiency of gas turbine engines.* Surface & Coatings Technology, 2006. **201**(6): p. 3016-3029.

3. Padture, N.P., M. Gell, and E.H. Jordan, *Thermal barrier coatings for gas-turbine engine applications.* Science, 2002. **296**(5566): p. 280-4.

4. Neu, R.W. and D.J. Smith, *Modeling Creep-Fatigue Deformation of Ni-Base Superalloys Using Crystal Viscoplasticity.* Journal of ASTM International, 2011. **8**(5): p. JAI103674.

5. Tinga, T., W.A. Brekelmans, and M.G.D. Geers, *Cube slip and non-Schmid effects in single crystal Ni-base superalloys.* Modeling and simulation in material science and engineering 2010. **18**.

6. Wahl, J.B. and K. Harris. *New Single Crystal Superalloys, CMSX-7 and CMSX-8*. in *Superalloys 2012* 2012. Seven Springs Mountain Resort,Seven Springs, PA: TMS.

7. Reed, R.C., *Superalloys - Fundamentals and Applications*. 2006: Cambridge University Press.

8. Nabarro, F.R.N. and H.L.d. Billiers, *The physics of Creep*. 1995: CRC Press.

9. Konter, M. and M. Thumann, *Materials and manufacturing of advanced industrial gas turbine components.* Journal of Materials Processing Technology, 2001. **117**(3): p. 386-390.

10. Lean, M.M., *Directionally Solidified Materials for High Temperature Service*. 1983: Metals Society.

11. Monkman, F.C. and N.J. Grant, *An Empirical Relationship Between Rupture Life and Minimum Creep Rate in Creep-Rupture Tests*, in *ASTM Proceeding 1956*. 1956.

12. Dunand, D.C., B.Q. Han, and A.M. Jansen, *Monkman-grant analysis of creep fracture in dispersion-strengthened and particulate-reinforced aluminum.* Metallurgical and Materials Transactions A, 1999. **30**(13): p. 829-838.

13. Olson, G.B., *Computational design of hierarchically structured materials.* Science, 1997. **277**(5330): p. 1237-1242.

14. Gong, J., H.Z.D.A. Peralta, D. Snyder, M.P. Enright, J. McFarland, J. Neumann, J. Sebastian, and G. Olson, *Integrated Thermal Process Optimization of Alloy 718PLUS® for Additive Manufacturing*, in *Superalloys 2016*, M. Hardy, E. Huron, U. Glatzel, B.

Griffin, B. Lewis, C. Rae, V. Seetharaman, and S. Tin, Editors. 2016, TMS (The Minerals, Metals & Materials Society): Seven Springs, PA. p. 1031-1040.

15. Xiong, W. and G.B. Olson, *Cybermaterials: materials by design and accelerated insertion of materials.* Npj Computational Materials, 2016. **2**: p. 15009.

16. Panchal, J.H., S.R. Kalidindi, and D.L. McDowell, *Key computational modeling issues in Integrated Computational Materials Engineering.* Computer-Aided Design, 2013. **45**(1): p. 4-25.

17. Zhu, Z., H. Basoalto, N. Warnken, and R.C. Reed, *A model for the creep deformation behaviour of nickel-based single crystal superalloys.* Acta Materialia, 2012. **60**(12): p. 4888-4900.

18. Cormier, J. and G. Cailletaud, *Constitutive modeling of the creep behavior of single crystal superalloys under non-isothermal conditions inducing phase transformations.* Materials Science and Engineering: A, 2010. **527**(23): p. 6300-6312.

19. Fedelich, B., A. Epishin, T. Link, H. Klingelhöffer, G. Künecke, and P.D. Portella, *Rafting during High Temperature Deformation in a Single Crystal Superalloy: Experiments and Modeling*, in *Superalloys 2012*. 2012, John Wiley & Sons, Inc. p. 491-500.

20. le Graverend, J.B., J. Cormier, F. Gallerneau, P. Villechaise, S. Kruch, and J. Mendez, *A microstructure-sensitive constitutive modeling of the inelastic behavior of single crystal nickel-based superalloys at very high temperature.* International Journal of Plasticity, 2014. **59**: p. 55-83.

21. Pollock, T.M. and A.S. Argon, *Directional Coarsening in Nickel-Base Single-Crystals with High-Volume Fractions of Coherent Precipitates.* Acta Metallurgica Et Materialia, 1994. **42**(6): p. 1859-1874.

22. Ford, D.A. and R.P. Arthey, *Development of single crystal alloys for specifit engine applications*, in *Superalloys 1984*, W.B.K. R. H. Bricknell, M. Gell, C.S. Kortovich, J. F. Radavich, Editor. 1984, The metallurgical society of AIME: Warrendale, PA. p. 114-124.

23. Harris, K., G.L. Erickson, S.L. Sikkenga, W.D. Brentnall, J.M. Aurrecoechea, and K.G. Kubarych, *Development of the rhenium containing superalloys CMSX-4 and CM 186 LC for single crystal blade and directionally solidified vane applications in advanced turbine engines*, in *Superalloys 1992*, R.W.S. S. D. Antolovich, R. A. MacKay, D. L. Anton, T. Khan, R. D. Kissinger, D. L. Klarstrom, Editor. 1992, The Minerals, Metals and Materials Society (TMS): Warrendale, PA. p. 297-306.

24. Cetel, A.D. and D.N. Duhl, *Second-generation nickel-base single crystal superalloy*, in *Superalloys 1988*, D.N.D. S. Reichman, G. Maurer, S. Antolovich, C. Lund, Editor. 1988, The metallurgical society: Pennsylvania, USA.

25. Giamei, A.F. and D.L. Anton, *Rhenium additions to a Ni-base superalloy: Effects on microstructure*. Metallurgical Transactions A, 1985. **16**(11): p. 1997-2005.

26. Blavette, D., P. Caron, and T. Khan, *An atom-probe study of some fine-scale microstructural features in Ni-based single crystal superalloys*, in *Superalloys 1988* D.N.D. S. Reichman, G. Maurer, S. Antolovich, C. Lund, Editor., The Metallurgical Society of AIME. p. 305-314.

27. Karunaratne, M.S.A., P. Carter, and R.C. Reed, *Interdiffusion in the face-centred cubic phase of the Ni-Re, Ni-Ta and Ni-W systems between 900 and 1300 degrees C*. Materials Science and Engineering a-Structural Materials Properties Microstructure and Processing, 2000. **281**(1-2): p. 229-233.

28. Darolia, R., D.F. Lahrman, and R.D. Field, *Formation of topologically closed packed phases in nickel base single crystal superalloys*, in *Superalloys 1988*, D.N.D. S. Reichman, G. Maurer, S. Antolovich, C. Lund, Editor. 1988, The metallurgical society: Pennsylvania, USA.

29. Wilson, B.C. and G.E. Fuchs, *The effect of composition, misfit and heat treatment on the primary creep behavior of single crystal nickel base superalloys PWA 1480 and PWA 1484*, in *Superalloys 2008*, K.A.G. R. C. Reed, P. Caron, T. Gabb, M. G. Fahrmann, E. S. Huron, S. A. Woodard, Editor. 2008, The Minerals, Metals & Materials Society: Pennsylvania, USA.

30. Wilson, B.C. and G.E. Fuchs, *The Effect of Secondary Gamma-Prime on the Primary Creep Behavior of Single-Crystal Nickel-Base Superalloys*. Metallurgical and Materials Transactions A, 2010. **41**(5): p. 1235-1245.

31. Yandt, S., X.J. Wu, N. Tsuno, and A. Sato, *Cyclic Dwell Fatigue Behaviour of Single Crystal Ni-Base Superalloys with/without Rhenium*, in *Superalloys 2012*. 2012, John Wiley & Sons, Inc. p. 501-508.

32. Safari, J. and S. Nategh, *On the heat treatment of Rene-80 nickel-base superalloy*. Journal of Materials Processing Technology, 2006. **176**(1-3): p. 240-250.

33. Mehta, K.K., R. Mitra, and S. Chawla, *Effect of post-solutionizing cooling rate on microstructure and low cycle fatigue behavior of a cast nickel based superalloy*. Materials Science and Engineering: A, 2014. **611**: p. 280-289.

34. Bower, A.F., *Applied mechanics of solids*. 2009: CRC press.

35. Donachie, M.J. and S.J. Donachie, *Superalloys: A Technical Guide, 2nd Edition*. 2002: ASM International.

36. Caron, P., Y. Ohta, Y.G. Nakagawa, and T. Khan, *Creep deformation anisotropy in single crystal superalloys*, in *Superalloys 1988*, D.N.D. S. Reichman, G. Maurer, S. Antolovich, C. Lund, Editor. 1988, The metallurgical society: Pennsylvania, USA.

37. Reppich, B., *Some new aspects concerning particle hardening mechanisms in γ' precipitating Ni-base alloys—I. Theoretical concept.* Acta Metallurgica, 1982. **30**(1): p. 87-94.

38. Reppich, B., P. Schepp, and G. Wehner, *Some new aspects concerning particle hardening mechanisms in γ' precipitating nickel-base alloys—II. Experiments.* Acta Metallurgica, 1982. **30**(1): p. 95-104.

39. Nembach, E. and G. Neite, *Precipitation hardening of superalloys by ordered γ'-particles.* Progress in Materials Science, 1985. **29**(3): p. 177-319.

40. Veyssière, P., *Yield stress anomalies in ordered alloys: a review of microstructural findings and related hypotheses.* Materials Science and Engineering: A, 2001. **309–310**: p. 44-48.

41. Caillard, D., G. Molénat, and V. Paidar, *On the role of incomplete Kear-Wilsdorf locks in the yield stress anomaly of Ni3Al.* Materials Science and Engineering: A, 1997. **234–236**: p. 695-698.

42. Veyssière, P. and G. Saada, *Chapter 53 Microscopy and plasticity of the L12 γphase*, in *Dislocations in Solids*, F.R.N. Nabarro and M.S. Duesbery, Editors. 1996, Elsevier. p. 253-441.

43. Ma, A., D. Dye, and R.C. Reed, *A model for the creep deformation behaviour of single-crystal superalloy CMSX-4.* Acta Materialia, 2008. **56**(8): p. 1657-1670.

44. Pollock, T.M. and A.S. Argon, *Creep Resistance of CMSX-3 Nickel-Base Superalloy Single-Crystals.* Acta Metallurgica Et Materialia, 1992. **40**(1): p. 1-30.

45. Tien, J.K. and R.P. Gamble, *Effects of stress coarsening on coherent particle strengthening.* Metallurgical Transactions, 1972. **3**(8): p. 2157-2162.

46. Kirka, M., *Thermomechanical behavior of a directionally solidified nickel-base superalloy in the aged state*, in *The George W. Woodruff School of Mechanical Engineering*. 2014, Georgia Institute of Technology: Atlanta, Georgia p. 230.

47. Arrell, D., Hasselqvist, M., Sommer, C., and Moverare, J., *On TMF Damage, Degradation Effects, and the Associated Tmin Influence on TMF Test Results in gamma/gamma prime Alloys.* Superalloys 2004, 2004.

48. Epishin, A., T. Link, H. Klingelhoffer, B. Fedelich, and P. Portella, *Creep damage of single-crystal nickel base superalloys: mechanisms and effect on low cycle fatigue.* Materials at High Temperatures, 2010. **27**(1): p. 53-59.

49. Clavel, M. and A. Pineau, *Fatigue behaviour of two nickel-base alloys I: Experimental results on low cycle fatigue, fatigue crack propagation and substructures.* Materials Science and Engineering, 1982. **55**(2): p. 157-171.

50. Rae, C.M.F. and R.C. Reed, *Primary creep in single crystal superalloys: Origins, mechanisms and effects.* Acta Materialia, 2007. **55**(3): p. 1067-1081.

51. MacKay, R.A. and L. Ebert, *The development of γ-γ′ lamellar structures in a nickel-base superalloy during elevated temperature mechanical testing.* Metallurgical Transactions A, 1985. **16**(11): p. 1969-1982.

52. Matan, N., D.C. Cox, P. Carter, M.A. Rist, C.M.F. Rae, and R.C. Reed, *Creep of CMSX-4 superalloy single crystals: effects of misorientation and temperature.* Acta Materialia, 1999. **47**(5): p. 1549-1563.

53. Matan, N., D.C. Cox, C.M.F. Rae, and R.C. Reed, *On the kinetics of rafting in CMSX-4 superalloy single crystals.* Acta Materialia, 1999. **47**(7): p. 2031-2045.

54. Suresh, S., *Fatigue of Materials*. 2 ed ed. 1998: Cambridge University Press.

55. Shyam, A. and W.W. Milligan, *Effects of deformation behavior on fatigue fracture surface morphology in a nickel-base superalloy.* Acta Materialia, 2004. **52**(6): p. 1503-1513.

56. Pineau, A. and S.D. Antolovich, *High temperature fatigue of nickel-base superalloys – A review with special emphasis on deformation modes and oxidation.* Engineering Failure Analysis, 2009. **16**(8): p. 2668-2697.

57. Fullwood, D.T., S.R. Kalidindi, S.R. Niezgoda, A. Fast, and N. Hampson, *Gradient-based microstructure reconstructions from distributions using fast Fourier transforms.* Materials Science and Engineering: A, 2008. **494**(1–2): p. 68-72.

58. Fullwood, D.T., S.R. Niezgoda, and S.R. Kalidindi, *Microstructure reconstructions from 2-point statistics using phase-recovery algorithms.* Acta Materialia, 2008. **56**(5): p. 942-948.

59. Fernandez-Zelaia, P., *Thermomechanical Fatigue Crack Formation in Nickel-Base Superalloys at Notches*, in *George W. Woodruff School of Mechanical Engineering*. 2012, Georgia Institute of Technology: Atlanta, GA.

60. Yamashita, M. and K. Kakehi, *Tension/compression asymmetry in yield and creep strengths of Ni-based superalloy with a high amount of tantalum.* Scripta Materialia, 2006. **55**(2): p. 139-142.

61. Tsuno, N., S. Shimabayashi, K. Kakehi, C.M.F. Rae, and R.C. Reed, *Tension/compression asymmetry in yield and creep strengths of Ni-based superalloys.* Superalloys 2008, 2008: p. 433-442.

62. Shah, D.M. and D.N. Duhl. *The Effect Of Orientation, Temperature and Gamma Prime Size on the Yield Strength of a Single Crystal Nickel Base Superalloy*. in *Superalloys 1984*. 1984. Seven Springs Mountain Resort, Champion, Pennsylvania: Metallurgical Society of AIME, 1984.

63. Wang-Koh, Y.M., *Understanding the yield behaviour of L12-ordered alloys.* Materials Science and Technology, 2016: p. 1-10.

64. Kulawinski, D., A. Weidner, S. Henkel, and H. Biermann, *Isothermal and thermo-mechanical fatigue behavior of the nickel base superalloy Waspaloy™ under uniaxial and biaxial-planar loading.* International Journal of Fatigue, 2015. **81**: p. 21-36.

65. Ewing, J.A. and W. Rosenhain, *The Crystalline Structure of Metals. (Second Paper).* Philosophical Transactions of the Royal Society A: Mathematical, Physical and Engineering Sciences, 1900. **195**(262-273): p. 279-301.

66. Bragg, W.H. and W.L. Bragg, *The crystalline state. Vol. 1 : A general survey*. 1933: Bell : London.

67. Taylor, G.I., *Plastic strain in metals.* Journal of the Institute of Metals, 1938. **62**: p. 307-324.

68. Taylor, G.I., *The Mechanism of Plastic Deformation of Crystals. Part I. Theoretical.* Proceedings of the Royal Society A: Mathematical, Physical and Engineering Sciences, 1934. **145**(855): p. 362-387.

69. Taylor, G.I. and C.F. Elam, *Bakerian Lecture. The Distortion of an Aluminium Crystal during a Tensile Test.* Proceedings of the Royal Society of London. Series A, Containing Papers of a Mathematical and Physical Character, 1923. **102**(719): p. 643-667.

70. Taylor, G.I. and C.F. Elam, *The Plastic Extension and Fracture of Aluminium Crystals.* Proceedings of the Royal Society of London. Series A, 1925. **108**(745): p. 28-51.

71. Asaro, R.J., *Crystal Plasticity.* Journal of Applied Mechanics-Transactions of the Asme, 1983. **50**(4B): p. 921-934.

72. Asaro, R.J., *Micromechanics of Crystals and Polycrystals*, in *Advances in Applied Mechanics*, W.H. John and Y.W. Theodore, Editors. 1983, Elsevier. p. 1-115.

73. Asaro, R.J. and J.R. Rice, *Strain localization in ductile single crystals.* Journal of the Mechanics and Physics of Solids, 1977. **25**(5): p. 309-338.

74. Hill, R. and K.S. Havner, *Perspectives in the mechanics of elastoplastic crystals.* Journal of the Mechanics and Physics of Solids, 1982. **30**(1): p. 5-22.

75. Schimd, E. *Recent investigations on metal crystals*. in *International congress for applied mechanics*. 1924.

76. Khan, A.S. and S. Huang, *Continuum theory of plasticity*, ed. J.W. sons. 1995, New York: Wiley-Interscience.

77. Fleischer, R.L., *Single crystal lattice rotation during compression.* Journal of the Mechanics and Physics of Solids, 1958. **6**(4): p. 301-306.

78. Dieter, G.E., *Mechanical metallurgy*. 1986: McGraw-Hill.

79. Kocks, U.F. and T.J. Brown, *Latent hardening in aluminum.* Acta Metallurgica, 1966. **14**(2): p. 87-98.

80. Kocks, U.F., *The relation between polycrystal deformation and single-crystal deformation.* Metallurgical and Materials Transactions, 1970. **1**(5): p. 1121-1143.

81. Jackson, P.J. and Z.S. Basinski, *Latent Hardening and the Flow Stress in Copper Single Crystals.* Canadian Journal of Physics, 1967. **45**(2): p. 707-735.

82. Bilby, B.A., R. Bullough, and E. Smith, *Continuous Distributions of Dislocations: A New Application of the Methods of Non-Riemannian Geometry.* Proceedings of the Royal Society of London. Series A. Mathematical and Physical Sciences, 1955. **231**(1185): p. 263-273.

83. Lee, E.H., *Elastic-Plastic Deformation at Finite Strains.* Journal of Applied Mechanics, 1969. **36**(1): p. 1-6.

84. Rice, J.R., *Inelastic Constitutive Relations for Solids - an Internal-Variable Theory and Its Application to Metal Plasticity.* Journal of the Mechanics and Physics of Solids, 1971. **19**(6): p. 433-+.

85. Hill, R. and J.R. Rice, *Constitutive analysis of elastic-plastic crystals at arbitrary strain.* Journal of the Mechanics and Physics of Solids, 1972. **20**(6): p. 401-413.

86. Shenoy, M.M., A.P. Gordon, D.L. McDowell, and R.W. Neu, *Thermomechanical fatigue behavior of a directionally solidified Ni-base superalloy.* Journal of Engineering Materials and Technology-Transactions of the Asme, 2005. **127**(3): p. 325-336.

87. McGuinty, R.D., *Multiscale representation of polycrystalline inelasticity*, in *George W. Woodruff School of Mechanical Engineering*. 2001, Georgia Institute of Technology: Atlanta, GA.

88. Srikanth, A. and N. Zabaras, *A computational model for the finite element analysis of thermoplasticity coupled with ductile damage at finite strains.* International Journal for Numerical Methods in Engineering, 1999. **45**(11): p. 1569-1605.

89. Shenoy, M.M., *Constitutive Modeling and Life Prediction in Ni-Base Superalloys*, in *George W. Woodruff School of Mechanical Engineering*. 2006, Georgia Institute of Technology: Atlanta.

90. Orowan, E., *Problems of plastic gliding.* Proceedings of the Physical Society, 1940. **52**: p. 8-22.

91. Tinga, T., *Multiscale Modelling of Single Crystal Superalloys for Gas Turbine Blades*. 2009, Technische Universiteit Eindhoven.

92. Keshavarz, S., S. Ghosh, A.C.E. Reid, and S.A. Langer, *A non-Schmid crystal plasticity finite element approach to multi-scale modeling of nickel-based superalloys.* Acta Materialia, 2016. **114**: p. 106-115.

93. Keshavarz, S. and S. Ghosh, *Hierarchical crystal plasticity FE model for nickel-based superalloys: Sub-grain microstructures to polycrystalline aggregates.* International Journal of Solids and Structures, 2015. **55**: p. 17-31.

94. Deutchman, H.Z., P.J. Phillips, N. Zhou, M.K. Samal, S. Ghosh, Y. Wang, and M.J. Mills, *Deformation Mechanisms Coupled with Phase Field and Crystal Plasticity Modeling in a High Temperature Polycrystalline Ni-Based Superalloy.* Superalloys 2012, 2012: p. 25-33.

95. Vorster, W.J.J. and F.P.E. Dunne, *Crystal plasticity and multiscale modelling of superalloy creep.* Philosophical Magazine, 2012. **92**(7): p. 830-848.

96. Mayeur, J.R. and D.L. McDowell, *A three-dimensional crystal plasticity model for duplex Ti–6Al–4V.* International Journal of Plasticity, 2007. **23**(9): p. 1457-1485.

97. Zhang, M., *Crystal Plasticity Modeling of Ti-6Al-4v and Its Application in Cyclic and Fretting Fatigue Analysis*, in *School of Mechanical Engineering*. 2008, Georgia Institute of Technology.

98. Patra, A., T. Zhu, and D.L. McDowell, *Constitutive equations, for modeling non-Schmid effects in single crystal bcc-Fe at low and ambient temperatures.* International Journal of Plasticity, 2014. **59**: p. 1-14.

99. Hafez Haghighat, S.M., G. Eggeler, and D. Raabe, *Effect of climb on dislocation mechanisms and creep rates in γ′-strengthened Ni base superalloy single crystals: A discrete dislocation dynamics study.* Acta Materialia, 2013. **61**(10): p. 3709-3723.

100. Messerschmidt, U., *Dislocation Dynamics During Plastic Deformation*. 2010, Springer-Verlag Berlin Heidelberg.

101. Gorgannejad, S., E.A. Estrada Rodas, and R.W. Neu, *Ageing kinetics of Ni-base superalloys.* Materials at High Temperatures, 2016. **33**(4-5): p. 291-300.

102. Estrada Rodas, E.A., S. Gorgannejad, R.W. Neu, R.W. Neu, Z. Dyer, P.M. Draa, Shinde, and S.R, *On the Development of ICME Tools for Creep and Aging of CMSX®-8*, in *Superalloys 2016*. 2016, John Wiley & Sons, Inc. p. 665-674.

103. Busso, E.P. and F.A. McClintock, *A dislocation mechanics-based crystallographic model of a B2-type intermetallic alloy.* International Journal of Plasticity, 1996. **12**(1): p. 1-28.

104. Ma, A. and F. Roters, *A constitutive model for fcc single crystals based on dislocation densities and its application to uniaxial compression of aluminium single crystals.* Acta Materialia, 2004. **52**(12): p. 3603-3612.

105. Ma, A., F. Roters, and D. Raabe, *A dislocation density based constitutive model for crystal plasticity FEM including geometrically necessary dislocations.* Acta Materialia, 2006. **54**(8): p. 2169-2179.

106. Sarkar, A. and J.K. Chakravartty, *Activation Volume and Density of Mobile Dislocations in Plastically Deforming Zr-1pctSn-1pctNb-0.1pctFe Alloy*. Metallurgical and Materials Transactions A, 2015. **46**(12): p. 5638-5643.

107. Kocks, U.F. and H. Mecking, *Physics and phenomenology of strain hardening: the FCC case.* Progress in Materials Science, 2003. **48**(3): p. 171-273.

108. Shenoy, M., Y. Tjiptowidjojo, and D. McDowell, *Microstructure-sensitive modeling of polycrystalline IN 100.* International Journal of Plasticity, 2008. **24**(10): p. 1694-1730.

109. Pyczak, F., B. Devrient, and H. Mughrabi, *The effects of different alloying elements on the thermal expansion coefficients, lattice constants and misfit of nickel-based superalloys investigated by X-ray diffraction.* Superalloys 2004, 2004: p. 827-836.

110. Daniel Leidermark, J.M. *Comparative Analysis of Stress Relaxation and Creep in a Single-Crystal Superalloy*. in *Proceedings of ASME Turbo Expo 2016: Turbine Technical Conference and Exposition*. 2016. Seoul, South Korea.

111. MacKay, R.A. and R.D. Maier, *The influence of orientation on the stress rupture properties of nickel-base superalloy single crystals.* Metallurgical Transactions A, 1982. **13**(10): p. 1747-1754.

112. Fedelich, B., G. Kunecke, A. Epishin, T. Link, and P. Portella, *Constitutive modelling of creep degradation due to rafting in single-crystalline Ni-base superalloys.* Materials Science and Engineering a-Structural Materials Properties Microstructure and Processing, 2009. **510-11**: p. 273-277.

113. Press, W.H., S.A. Teukolsky, W.T. Vetterling, and B.P. Fannery, *Numerical recipies in C: the art of scientific computing*. 2nd ed. 1992: Press Syndicate of the University of Cambridge.

114. ABAQUS, I., *ABAQUS: Analysis User's Manual*. 2014: ABAQUS Incorporated.

115. le Graverend, J.-B., J. Cormier, F. Gallerneau, S. Kruch, and J. Mendez, *Strengthening behavior in non-isothermal monotonic and cyclic loading in a Ni-based single crystal superalloy.* International Journal of Fatigue, 2016. **91, Part 1**: p. 257-263.

116. Epishin, A., T. Link, M. Nazmy, M. Staubli, H. Klingelhöffer, and G. Nolze, *Microstructural Degradation of CMSX-4: Kinetics and Effect on Mechanical Properties.* Superalloys 2008, 2008: p. 725-731.